Energy management of multi-source DC microgrid systems for residential applications

Sadaqat Ali

UNIVERSITÉ DE LORRAINE

IAEM Doctoral School

Energy management of multi-source DC microgrid systems for residential applications

Thesis

Presented and defended on 29 September 2023

in order to get

Doctorate in Electrical Engineering

By

Sadaqat ALI

Jury Members

Président :	M. Damien Guilbert, Pr, GREAH, Université Le Havre Normandie, Le Havre, France
Rapporteurs :	M. Gilles Notton, Pr, Université de Corsica, Ajaccio, France Mme. Anne Migan Dubois, Pr, GeePs, Université Paris-Saclay, Paris, France
Examinateurs :	M. Claude Delpha, Pr, L2S, Université Paris-Saclay, Paris, France Mme. Melika Hinaje, Pr, GREEN, Université de Lorraine, Nancy, France
Invité :	Javier Solano, Dr , European Institute for Energy Research, Karlsruhe, Germany
Directeur :	M. Michel Aillerie, Pr, LMOPS, Université de Lorraine, Metz, France
Codirecteur :	Mme. Zhixue Zheng , Dr, LMOPS, Université de Lorraine, Metz, France

Laboratoire Matériaux optiques, photonique et systèmes (LMOPS)
Université de Lorraine & CentraleSupélec - 57070 Metz, France.

Mis en page avec la classe thesul.

Acknowledgments

First and foremost, I would like to extend my sincere gratitude to my thesis supervisors **Zhixue Zheng**, and **Michel Aillerie**, for their unwavering personal and professional support and guidance throughout the entirety of this thesis. I am immensely thankful to both of them, not only for their technical advice but also for their moral support in helping me to overcome the various challenges encountered during this journey and ensuring the success of this thesis. It has been an absolute pleasure and privilege to work alongside them.

I would like to acknowledge the esteemed members of my PhD thesis Panel.

I would like to express my sincere gratitude to Prof. Daniel Hissel and Prof. Marie Cécile Pera from Université de Franche-Comté for their invaluable contributions to the project and this work. Their insightful feed-backs on the reports and presentations have greatly enhanced the progress of my thesis.

I would also like to extend my appreciation to Prof. Alexandre De Bernardinis and Dr. Jean-Paul Sawicki for their guidance and fruitful discussions on advancing the work during my stay at IUT Thionville-Yutz.

I would like to give special thanks to Javier Solano for his valuable suggestions in my work, particularly in the area of EMS, and for his assistance in the development of the EMS testbench evaluator. His support has been immensely helpful.

Furthermore, I would like to express my gratitude to all my colleagues at LMOPS in Metz and Thionville, particularly Christelle Habis, Xin Wang, Wafae El Berjali, Rodolph Iskander, Waqar Iqbal, Luis Antonio Garcia Gutierrez, Bachirou Bogno, and at Thionville, Sandhya Malladi, and Dani Shukkar for the invaluable experiences we have shared and the insightful discussions we have had.

I would like to convey my heartfelt appreciation to my wife, Mehwish, for her unwavering love and continuous support. I am grateful for her understanding and patience during these years, as she cared for our childrens, Arham and Anas.

Last but certainly not least, I am deeply grateful to my parents and siblings for their moral support and encouragement. Without their support and prayers, I would not have reached this significant milestone.

Lastly, I would like to acknowledge and express my thanks to the funding agency that supported this project. This research was conducted within the framework of the ANR JCJC EREMITE project, with the agreement number ANR-19-CE05-0008-01, and received support from the French National Agency for Research (ANR).

I dedicate this dissertation to my parents, my siblings, my wife Mehwish, and my sons, Arham & Anas.

Abstract

Title: Energy management of multi-source DC microgrid systems for residential applications.

Over the last decade, remarkable progress has been made in the penetration of renewable energy sources (RES) for residential applications. Compared with AC microgrid, DC microgrid has demonstrated numerous advantages such as its natural interface with RES, energy storage systems and DC loads, higher efficiency with less conversion stages, and simpler control without skin effect and reactive power flow considerations.

Despite its numerous advantages and wide applications, DC microgrid is still a relatively new technology, and its grid architectures, control strategies, stabilization techniques, etc. deserve enormous research efforts. In this context, this thesis is targeted at the energy management issues of a multi-source DC microgrid dedicated to residential applications. The DC microgrid consists of distributed generators (PV panels), a hybrid energy storage system (HESS) with batteries and a supercapacitor (SC), and DC loads, interconnected via DC /DC power converters. The main objective of this research is to develop an advanced energy management strategy (EMS) to improve the system operational efficiency while reinforcing its reliability and durability.

In one aspect, a hierarchical DC microgrid simulation platform was developed under MATLAB/Simulink environment. The simulation platform consists of two layers with different timescales, i.e., a local-level control layer (with a timescale from seconds to minutes due to converter switching behaviors) for local component controls, and a system-level control layer (with a timescale from days to months with accelerated test) for long-term EMS validation and its performance evaluation. In the local-level control layer, PV panel, batteries and SC were separately modeled and controlled. Different control modes such as current control, voltage control and maximum power point tracking (MPPT) control were implemented. In addition, a low pass filter (LPF) was applied to split the total HESS power into low and high frequency components for batteries and SC respectively. The influence of different cut-off frequencies of LPF for power sharing was studied as well. In the system-level control layer, a combined automatic sizing and bi-level hybrid EMS was proposed and validated. It mainly covers five operating scenarios including PV curtailment, load shedding and three scenarios via HESS control associated with SC state of charge (SOC) retaining hysteresis control. Meanwhile, an objective function considering both capital cost (CAPEX) and operating cost (OPEX) functions was designed for EMS performance evaluation. The mutual effect between the HESS sizing and EMS design was jointly studied based on an open dataset of residential power profiles covering both summer and winter.

In the other aspect, a multi-source DC microgrid experimental platform was developed as part of this work in the laboratory for real-time EMS validation. It consists of four lithium-ion batteries, a supercapacitor, a programmable DC power supply, a programmable DC load, corresponding DC/DC converters, and a real-time controller (dSPACE/Microlabbox). Accelerated tests were carried out to verify the proposed EMS in different operating scenarios by integrating real PV generation and load consumption power profiles into programmable DC supply and load. Both the developed hierarchical DC microgrid simulation platform and experimental platform can serve as general uses for verifying and evaluating various EMS.

Keywords: DC microgrid; renewable energy sources; energy management strategy; EMS testbench evaluator; hybrid energy storage system; rule-based EMS; filtration-based EMS.

Résumé

Titre: Gestion de l'énergie des systèmes de micro-réseau à courant continu multi-source pour les applications résidentielles.

Au cours de la dernière décennie, d'importants progrès ont été réalisés dans la pénétration des sources d'énergie renouvelable (RES) pour les applications résidentielles. Comparé au réseau électrique alternatif (AC), le réseau électrique en courant continu (DC) a démontré de nombreux avantages tels que son interface naturelle avec les RES, les systèmes de stockage d'énergie et les charges en courant continu, une efficacité supérieure avec moins d'étapes de conversion, et un contrôle plus simple sans effet de peau et sans considérations sur le flux de puissance réactive.

Malgré ses nombreux avantages et ses applications étendues , le micro-réseaux DC reste une technologie relativement nouvelle, et ses architectures de réseau, stratégies de contrôle, techniques de stabilisation, etc. méritent d'énormes efforts de recherche. Dans ce contexte, cette thèse porte sur les problèmes de gestion de l'énergie d'un réseau électrique en courant continu multi-source dédié aux applications résidentielles. Le réseau électrique en courant continu est composé de générateurs distribués (panneaux solaires), d'un système de stockage d'énergie hybride (HESS) avec des batteries et un supercondensateur (SC), et de charges en courant continu, interconnectées via des convertisseurs de puissance DC/DC. L'objectif principal de cette recherche est de développer une stratégie avancée de gestion de l'énergie (EMS) afin d'améliorer l'efficacité opérationnelle du système tout en renforçant sa fiabilité et sa durabilité.

Dans un aspect, une plateforme de simulation hiérarchique de réseau électrique en courant continu a été développée sous l'environnement MATLAB/Simulink. La plateforme de simulation est composée de deux couches avec des échelles de temps différentes, à savoir une couche de contrôle de niveau local (avec une échelle de temps de quelques secondes à quelques minutes en raison des comportements de commutation des convertisseurs) pour les contrôles des composants locaux, et une couche de contrôle de niveau système (avec une échelle de temps de quelques jours à quelques mois avec un test accéléré) pour la validation à long terme de l'EMS et son évaluation de performance.

Dans la couche de contrôle de niveau local, les panneaux solaires, les batteries et le SC ont été modélisés et contrôlés séparément. Différents modes de contrôle tels que le contrôle de courant, le contrôle de tension et le contrôle du point de puissance maximale (MPPT) ont été mis en œuvre. De plus, un filtre passe-bas (LPF) a été appliqué pour diviser la puissance totale du HESS en composantes basse et haute fréquence pour les batteries et le SC respectivement. L'influence des différentes fréquences de coupure du LPF pour le partage de puissance a également été étudiée. Dans la couche de contrôle de niveau système, un EMS hybride bi-niveau combiné et un dimensionnement automatique ont été proposés et validés. Il couvre principalement cinq scénarios d'exploitation, notamment la réduction de la production des panneaux solaires, la réduction de la charge et trois scénarios via le contrôle du HESS associé à la rétention du contrôle de l'état de charge (SOC) du SC. Parallèlement, une fonction objective prenant en compte à la fois le coût en capital (CAPEX) et les coûts d'exploitation (OPEX) a été conçue pour l'évaluation des performances de l'EMS. L'effet mutuel entre la dimensionnement du HESS et la conception de l'EMS a été étudié conjointement sur la base d'un ensemble de données ouvertes de profils de consommation électrique résidentielle couvrant à la fois l'été et l'hiver.

Dans un autre aspect, une plateforme expérimentale de réseau électrique en courant continu multi-source a été développée dans le cadre de ce travail en laboratoire pour la validation en temps réel de l'EMS. Elle est composée de quatre batteries lithium-ion, d'un SC, d'une alimentation électrique en courant continu programmable, d'une charge en courant continu programmable, des convertisseurs DC/DC correspondants et d'un contrôleur en temps réel (dSPACE/Microlabbox). Des tests accélérés ont été réalisés pour vérifier l'EMS proposé dans différents scénarios d'exploitation en intégrant la génération réelle de panneaux solaires et les profils de consommation de charge dans l'alimentation en courant continu programmable et la charge. Les deux plateformes développées, la plateforme de simulation hiérarchique de réseau électrique en courant continu et la plateforme expérimentale, peuvent être utilisées de manière générale pour vérifier et évaluer divers EMS.

Mots-clés: Réseau électrique en courant continu ; sources d'énergie renouvelable ; stratégie de gestion de l'énergie ; évaluateur de banc d'essai de l'EMS ; système de stockage d'énergie hybride ; EMS basé sur des règles ; EMS basé sur la filtration.

Introduction générale

Ce travail de thèse intitulé **"Gestion de l'énergie des systèmes de micro-réseau à courant continu multi-source pour les applications résidentielles."** est supervisé par Zhixue Zheng, Maîtresse de conférences et Michel Aillerie, Professeur à l'Université de Lorraine. Le travail s'est principalement déroulé au Laboratoire Matériaux Optiques, Photonique et Systèmes **(LMOPS)**, de l'Université de Lorraine et CentraleSupélec à Metz, à l'école doctorale IAEM. La partie expérimentale a été développée au sein de l'IUT de Thionville-Yutz, où se base l'équipe de recherche. Cette thèse s'inscrit dans le cadre du projet ANR JCJC EREMITE (Efficiency and Reliability Enhancement of a Multi-Source DC Microgrid Dedicated to Residential Applications by Integrating Bi-Level Managements).

0.1 Contexte

Les défis liés à la limitation des ressources énergétiques, à l'approvisionnement en combustibles fossiles disponibles et aux problèmes environnementaux, liés à l'augmentation des gaz à effet de serre obligent à rechercher des solutions durables dans les sources et les usages de l'énergie. Au cours de la dernière décennie, des progrès positifs ont été réalisés grâce aux efforts conjoints des scientifiques et des industriels.

Dans ce contexte, l'utilisation des sources d'énergie renouvelable dans le mix énergétique en particulier pour la production et la gestion des systèmes électriques a augmenté pour répondre à la demande. C'est ainsi que de nombreux pays ont pris l'initiative de déployer des technologies d'énergie renouvelable à grande échelle. Par exemple, selon le rapport énergétique 2023 de l'IEA, la France a récemment fixé des objectifs de développement visant à améliorer son équilibre « offre-demande » sur la période 2023-2025, car la génération d'électricité renouvelable a diminué de 4% en 2022 en raison d'une moindre production hydroélectrique par rapport à 2021. Par ailleurs et pour la première fois, en plus de deux décennies, la France a importé de l'électricité pour répondre à environ 4% (18 TWh) de sa demande [1]. En raison de cela et pour un développement durable, le pays vise à réduire sa consommation d'énergie primaire de 10% d'ici 2024 par rapport à 2019. Conformément aux objectifs de la Commission européenne, le gouvernement français vise également la neutralité carbone d'ici 2040, avec une réduction de la consommation énergétique de 40%. À cette fin, des mesures d'urgence sont annoncées pour accélérer l'utilisation des sources d'énergie renouvelable en France, notamment dans le secteur résidentiel, qui représente 34,7% de la consommation finale d'énergie en 2020 [2].

Pour atteindre cet objectif, on estime que les énergies renouvelables devraient être largement intégrées dans le secteur industriel mais également dans le secteur résidentiel en utilisant les technologies et les structures des micro-réseaux. Le micro-réseau offre une solution prometteuse et efficace en intégrant diverses sources d'énergie distribuées, des systèmes de stockage d'énergie et des charges interconnectées qui agissent comme une entité contrôlable unique par rapport au réseau électrique traditionnel et centralisé. Ces dernières décennies, des progrès remarquables ont été réalisés dans l'augmentation de la pénétration des sources d'énergie renouvelable, principalement dans les micro-réseaux AC en raison de la dominance actuelle des systèmes électriques à courant alternatif. Néanmoins, les micro-réseaux DC, également à l'étude, présentent plus d'avantages pour de nombreux usages en raison des facteurs suivants :

- Interface naturelle avec en amont les sources d'énergie renouvelable de type DC et en aval les systèmes de stockage et les charges comme, par exemple, les systèmes d'éclairage, les ordinateurs, les véhicules électriques, les systèmes de ventilation et de climatisation ;

- Efficacité et fiabilité accrues grâce à la réduction des étapes de conversion (élimination des conversions DC-AC et AC-DC inutiles) ;
- Système de contrôle plus simple sans problèmes d'effets de peau, d'harmoniques, de synchronisation et de flux de puissance réactive.

Avec l'augmentation significatives du nombre et du type de sources d'énergie renouvelable DC et des charges DC, le micro-réseau DC offre des solutions potentiellement viables et économiques pour les besoins énergétiques futurs. Il devient ainsi une solution attrayante pour les applications résidentielles et industrielles, telles que les foyers DC, les parcs d'énergie renouvelable, les stations de recharge de véhicules électriques et les systèmes hybrides de stockage d'énergie.

0.2 Problématiques et objectifs de la thèse

Ce projet contribue principalement au programme de travail ANR 2019, dans l'axe « Energie Propre, Sûre et Efficace » en traitant principalement des sujets liés à l'efficacité énergétique, aux systèmes de stockage, à la gestion dynamique de l'énergie et à l'efficacité des composants.

Ces études dans le cadre du projet ANR EREMITE porte alors de façon originale sur deux principaux aspects de la gestion des micro-réseaux DC, à savoir : le système de gestion de l'énergie (EMS), objet principal de cette thèse et le système de gestion de la santé (HMS) des micro-réseaux, objet d'une seconde thèse et leur considération conjointe. En effet, des études présentées dans la littérature sont généralement menées de manière indépendante sur ces deux systèmes de gestion des micro-réseaux. En intégrant les deux aspects, il est attendu que le projet propose une amélioration de l'efficacité et de la durabilité des micro-réseaux DC grâce à l'interaction des deux stratégies et contribue à explorer une nouvelle direction de recherche pour le domaine des micro-réseaux DC. Les résultats obtenus contribueront à l'évaluation de l'efficacité et de la fiabilité du système de micro-réseau DC à court et à long terme.

Le travail effectué dans la présente thèse aborde également la gestion des micro-réseaux DC du point de vue économique. Les résultats contribuent à évaluer le coût de l'application des micro-réseaux DC et l'utilisation de techniques de génération d'énergie renouvelable. En proposant une méthodologie d'analyse des coûts, cette étude contribuera à évaluer le coût des énergies renouvelables dans la consommation finale d'énergie.

En ce qui concerne l'aspect social, l'amélioration de la fiabilité et de la durabilité des micro-réseaux DC pour les applications résidentielles favorisera l'acceptation sociale de l'énergie renouvelable et encouragera sa participation à l'installation de micro-réseaux résidentiels, en plus des autres avantages environnementaux qui leurs sont associés.

0.3 Organisation du manuscrit de thèse

The thesis is organized as follows:

Le présent manuscrit de thèse est le résultat de trois années d'études sur le sujet. Il est présenté en 4 chapitres principaux et conclusion avec des perspectives à la fin.

Chapitre 1 :
Le chapitre 1 repose sur une revue de littérature dans laquelle plusieurs aspects critiques des micro-réseaux DC pour les applications résidentielles sont résumés, notamment son architecture, sa structure de contrôle et la classification des EMS. Dans ce chapitre, une attention particulière a été accordée aux applications des EMS pour le secteur tertiaire, spécifiquement pour les applications résidentielles.

Dans ce premier chapitre nous avons ainsi montré que par rapport au micro-réseau AC et au micro-réseau hybride AC/DC traditionnellement utilisés, le type DC présente des avantages en termes d'efficacité, de fiabilité et de coût du système. Néanmoins, diverses questions, telles que son système de protection, la conception de l'architecture, les stratégies de contrôle et les techniques de stabilisation, méritent

d'énormes efforts de recherche. Nous avons spécifiquement examiné plusieurs problèmes critiques concernant les micro-réseaux DC dans les applications résidentielles, y compris la conception de leur architecture, les technologies de communication, la structure de contrôle et la classifications EMS.

Concernant son architecture, le niveau de bus DC de 48V a été considéré comme un niveau de tension approprié pour le bus DC commun, compte tenu des différents niveaux de tension et les gammes de puissance des appareils résidentiels. Cependant, différentes normes de tension continue peuvent exister dans le futur micro-réseau pour améliorer encore l'efficacité du système et réduire l'étage de conversion de puissance. Les technologies de la communication ont également été brièvement évoquées, y compris les technologies filaires et sans fil. Par rapport à la dominante technologies filaires, le type sans fil a suscité plus d'intérêt en raison de son faible déploiement, son faible coût, sa grande flexibilité et sa faible consommation d'énergie. Comme illustré dans la partie discussion de ce chapitre, la partie TIC sera essentielle pour construire des micro-réseaux modernes et intelligents. Mais des efforts en recherche sont encore nécessaires à l'avenir.

Une attention particulière a été accordée aux questions de EMS au niveau tertiaire, en particulier pour les applications résidentielles. Deux grandes catégories de systèmes EMS ont été résumées, comprenant les méthodes classiques et les méthodes d'intelligence artificielle. Selon la recherche documentaire, les méthodes classiques ont été principalement utilisées pour résoudre des problèmes d'optimisation, en utilisant des algorithmes itératifs, de la programmation linéaire en nombres entiers mixtes, de la programmation stochastique et robuste et le contrôle prédictif du modèle. Les méthodes d'intelligence artificielle, comprenant la logique floue, les réseaux neuronaux, les méthodes de calcul évolutionnaire ainsi que les systèmes multi-agents, ont gagné en popularité pour la gestion énergétique des micro-réseaux. Dans cette catégorie, les techniques avancées sont utilisées pour résoudre des problèmes d'optimisation à objectif unique (SOO) et d'optimisation à objectifs multiples (MOO). Ces derniers sont en général plus flexibles et efficaces pour traiter des problèmes d'optimisation complexes. De plus, dans des publications récentes, les fonctions prédictives sur la production future d'énergie, la faible demande et la variation du marché de l'énergie, etc., ont été intégré à l'EMS. Des stratégies de gestion de la santé (HMS) tenant compte du coût de dégradation et de la fiabilité de chaque composant ont également été considérées dans les fonctions d'objectif de l'EMS. L'interaction des EMS et des HMS pourrait être une direction de recherche intéressante pour garantir le fonctionnement efficace et fiable des micro-réseaux DC.

Dans ce chapitre, certains outils logiciels existants ont également été répertoriés, tels que HOMER, i-HOGA, TRANSYS, OPAL-RT, Typhoon, et dSPACE. qui pourraient être intéressants pour les utilisateurs finaux résidentiels en raison de leur bonne interprétabilité.

L'analyse finale a été effectuée sur la base de plusieurs exemples de micro-réseaux DC pour des applications résidentielles, y compris les éléments du système avec leurs types et niveaux de puissance, l'objectif de contrôle de chaque partie et l'EMS global. Ils pourraient fournir des exemples concrets aux futurs concepteurs de micro-réseaux à courant continu pour des applications résidentielles. La littérature a montré que, en raison des fonctions multi-objectifs présentes dans la stratégie de gestion de l'énergie, aucune méthode unique ne peut satisfaire toutes les exigences, et des méthodes hybrides peuvent être utilisées en combinaison pour concevoir un EMS efficace. Ce point particulier est discuté plus en détail dans le chapitre 3.

Il est à noter que ce travail a donné lieu à une publication internationale :

S. Ali, Z. Zheng, M. Aillerie, J.-P. Sawicki, M.-C. Péra, D. Hissel, « A Review of DC Microgrid Energy Management Systems Dedicated to Residential Applications ».
Energies 2021, 14, 4308. doi.org/10.3390/en14144308

ayant reçue le Premier prix pour un article de revue en juin 2023:

The First Prize: (CHF 1000 + one free publication + a certificate) A Review of DC Microgrid Energy Management Systems Dedicated to Residential Applications By Sadaqat Ali et al.

Chapitre 2 :
Ce chapitre est consacré à l'étude de l'architecture d'un micro-réseau DC. L'architecture choisie vise à être

aussi universelle que possible. Elle intègre une source d'énergie renouvelable et un système de stockage d'énergie permettant l'alimentation de différentes charges électriques en courant continu, comme le montre la Figure 1.

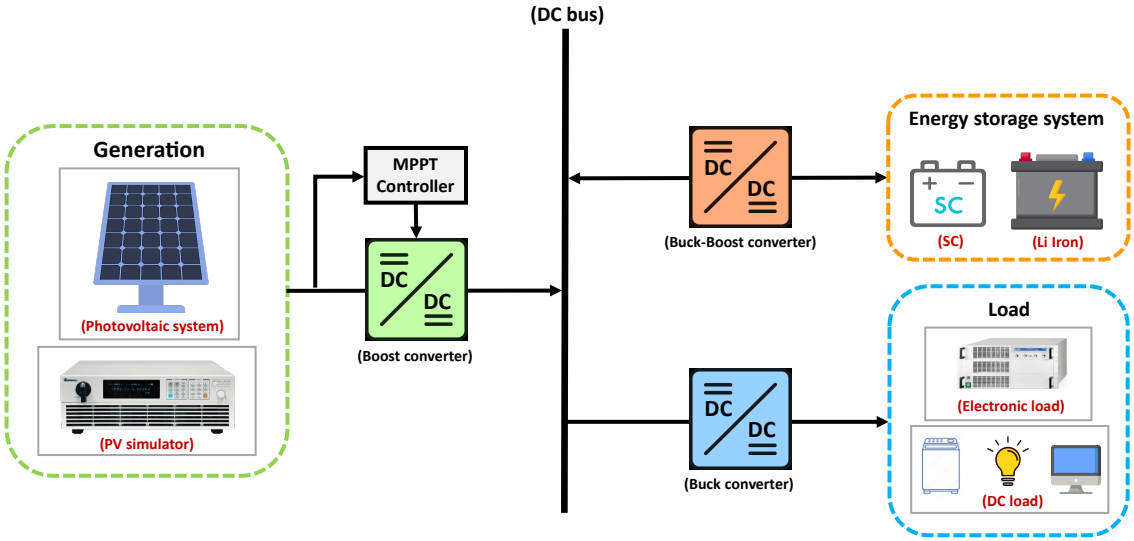

Figure 1: Schéma du micro-réseau DC utilisé dans notre étude.

Dans le schéma considéré, le PV est utilisé comme principale source d'énergie. En raison de sa dépendance aux conditions météorologiques et pour stabiliser la tension du bus DC à une valeur déterminée, des systèmes de stockage d'énergie hybrides intégrant des batteries et des supercondensateurs sont utilisés comme éléments de stockage de l'énergie, de stabilisation du réseau et de sources d'alimentation de secours permettant de répondre aux demandes de la charge : Le système de stockage est utilisé comme source d'énergie lorsque les sources d'énergie renouvelable ne peuvent pas répondre à la demande. Il est utilisé comme charge lorsque les sources fournissent suffisamment d'énergie. L'excès de puissance peut y être stocké afin de garantir l'équilibre du système.

Dans ce chapitre, le système de micro-réseau DC étudié est établi dans l'environnement MATLAB/Simulink car la simulation est une étape nécessaire avant la mise en œuvre expérimentale. Par conséquent, la plateforme de micro-réseau DC a d'abord été développée sous l'environnement MATLAB/Simulink, puis testée sur une plateforme expérimentale. Ce travail sera présenté et discuté dans le chapitre 4. Dans le présent chapitre, chaque élément a été modélisé et contrôlé séparément au niveau local. La simulation et quelques résultats expérimentaux préliminaires sont inclus. La commande de suivi du point de puissance maximale (MPPT) a été mise en œuvre pour le système PV. Pour les batteries et les supercondensateurs, différents modes de commande tels que la commande de courant et la commande de tension ont été développés et testés pour chaque élément séparément. Cette partie du travail nous a permis de tester chaque composant séparément afin d'observer le comportement de charge et de décharge de la batterie et du SC individuellement puis ensemble en tant que système de stockage de l'énergie hybride, HESS en utilisant différentes méthodes telles que le courant constant (CC) et la tension constante (CV). Pour le contrôle au niveau local, dans cette partie du travail, un schéma de commande conventionnel est utilisé pour répartir les composantes de basse et haute fréquence du courant utilisé comme référence pour la batterie et le supercondensateur, respectivement, comme le montre la Figure 2.

Dans ce schéma, la tension du bus DC est contrôlée de manière coordonnée par la batterie et le SC. Tout d'abord, la tension mesurée du bus DC, Vdc, est comparée à la tension de référence du bus DC, V_{dc_ref}, et la différence est envoyée à un régulateur proportionnel intégral (PI) pour obtenir la référence de courant, I_{ref}, ou le courant total, I_{tot}. Ce courant total est divisé en deux parties. L'une est la référence de courant de la batterie, I_{ref_bat}, qui est obtenue en appliquant un filtre passe-bas (LPF) et un coefficient K à I_{ref}. L'autre partie, I_{ref_SC} est la différence entre I_{ref} et I_{ref_bat}. Ainsi, la partie

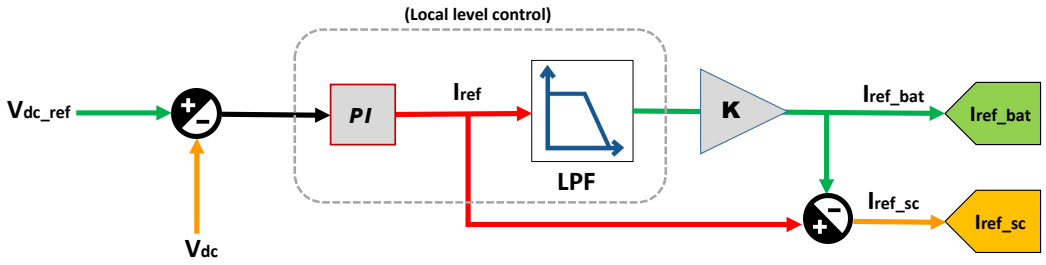

Figure 2: Diagramme en blocs de contrôle pour le schéma de contrôle conventionnel.

haute fréquence des perturbations du bus DC sera atténuée par le SC, tandis que la partie basse fréquence de la perturbation est lissée par la batterie.

L'influence de différentes fréquences angulaires ω du **LPF** sur le partage de puissance a également été étudiée et présentée dans ce chapitre. Dans le travail développé dans cette étude et présenté dans ce chapitre, nos résultats obtenus ont montré une bonne concordance entre les résultats de simulation et expérimentaux. Sur la base de ces résultats de simulation et expérimentaux, une comparaison a été réalisée et analysée en fonction de la fréquence angulaire de coupure ω du LPF. Nous avons constaté que $\omega = 50 rad/s$ est une valeur appropriée avec l'intégration dans le micro-réseau d'une batterie et d'un supercondensateur ayant les spécifications décrites dans le chapitre 2.

Chapitre 3 :
Ce chapitre présente la plateforme de simulation au niveau système avec sa modélisation et son contrôle. Dans ce travail, un système de gestion de l'énergie (EMS) dédié au DCMG est introduit au niveau système, ce qui diffère de la modélisation à niveau local en termes de complexité temporelle, de problème de mémoire et surtout de comportement de contrôle. Il nécessite un EMS efficace, capable d'analyser, de surveiller et de contrôler la production d'énergie, la distribution et la consommation de charge au niveau système. Une vue d'ensemble de la plateforme DCMG intégrée à l'EMS est présentée dans la Figure 3.

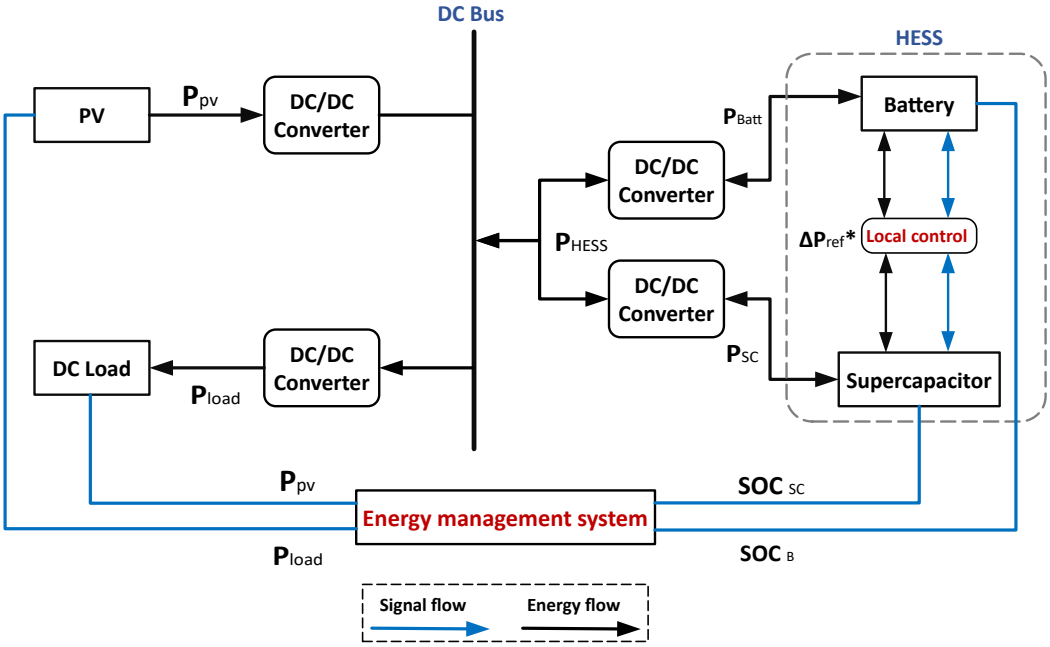

Figure 3: Plateforme DC MG intégrée à l'EMS.

Comme nous pouvons le voir dans la Figure 3, l'EMS est l'organe de contrôle central qui joue un rôle important dans le fonctionnement, le contrôle et la supervision d'un DCMG au niveau système. Dans cette plateforme de simulation au niveau système, le comportement de contrôle local tel que les commutations des différents convertisseurs DC/DC est ignoré. Dans un système DCMG intégrant des sources renouvelables, la puissance PV (P_{pv}) électrique disponible à la sortie de la source du fait des conditions environnementales d'ensoleillement, d'ombrage et de température est incertaine et peu fiable. La même considération peut être accordée à la puissance de la charge (P_{load}) car elle varie constamment en fonction de la demande de l'utilisateur. Pour obtenir un système énergétique performant, les deux doivent donc être bornées et contrôlées, puis gérées par un EMS approprié.

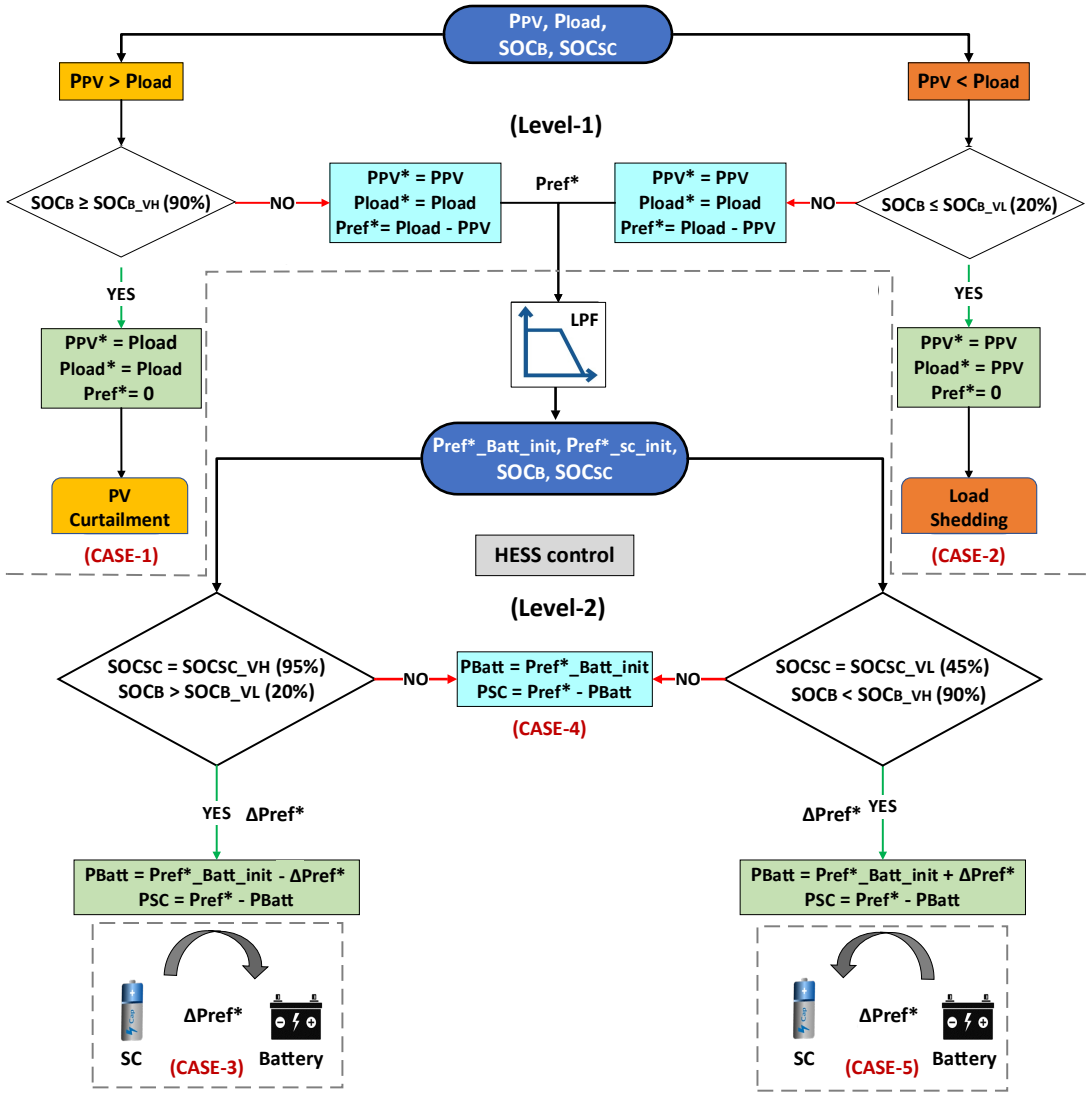

Figure 4: Stratégie de gestion de l'énergie : EMS basé sur la filtration + EMS basé sur des règles.

Un défi majeur pour un DCMG est de faire face aux sources renouvelables stochastiques et aux charges volatiles afin d'obtenir de meilleures performances opérationnelles. Pour cette raison, que ce travail se base sur une étude approfondie de la littérature quant au rôle de l'EMS et les différentes stratégies liées à la gestion de l'énergie des MG ont déjà été présentée dans le chapitre 1. Dans ce chapitre, nous examinons et analysons trois d'entre elles, notamment : l'EMS basé sur la filtration, l'EMS basé sur les règles et la combinaison de l'EMS basé sur la filtration et sur les règles. Chaque stratégie présente ses propres

avantages et inconvénients en termes de contraintes, de contrôle et d'efficacité. Aucune méthode unique ne peut satisfaire toutes les exigences ; c'est pourquoi la combinaison de l'EMS basé sur la filtration et sur les règles est introduite, ce qui constitue une forme améliorée de l'EMS devant combiner les avantages des deux stratégies précédentes. L'EMS proposé est divisé en deux niveaux (Niveau 1, Niveau 2) comprenant cinq cas différents, comme le montre la Figure 4.

Pour tester l'EMS développé, un banc d'essai a été conçu au laboratoire et l'objectif principal est d'évaluer et de valider l'EMS avec un temps de calcul réduit. Il dispose de deux principales entrées (P_{pv}) et (P_{load}) et un profil résidentiel de 24 heures pour la saison été et pour la saison hiver avec un temps d'échantillonnage de 10 secondes utilisé en tant qu'entrée pour l'évaluateur du banc d'essai de l'EMS afin de valider tous les cas. Les deux profils de puissance, été et hiver sont présenté dans la Figure 5.

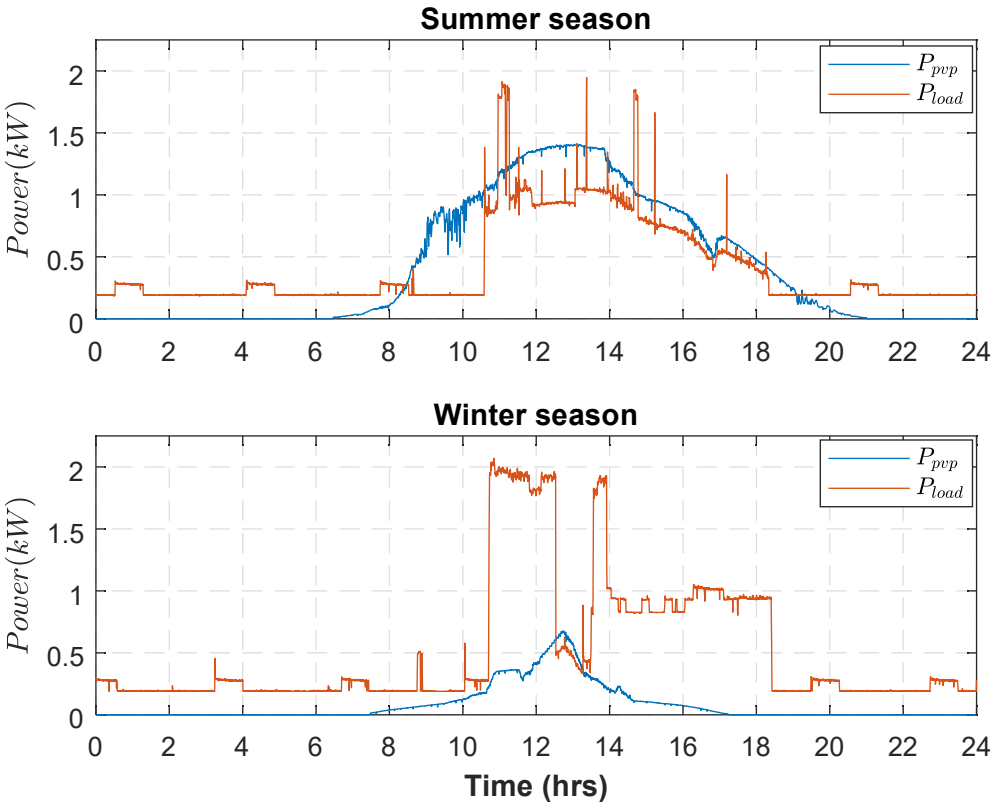

Figure 5: Profil de puissance ; (a) Saison estivale (b) Saison hivernale.[3]

Sur la base des profils de puissance indiqués ci-dessus, tous les cas ont été validés et les résultats sont inclus dans le chapitre 3.

Enfin, dans cette partie du travail, une méthode de dimensionnement automatique a été développée dans laquelle le dimensionnement de la batterie est effectué pour un horizon temporel de 24 heures basé sur des profils d'été et d'hiver, et le dimensionnement du SC pour une demande continue en énergie à haute puissance. Une fonction de coût est également prise en compte pour calculer les coûts d'exploitation (OPEX) pour la batterie et le HESS et comparer les résultats dans les deux cas sont présenté dans la Figure 6, 7, 8.

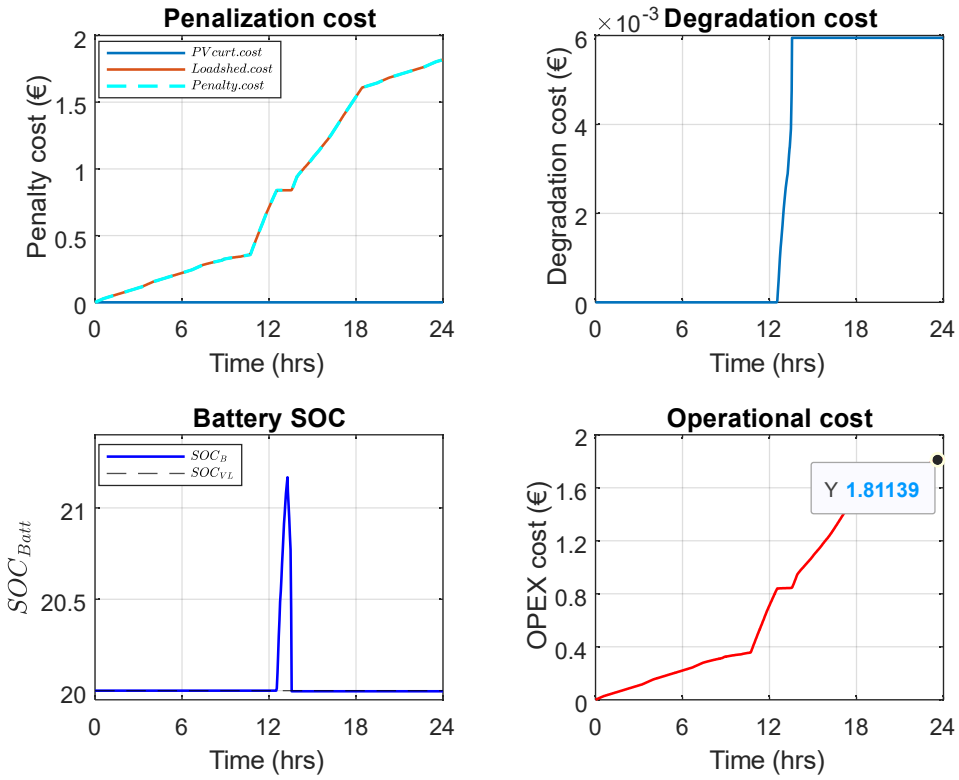

***(A)** Only- battery, Scenario 1*

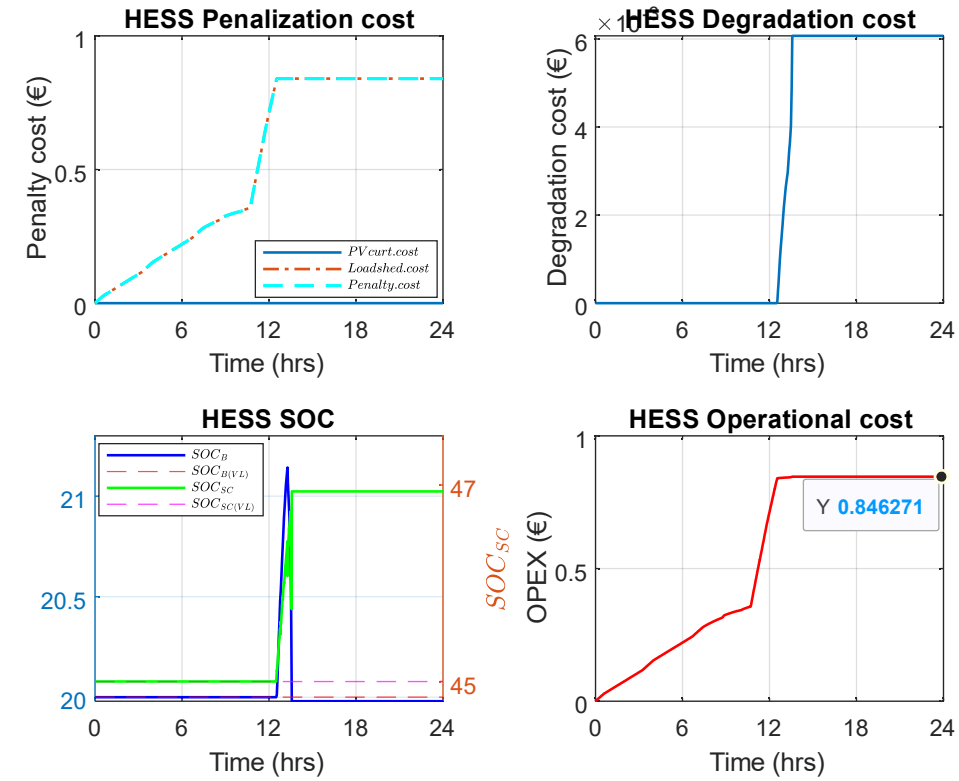

***(B)** HESS, Scenario 1*

Figure 6: OPEX comparison (VL); **(A)** Only-battery case, **(B)** HESS case.

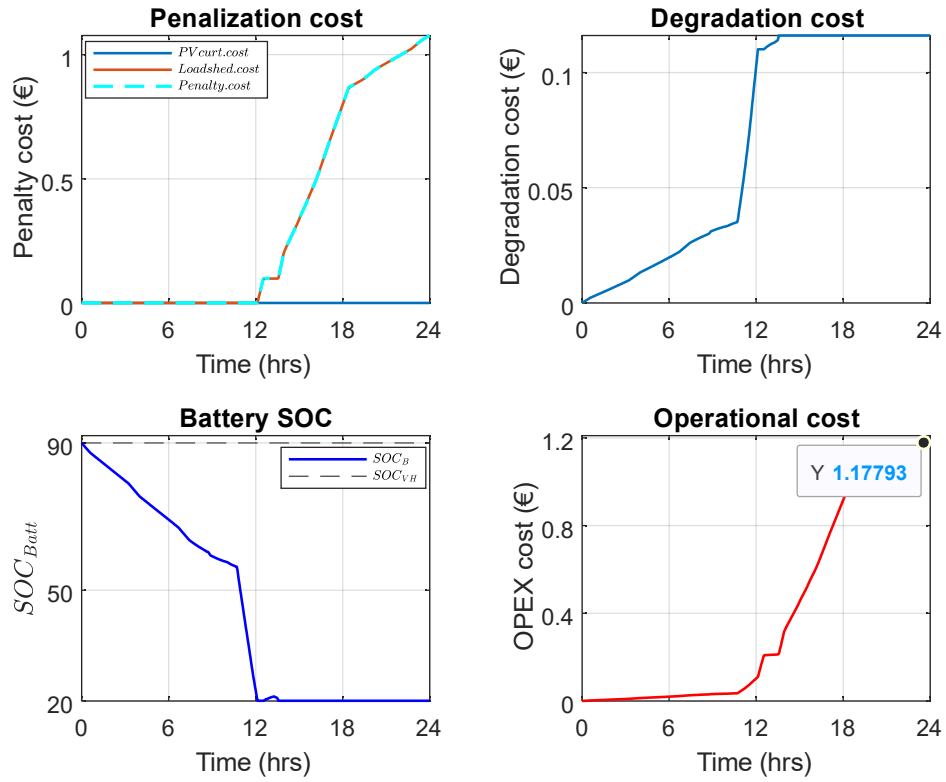

***(A)** Only- battery, Scenario 2*

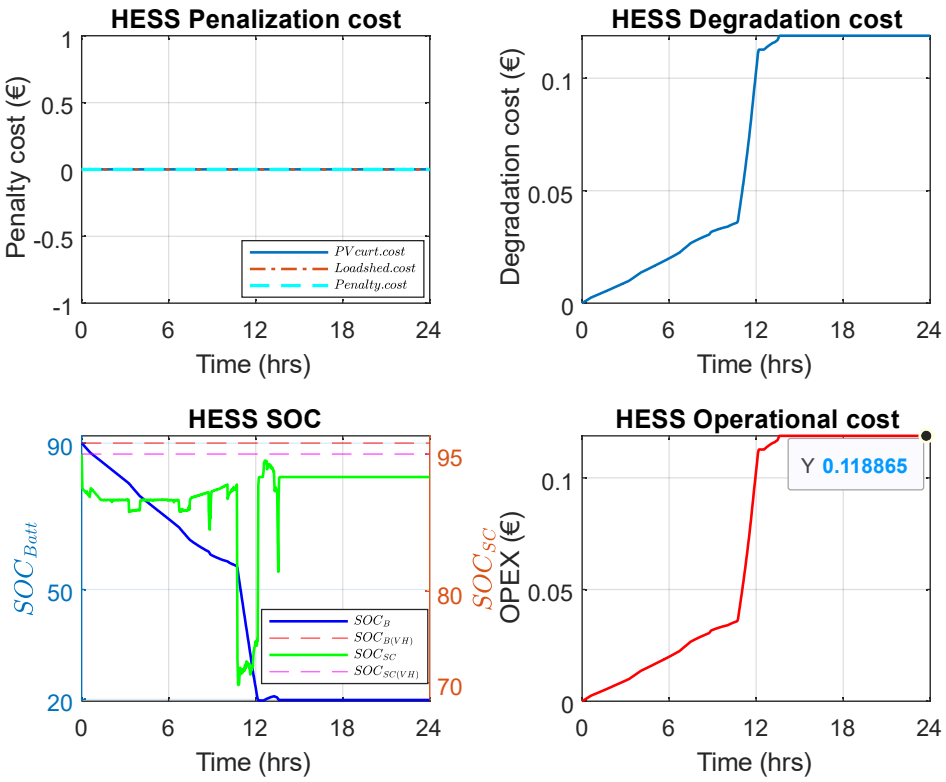

***(B)** HESS, Scenario 2*

Figure 7: OPEX comparison (VH); **(A)** Only-battery case, **(B)** HESS case.

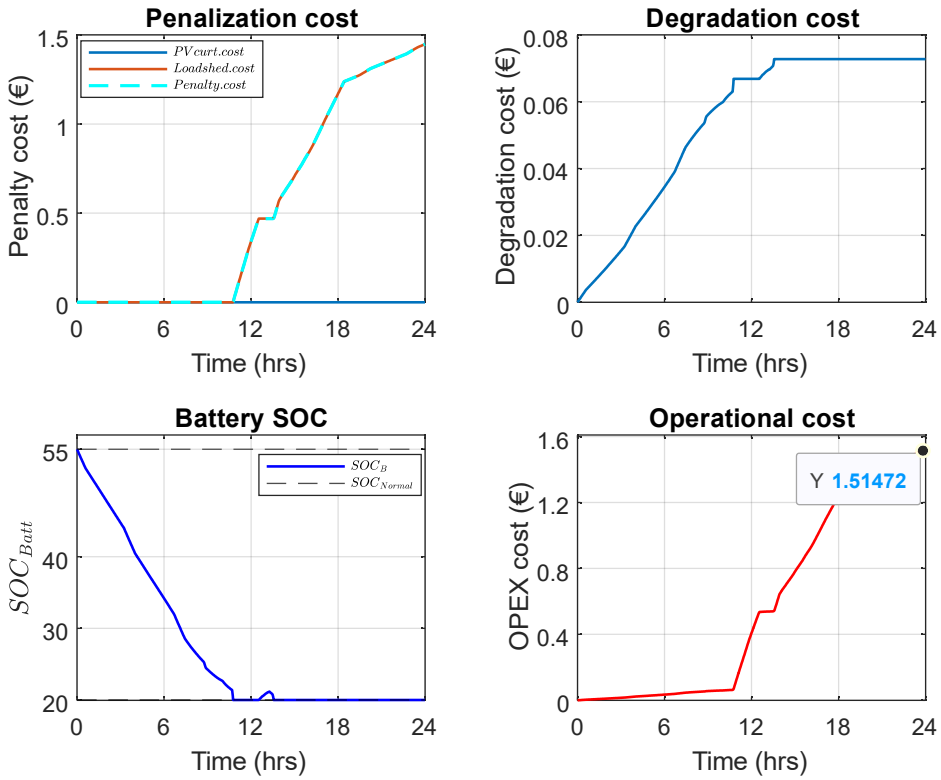

***(A)** Only- battery, Scenario 3*

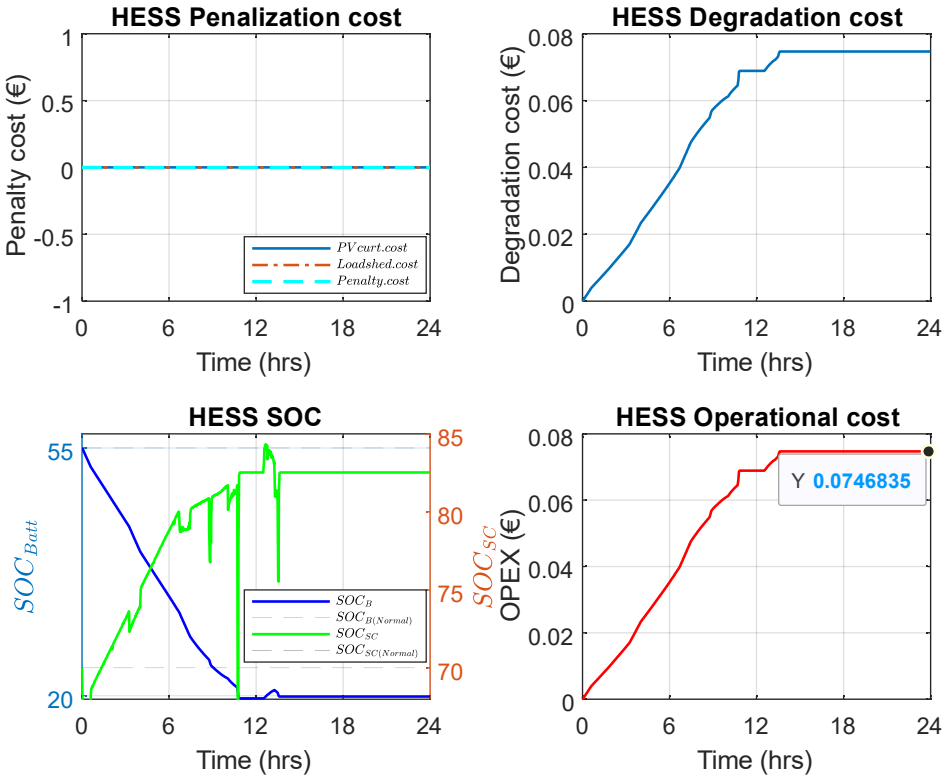

***(B)** HESS, Scenario 3*

Figure 8: OPEX comparison (Normal); **(A)** Only-battery case, **(B)** HESS case.

Chapitre 4 :
Le chapitre 4 concerne le développement de la plateforme expérimentale. Il détaille les principaux résultats de cette contribution expérimentale qui a permis la validation de toute notre étude depuis l'étude bibliographique, le choix des systèmes et du matériel, le choix des stratégies de contrôle du système EMS et tout le travail important de simulation effectué pendant les premières années de cette thèse.

Une plateforme expérimentale de micro-réseau DC à multi-sources a été développée dans le cadre de ce travail au laboratoire pour la validation en temps réel de l'EMS. Elle est composée de quatre batteries lithium-ion, d'un supercondensateur, d'une alimentation électrique DC programmable, d'une charge DC programmable, des convertisseurs DC/DC correspondants et d'un contrôleur en temps réel (dSPACE/Microlabbox) comme illustré à la Figure 9.

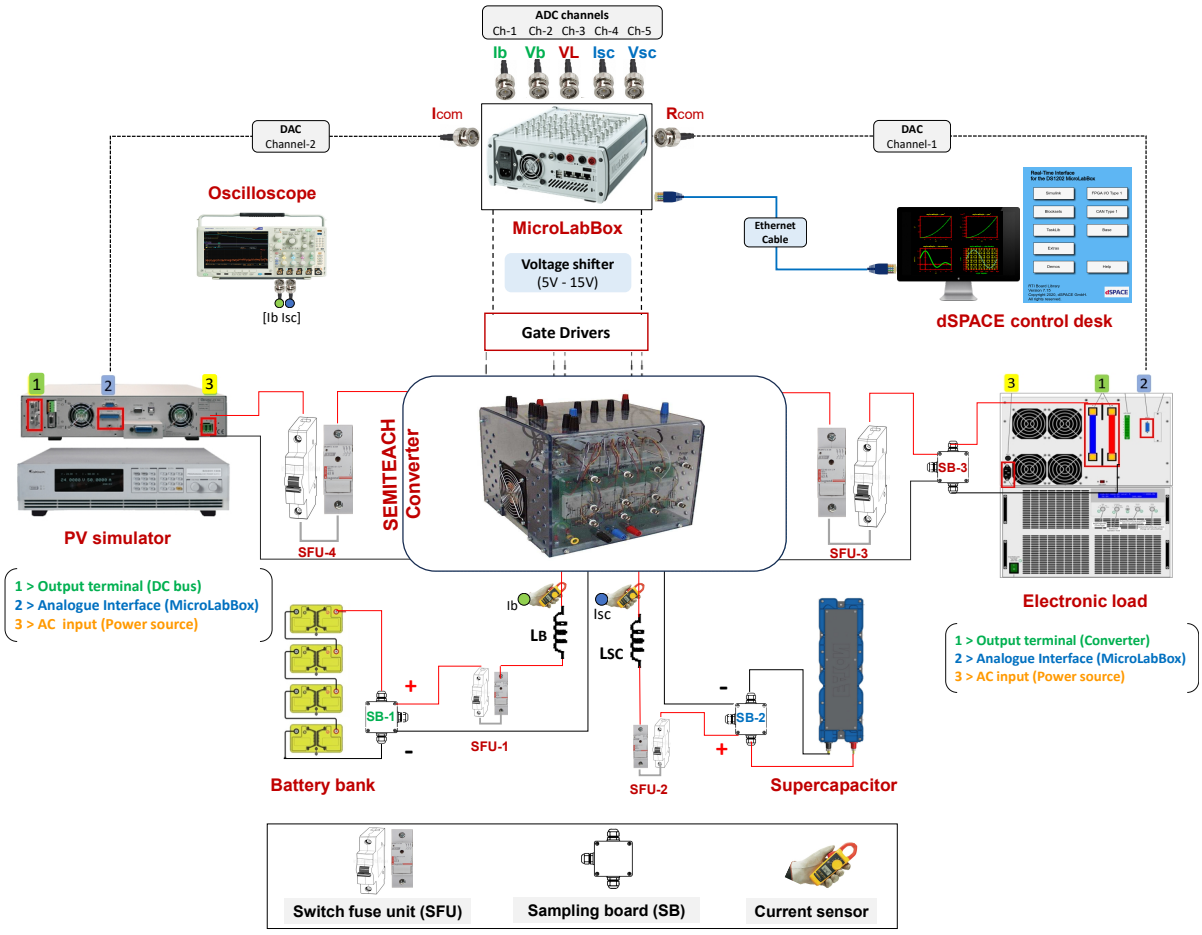

Figure 9: Configuration du Systèmes matériel

L'EMS proposé a été initialement vérifié dans le testbench évaluateur développé sous MATLAB/Simulink et les résultats de simulation ont été présentés et analysés dans le chapitre 3. Dans ce chapitre, le même EMS a été validé sur la plateforme expérimentale en temps réel. Des tests accélérés ont été réalisés pour vérifier l'EMS proposé dans différents scénarios de fonctionnement en intégrant de véritables profils de génération PV et de consommation de charge dans une alimentation DC programmable et une charge.

Contributions, conclusions et perspectives

Les contributions apportées par cette thèse sont les suivantes :

Les contributions de cette thèse sont les suivantes :

- Contribution en modélisant une plateforme de simulation de microgrid DC à sources multiples sous l'environnement MATLAB/Simulink.
- Contribution en étudiant et analysant différentes stratégies de gestion de l'énergie pour développer un EMS avancé pour le schéma de microgrid DC proposé.
- Contribution en testant l'ensemble du système à deux niveaux avec des échelles de temps différentes : une couche de contrôle de niveau local pour le contrôle des composants à une échelle de temps plus rapide (secondes à minutes) en raison des comportements de commutation des convertisseurs, et une couche de contrôle de niveau système pour la validation à long terme de l'EMS et l'évaluation de la performance (échelle de temps de jours à mois, accélérée à des fins de test). Dans la couche de contrôle de niveau local, les panneaux solaires PV, les batteries et les supercondensateurs (SC) ont été modélisés et contrôlés séparément. Dans la couche de contrôle de niveau système, une méthode combinant un dimensionnement automatique avec un EMS hybride bi-niveau a été proposée et validée.
- Contribution en développant l'évaluateur de banc d'essai EMS pour la validation à long terme de l'EMS et son évaluation de performance.
- Contribution en construisant une plateforme expérimentale de microgrid DC au laboratoire qui a le potentiel d'être utilisée pour la vérification et l'évaluation de divers autres EMS à l'avenir.

Conclusions générales

Certaines des conclusions de cette thèse sont les suivantes :

Le chapitre 1 repose sur l'examen de la littérature, qui résume plusieurs aspects critiques du DCMG pour les applications résidentielles, notamment l'architecture, la structure de contrôle et la classification de l'EMS.

- En ce qui concerne son architecture, les éléments suivants sont choisis pour la formation du DCMG, à savoir les DG (panneaux PV), le SS (batterie et SC), le convertisseur DC/DC bidirectionnel et la charge DC.
- En ce qui concerne le contrôle, une attention particulière a été accordée aux problèmes de l'EMS au niveau tertiaire, spécifiquement pour les applications résidentielles. Une analyse complète a été réalisée, classant les méthodes de contrôle en deux groupes principaux : les méthodes classiques et les techniques d'intelligence artificielle (IA). À travers cette analyse, il a été reconnu qu'aucune méthode unique ne peut répondre pleinement à toutes les exigences imposées par les fonctions multi-objectifs inhérentes à l'EMS. En combinant différentes approches de contrôle, les méthodes hybrides offrent la possibilité d'optimiser les performances de l'EMS et de gérer efficacement les objectifs et les contraintes divers associés à la gestion de l'énergie dans les applications résidentielles.
- Dans cette revue, différents niveaux de tension (5V, 12V, 24V, 48V, 380-400V) ont été examinés afin de déterminer le niveau de tension le plus approprié pour le système DCMG proposé, conçu pour les applications résidentielles. Après une étude approfondie, le niveau de bus DC de 48V a été initialement choisi comme le niveau de tension adéquat dans cette étude. Cette sélection est basée sur plusieurs facteurs, notamment la compatibilité avec les appareils et équipements résidentiels, la disponibilité des composants et des convertisseurs, ainsi que l'efficacité globale du système. En adoptant un niveau de bus DC de 48V, le système DCMG proposé est bien adapté pour répondre aux exigences spécifiques et aux caractéristiques opérationnelles des applications résidentielles.

- Plusieurs outils logiciels et composants matériels, qui sont très bénéfiques pour les utilisateurs finaux résidentiels, ont été présentés. Ces outils et composants incluent HOMER, i-HOGA, TRNSYS, OPAL-RT, Typhoon et dSPACE.

Au chapitre 2, la principale motivation est l'introduction de la plateforme de simulation du micro-réseau en courant continu (DC microgrid), les principes fondamentaux et la modélisation du micro-réseau en courant continu au niveau local.

- La première partie de ce chapitre concerne la construction et le développement du schéma de micro-réseau en courant continu à sources multiples utilisé dans cette étude. Le système de micro-réseau en courant continu étudié est établi dans l'environnement MATLAB/Simulink et comprend divers éléments tels que des panneaux photovoltaïques (PV) considérés comme la principale source de génération, une batterie et un supercondensateur (SC) comme système de stockage connecté à une charge en courant continu via un convertisseur de puissance indépendant en courant continu (DC/DC).
- Dans la deuxième partie du chapitre, la modélisation au niveau local avec sa structure de contrôle est brièvement discutée. Le contrôle MPPT a été mis en œuvre pour le système PV. Pour les batteries et le SC, différents modes de contrôle tels que le contrôle de courant et le contrôle de tension ont été développés et testés. De plus, un filtre passe-bas (LPF) a été appliqué pour diviser la puissance totale du système de stockage en composantes de basse et haute fréquence pour les batteries et le SC, respectivement. De plus, l'influence des différentes fréquences angulaires ω du LPF sur le partage de puissance a également été étudiée, et nous avons constaté que $\omega = 50 rad/s$ est une valeur appropriée pour le schéma de contrôle conventionnel.

Le chapitre 3 fournit un aperçu global de la plateforme de simulation du micro-réseau en courant continu (DCMG) intégrée à l'EMS. Différents aspects importants liés à la gestion de la production d'énergie, de la distribution et de la consommation de charge au niveau du système sont discutés.

- Une stratégie de gestion de l'énergie améliorée (EMS basée sur la filtration + EMS basée sur les règles) est développée et expliquée, comprenant deux niveaux (Niveau 1 et Niveau 2) avec cinq cas différents.
- Un évaluateur de banc d'essai EMS est introduit pour valider la stratégie de contrôle à deux niveaux au niveau du système.
- Un contrôle EMS local pour le HESS est introduit, non seulement pour la régulation de l'état de charge (SOC), mais aussi pour l'échange de puissance entre la batterie et le SC afin d'obtenir une charge et une décharge équilibrées de chaque élément. Une stratégie d'hystérésis de contrôle de maintien du SOC du SC a été introduite pour réguler le SOC du SC.
- Une méthode de dimensionnement automatique a été développée, où le dimensionnement de la batterie est effectué pour une période de 24 heures sur la base des profils d'été et d'hiver, et le SC pour une demande continue de puissance élevée. Le même filtre passe-bas (LPF) dans l'EMS a été appliqué pour diviser la puissance totale entre les batteries et le SC.
- Une fonction de coût est également prise en compte pour calculer les coûts d'exploitation (OPEX) et d'investissement (CAPEX) du HESS et les comparer avec le cas de la batterie en fonction des coûts de dégradation et des coûts de pénalité. Lors d'une comparaison des coûts entre le cas de la batterie seule et le cas du HESS, il devient évident que le HESS représente le choix supérieur, à la fois sur le plan économique et en termes de durabilité de la batterie.

Dans le chapitre 4, la plateforme expérimentale auto-développée est introduite et présentée.

- Dans la première section, la plateforme développée est présentée avec sa configuration matérielle et ses paramètres système. Elle comprend divers composants, notamment une alimentation programmable de simulateur PV, une charge électronique, un HESS composé d'une batterie et d'un SC connectés à un ensemble de convertisseurs de puissance multifonctions, ainsi qu'un contrôleur en temps réel (dSPACE/MicroLabBox).

- La deuxième partie concerne la validation de l'EMS sur la configuration expérimentale. L'EMS proposé a été initialement validé à l'aide d'un évaluateur de banc d'essai développé dans MATLAB/Simulink. Le même EMS est ensuite validé sur une plateforme expérimentale réelle.
- Des tests accélérés ont été réalisés pour vérifier l'EMS proposé dans différentes situations de fonctionnement et tous les cas ont été validés étape par étape.

Perspective

- Les applications de cette thèse tournent autour de la modélisation des systèmes de microgrids à courant continu (DC), en intégrant une stratégie de gestion de l'énergie spécifiquement adaptée aux applications résidentielles. Cette étude fait partie intégrante d'un projet de recherche visant à fournir des solutions pratiques pour la mise en œuvre de systèmes de microgrids à courant continu. Ces systèmes peuvent être utilisés aussi bien pour les ménages individuels que pour les petites communautés sous forme de nano-grids. Les résultats et les connaissances issus de ce projet de recherche contribueront à l'installation et au fonctionnement réels de systèmes de microgrids à courant continu efficaces, offrant des avantages tangibles aux utilisateurs finaux et favorisant des solutions énergétiques durables au niveau local.
- Le développement de l'EMS doit être amélioré en utilisant des techniques d'intelligence artificielle. En utilisant des techniques d'intelligence artificielle telles que l'apprentissage automatique et les réseaux neuronaux, l'EMS peut être affiné pour optimiser les décisions de gestion de l'énergie, améliorer l'efficacité du système et s'adapter aux conditions opérationnelles dynamiques.
- L'évaluateur du banc d'essai de l'EMS peut être amélioré en intégrant d'autres fonctions objectives. En élargissant les fonctions objectives de l'évaluateur du banc d'essai de l'EMS, sa valeur en tant qu'outil de test et de validation de différentes stratégies d'EMS serait accrue, ce qui faciliterait l'avancement des solutions de gestion de l'énergie.
- Pour améliorer la précision et le réalisme de la plateforme expérimentale, il est recommandé de remplacer le simulateur de panneaux solaires par de véritables panneaux solaires afin d'extraire la puissance maximale. De même, l'intégration d'une charge continue réelle dans le système validerait davantage les performances de l'EMS. En utilisant des composants réels, la plateforme expérimentale simulerait de près les conditions opérationnelles et les défis rencontrés dans les applications pratiques. Cela permettrait une évaluation plus fiable de l'EMS et fournirait des informations précieuses pour son développement et son optimisation ultérieurs
- À l'avenir, il serait bénéfique de mener une enquête plus approfondie sur les coûts en capital (CAPEX) associés aux panneaux solaires et aux éoliennes. Cela permettrait de calculer le coût total du système conçu, en tenant compte des dépenses liées à ces composants.

List of Figures

List of Tables

Contents

Chapter 1

State of the Art: Literature Review

Prior to the 21st century, the traditional power grid was highly centralized in its management, transported electricity produced by a few large generating stations to serve customers. Since its inception and due to the development of the use of renewable energy sources, the electricity grid has developed gradually, in terms of production, transmission and distribution. It is also the result of rapid urbanization and infrastructure development, which has been influenced by economic, political and geographical factors [5]. As a result of this evolution, the current electricity grid has entered a new phase of development moving to a bidirectional energy flow, produced by large power plants but also by small producers thus creating a distributed electricity grid.

Modern grid include microgrid (MG) and smartgrid. A MG is a low-voltage (LV) grid that includes distributed energy resources (DERs) such as photovoltaic (PV) arrays, micro-wind turbines, fuel cells, and energy storage devices (e.g., batteries, supercapacitors, and flywheels). The MG concept is very useful for small communities that want to manage their energy consumption and reduce carbon emissions through an innovative way of generating and using energy. With the internet era, the microgrid is evolving into a smart grid through the integration of information and communication technology (ICT). The modernized form of the microgrid is called smart grid, which uses smart meters and smart sensors to monitor and control the overall system. Unlike MG, smart grid is designed to provide power to large communities by using digital technologies for two-way communication between utilities and their customers [6].

1.1 Conventional electrical grid

The conventional electrical grid is a unidirectional grid in which electricity flows in one direction, i.e., from the generators to the substations, through the transmission lines and finally to the consumers. As shown in Figure 1.1, the individual operations of power grids include generation, transmission, and distribution. Electricity is first generated and then transmitted over long distances to substations, where it is further distributed to consumers [7].

The conventional electrical grid consists of three main components; generation, transmission and distribution.

Generation
The generation system is powered by various forms of energy such as coal, gas, and oil, as well as diffusible renewable energy sources such as hydropower, biomass, solar, and wind. Generation can be centralized or decentralized, depending on the scale of generation.

Transmission
Transmission lines and transformers are used to transport electrical power from generation end to consumers. Transmission lines can be either underground or overhead. For long distances, step-up transformers are used to boost the electrical power to a higher voltage. When the stepped-up power reaches

the distribution substation, a step-down transformer is used to bring the high voltage to low voltage for the end users. In both cases, local substations are required to perform this operation.

Distribution
For power distribution, different types of distribution transformers are used depending on the type of load. For example, an industrial consumer has a different voltage level than a residential user. Therefore, different power requirements should be taken into account for power distribution.

It is important to note that most of equipment's and lines in conventional grids were installed many years ago. These grid elements are outdated and require frequent maintenance to keep the power flowing, which is a large investment. In addition, conventional power plants is the emission of harmful CO_2 gases that cause the greenhouse effect, global warming and environmental hazards. So, it is of high need to change the energy source from fossil fuels to renewable energy sources (RES). Considering all these points, the conventional electrical grid has been continuously evolved by the deployment of RES in grid systems, which has in fact become a distributed grid offering many advantages compared to the traditional centralized historical network.

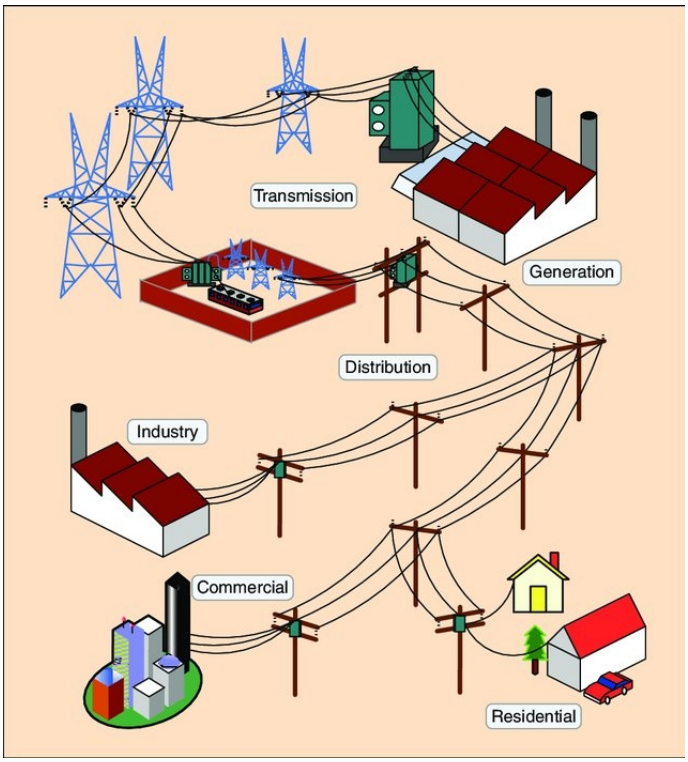

Figure 1.1: Conventional electrical grid [7].

1.2 Microgrid

A microgrid is a modern distributed power system using local sustainable power resources designed through various smart-grid initiatives. Microgrids are a suitable, reliable and clean solution to integrate distributed generation into the main grid. Many definitions and functional classifications of microgrid are cited in the literature [8, 9].

One of the definitions coming from the U.S. Department of Energy is:

"A Microgrid is a localized electric grid interconnected loads and distributed energy

resources that can disconnect from the traditional electric grid and operate autonomously in the event of a power outage" [10].

According to the given definition, microgrid has two important characteristics. First, a microgrid is an integration of DERs and loads. Second, a microgrid must be a controllable entity that can operate in either grid-connected or islanded mode.

The addition of microgrids in the power sector is a reassuring attempt to overcome the problems such as power flow issue. Existing distributed systems were designed and set up assuming unidirectional power flow from the substation to the load. However, integrating a microgrid into a distribution network changes the concept of unidirectional power flow to a bidirectional concept. It has many operational advantages over the conventional grid [11], such as:

- Improving the stability of the power grid.
- Increasing the efficiency by reducing transmission and distribution losses.
- Reducing global warming and pollution by using low-carbon technologies.
- Providing independent, continuous supply of electrical power to all consumers in stand-alone mode.
- Offering plug-and-play capability to switch to either grid-connected mode or autonomous mode
- Acting as a backup power source during main grid power outages.

Microgrid is defined as a low-voltage distribution network, in which DERs are interconnected with the different kinds of load. As can be seen in Figure 1.2, it can operate either in grid-connected mode or islanded mode subject to the operational characteristics of the main grid [12]. Various RES such as PV panels, wind turbine (WT), energy storage system (ESS) and loads are connected in the microgrid via power converters, with proper protection, communication, monitoring, and control systems.

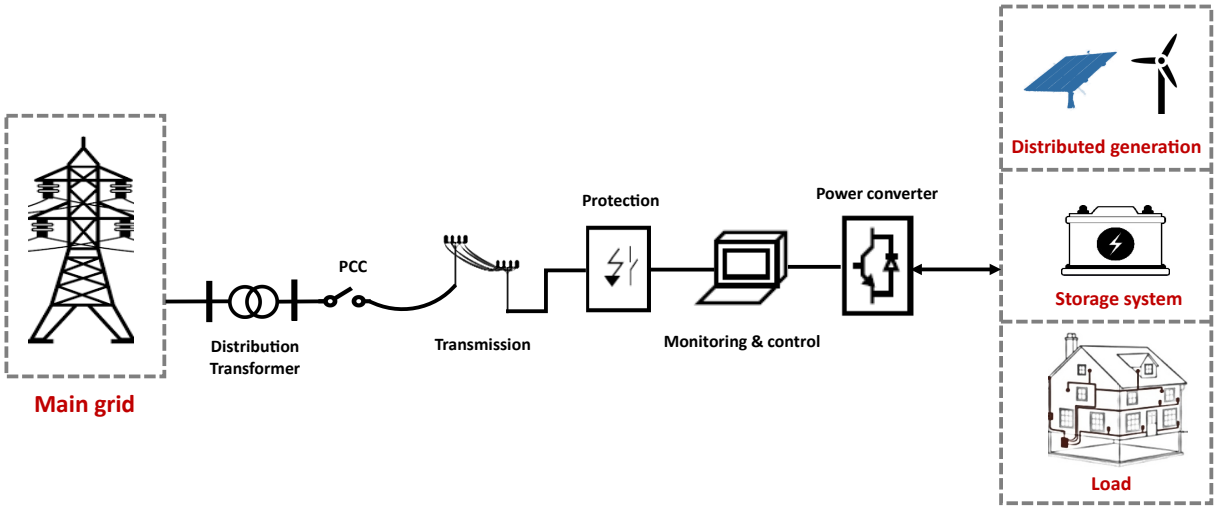

Figure 1.2: A typical microgrid architecture, adapted from [12].

Microgrids can present both AC and DC distribution lines. Each type has their own transmission and distribution levels. Points of common coupling (PCC) constitute the gateway between the main grid and microgrid. The protection mechanisms guarantee an operation, which is designed by different principles and parameters according to the system. Parameters such as voltage, frequency and power quality are continuously supervised and controlled by means of proper monitoring systems based on specific control strategies adapted to the topology of the considered grid. Thus, power converters are the essential components of the grid for AC/DC, DC/DC, or DC/AC conversions. In distributed generation systems, two types of generation technology are applicable for microgrid, i.e., renewable distribution generation systems from RES (e.g., solar thermal, PV, wind, fuel cell and biomass), and systems from non-renewable ones (e.g., diesel engine, stream turbine and gas engine) [13]. Among them, solar and wind technologies have rapidly increased and become significant energy sources in microgrids. Moreover, storage systems

(SS) are generally present in microgrids as they hold great importance for the stability, reliability, and the overall performance of the entire microgrid system. An overview of the different storage technologies, which can be separated into chemical, electrical, electrochemical mechanical and thermal systems, are discussed in [14]. Some key energy storage technologies used for microgrid applications are discussed in [15].
As already mentioned, considering the nature of a microgrid, there are different types of loads (AC, DC). The classification of the load is important for the operational strategy of the overall microgrid management [16].

Based on the type AC or DC and the way their busses are connected, MGs can be categorized into three categories: AC microgrid **(ACMG)**, DC microgrid **(DCMG)** and Hybrid microgrid **(HMG)** [17, 18], which are shown in Figure 1.3, respectively. Each category has distinctive features, which provide different advantages and disadvantages that need to be contemplated. Comparison between each type of microgrid in terms of control, protections and power losses has been discussed in [11, 19].

The **ACMG** has the benefit of using power from the main grid. The AC microgrid structure is based on AC bus and different energy sources (e.g., wind turbines (WT) which can directly deliver AC power) with variable frequency and different voltages connected to the bus through AC/AC power converters. Sources with DC output (e.g., PV panels) and DC loads are connected to the AC bus through DC/AC converters, as shown in Figure 1.3a. However, an AC microgrid needs a relatively complex controller for importing and exporting power while maintaining the system stability and reliability.

While in the **DCMG** structure, sources with DC output (e.g., PV panels) are directly connected to the bus via DC/DC converters. Sources with AC output (e.g., WT) are interfaced to the DC bus through AC/DC converters, as shown in Figure 1.3b. Thus, for the same delivered power, as DC conversion is less complex than AC conversion having to consider both voltages and frequencies of the input-and output powers, the DC microgrid has advantages over the AC microgrid in terms of system efficiency and size, which also result in an advantage considering the system investment and operating cost. Due to that, always for the same delivered power,in the DC grid , a lesser number of power converters are required than in AC one, making possible an optimization of the size and an improvement of the overall efficiency. Nevertheless, the protection system of DC distribution is currently not mature enough compared to the AC system. More research is needed on the aspects such as its protection system, architecture design, control strategies and stabilization techniques in future power systems [16].

HMG combines both ACMG and DCMG in the same distribution system. In this topology, both AC and DC components can be directly integrated due to hybridising of an AC and a DC buses, as shown in Figure 1.3c. A prior, this microgrid topology seems more complex because it integrates the two forms of DC and AC signals, but it globally makes it possible to optimize and therefore simplify production, transmission and distribution depending on the nature of the sources and loads. Finally, HMG will benefit from all the advantages of ACMGs and DCMGs, such as the least number of interface devices, easier DERs integration, fewer conversion stages, lower power losses, and lower overall cost [20, 21, 22].

Among these three categories, DCMG is an attractive technology in the modern electrical grid system because of its natural interface with renewable energy sources, such as the increasingly widely developed photovoltaic, electric loads, such as electronic and lighting devices (LED) and energy storage systems, such as batteries and supercapacitors. In DCMG system, the energy sources and the power electronic loads can be supplied more effectively and efficiently by choosing a suitable voltage level and thus avoiding some conversion stages but each chosen solution has advantages and disadvantages depending on the applications and their requirements. For example considering the energy storage system, a battery system does not have a constant output voltage and the variation of the output voltage depends on the battery chemistry, current, ambient temperature and state of charge (SOC). Connecting a battery directly to the DC bus can cause fluctuations in the bus voltage and inrush current, thereby shortening the battery's service life. Fluctuating DC voltage can cause stability and protection problems in the DC grid system. Therefore, DC/DC converter are normally recommended for connecting battery systems to the DC bus. DC/DC converter can ensure controllable current and output voltage levels, providing opportunities to integrate a number of batteries despite of their SOC level. In contrast to ACMG and HMG, DC distribution systems offer a number of other advantages, among them, reactive power compensation,

power quality and controllability are the most important factors [19, 23, 24].

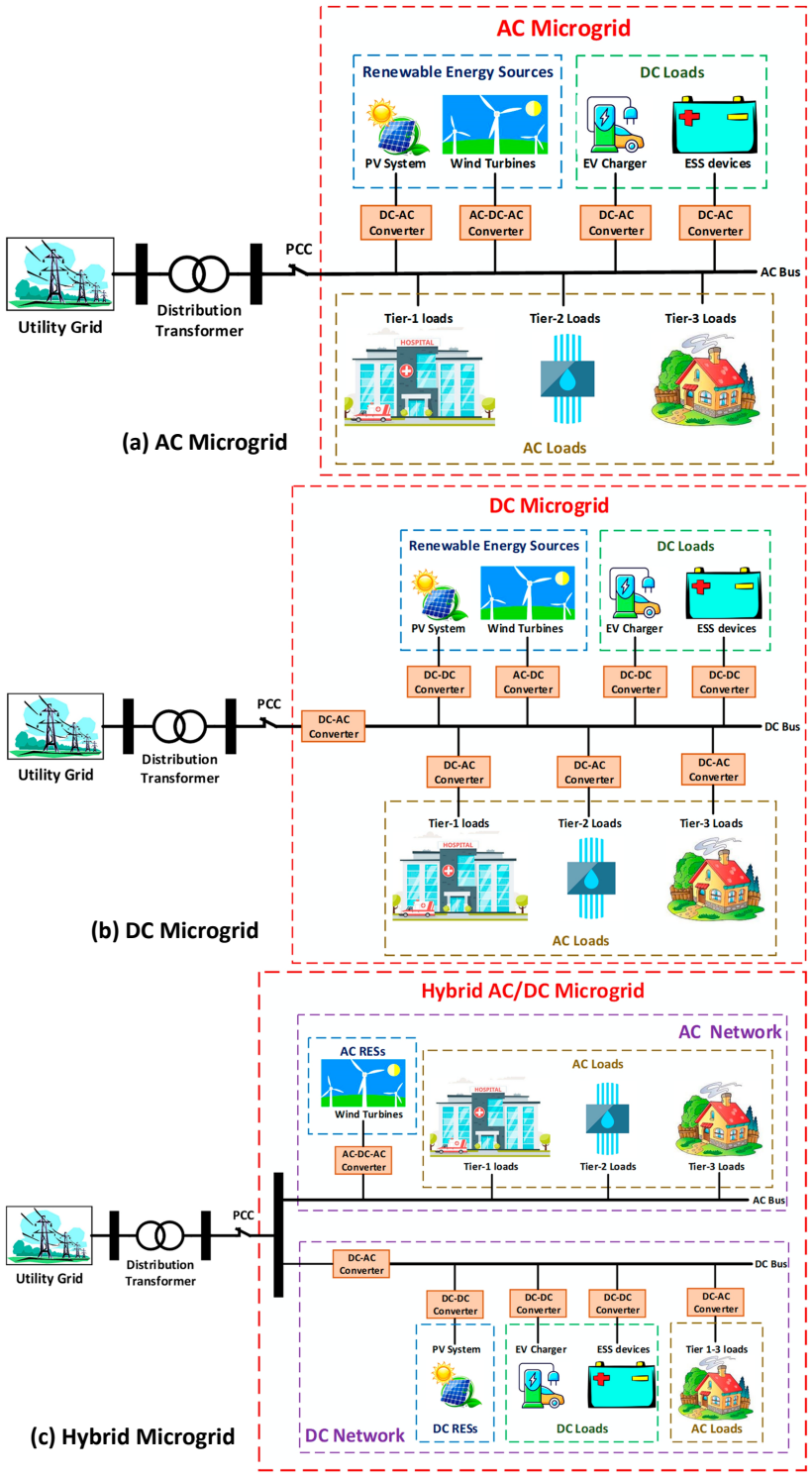

Figure 1.3: Different Microgrid types [18].

Due to the many technological developments, the structure of DCMG is not definitively fixed and, on the contrary, is constantly evolving, particularly in recent decades with the acceleration of the devel-

opment of the integration of renewable energies into the energy mix. In particular, in-depth research is being carried out to develop the DCMG system, better understand and optimize its control and management of the energy mix. To obtain optimal energy management for any type of MG and beyond the purely technological and functional aspects, several other aspects must also be taken into account, in particular the investment and operating costs of the MG i.e., the operating costs, the emission costs, demand response incentives, degradation costs, load shedding costs, energy transaction costs, etc. Each of these points should allow optimal operation of MG subject to various constraints, such as energy balance, grid constraints, demand response, reactive power support, reliability, limits of ESS, and generating unit constraints.
For each MG type, the problems and challenges related to energy management are different. Various methods and techniques are discussed in the literature to address the energy management strategy (EMS) problems of ACMG, DCMG, and HMG systems [25, 26]. Within this context related to the EMS problematic, and in accordance with the objective of the thesis work, DC microgrid system is chosen to discuss all possible aspects such as, DCMG architecture, operation and control, and energy management of the DCMG system. Therefore, the focus of this research is on the DCMG system.

The next section starts with the conceptual design of DCMG and provides a comprehensive overview of the DCMG architecture, control system, and energy management of DCMG.

1.3 DC microgrid concept

The concept of a DCMG is introduced to overcome environmental depletion by harvesting distributed energy from RES, such as PV and wind energy, which are playing a major role in clean energy production. Since the renewable energy technologies has introduced to ancient grid system, the grid dynamics has been totally changed and it completely distinguishes them from other power sources. Such energy sources completely reshaped the power grids, because economic and environmental growth has always been the main concern. Due to the fact, DCMG have demonstrated three principle beneficial properties, namely reliability (physical, cyber), sustainability (environmental considerations), and economic (cost optimizing) [12]. The advantages of DCMG can be harvested in many applications to improve their reliability and efficiency. However, there are some obstacles in the practical implementation of the DCMG which need more attention. Some of these are:

- For the same voltage and power, protecting a DC system is more difficult compared to an AC one because no natural zero crossing of the current exists.
- As previously mentioned, the conversion from AC to DC in low voltage distribution grids requires several steps such as new standards for products and voltage levels.
- Grounding and corrosion issues is higher in DC system than in AC ones.

Despite these problems, DCMG remains an interesting solution and a grid architecture must be redesigned mainly due the introducing of new technologies such as RES and ESS to further improve its flexibility, reliability and controllability. A number of researchers from industry and academia have proposed various possible architectures for DCMG systems, depending on the particular application. In this work, the focus is on DCMG systems for residential applications, which is discussed in more detail in the next section.

1.3.1 DC microgrid architecture

In an architectural context, a DC microgrid comprises distributed generators (DGs), a storage system (SS), power converters and loads interconnected through one or more DC buses, as shown in Figure (1.4).

The different types of AC/DC, DC/DC and DC/AC power converters are always necessary in DCMGs because some sources and/or loads deliver or operate either in AC or in DC modes but most often with an operating voltage different from that of the bus and cannot be directly connected to it. During normal operating conditions, DC bus is interconnected with the utility grid through a Point of Common Coupling (PCC) while the loads are supplied from the local sources (RES based on Distributed Generator (DG)

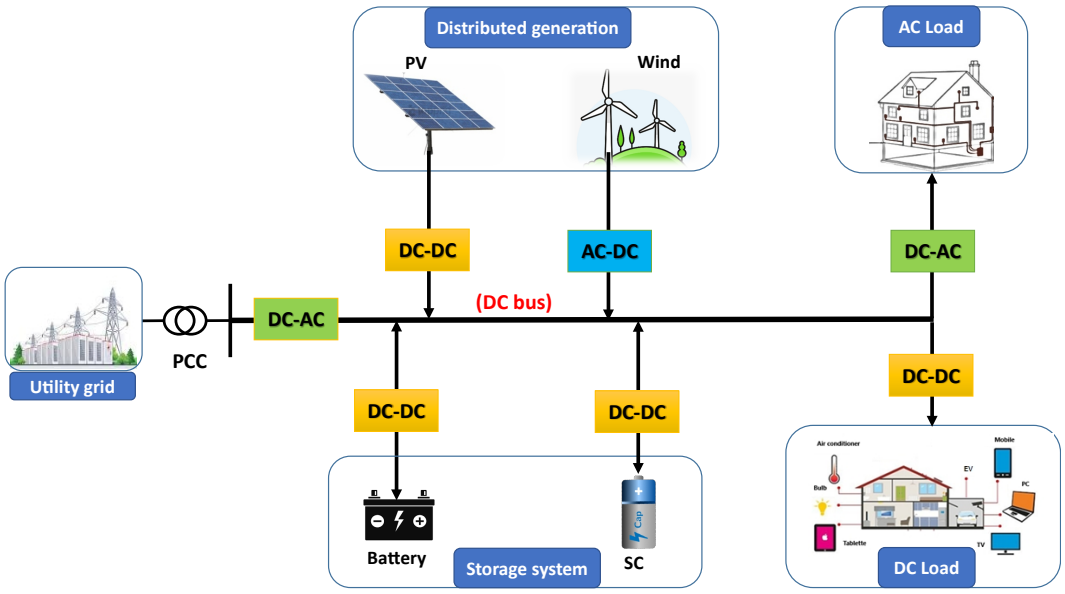

Figure 1.4: Illustration of DC microgrid scheme.

units) and, if necessary, from the utility grid. If the load power demand is less than the power produced by DG units, excess power can be exported to the main grid which can be utilized in case of short production. With the integration of these components, the whole system becomes simpler as compared to an AC microgrid. A smaller number of converters are required because most of the microgrid elements have DC nature, which gives higher efficiency, i.e., energy conversion with reduced losses, and reduces the system cost. In addition due to the system's simplicity, reactive power and harmonic distortion is not a problem in such kind of system.

DCMG presents a new paradigm for the definition of the distributed generation operation, in which AC and DC sources are connected to a common DC bus. All the elements are connected with different converters separately and linked with a DC/AC converter to connect with the main grid as presented in Figure 1.4.

Several voltage levels are used in DCMG and as mentioned in literature concerning residential DC microgrids varying from 5V to 400V. These DC bus voltages are specified by existing DC applications. Three examples can be cited concerning current applications: The universal serial bus (USB), which is the most universal way to distribute 5V of DC power for all electronic equipment in a house or in offices. The second example is the embedded grids in mobile objects such as road vehicles which operate at 12–24V and which are regularly connected to a conventional DCMG for recharging. Finally, we can cite telecommunication applications operating at a level of 48V. [27].

Concerning residential application operating on a 24V DC bus, a design of a 250W DC solar nano-grid with 24V DC distribution bus was presented in [28]. In some literature, a small scale of DG such as a single house or a building is considered as a nano-grid but in this article, the microgrid term is used in a general sense. In [29], 220V DC grid is proposed and modeled for applications in residential houses in parallel of the traditional AC grid. Another voltage level of 380–400V was investigated in the literature used for the data centers. 380V DC test system was presented in [30], which has been developed in Obihiro, Japan. It was concluded that the system allowed not only the reduction of the environmental load while improving energy efficiency but also the formation of an independent community energy system. In a similar approach, in [31], the authors have implemented an experimental platform of DC microgrid with a bus voltage level of 380V. The system is composed, for the energy sources of a PV array and a WT, for the energy storage an ESS by lithium battery pack and a supercapacitor, and for the loads, LED lights and controllable electric loads. It has been shown that converter performances were well achieved. Moreover, the ability to control the power distribution between each unit connected to the bus was validated.

Table 1.1: DC bus levels for residential application [28, 30, 31, 32, 33].

Voltage level	Application	Advantages/disadvantages
5 V	Universal serial bus (USB) connections. Small rechargeable batteries.	+ Easy to connect with a device and distribute power. - Short application range.
12 V	Low load applications for short distance.	+ Safe and same level of DC appliances. + Designed for low power usage.
24 V	High power applications forlong distance.	+ Low level power distribution according to the standard.
48 V	New automobiles charging infrastructure. Telecommunication instruments such as; wireless phones, ethernet.	+ Within the standard of IEEE for DC microgrid. + Simple protection.
380–400 V	For DC computer data centers and possibly commercial buildings as a residential application.	+ Within the standard of Emerge Alliance of buildings. + Easily compatible with main grid. + More appropriate for DC microgrid residential applications. - Additional converter required. - Protection is compulsory.

The existing DC bus levels in residential applications in the literature, with their pluses and minuses, are summarized in Table 1.1.

1.3.2 DC microgrid components

The main body of DC microgrid consists of DGs, SS, converters and loads. Each part is further classified into a number of components having different types and characteristics.

1.3.2.1 Distributed generation elements

Two types of power generation technologies suitable for microgrid design can be found in the literature: renewable generators (e.g., solar thermal, PV, WTs, fuel cells, CHP, hydropower, biomass, biogas) and non-renewable generators (e.g., diesel engines, electric turbines, gas engines, induction and synchronous generators) [34]. Among all these generators, those dedicated to the production of wind and solar energy are currently leading in terms of research and development and in terms of increasing their implantation in the energy mix. According to [35], the use of wind and solar energy has rapidly increased worldwide at a rate of about 30% per year and has become a significant resource in microgrids. Among these two, these last decades, solar technologies are emerging in residential microgrid systems. For this reason, solar energy is considered as a DG in this work.

1.3.2.2 Energy storage elements

Energy storage part has a great importance for the stability, reliability and the overall performance in a microgrid system. There are several energy storage technologies that can be commonly used for MG applications. Each of them has different characteristics such as capacity, energy, efficiency, lifetime, and cost. Various storage technologies are discussed in the literature [36], which are divided into chemical, electrical, electrochemical, mechanical, and thermal systems.

Among all these technologies, electrochemical and electrical ones have been under discussion since many years. In electrochemical technologies, lithium-ion batteries and lead-acid batteries are very popular in grid applications. Lithium-ion technology is now very common, and is well-adapted for integration in small households . The reason for this is the progress that has been made in lithium-ion technology in recent years, especially the increase in energy density which in some cases become superior to other technologies.and its constant cost reduction. In terms of cost, they are until now, more expensive than lead-acid batteries, but the cost of lithium-ion batteries is expected to continue to decline. In hybrid systems based on renewable energy sources (e.g., PV and WT), production varies greatly inducing high

power fluctuations. In these MG types,supercapacitor (SC) storage is also a good choice due to its high power density, low cost, safety features, and high scalability [36]. When considering application requirements such as power and energy profiles, available volume, and operating temperature, these two technologies (lithium-ion batteries and supercapacitors) are at the top of the list of storage systems. These two technologies are thus very complementary for MG applications in terms of temporal dynamics, response time making it possible to adapt to a wide variety of loads. For this reason, lithium-ion batteries and SC are used as SS in the proposed DCMG system.

1.3.2.3 Power converters

As previously mentioned, power converters are important components in the grid system. In any type of grid (AC or DC), power converters are needed to convert the generated power into suitable types of electricity, which are supplied directly to a grid or to consumers. They allow each individual element to be connected to a common DC bus.

The literature discusses various types of power converters [37, 38, 39]. In this study, some of them are listed that are commonly used.

AC/AC converter:
An AC/AC converter is known as a voltage regulator or voltage controller that controls the voltage, current, and average power delivered from a AC source to a AC load. It is used to adjust AC output voltage regarding to the AC input voltage. AC voltage regulators have several practical applications, such as light dimmer circuits and induction motor speed control. In this type of converter, the input voltage source is AC and the output is AC, so the circuit is classified as a AC/AC converter [38].

AC/DC converter:
AC /DC converters are electronic circuits that convert a AC input to a DC output. The input can be a single-phase or a three-phase voltage AC. AC / DC converters are also called rectifiers that convert the input AC voltage to a variable DC voltage. AC /DC converters are used in a variety of applications, including consumer appliances, uninterruptible power supplies (UPS), medical equipment and renewable energy conversion systems. However, they have power quality issues in the form of harmonics that cause poor power factor. There are several methods to mitigate these problems in AC /DC converters. Typically, filters are recommended to remove the AC ripple and maintain an unregulated DC voltage. However, in some cases, the ratings of these filters are close to the ratings of the converters, which not only increases the cost, but also increases the losses and the number of components, resulting in lower system reliability [40].

DC/AC converter:
DC/AC converters are also called inverter and they produce AC outputs with controllable phase, frequency, and magnitude. They are used in numerous applications, including PV systems, battery storage systems, traction drives etc. Such converters are more complicated because it needs some kind of oscillator that reverses the current direction at the required frequency.

DC/DC converter:
DC/DC converters are electronic circuits that convert a DC voltage to a different DC voltage level, often providing a regulated output. The DC output voltage can be higher or lower than the DC input voltage, but is always controlled by the variable duty cycle. The DC/ DC converter works only with DC sources (DC) and not with AC sources (AC). Therefore, the DC /DC converter is used in electric vehicles to convert the high battery voltage to a low voltage for use by conventional loads (e.g., lights, power windows, etc.). Some important applications where DC /DC converters are widely used are renewable energy integration, medical devices, smart lighting and other small electronic devices. In microgrid applications, the use of DC /DC converters is limited to DC microgrids, as such converters are mainly used to connect various renewable energy sources (PV), energy storage systems (batteries) to the DC bus or load. Several types of DC /DC converters are discussed in the literature [41] , but the most commonly used converters in DCMG systems are buck converters, boost converters, and buck-boost converters, which is further discussed in chapter 2.

1.3.2.4 Loads

The different types of loads play an important role in the stability of the microgrid and thus in the type of operation and control that must be developed. As mentioned earlier, there are several voltage levels defined for residential applications that have been discussed in the literature. Depending on the power of each appliance (low power, medium power, and high-power appliances), different voltage levels (5V, 12V, 24V, 48V, 380-400V) could be defined.

Based on the literature review, we have chosen microgrids with a bus voltage level of 48V for the proposed DC system environment for this work. This choice was indeed driven by its numerous advantages, see Table 1.1, mainly because it responds to the standards defined by IEEE for DC microgrids. At this voltage level, no additional converters are required to match mostly household equipment, and it can easily be compatible with the 230V supply voltage AC with a minor modification to achieve the required voltage level [32, 33]. Therefore, for residential applications, a 48V DC bus could be a suitable voltage level.

1.4 Operation and control of DC microgrid

Thus, in regard to microgrid efficiency, reliability and stability, the control structure has great importance. Many researchers have addressed the operational and control issues in microgrids to allow their efficient and stable operation [42, 43, 44] . Focusing on the microgrid control structure, this classification can be done by following various objectives. For example, based on their controller function, grid connection and response time, a systematic classification of various control techniques is presented in Figure 1.5 that we will discuss in the following paragraphs.

1.4.1 Microgrid control classification

With reference to power system control architecture, control techniques can be categorized into centralized, decentralized, and distributed control, as illustrated in Figure 1.6.

In **centralized control**, the microgrid central controller (MGCC) controls the actions of all units. In this control, substantial bidirectional point to point communication is required between all units and the central controller. Nevertheless, in practice and due to large geographical area and distance between the various elements constituting microgrids, it is not feasible to have a fully centralized control among them.

At the other extreme solution for the control, in **decentralized control**, every single unit is controlled by its own local controller, receiving for the command only local information such as frequency, voltage, maximum available power, and so on. In fully decentralized control based as example on a neuronal topology, some local controllers can exchange information with some other neighbor control units. However, fully decentralized control is also not an available solution in practice because of the dependency of various units within the system. It can cause the system to become unstable or operate non-optimally.

Therefore, as often usual in industrial and technical systems, a compromise between these two controls is preferred and can be obtained by introducing a mixed approach called the **distributed control** scheme. It consists of some degree of centralizing along with some degree of decentralized properties. In the distributed control method, each unit uses local information such as frequency and voltage provided by its neighbors. In this method, local units exchange information through two-way communication links. This method can also preserve the unit's privacy because a lot of important information is not shared globally [45].

It is important to note here that PV, WTs, and SS with the loads are used as an illustration in a nano-grid scale. Each unit can be further replaced by one or several nano-grids to constitute a larger scale microgrid.

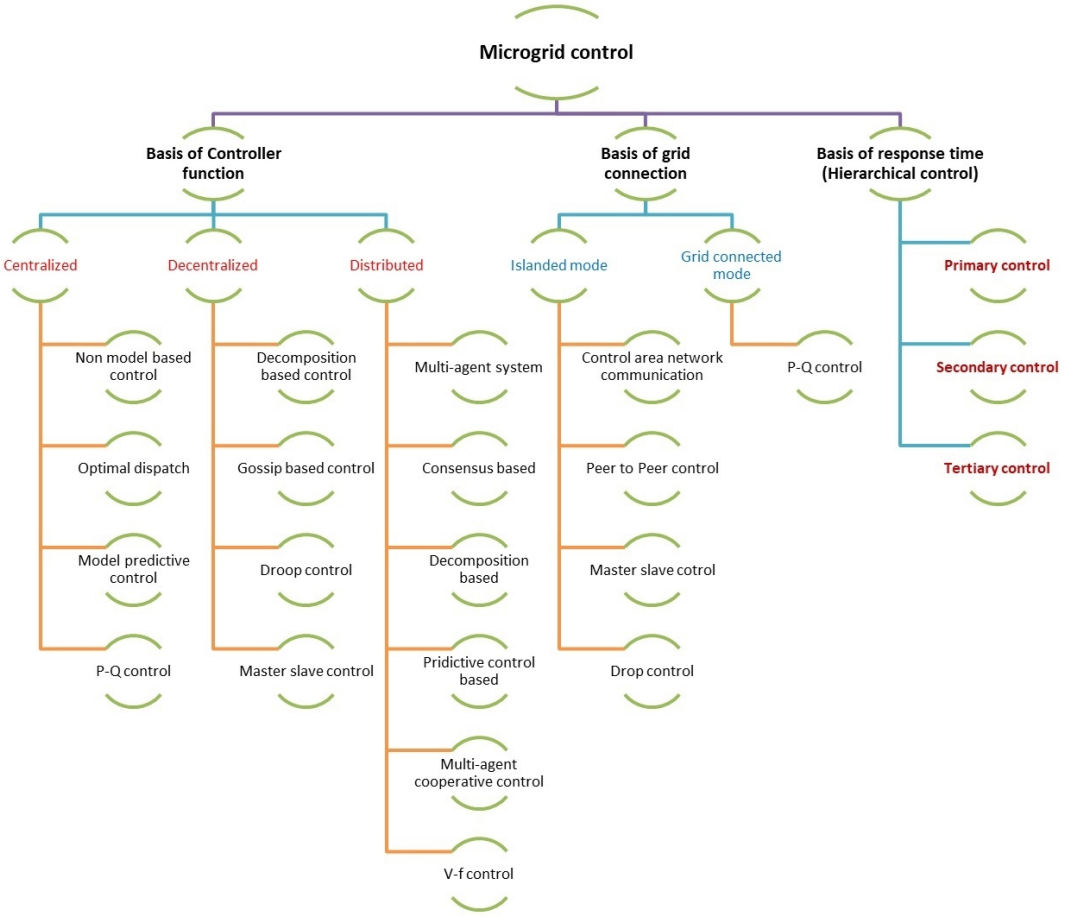

Figure 1.5: Classification of various microgrid control techniques, summarization based on [42, 43, 44].

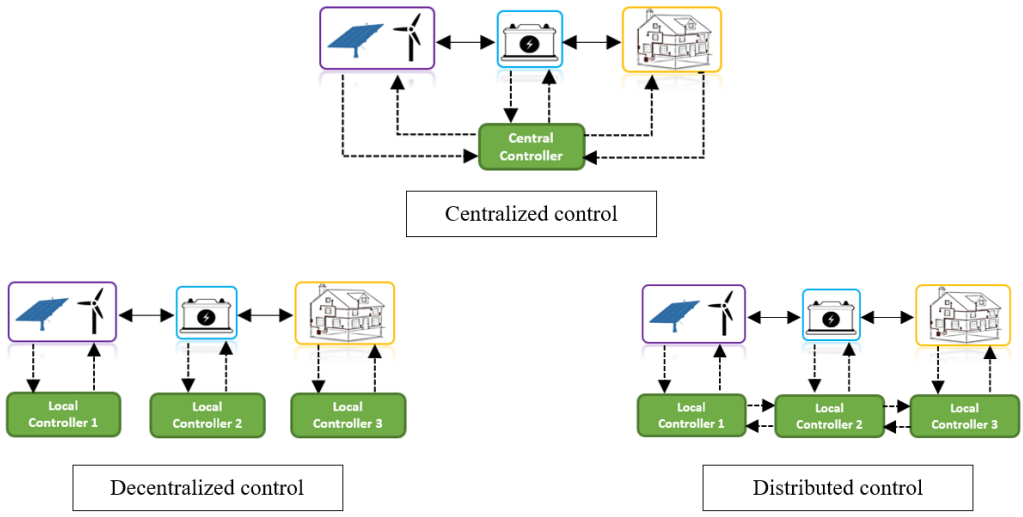

Figure 1.6: Illustration of centralized, decentralized, and distributed control scheme, adapted from [42].

The main building block of a microgrid integrates several DG units, ESS and loads together to build a small power system. To control such system, it is necessary to implement a full distributed control strategy involving different time scales, referring to the hierarchical control structure and adapted to each elements constituting the microgrid. This hierarchical control structure has been proposed several times in the literature [46, 47] and consists of three levels, i.e., primary, secondary, and tertiary control, as shown in Figure 1.7.

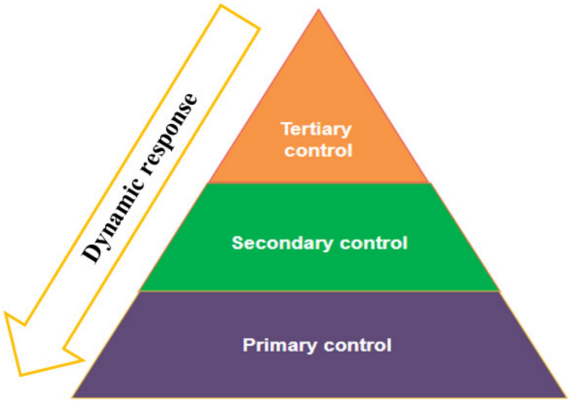

Figure 1.7: Hierarchical control levels in a microgrid structure, adapted from [47].

1. The **primary control** is assumed by local DG controllers, with the essential objective to regulate the local voltages and currents. Thus it mainly involves voltage loop control, current loop control, MPPT control or SOC estimation. It also controls the breakers/switches (on/off and protection functions) and load control (curtailment functions). As there is no information exchange between each DG, this control is totally decentralized.

2. Primary control may cause voltage deviations, especially when the heavy loads are connected to or disconnected from the microgrid. The system might run abnormally or drop into under or over voltage protection.

2. The **secondary control** is at a higher level than the primary one assuming the interface control between the DGs and the supervision control of the microgrids, i.e., the tertiary control. It is linked with the voltage compensation and sharing performance enhancement. It deals with voltage control for the regulation of DC bus voltage. Indeed, primary control may cause voltage deviations, especially when the heavy loads are connected to or disconnected from the microgrid. The system might run abnormally or drop into under or over voltage protection. Thus, the objective of secondary control is to develop a distributed supervision control scheme for voltage quality enhancement, such as voltage unbalance compensation. For regulating the DC bus voltage, droop control is recommended for the voltage control among microgrids. The proposed control scheme should be flexible and make the controller have the plug-and-play property.

3. The **tertiary control** is on the top layer of the microgrid control diagram. Its dynamic response is the slowest one among the three layers. In the tertiary control, economic dispatch, power flow optimization, and optimal energy scheduling issues are usually considered. The tertiary control is regarded as the energy management system (EMS) of the microgrid as proposed in reference [46] . It is designed to achieve the accurate power sharing control among DG units, and the power exchange between microgrid and external grid in the case of grid-connected mode. It is developed in a way that the microgrid central controller considers the optimal power flow, economic dispatch, and optimal energy scheduling problems in the microgrid to formulate an EMS. The EMS uses inputs (e.g., weather forecast, load demand, SOC, energy prices, etc.) to carry out scheduling and optimization procedures. It determines the optimal set points for distributed generation (DG) and load operation in the microgrid. Additionally, it deals with the energy market, organizing the energy dispatch scheduling from an economic point of view. Based on

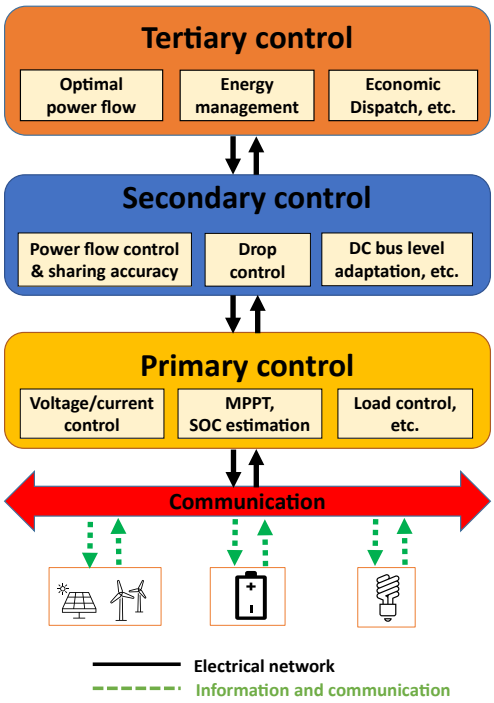

Figure 1.8: Typical control objectives and functions in a DC microgrid.

the hierarchical control, energy management strategies can be defined. Hence, the decisions on microgrids are made by the EMS. In this sense, multi-objective functions ought to be specified by using information such as demand forecasting, power generation, energy storage, weather forecasts, and finally, some non technical aspects as the energy grid prices, and so on [48, 49, 50]. Based on the previous literature review [51, 52, 53, 54], analysis has been conducted based on multi-objective functions.

Based on the objective functions, a typical hierarchical control for a DC microgrid is summarized and presented in Figure 1.8. In this way, the control system can be more flexible and reliable while respecting the system objectives and the operating constraints.

1.5 DC microgrid energy management system

The microgrid EMS is a multi-objective system that deals with technical, economical, and environmental issues. The main objectives of the EMS are to optimize the operation, energy scheduling, and system reliability in both grid-connected mode and islanded mode. Therefore, for control purposes, it is necessary within a microgrid that an EMS has a connection with each part of the system, as shown in Figure 1.9. The whole microgrid operation is controlled and coordinated by a microgrid central controller (MGCC) and local controllers (LCs) via a communication network called information and communication technology (ICT) [55]. It should be noted that as a single microgrid is illustrated herein (with less geographical area and distance), a DCMG is applied for illustration.

Different EMS have been proposed in the literature to achieve optimal and efficient microgrid operations. Common techniques and methods used for the energy management of microgrid systems can be classified into two major categories, i.e., classical methods and artificial intelligence methods, as shown in Figure 1.10. A practical EMS may be a combined form of different methods.

We present in the next section the various existing EMS methods as presented in literature. In addition, several existing software tools and hardware components dedicated to residential applications are also listed at the end of this section.

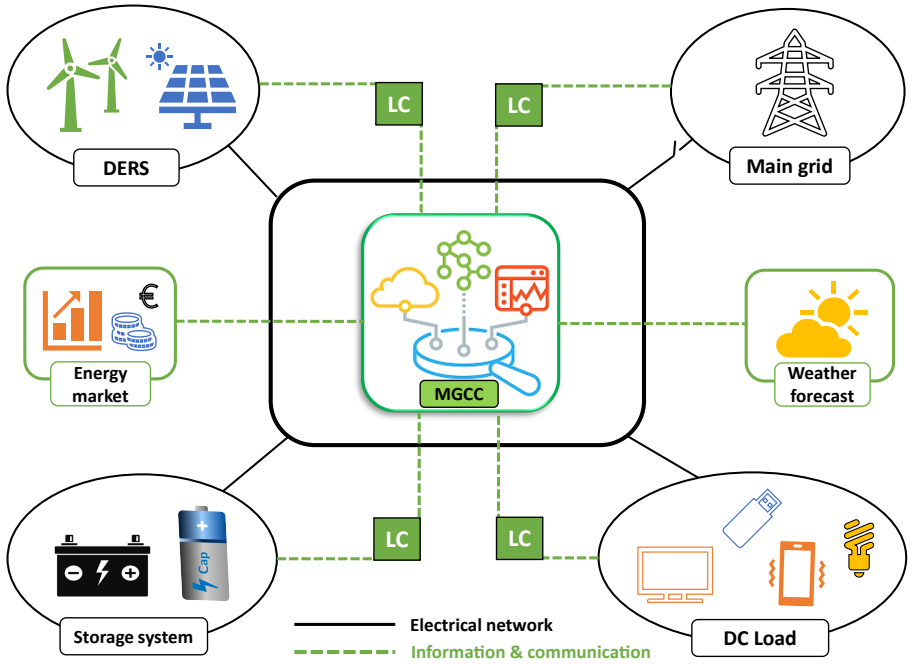

Figure 1.9: EMS-based DC microgrid architecture, adapted from [56].

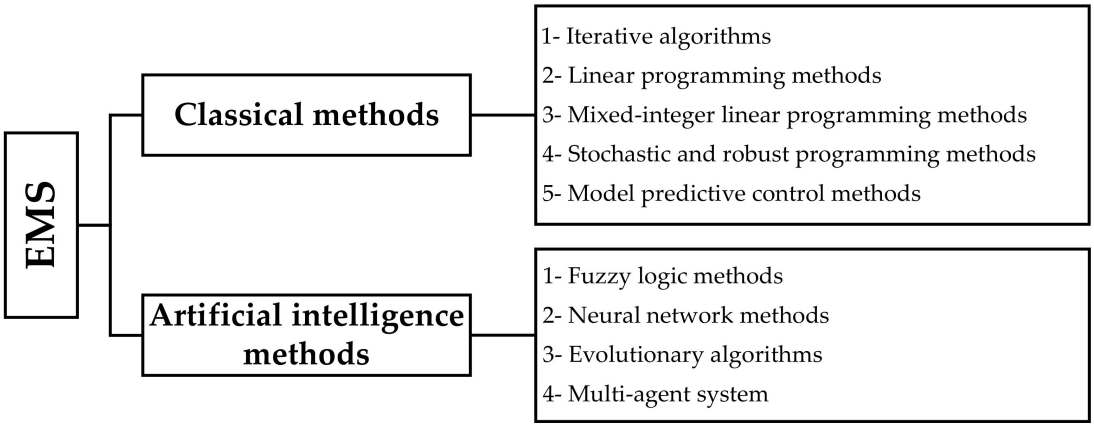

Figure 1.10: Proposed classifications of energy management strategies.

1.5.1 Energy management based on classical methods

A limited number of studies have been carried out using classical methods for the energy management of a DC microgrid system. Most of the research has been conducted in the size optimization of standalone PV-WT HES [57, 58, 59, 60, 61]. However, they may provide useful guides for EMS design for residential applications. Commonly used classical methods include iterative, linear programming (LP), mixed integer linear programming (MILP), stochastic and robust programming methods, and model predictive control, which are reviewed in the following subsections.

1.5.1.1 Iterative algorithms

In the literature, iterative algorithms are utilized to realize different objective functions. It has been implemented for the sizing optimization of standalone systems with single objective optimization (SOO)

functions. In Reference [62], Hosseinalizadeh et al. applied an iterative algorithm to optimize a standalone PV-WT-FC-BS-HT HES in terms of minimizing the system's total cost of energy for four different regions in Iran. The authors of [61] evaluated the reliability of the HES by using loss of energy expectation (LOEE) and loss of load expectation (LOLE) as estimation parameters. In this study, it was assumed that the value of LOLE parameter must be less than 2% to achieve system reliability. The study found that the PV-WT-BS HES was more economical and reliable without the FC system. Bhuiyan et al. [63] proposed an enumeration-based iterative algorithm to perform energy management in terms of component size optimization within microgrid residential communities. This system comprised PV, WTs, a BS and DGs. In this research, the system reliability was evaluated by analyzing the battery SOC and the power balance between generation and demand. Furthermore, the study found the PV-WT-DG HES system to be an interesting techno-economic solution in meeting the energy demand of remote consumers.

1.5.1.2 Linear programming methods

This last decade, few studies have used linear programming (LP) to implement energy management in terms of optimizing the standalone HES with PV and WTs [64, 65]. Nogueira et al. [64] suggested a methodology that uses LP to size and simulate a standalone PV-WTBS HES for a remote rural area by minimizing the total cost of the system while assuring the system reliability by using the measure of loss of power supply probability. Indu Rani et al. [66] proposed a residential microgrid system in which PV panels were connected to the grid to supply DC loads without any interruption. An effective power flow management system was designed to achieve this goal. Its effectiveness in providing uninterruptible power to DC loads and maintaining the total harmonic distortion (THD) of the injected grid current was proved. In Reference [67], Battistelli et al. suggested a practical prototype to assess the contribution of vehicle-to-grid (V2G) systems to supporting the electricity market.

An optimization model based on a linear programming algorithm was integrated into the EMS to assess the interaction between the small electric energy systems (e.g., microgrids) and the main grid. Meanwhile, stochastic programming and robust optimization (more details in subsection 1.6.1.4) were applied to deal with uncertainties related to renewable power generation and vehicle aggregation separately. Karami et al. [68] proposed a simple and efficient EMS for a hybrid system comprising a PV panel, a FC system, a battery, and a super-capacitor. Sixteen different scenarios covering both night and daylight were considered for the power flow management. The optimal energy production was achieved by the application of MPPTs on both PV and FC and the use of compensators. Pascual et al. [69] proposed an EMS for a residential microgrid system consisting of PV panels, a WT, and a battery connected to the main grid. The main objective was to minimize the power peaks and fluctuations for energy exchange with the grid. The renewable generation and load forecasting together with the battery SOC were considered in a single control rule to achieve the goal.

1.5.1.3 Mixed-integer linear programming (MILP)

MILP is used for the modeling of energy management problems because it considers integer and binary variables to decide the operation system. In the literature, several authors used MILP methods for microgrid EMS according to the variables and objective functions. In Reference [70], Sukumar et al. proposed a power sharing, continuous run, and on/off-based mix-mode microgrid EMS. The on/off mode was modeled and solved by a MILP solution approach that optimizes the operation of the microgrid with respect to on/off connection status of the FC system. Meanwhile, the other two modes were modeled and solved by an LP method. Comodi et al. [71] introduced a MILP energy trade profit model-based EMS for a residential microgrid system. The PV power was forecasted by a basic neural network (NN) method. The integration of thermal storage and batteries was realized by load management. The batteries were concluded noncompetitive for the residential applications because of their high investment and replacement cost in the residential market. For optimal energy management of residential microgrid systems, an operating cost-minimization model based on MILP was proposed in [72]. It encompassed energy trading cost and penalty cost on adjustable load shedding. Both energy costs and battery wear costs were included in the minimization. In this study, three types of loads were considered, namely:

critical, adjustable, and shiftable loads. The loads were divided into different power levels which analyzed the tradeoff between load demand and the battery state of charge (SOC).

1.5.1.4 Stochastic and robust programming methods

Stochastic and robust programming is considered as a two-stage approach which deals with constrained optimization with uncertainty. In microgrid systems, energy management is facing new challenges due to the increasing number of variable generation sources. To meet these challenges, stochastic and robust optimization methods are proposed to overcome the uncertainties in Reference [73]. A probabilistic scenario-based optimal day-ahead economic operation was presented for a hybrid AC/DC microgrid system. It minimized the overall operating cost by using the forecasting values of electricity price, solar power, wind power, AC and DC loads. A two-stage stochastic programming model was presented in Reference [74] to optimize microgrid operation while considering uncertainties of RERs and load demand. The first stage was associated with optimization of investment cost of microgrid, and the second stage deals with the energy management operation of the microgrid.

1.5.1.5 Model predictive control methods

Model predictive control (MPC) is very useful for defining the EMS in microgrid systems. In the literature, MPC is widely used to minimize the daily generation cost and emission of the microgrid system while considering the technical constraints in real operations. In Reference [75], Solanki et al. presented an EMS strategy based on a MPC approach. Authors put emphasis on the use of smart loads to perform an efficient operation. A supervised NN was used to estimate the residential controllable load. In another study [76], an MPC-based EMS of a grid-connected microgrid was presented to minimize the energy trading cost with the main grid, and to ensure a better utilization of the battery during peak load demand. It also ensured the maximum use of wind power to meet the local demand. Authors introduced a fault tolerant scheme to have a smooth operation of the microgrid during sudden failures of WTs and power supply shortage. Akter et al. [77] suggested a hierarchical model for power sharing among residential consumers. Each house was equipped with a central EMS controller to share information in a grid-connected mode residential microgrid. The intention was to maximize the energy sharing among houses in comparison with the main grid to minimize the investment cost. The authors concluded that the payback period was reduced due to power sharing among residential consumers.

1.5.2 Energy management based on artificial intelligence methods

Diverse studies have been focused on the utilization of artificial intelligence methods for the multi-objective energy management of microgrids. In this category, artificial intelligence techniques are used to solve single-objective optimization (SOO) and multi-objective optimization (MOO) problems. In general, artificial intelligence methods are more flexible and efficient in dealing with complex optimization problems, such as fuzzy logic (FL), neural network (NN) and evolutionary computation methods. In addition, a multi-agent system (MAS) composed of multiple interacting intelligent agents has also been introduced to microgrids. This subsection gives a more detailed review of these studies.

1.5.2.1 Fuzzy logic methods

FL techniques are widely used for energy management in standalone or grid-connected hybrid renewable energy systems. FL can effectively manage the multi-control functions. Several studies have been found in the literature discussing FL-based EMSs. The design and implementation of an EMS based on fuzzy control for a DC microgrid system was presented in Reference [78]. In this work, the modeling, analysis, and control of the DERs and ES devices were completed in a MATLAB/Simulink environment. The FL controller managed the battery SOC to ensure a longer battery life and to offer better performance for the entire system at low cost. Different membership functions with variables were defined for both inputs and outputs of the system. The simulation result validated the accuracy of the proposed system with a fuzzy controller that can maintain the battery SOC at a certain level, irrespective of the amount of power generated from the microgrid system. Erdinc et al. [79] studied a FL-based EMS for a standalone

hybrid power system. This residential system comprised WTs, PV, a FC system, and batteries. The PV and wind energy served as the primary power sources, the FC provided backup power during the unavailability of the primary sources, and the battery unit was used for storage. The main objective of this study was to employ an FL-based EMS to regulate the overall system power flow while maintaining the battery SOC. The authors herein justified the advantages of the FL-based EMS over other previously developed approaches, in the aspects of fast response capability and ease of adapting to new conditions during the period of operation.

1.5.2.2 Neural network methods

The neural network (NN) is another intelligent technique commonly used for control and energy management of microgrid systems. It is an advanced approach which is computationally intelligent and has human-like expertise. NN has achieved remarkable success in control system applications due to its reliability, computational capability, and adoptability to handle complex nonlinear systems. Wang et al. [49] introduced a Lagrange programming NN approach to optimize economic dispatch and minimize the system objective function. Meanwhile, a radial basis function NN was applied for the day-ahead prediction of renewable energy production and load demand. In Reference [80], Venayagamoorthy et al. proposed an intelligent adaptive dynamic EMS for a grid-connected microgrid. An action-dependent heuristic dynamic programming (ADHDP) combining the concept of dynamic programming and reinforcement learning was developed by using two NNs. Meanwhile, an evolutionary strategy was proposed to dynamically optimize the EMS over time. It maximized the utilization of RERs and minimized carbon emissions to achieve a reliable and self-sustainable system. It can also improve the battery life. Jifang et al. [81] proposed a NN-based control strategy for a multi-energy common DC bus hybrid power system. The authors developed a hybrid model for an hourly forecast of a PV and wind renewable energy system.

1.5.2.3 Evolutionary computation

Evolutionary computation is inspired by biological evolution and forms another popular sub-field of artificial intelligence. Genetic algorithm (GA) is a random-based classical evolutionary algorithm. It is one of the most powerful optimization algorithms. In several studies [82, 83], GA has been implemented to find the optimal sizing of a hybrid system. Ogunjuyigbe et al. [79] used GA for the optimal sizing of a hybrid energy storage system (HESS) in standalone mode. In this study, the authors inspected five different combinations for residential loads. The study found that PV-WT with HESs is the most optimal combination in terms of cost, net dump energy and CO_2 emissions. In Reference [83], the authors used GA for the optimal sizing of renewable energy sources (RES) with a battery storage system (BSS) for four different residential zones in Karnataka India. The study found that PV, WT, and BSs are the most cost-effective solution for residential applications. An improved version of GA, called non-dominated sorting genetic algorithm (NSGA-II), was discussed in [84, 85]. Kamjoo et al. [84] applied the NSGA-II algorithm to optimize a standalone PV-WT-BSs combination for residential loads in Kent, UK and provided promising results in solving MOO problems.

Meanwhile, several other algorithms are also used to solve the non-linear optimization problem including particle swarm optimization (PSO), ant colony optimization (ACO), fruit fly optimization algorithm (FOA) and others. PSO is one of the most popular heuristic algorithms in solving the non-linear optimization problem because of its simplicity, ease of implementation and fast convergence. Suhane et al. [86] used ACO to find the optimal sizing of PV, WT, BS, and DG in terms of minimizing the total cost for a small village in India. Fruit fly optimization algorithm (FOA) is a heuristic evolutionary computation method used in finding global optimization. In Reference [87], authors utilized an improved FOA (IFOA) algorithm for the optimization design of a standalone PV-WT-BS-DG system on Dongao island in China. The study found that with a smaller number of WTs and battery units, the total cost can be reduced.

1.5.2.4 Multi-agent system (MAS)

A multi-agent system (MAS) is made up of intelligent agents embedded in different sources and loads working all together to solve the problem of energy consumption control in the network. A MAS-based

approach is used for optimal operation of a microgrid system. All the system elements, such as storage units, generation units, grid and consumer side, are considered as an agent. Anvari-Moghaddam et al. [88] suggested a MAS-based EMS for efficient operation of a grid-connected residential microgrid. The agents were classified into central coordinator agent, building management agent, RER agent, battery agent, and service agent. The objectives of the proposed method were to minimize operating cost while satisfying the consumer's comfort level.

1.5.3 Existing software tools and hardware components

This section introduces both software tools and hardware components used for energy management of microgrid applications. In the literature, many open-source software tools have been used for the optimization of hybrid renewable energy systems. The most used software tool in size optimization for PV-WT HES is Hybrid Optimization Model for Electric Renewable (HOMER) [89]. Another software, named Improved Hybrid Optimization by Genetic Algorithm (i-HOGA), has been used in several studies for sizing optimization for standalone PV-WT HES [90]. TRNSYS and graphical user interface (GUI) are graphically based software tools and are extremely flexible [91]. Several hardware micro-controller boards based on Arduino, Raspberry Pi (RPi), and Color Control GX (CCGX), and SCADA, are explored in [92]. All these tools are primarily used for the energy management of microgrids.

1.5.3.1 Software tools

Primarily, researchers throughout the world have used the software environment HOMER to optimize their suggested hybrid systems. HOMER is a computer software that can evaluate various design options for both standalone and grid-connected energy systems. Three main tasks that HOMER can perform are simulation, optimization, and sensitivity analysis [93]. Bhakta et al. [94] utilized HOMER for sizing, optimizing, and performing the economic analysis of a PV/wind hybrid system with a battery bank for microgrid residential application in Northeast India. In Reference [95], Das et al. carried out a feasibility study to find the optimal size combination of hybrid energy system for a household user, applied for inhabitants in Kuakata, Bangladesh. Giannoulis and Haralambopoulos [96], Al-Karaghouli and Kazmerski [97], Bekele and Palm [98], Ma et al. [99], Adaramola et al. [100], Olatomiwa et al. [101], Nandi and Ghosh [102], Sen and Bhattacharya [103], and Lau et al. [104], used HOMER to optimize their proposed standalone hybrid systems. Different locations throughout the world (Nigeria, Bangladesh, Ethiopia, Iraq, Hong Kong, Ghana, India, Malaysia, and Greece) are covered. Each survey suggested a particular combination of components which is different from others in terms of performance, according to a certain location.

HOMER is not the only software environment used to optimize hybrid systems. Some researchers have preferred to developed under i-HOGA environment which is a hybrid energy system optimization software developed by the University of Zaragoza-Spain [105]. It utilizes the genetic algorithm for the size optimization of single- or multi-objective functions. i-HOGA performs optimal control strategies with less computational time compared to the use of GA alone. In Reference [106], Fadaeenejad et al. used the i-HOGA software to analyze the optimal size combination for a remote village in Malaysia in terms of minimizing the amount of cost of energy and CO2 emission.

Beside these two softwares, TRNSYS software can be used to simulate the behavior of transient systems. In Reference [91], Behzadi and Niasati examined a hybrid system consisting of PV, FC, and battery. In this system, TRNSYS software was used to conduct the performance analysis. Nevertheless, the system sizing could be carried out by using the GA via i-HOGA, manual calculation, or HOMER. Authors used three different energy management strategies to dispatch energy in this hybrid system. Firstly, the value of excess energy is checked. If it is positive, the excess energy will be directed to charge the battery to its maximum SOC. The excess energy is then directed to produce more hydrogen. However, if the excess energy is negative and the SOC of the battery is less than its minimum SOC, then FC system will supply the load if the pressure in the hydrogen tank is higher than the critical value; otherwise, the battery will supply the load. In the second step, the control system never checks for the minimum SOC. It only checks for the level of pressure in the hydrogen tank. Lastly, the nominal power

of each component is checked, and control system decides how much amount of power can flow toward each storage device.

A similar approach was presented in Reference [107], in which a hybrid energy system (hydrogen storage and a supercapacitor) was used as a SS. In this reference, the aim of the proposed energy management strategy was to satisfy the load requirement. The PV panels prioritize supplying the load, and surplus energy is used to generate hydrogen. When the hydrogen SS is filled, excess energy is directed to the supercapacitor. If the SS is fully charged, then the solar system will be automatically shut down.

GUI integrating different algorithms is graphically used for sizing optimization and measuring system efficiency in homes and offices for residential applications. In several articles, GUI is considered as a real-time monitoring and energy management tool. In Reference [108], GUI was used to optimize the size of a hybrid PV, WT, BS, and DG system while considering the peaks and troughs of wind speed and solar irradiance for a complete year. The proposed method used the measured annual hourly solar irradiation and wind speed to simulate the real time operation of the hybrid system. In the study, authors found that the peaks of solar irradiation and wind speed affect the size optimization results.

1.5.3.2 Hardware components

Arduino is an open-source hardware platform supportive of electronic prototyping. It has been used in different projects and had several applications Arduino micro-controller has been used to verify the smart grid features [109]. In this study, a multi-agent approach was used to address the complexity issues in the microgrid network.

Raspberry Pi (RPi) is an open-source and series of small single-board computers (SBCs) developed by the Raspberry Pi Foundation of the University of Cambridge in 2012. It provides huge computation resources and wide connectivity options. Raspberry Pi features a Broadcom system on a chip with an integrated ARM cortex A72 processor and on-chip graphics processing unit (GPU). In addition, USB 3.0 and Gigabit Ethernet ports are available. In the context of EMS, it can bring new possibilities for the integration and development of an operating system (OS). According to authors, it gives easy access to a high level of computation while providing the same input/output pins as a microcontroller [3].

In 1983, Texas Instruments (TI) produced the first DSP TMS32010 with 16-bits operation. Progressively, a series of processors such as, C6000 DSPs, C5000 DSPs, OMAP Processors, and C2000 DSPs are made available with different features and various applications [110]. To date, various types of digital signal processors (DSPs) are invented and discussed in the literature. In [111], a DS -1104 controller is used for the control strategy. It is expensive and bulky compared to the newer processors. Another version of the DSP board (TMS320F2812) is discussed in [110]. It is an old technology that has many drawbacks, such as the lack of floating point computation support. In [112] TMS320F28335 processor is discussed, which is very up-to-date and better than others in terms of efficiency and control objectives.

Another category of powerful and real-time simulation devices is investigated in the literature, including real-time simulators from companies such as OPAL-RT, Typhoon and dSPACE. It provides real-time simulations for electrical conversion and enables customers to conduct precise and exhaustive testing more quickly. In [103], authors designed a real-time simulation platform to simulate and control the system. In the studied system, PV panels and a WT were linked with the batteries. The objective of this study was to control the speed of the WT and maintain the battery SOC.

1.5.4 Energy management strategies analysis

EMS integrated DCMG structure is presented previously in Figure 1.9, consisting of PV panels and a WT connected with a SS (e.g., batteries and supercapacitors) via power converters. Numerous energy management strategies have been discussed in the literature, but few of them relate to the DC microgrid system for residential applications. Most adopted energy management strategies, such as linear programming-based EMS, artificial intelligence-based EMS, and hardware and software tool-based EMSs, such as SCADA and HOMER, are chosen with the system configuration (PV/WT/fuel cell/storage) and control objectives, are summarized in Table 1.2. It should be noted that no single method can satisfy all the requirements, and hybrid methods may be used in combination in an EMS, which is further discussed in chapter 3.

Table 1.2: Several examples of EMS strategies with their control objectives

System configuration	**EMS Approach**	**Control objectives**
PV/Battery/Fuel cell [65]	Linear programming (LP)	Battery overcharging protection.
PV/Wind/Fuel cell/Battery [61]	Linear programming (LP)	Reduce the computational time. Minimize the energy cost and CO_2 emissions. Increase the battery life.
PV/Fuel cell/Battery [60]	Model predictive control (MPC)	Weather forecasts. Optimize microgrid operation while considering uncertainties of RERs and load demand. Minimize the daily generation and CO_2 emission.
PV/Wind/Fuel cell/Battery [48]	Fuzzy logic (FL)	Satisfy the load demand while maintaining the battery SOC, and keeping the hydrogen storage tank at maximum level. Cost optimization.
Hybrid RES based on SS integrated with a grid [78]	Fuzzy logic (FL)	Optimization and design of control strategy such as; power, energy efficiency, economic evaluation, environmental effects.
PV/Wind/Fuel cell/Battery [79]	Fuzzy logic (FL)	Regulate the overall system power flow. Batteries' life cycle.
Standalone and grid-connected system with different configurations [103, 104]	HOMMER	Making energy balance calculations on an hourly basis for a complete year. Size optimization of each component to achieve the minimum cost of energy production.

Table (1.2) and (1.3) have summarized the research conducted in comparing several algorithms and techniques used for size optimization and EMS. Table (1.2) classified different methods for the energy management of microgrid systems coupled with various RES and SS. In Table (1.3), more specifications are given on the existing microgrid systems in the literature with their element characterization, and different EMS strategies.

Table 1.3: Analysis of EMS strategies with element characterization.

Intelligent EMS based on SCADA system [113] **(MATLAB/Simulink integrated with Modbus and Konnex**			
System Element	**Type**	**Capacity**	**Objective**
PV Panels	Monocrystalline	5 kW	MPPT
Battery	Li-ion	6.5 kWh	Charging/discharging
Load	-	9 kW	Reveals daily consumption
EMS with fuzzy control for a DC microgrid system [78] (MATLAB/Simulink, LabVIEW, Rs-485/Zigbee tools)			
System Element	**Type**	**Capacity**	**Objective**
PV Panels	Monocrystalline	5 kW	MPPT
Wind turbine	AWV 1500	1.5 kW	MPPT
Battery	Li-ion	1.5 kWh	SOC
Load	-	6.5 kW	
DC bus voltage	-	380V (+/- 20V)	
EMS for islanded microgrid based on rule-based power flow control [58] (PSCAD simulation tool)			
System Element	**Type**	**Capacity**	**Objective**
PV Panels	Monocrystalline	30 kW	MPPT
Battery pack	Li-ion Lead acid	800 Ah	SOC
Wind turbine	-	3 kW	MPPT
Load	10 kW + 15 kW	25 kW	
EMS for residential microgrid system based on NN and MILP [71] (Neural network and Mixed integer linear programming algorithm)			
System Element	**Type**	**Capacity**	**Objective**
PV Panels	-	6 kW	MPPT
Battery	Li-ion	5.8 kWh	SOC
EMS for real time laboratory control based on feedback & PI cascaded control [114] (MATLAB/Simulink integrated with RT-LAB tool)			
System Element	**Type**	**Capacity**	**Objective**
PV Panels	-	260 W	MPPT
Wind turbine	-	260 W	Speed , Torque
Battery	Lead acid	1.5 kWh	SOC
DC bus voltage	-	20 V	
Intelligent EMS with linear programming based multi-objective optimization [115] (Artificial neural network and Fuzzy logic controller)			
System Element	**Type**	**Capacity**	**Objective**
PV Panels	-	20 kW	Cost minimization
Wind turbine	-	25 kW	Cost minimization
Battery	Lead acid	15 kWh	SOC
Fuel cell	-	15 kWh	Cost minimization
EMS with multi-agent system [116] (MATLAB Simulink tool)			
System Element	**Type**	**Capacity**	**Objective**
PV panels	Titan S-60	100 kW	MPPT
Wind turbine	PMSG	200 kW	MPPT
Battery	Lead acid	300 kW	SOC
Load		80 kW	

Conclusion

Compared to AC microgrids and hybrid microgrids, the DC type has advantages in terms of system efficiency, reliability and cost. Nevertheless, and still today, various specific points must be addressed in research in order to continue to optimize its operation, such as its protection system, the design of its architecture, its control strategies and its stabilization techniques, deserve enormous research efforts.

In this chapter 1, based on a literature review, we have summarized several critical aspects of DC microgrids for residential applications, including architecture, control structure, and EMS classification. Concerning its architecture, following elements are chosen for the formation of DCMG, i.e., DGs (PV panels), SS (Battery & SC), Bi-directional DC/DC converter and DC load. In this review, it appears that DC bus level of 48V can be considered as an appropriate voltage level for the common DC bus, taking into account the different voltage levels and power ranges of household appliances. However, it can appear that different DC voltage standards may exist in a future microgrid to further improve system efficiency and reduce power conversion stages and enormous efforts will be required in this area in the future.

In this chapter, special attention has been given to EMS issues in the tertiary level specifically for residential applications. Two major categories have been summarized, including classical and artificial intelligence methods. According to the literature research, classical methods have been majorly applied for solving optimization problems. Artificial intelligence methods, including fuzzy logic, neural network, evolutionary computation methods together with multi-agent system, have gained popularity for the multi-objective energy management of microgrids. The literature has shown that due to multi-objective functions occurring in the energy management strategy, no single method can satisfy all the requirements, and hybrid methods may be used in combination in an EMS.

The introduction of EMS systems has been completed with an analysis based on several typical examples of DC microgrids for residential applications, including the system elements with their types and power levels, the control objectives of each part and the whole EMS.

Finally, due to their good interpretability, some existing software tools such as HOMER, i-HOGA, TRNSYS, and hardware components such as OPAL-RT, Typhoon and dSPACE are presented in this chapter, since these tools and components are very useful for the residential end users.

Chapter 2

DC Microgrid Modeling

This chapter is devoted to the study of the basic diagram of a DC microgrid which aims to be as universal as possible integrating a renewable energy source, an energy storage bank allowing the supply of various DC electrical loads. This DC microgrid architecture constitutes the support of our study. In this chapter, the main motivation is the introduction of the DC microgrid simulation platform, the fundamental principles and the modeling of DC microgrid at the local level.

Simulation is a necessary step before performing the experimental implementation. Therefore, the DC microgrid platform was firstly developed under a MATLAB/Simulink environment and later tested on an experimental platform. Each element was separately modelled and controlled. The simulation and some initial experimental results are included in this chapter.

2.1 DC microgrid scheme used in our study

A typical DC microgrid architecture consists of various elements as described in the previous chapter. In this work, the focus is on DC microgrid systems used for residential applications. Photovoltaic (PV) panels are considered as the main generation source, battery and SC as the storage system connected with a DC load via independent DC/DC power converter as shown in Figure 2.1.

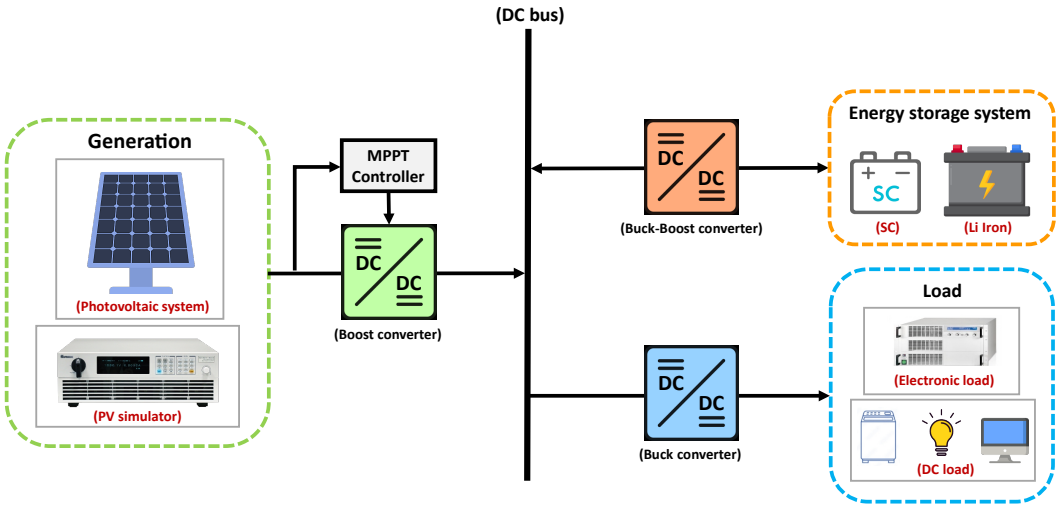

Figure 2.1: DC microgrid scheme used in our study.

In the considered microgrid, PV is used as the main energy source. Due to its dependence on meteorological conditions, and to stabilize the voltage of the DC bus in an allowable range, hybrid energy storage systems (battery & SC) are used as backup power sources allowing to meet load demands. The storage system is used as an energy source when renewable energy sources cannot meet demand. It is used as a load when the sources supplying enough energy. The excess power can be stored in it in order to ensure that the system remains in balance.

2.1.1 The photovoltaic system

The PV system consists of a PV panel and a maximum power point tracking (MPPT) controller. DC/DC boost converter is used to interconnect PV system with DC bus as shown in Figure 2.2.

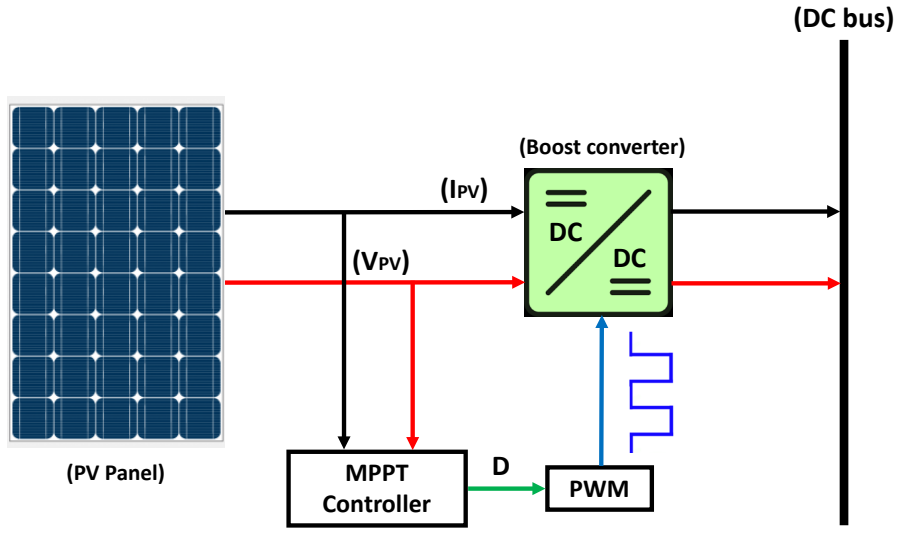

Figure 2.2: PV system with MPPT controller.

It is well known that PV generators exhibit nonlinear characteristics represented by current versus voltage ($I_{pv} - V_{pv}$) curves and power versus voltage ($P_{pv} - V_{pv}$) curves depending on various parameters of the system itself and of environmental conditions such as temperature and irradiance levels as shown in Figure 2.3, 2.4.

Irradiance effect:
Figure 2.3 shows the current-voltage characteristic ($I_{pv} - V_{pv}$) and the power-voltage characteristic ($P_{pv} - V_{pv}$) of the PV cell for different irradiances. It is observed that the current I_{sc} increases quasi-linearly with the irradiance and that the voltage V_{oc} increases slightly. Then the maximum electric power increases faster than the irradiance (i.e. the efficiency is better at high irradiance). The reference conditions are generally chosen with an irradiance of 1000 W/m^2. In practice, the irradiance on PV systems without light concentration is lower, so the efficiency is lower than its rated value.

Temperature effect:
As the internal temperature T_j increases, the short-circuit current I_{sc} increases slightly due to better light absorption (as a result of the gap energy decreasing with temperature), but the open-circuit voltage decreases sharply with temperature. The maximum electrical power also decreases strongly with temperature as shown in Figure 2.4.

2.1.1.1 Modelling of PV array

In the literature, several models such as single-diode model, double-diode model and three-diode model have been discussed. These models differ in the calculation procedure, accuracy and the number of

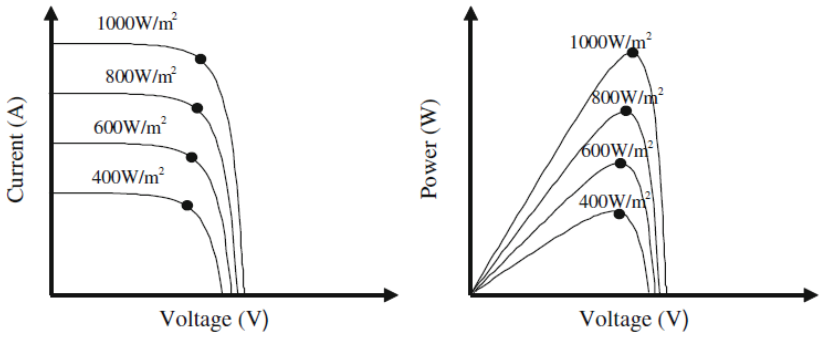

Figure 2.3: Irradiance effect on electrical characteristics [117].

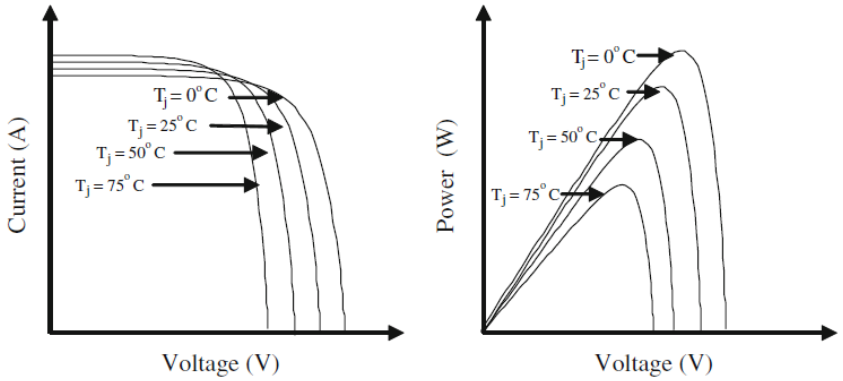

Figure 2.4: Temperature effect on electrical characteristics [117].

parameters involved in the calculation of the current–voltage characteristic but the electrical equivalent circuit is very common in most studies [118, 119, 120]. Due to its simplicity and sufficient accuracy, the one-diode model is considered in this study, since the main focus of the work is at the scale of the grid system and its management.

2.1.1.1.1 The single-diode model In the single-diode model, there is a current source parallel to a diode as shown in Figure 2.5. The current source represents the current I_{ph} generated by light, which varies linearly with solar irradiance. I_d is the current shunted through the intrinsic diode. The resistance between the multiple surfaces and the current flow resistance are modeled as series resistance R_s. The shunt resistance R_{sh} reflects the leakage current in the $p-n$ junction and improves the model's response to temperature changes.

Based on the equivalent circuit, the characteristic equation can be derived as follows with 2.1:

$$I = I_{ph} - I_d - IR_{sh} \tag{2.1}$$

that can be developed with the equations of I_d and IR_{sh} :

$$I = I_{ph} - I_0 \left[exp\left(\frac{q\,(V + I \times Rs)}{N_{s-cell} \times KT} - 1 \right) \right] - \frac{(V + I \times Rs)}{R_{sh}} \tag{2.2}$$

where;
I- Output current, V - Output voltage,
I_d - Diode current,

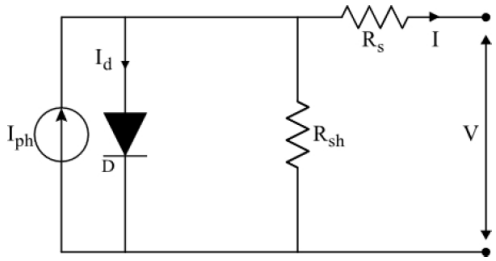

Figure 2.5: Single diode model [117].

I_{ph} - Photo-current,
I_0 - reverse saturation current of the diode,
I - Resistance current,
R_s - Series resistance,
R_{sh} - Parallel resistance,
K - Boltzmann constant ($1.35 \times 10^{-23} J/K$),
T – Temperature of the PV cell in Kelvin,
q = charge of electron ($1.6 \times 10^{-19} C$),
N_s = Number of cells in series.

There are several methods for solving equation 2.2, leading to different mathematical approximation models, which usually include parameters provided by photovoltaic module manufacturers. To determine the following parameters in the equation 2.2, various methods have been proposed in the literature [121, 122]. The simplified model with four parameters (I_{ph}, I_0, R_s, α) is introduced in [123]. These four parameters (I_{ph}, I_0, R_s, α) are corrected for environmental conditions. To identify the four parameters required for equation 2.2, a method is proposed by [124]. This model assumes the shunt resistance as infinite yielding the possibility to neglect the shunt current and the equation 2.2 presented can be simplified as

$$I = I_{ph} - I_0 \left[exp\left(\frac{V + I * Rs}{\alpha} - 1 \right) \right] \tag{2.3}$$

Each element is explained independently in the rest of this section. PV array is controlled by the MPPT controller which makes this system grid-friendly, described as follows.

2.1.1.2 The MPPT controller of PV panel

The power delivered by the PV array varies with solar irradiance and temperature, as these parameters influence the I-V characteristics of the solar cells. The PV array has a unique operating point that can supply maximum power to the load. This point is called the maximum power point (MPP) as shown in Figure 2.6. In order to operate the PV array at its MPP, the PV system must contain a MPPT controller.

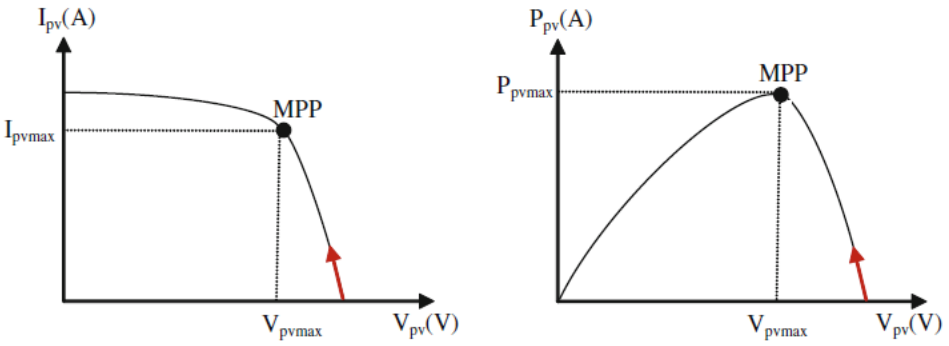

Figure 2.6: $I_{Pv} - V_{Pv}$ and $P_{Pv} - V_{Pv}$ curves [125].

The MPP is obtained when the derivative of PV power by voltage ($\frac{dP_{pv}}{dV_{pv}}$) is equal to zero. To reach the MPP of operation, the generator voltage V_{Pv} is regulated. So that it increases when the slope ($\frac{dP_{pv}}{dV_{pv}}$) is positive and it decreases when the slope ($\frac{dP_{pv}}{dV_{pv}}$) is negative. A control that allows continuous extraction of the maximum power point is given by:

$$V_{opt} = K_G \int \frac{dP_{pv}}{dV_{pv}} dt \cong K_G \int \frac{\triangle P_{pv}}{\triangle V_{pv}} dt \tag{2.4}$$

where V_{opt} is the optimal voltage which gives maximum power, K_G is a proportional gain, ΔP_{pv} is the power variation between two operating points and ΔV_{pv} is voltage variation between two operating points. The control block diagram is shown in Figure 2.7.

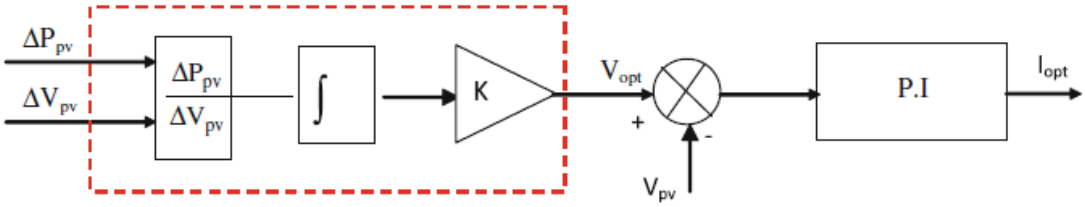

Figure 2.7: MPPT control scheme and voltage regulation of V_{Pv} [126].

The MPPT algorithm in the photovoltaic system keeps the voltage of the panel close to the equivalent voltage of the MPP.

In literature, several methods for tracking the MPP were practically implemented in controllers and have been discussed to determine the MPP. In [127], a lookup table on a microcomputer is used to track the MPP. It is based on the use of a database containing parameters such as typical curves of the PV generator for different irradiances and temperatures.

In [128], the curve-fitting method is used, in which the nonlinear characteristics of the PV generator are modeled either by mathematical equations or numerical approximations.

The two corresponding algorithms have the disadvantage that they may require a large storage capacity, both for the calculation of the mathematical formulas and for the storage of the data. These methods are apparently simple and economical, but they are not able to adapt to changeable environmental conditions.

Santos et al. [129] present the perturb and observe (P&O) method which is based on iterative algorithms to track continuously the MPP through the real-time current and voltage measurements of

the PV module. Most control schemes use the P&O technique because it is easy to implement but the oscillation problem is unavoidable.

To overcome the disadvantage of the P&O method in case of fast atmospheric changes, an improved, step-wise P&O method is used to realize the MPP of the PV panel as shown in Figure 2.8 [130]. This method is characterized by simple control, fast tracking and small steady-state power oscillations.

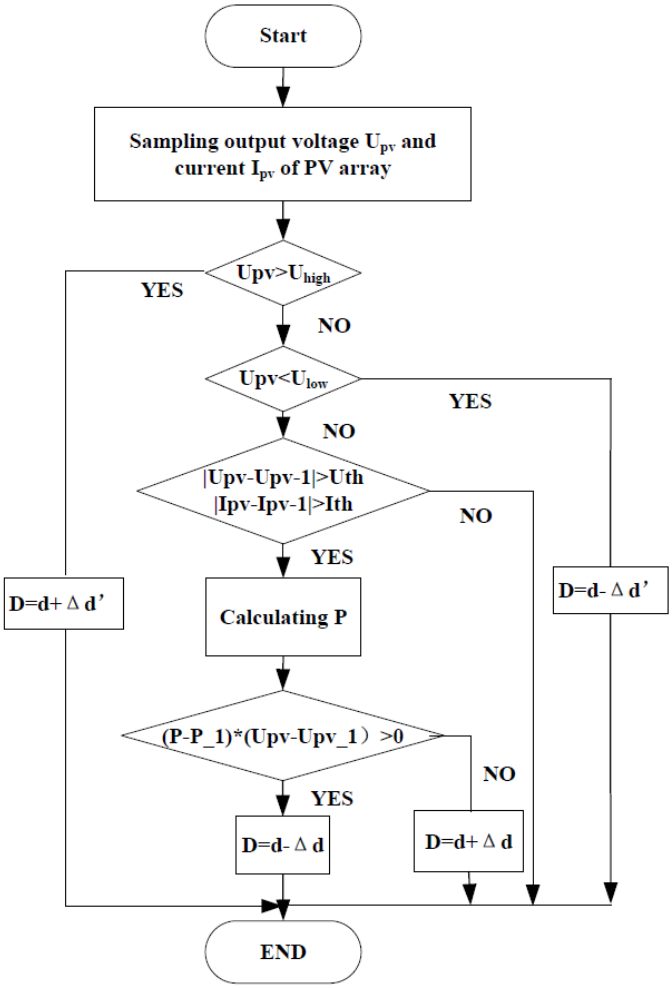

Figure 2.8: P&O MPPT algorithm flowchart [130].

For the PV array, the small-signal variation of output power ΔP and the variation of duty cycle ratio Δd around the MPP have the following approximate relationship;

$$\Delta P = -\frac{\Delta Upv^2}{R_{MPP}} \cong -\frac{\mu^2 \Delta d^2}{R_{MPP}} f\left(T_a\right) \tag{2.5}$$

where R_{MPP} is the equivalent resistance of the PV array at MPP; $f.(T_a)$ is the function of sample time $_a$; μ is output voltage of boost converter. Appropriate Δd and T_a can be selected to carry on power tracking. Meanwhile, in order to accelerate the tracking speed, a variable-step control is added. When the output voltage of PV array U_{pv} is in a certain range (U_{low} and U_{high}), a short step is used for the disturbance. Instead, a larger step is employed if U_{pv} is out of this range. The open-circuit voltage of the PV array U_{oc} multiplied by 0.78 is the intermediate value of U_{low} and U_{high}. The corresponding control diagram for PV array is shown in Figure 2.8. Two main parameters, Δd and T_a , are essential

to this MPPT control algorithm. A small Δd can reduce power loss around the steady-state working point caused by oscillation. However, the small Δd may lead to algorithm failure when the weather condition changes fast, e.g., in a cloudy day. Sample time T_a should be greater than a given threshold in order to avoid algorithm instability. Otherwise the MPP maybe missed due to the whole system's transient response. Both PV array's and converter's dynamic performance should be considered in the determination of the values of Δd and T_a .

2.1.2 The energy storage system

Batteries have high energy density, but less power density. On the other hand, supercapacitors have high power density and fast response time. The mixed use of these two energy storage devices can make them complement each other for the energy storage in a microgrid. Based on the above characteristics of battery and supercapacitor, a hybrid energy storage system is then chosen in this study.

The advantages resulting of adding supercapacitors in the hybrid energy storage system (HESS) are cited as follows:

- Longer battery run time.
- Extra backup power.
- Easier to meet current specifications.
- Minimizes space requirements and battery size.
- Enhances load balancing when used in parallel with a battery.

In regard of these aspects, a HESS integrating battery and supercapacitor is considered in the study. Both elements are connected in parallel in the microgrid. As they can be either discharged or charged, a bidirectional buck-boost DC/DC converter is used to interconnect the battery and SC to the DC microgrid as shown in Figure 2.9.

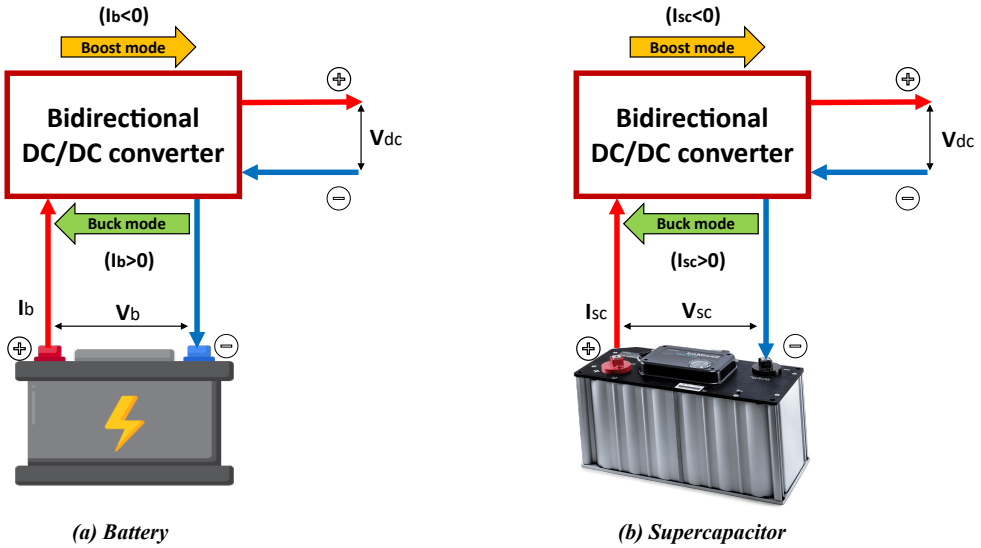

(a) Battery *(b) Supercapacitor*

Figure 2.9: Energy storage system.

In our system, we have considered a battery storage system consisted of a Li-iron phosphate (LiFOS) battery and a bidirectional buck-boost DC/DC converter as shown in Figure 2.9a.

As discussed in the previous chapter, lithium-ion batteries are the preferred power devices for many storage system applications due to their advantages such as high energy density and low self-discharge rate

as compare to other battery types. Despite all the advantages of Li-ion batteries, they must be handled with special care because, unlike other battery types, they contain a volatile, extremely flammable solvent that burns very easily. Overcharging/discharging is the main reason for most accidental explosions of Li-ion batteries. To overcome this risk, LiFOS battery is designed with the built-in battery management system. It means that LiFOS battery can be charged with most standard battery chargers (up to 40Amp capacity). The battery also features a Bluetooth output, which gives the user a huge range of information about the state of the battery when combined with the free LiFOS smartphone App (available for Apple or Android).

We have also considered a supercapacitor module, used in parallel with a battery to construct HESS. Same like for the battery storage system, a separate bidirectional buck-boost DC/DC converter is used to interconnect SC with DC bus as shown in Figure 2.9b.

2.1.2.1 Modelling of the energy storage system

The energy storage system considered in our study includes a battery bank and a supercapacitor. We present in the following the various models that are developed and used in the HESS.

2.1.2.1.1 The general battery model

In the field of battery modeling, various models have been proposed in the literature [131, 132, 133, 134]. Battery modeling includes two categories: electrochemical modeling and electrical circuit modeling. The electrochemical model of a battery is structurally based on the internal electrochemical reactions and responses of a cell. It is not obtained from an electrical network. Electrical circuit modeling is another useful model that has been presented by many researchers. In the electrical circuit modeling the electrical properties of the battery are considered and such models are used for the control applications [134]. In accordance with the developed system objectives, it is beyond the scope to include and discuss all electrical circuit models in this thesis work.

Thus at first, an ideal battery model is considered for discussion, then a simplified battery model is included for mathematical modeling in the MATLAB simulink environment.

Ideal battery model

The ideal battery model is shown in Figure 2.10. It consists of an ideal voltage source V_{oc} and internal resistance R_o as a function of SOC.

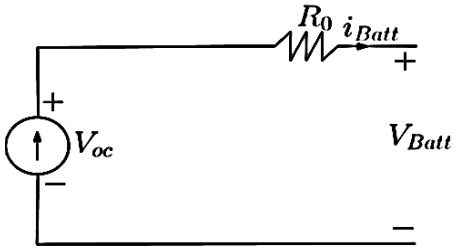

Figure 2.10: Ideal battery model [135].

Based on the equivalent circuit, the characteristic equation can be derived as follows by equation 2.6

$$V_{Batt} = V_{oc} - R_o \times i_{Batt} \tag{2.6}$$

with i_{Batt}, the battery output current being positive during discharging, and negative during charging. V_{Batt} represents the battery terminal voltage.

A simple circuit oriented battery model is shown in Figure 2.11.

Based on the equivalent circuit, the characteristic equation can be derived as follows see equation 2.7

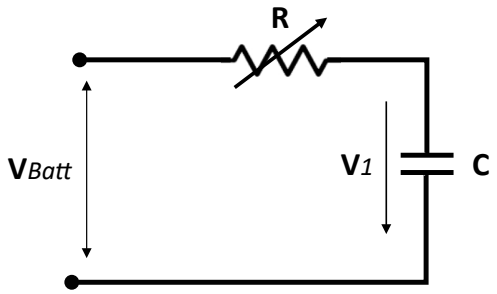

Figure 2.11: Simplified battery model.

$$V_{Batt}(t) = R_i(t) + V_1(t) \tag{2.7}$$

where V_{Batt} is the voltage across battery terminal, R is the variable resistance varying with the mode of operation (charging/discharging) and temperature, V_1 is the voltage across capacitor.

For the mathematical model of battery, equation 2.8 is derived from the equation 2.7. The values are taken for single battery cell of Li-ion battery. It has a nominal current equal to 1.1Ah a nominal open circuit voltage equal to 3.8V [126].

$$V_{Batt}(t) = R_i(t) + \frac{1}{C}\int_0^t i(t)dt \tag{2.8}$$

Based on the equation 2.8, a mathematical model was developed as shown in Figure 2.12.

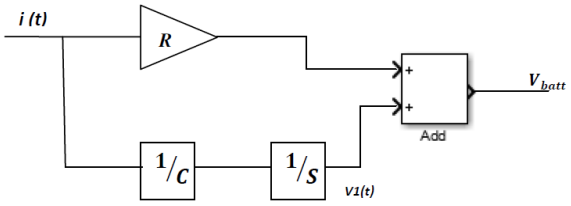

Figure 2.12: Battery mathematical model.

To determine the battery voltage V_{Batt} , the voltage of each cell has to be calculated as follows:

- The open-circuit voltage as a function of state of charge: $V_{oc} = f(SOC)$.
- The cell voltage behaviour due to internal impedance. It has to be decomposed in two parts, i.e., charging and discharging: $R_d, R_c = f(SOC)$.

Open-circuit voltage

The open-circuit voltage, V_{oc} behavior is fully discussed in literature., especially its strong dependence on the SOC that must be determined experimentally [126]. Therefore V_{oc} of each cell is modeled as a function of SOC derived from equation 2.9 ;

$$V_{oc}(SOC) = a_1 e^{-a2SOC} + a_3 + a_4 SOC + a_5 . e^{\frac{-a6}{1-SOC}} \tag{2.9}$$

with $a_1 = -5.863E^{-1}, a_2 = 21.90, a_3 = 3.414, a_4 = 1.102E^{-1}, a_5 = -1.718E^{-1}, a_6 = 8.000E^{-3}$.

By using the following fitting parameters, Figure 2.13 is obtained. It can be seen that the curve is specifically linear between $(20\% - 80\%)$ SOC.

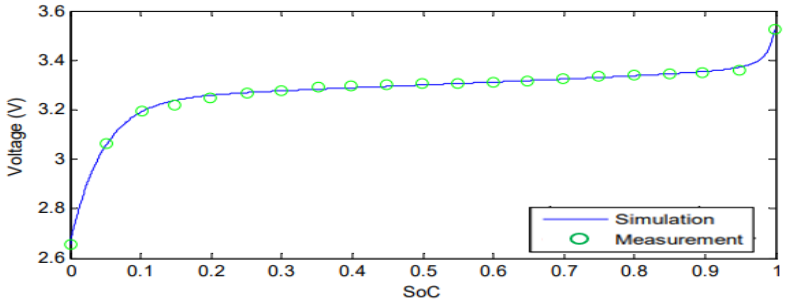

Figure 2.13: Battery open circuit voltage [126].

Internal impedance

The internal impedance of the battery can be described by the polynomial and exponential functions of the empirical equation. 2.10, and equation. 2.11.

To distinguish the impedance elements for charging and discharging, a subscript c for the charging elements and a subscript d for discharging impedance elements will be added.

Empirical equations obtained for discharging (R_{od}) will be fitted with a 4^{th} order polynomial because with higher order more accuracy can be achieved. If (R_{od}) and (R_{oc}) are modelled with higher order polynomials, the voltage behaviour of the cell for both discharging and charging is accurately modelled as shown in Figure. 2.14, and Figure. 2.15.

$$R_{od}(SOC) = b_{1d}SOC^4 + b_{2d}SOC^3 + b_{3d}SOC^2 + b_{4d}SOC + b_{5d} \tag{2.10}$$

with $b_{1d} = 1.298E^{-1}, b_{2d} = -2.892E^{-1}, b_{3d} = 2.273E^{-1}, b_{4d} = -7.2162E^{-2}, b_{5d} = 8.980E^{-2}$.

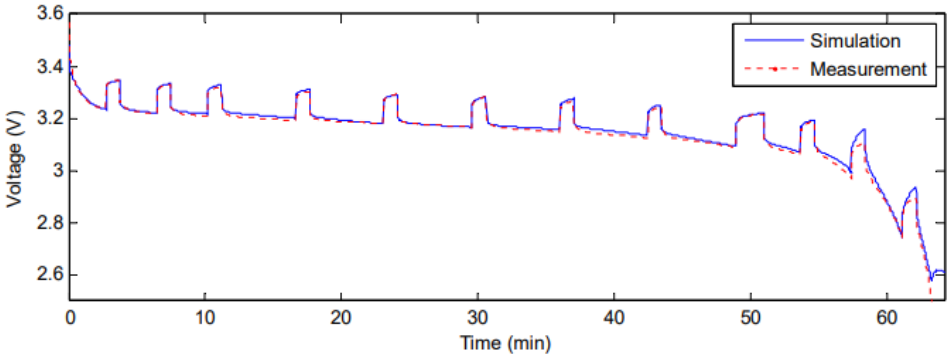

Figure 2.14: Cell voltage behaviour during discharging [126].

The same analysis is used to model the internal impedance elements for charging (R_{oc}).

$$R_{oc}(SOC) = b_{1c}SOC^4 + b_{2c}SOC^3 + b_{3c}SOC^2 + b_{4c}.SOC + b_{5c} \tag{2.11}$$

with $b_{1c} = 1.369E^{-1}, b_{2c} = -2.518E^{-1}, b_{3c} = 1.609E^{-1}, b_{4c} = -4.100E^{-2}, b_{5c} = 8.210E^{-2}$.

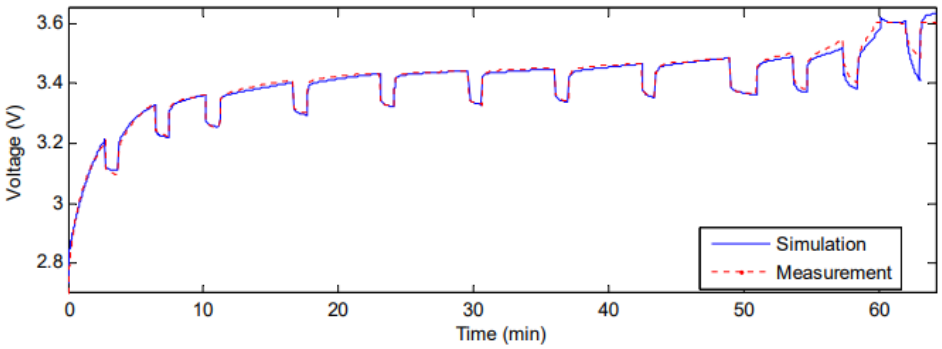

Figure 2.15: Cell voltage behaviour during charging [126].

2.1.2.1.2 The general supercapacitor model

SCs are electrochemical devices whose storage mechanism is based on a faradic process. SCs are cited as a storage system between traditional capacitors and batteries [136]. They feature fast charge/discharge rates and long lifetime [137, 138]. Because of these characteristics, they are used in various applications, such as smart grids, electric vehicles, and uninterruptible power supplies. Three types of models are discussed in the literature. The first is the RC model, the second is the two-branch model, and the third is the multi-branch model. In [139], author presents all three models and compares them with the experimental model of Belhachmi. Among the three models,the RC model is simplest, which can provide sufficient accuracy for system-level simulation. Therefore, a simple RC model is considered for DC microgrid modeling in MATLAB/Simulink environment.

The RC model of a supercapacitor

A simple schema of SC model is shown in Figure 2.16.

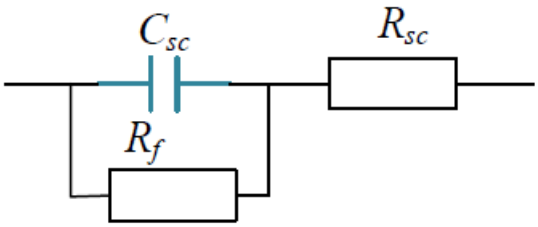

Figure 2.16: RC model of SC [139].

where R_{sc} is series resistance , R_f is a leakage resistance, and C_{sc} is storage capacitor. R_f describes the behaviour of the component during the self-discharge process.

Based on the equivalent circuit, the characteristic equation can be derived as follows:

$$U_{sc}(t) = R_{sc} i_{sc}(t) + \int_0^t \frac{i_{sc}(t)}{C_{sc}} dt \tag{2.12}$$

Following the equation 3.4, a mathematical model was developed as shown in Figure 2.17.

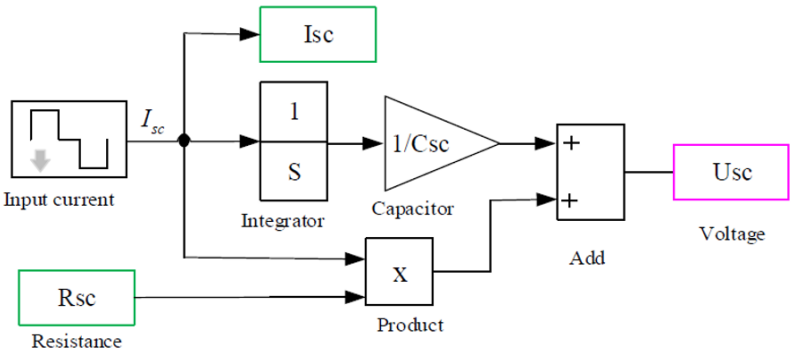

Figure 2.17: RC model of SC under MATLAB/Simulink [139].

The modelling of the RC model in the SC in the MATLAB/Simulink environment is shown in Figure 2.17 by neglecting the leakage current, R_f .

2.1.3 The DC/DC converter

The DC/DC converters used in DC microgrids are mainly to interface various RES to the DC bus or to the load. Two types of boost converters are mainly considered for the formation of DC microgrid scheme. One is simple unidirectional boost converter used between PV panel and DC bus and other is bidirectional buck-boost converter which is used between HESS and DC bus as shown in Figure 2.1.

In this work, a multi-function IGBT converter from SEMITEACH company is considered as practical model and for the experimental application. This converter can be used in buck mode, boost mode and buck-boost mode together at the same time. Datasheet of SEMITEACH IGBT module stack is given at the end of this thesis manuscript in the Annex section.

2.1.3.1 Modelling power converters

In simulation platform, three type of DC/DC converters are used to interface each element with a common DC bus as shown in Figure 2.18:

- A boost converter is used for PV panel;
- A buck converter for DC load;
- A buck-boost converter for battery and SC separately.

Various kinds of DC/DC converters have been proposed in the literature [141, 38, 142, 143]. In a general switching converter circuit, the transistor operates as an electronic switch being completely ON or completely OFF (saturation or cutoff for a BJT or the triode and cutoff regions of a MOSFET). Assuming the switch is ideal in Figure 2.19a, the output is the same as the input when the switch is closed, and the output is zero when the switch is open. Periodic opening and closing of the switch results in the pulse output shown in Figure 2.19b.

The average of dc component of output voltage is

$$V_o = \frac{1}{T}\int_0^{DT} V_s dt = V_s D \tag{2.13}$$

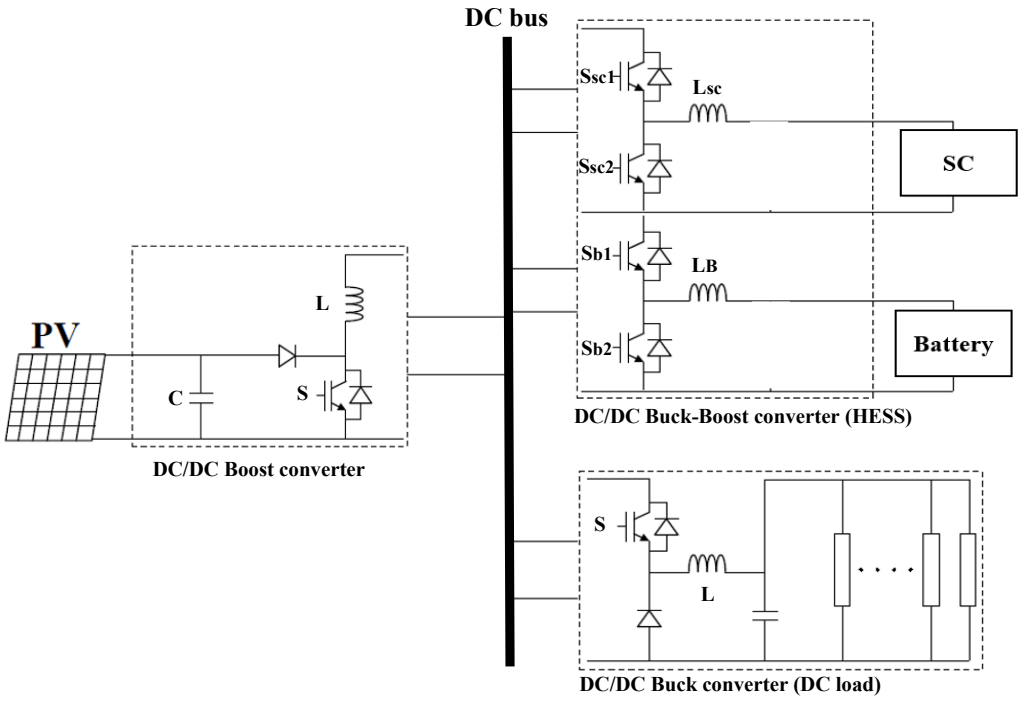

Figure 2.18: DC/DC converters used in simulink model, adapted from [140].

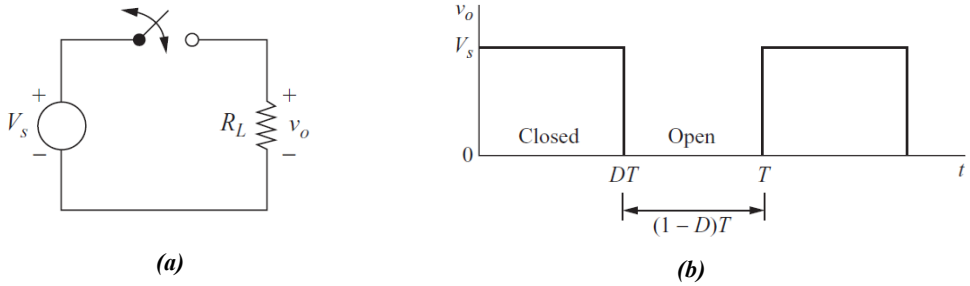

Figure 2.19: (a) DC/DC switching converter, (b) Output voltage [38].

The dc component of the output voltage is controlled by adjusting the duty ratio D, to a fraction of the switching period:

$$D = \frac{t_{on}}{t_{on} + t_{off}} = \frac{t_{on}}{T} = t_{on}.f \tag{2.14}$$

where f is the switching frequency, T is the total switching time, t_{on} is switching ON time, and t_{off} is switching OFF time.

2.1.3.1.1 The DC/DC boost converter for PV

The boost converter is shown in Figure 2.20. This converter is a switching converter, i.e., based on an active electronic switch that operates by a periodical opening and closing.

The switch is closed

Then, the diode is reverse biased. Kirchhoff's voltage law around the path containing the source, inductor,

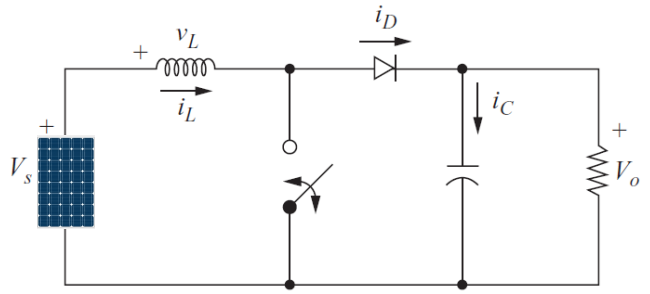

(a) Equivalent circuit.

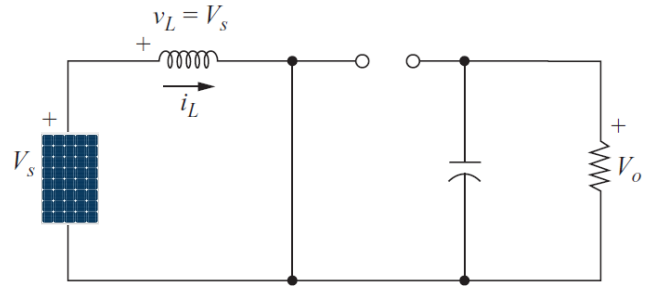

(b) switch closed.

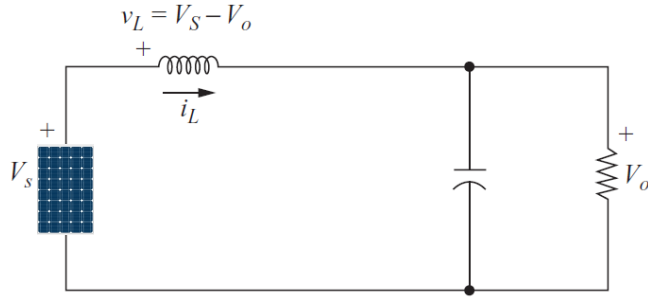

(c) switch open.

Figure 2.20: DC/DC boost converter; (a) Equivalent circuit, (b) when switch is closed, (c) when switch is open, adapted from [38].

and closed switch yields to

$$V_L = V_s = L.\frac{di_L}{dt} \tag{2.15}$$

and the corresponding rate of change of current is a constant. So, the current increases linearly while the switch is closed. The change of the inductor current can be computed from the following equation

$$\frac{\triangle i_L}{\triangle t} = \frac{\triangle i_L}{DT} = \frac{V_s}{L} \tag{2.16}$$

Solving equation 2.16 for Δi_L for closed switch, we obtained

$$(\triangle i_L)_{closed} = \frac{V_s.DT}{L} \tag{2.17}$$

The switch is open

Then, the inductor current cannot change instantaneously, so the diode becomes forward-biased to provide a path for inductor current. Assuming that the output voltage V_o is a constant, then the voltage across the inductor will be

$$V_L = V_s - V_o = L.\frac{di_L}{dt} \tag{2.18}$$

The rate of change of the inductor current is a constant, so while the switch is open, the current must change linearly. The change in inductor current while the switch is open can be expressed as

$$\frac{\triangle i_L}{\triangle t} = \frac{\triangle i_L}{(1-D)T} = \frac{V_s - V_o}{L} \tag{2.19}$$

Solving equation 2.19 for Δi_L for opened switch, we obtained

$$(\triangle i_L)_{Open} = \frac{(V_s - V_o)(1-D)}{L} \tag{2.20}$$

For steady-state operation, the net change in inductor current must be zero. Using equations 2.17, 2.20, we can write

$$(\triangle i_L)_{closed} + (\triangle i_L)_{Open} = 0 \tag{2.21}$$

$$V_s(D + 1 - D) - V_o(1 - D) = 0 \tag{2.22}$$

Solving equation 2.22 for V_o, we finally obtained

$$V_o = \frac{V_s}{1-D} \tag{2.23}$$

Equation 2.23 shows that if the switch is always open and D is zero, the output voltage is the same as the input. As the duty ratio increased, the denominator of equation 2.23 becomes smaller, resulting in a larger output voltage. The boost converter produces an output voltage greater than or equal to the input voltage, this output voltage cannot be lower than the input one.

2.1.3.1.2 The DC/DC buck-boost converter for battery & SC

In the simulink model two separate bidirectional DC/DC converters are used in HESS modelling as shown in Figure 2.18.

The HESS system involves 4 bidirectional switches; S_{b1} and S_{b2} for battery and S_{s1} and S_{s2} for SC. Both typologies operates on the same working principle but here they are presented separately as shown in Figure 2.21a, 2.21b.

In literature, several HESS typologies used for different modes of operations are discussed. In [145], authors presented the topology which is similar to HESS configuration used in the simulation platform that we have developed and that will be explained in the following sections.

The HESS charging mode

Whenever the PV power exceeds the load demand or the load demand decreases, there is an excess of power in the DC microgrid, which leads to an increase in the DC grid voltage. This excess amount of energy charges both the battery and the supercapacitor to stabilize the DC microgrid. Hence in this mode, current flows from the DC microgrid to the HESS. The converter operation in this mode can be divided into two time intervals named T1 and T2. During the time interval T1, switches S_{b2} and S_{s2} are operated with duty cycle, charging both inductors L_B and L_S by corresponding sources V_B and V_{SC}. At the end of this interval, i.e. starting at T2, both the switches are turned off providing freewheeling path for I_{LB} and I_{LS} through D_{b1} and D_{s1} respectively. The two steady-state equations for charging mode are:

$$V_{DC} = \frac{V_B}{d_B} \tag{2.24}$$

$$V_{DC} = \frac{V_{SC}}{d_{SC}} \tag{2.25}$$

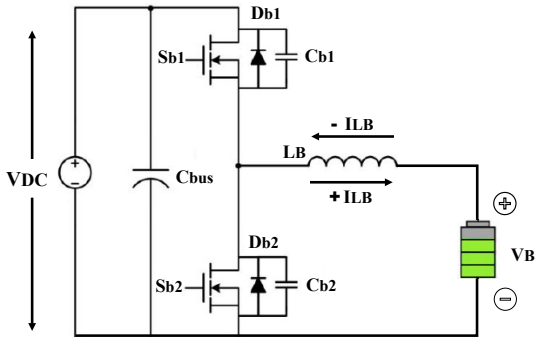

(a) Bidirectional DC/DC converter for battery.

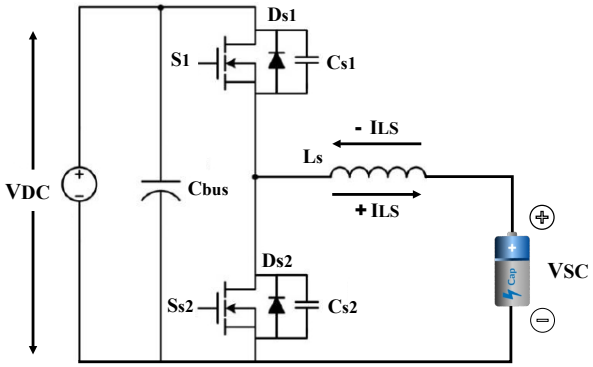

(b) Bidirectional DC/DC converter for SC.

Figure 2.21: (a) Battery Bidirectional DC/DC converter, (b) SC Bidirectional DC/DC converter, adapted from [144].

where d_B and d_{SC} are the duty cycles.

The HESS discharging mode

The DC microgrid voltage decreases if load exceeds PV generation capability or when PV generated power falls due to a reduced solar irradiation. During this time interval power has to be supplied by HESS. By operating on devices S_{b1} and S_{s1}, power flows from HESS to DC microgrid in this mode, by properly controlling bidirectional converter during two time intervals T3 & T4. During the time interval T3, switches S_{b1} and S_{s1} are gated-on, inductors (L_B and L_{Sc}) stores energy in opposite direction. After end of this time period T3 (during time period T4) as sum of battery and inductor voltages exceeds DC microgrid voltage, so power flows from HESS to DC microgrid. Steady-state equations for discharging mode are;

$$V_{DC} = \frac{V_B}{1 - d_B} \tag{2.26}$$

$$V_{DC} = \frac{V_{SC}}{1 - d_{SC}} \tag{2.27}$$

where d_B and d_{SC} are the duty cycles.

Steady state waveforms for HESS charging and discharging modes with current directions of each time interval is demonstrated in Figure 2.22.

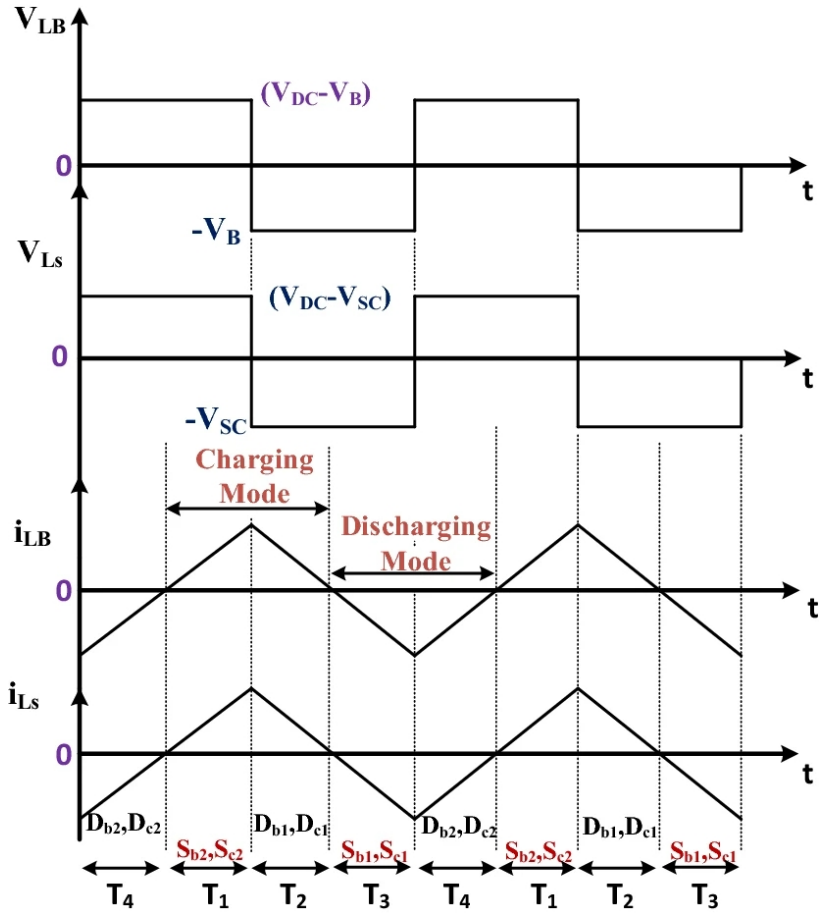

Figure 2.22: Steady state waveforms for HESS charging/discharging mode [145].

since Sb1, Sb2, Sc1, and Sc2 are the switches which are switched in the complimentary way. For each switching leg, only 1 gate circuit is required in HESS.

2.1.3.2 The DC/DC buck converter for DC load

DC/DC buck converter is another type of switching converter that operates by periodically opening and closing an electronic switch as shown in Figure 2.23. The diode provides a path for the inductor current when the switch is opened and is reverse-biased when the switch is closed. This circuit is called a buck converter or a step-down converter because the output voltage is less than the input.

The switch is closed

Then, in the buck converter circuit the diode is reverse-biased and Figure 2.23b is an equivalent circuit. The voltage across the inductor is

$$V_L = V_s - V_o = L.\frac{di_L}{dt} \tag{2.28}$$

Since the derivative of the current is a positive constant, the current increases linearly. The change in current while the switch is closed is computed by modifying the preceding equation as

$$\frac{di_L}{dt} = \frac{\triangle i_L}{DT} = \frac{V_s - V_o}{L} \tag{2.29}$$

Solving equation 2.29Δi_L for closed switch,

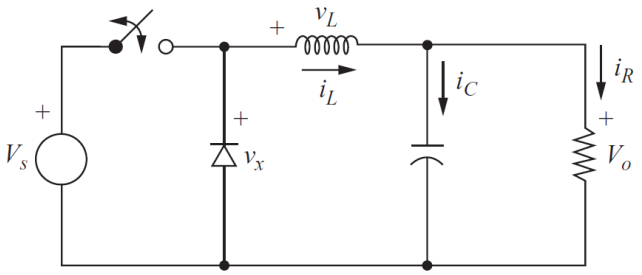

(a) Equivalent circuit.

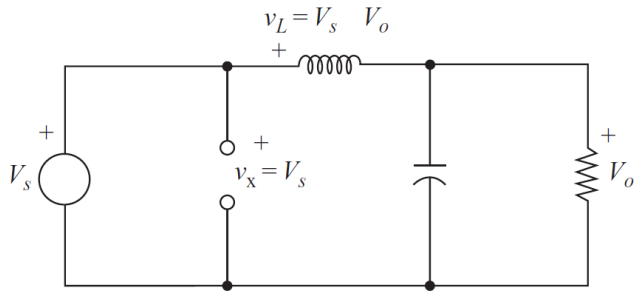

(b) switch closed.

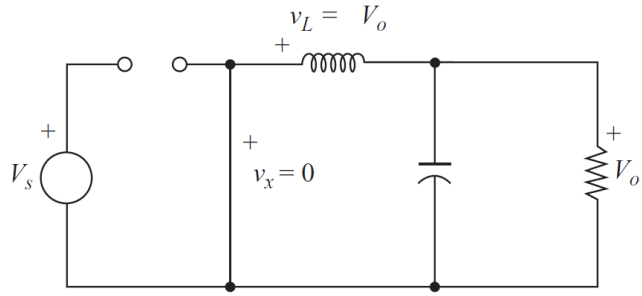

(c) switch open.

Figure 2.23: DC/DC buck converter circuit: (a) Equivalent circuit, (b) when switch closed, (c) when switch open [38].

$$(\triangle i_L)_{closed} = (\frac{(V_s - V_o)}{L}).DT \tag{2.30}$$

The switch is open

Then, the diode becomes forward-biased to carry the inductor current and the equivalent circuit of Figure 2.23c applies. The voltage across the inductor when the switch is open is;

$$V_L = -V_o = L.\frac{di_L}{dt} \tag{2.31}$$

The derivative of current in the inductor is a negative constant, and the current decreases linearly. The change in inductor current when the switch is open is;

$$\frac{\triangle i_L}{\triangle t} = \frac{\triangle i_L}{(1-D)T} = -\frac{V_o}{L} \tag{2.32}$$

Solving Δi_L for open switch,

$$(\triangle i_L)_{Open} = -\frac{(V_o)}{L}.(1-D)T \tag{2.33}$$

Steady-state operation requires that the inductor current at the end of the switching cycle be the same as that at the beginning, meaning that the net change in inductor current over one period is zero. Using equation 2.30, and 2.33;

$$(\triangle i_L)_{closed} + (\triangle i_L)_{Open} = 0 \tag{2.34}$$

$$(\frac{V_s - V_o}{L}).DT - (\frac{V_o}{L})(1 - D)T = 0 \tag{2.35}$$

Solving equation 2.35 for V_o,

$$V_o = V_s.D \tag{2.36}$$

The buck converter produces an output voltage that is less than or equal to the input.

2.1.4 The DC load

Generally in DC microgrid system, a DC load is connected with the DC bus via buck converter as shown in Figure 2.1. In this work the electronic load EL-9000 HP is considered for the experiment as shown in Figure 2.24.

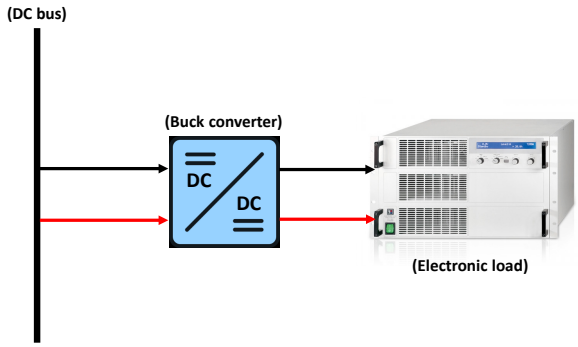

Figure 2.24: DC load.

Technical specifications of load device is given at the end of thesis in Annex section.

2.2 DC microgrid simulation platform

A joint effort has been done to develop a prototype of a multi-source DC microgrid system for residential applications. The investigated DC microgrid system is established in MATLAB/Simulink environment as shown in Figure 2.25.

As can be seen in MATLAB simulink model Figure 2.25a, PV panel is connected to the DC bus through a boost DC/DC converter. To track maximum power point under fast varying of sunlight levels MPPT controller is used. The hybrid energy storage unit is composed of lithium iron battery and SC are connected to a common DC bus through two bidirectional buck-boost DC/DC converters. Each bidirectional converter operates in two different modes such as; mode-1 (M1) and mode-2 (M2). The converter work in a boost mode with a gate signal (1) and in a buck mode with a gate signal (2) as shown in control diagram of buck and boost mode for battery in Figure 2.27, 2.29 and for SC in Figure 2.28, 2.30 respectively. For that purpose, a separate control block has been introduced in the simulation platform as shown in Figure 2.25b, which is further explained in the following section.

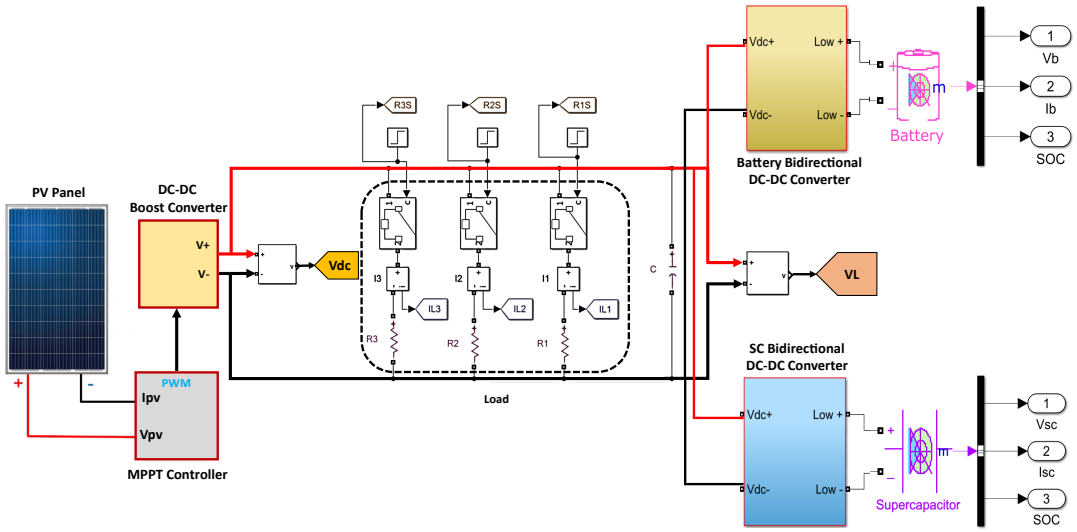

(a) MATLAB simulink model.

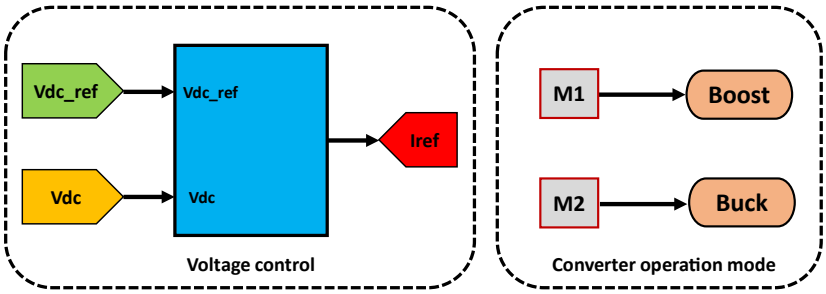

(b) Control block.

Figure 2.25: DC MG simulation platform : (a) MATLAB simulink model, (b) Control block .

In this work, one Photovoltaic CLIPSOL PV-175 module is used as a power source. One battery (LiFOS-68) and one SC (XLM-62) are used as energy storage. Electrical specifications of PV panel, technical details of battery and SC are shown below in Table 2.1 and Table 2.2.

Table 2.1: PV panel specification.

PV type	**CLIPSOL (PV-175)**
Nominal power	175W
Max voltage	36.45V
Max current	4.81A
No of cells	72 cells

Table 2.2: HESS technical parameters.

Battery type	**Lithium ion phosphate (LiFOS)**	**Supercapacitor type**	**XLM-62R1137A-R (EATON)**
Nominal voltage	12.8V	Nominal voltage	62.1V
Nominal capacity	68Ah	Capacitance	130F
Charging current	10-30A	Maximum current	2000A
Discharge current	60A	Stored energy	69.6Wh
Charging voltage	14.4V	Peak power	140kW

Detailed data-sheets of PV panel, battery and SC are given at the end of thesis in Annex section.

In the developed simulation platform, the low and high frequency components of the current used as reference for the battery and SC, respectively are considered thanks to a conventional control scheme as shown in Figure 2.26.

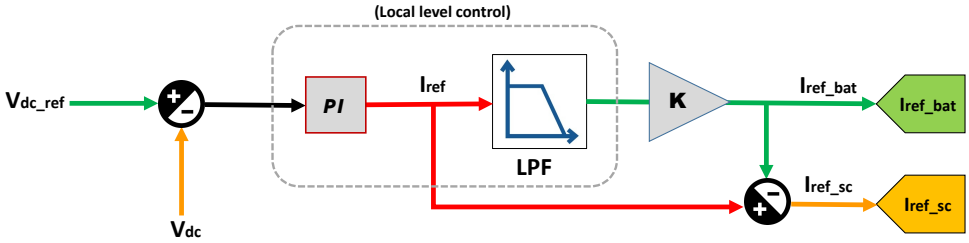

Figure 2.26: Control block diagram for conventional control scheme.

In this scheme, the DC bus voltage is coordinately controlled by battery and SC. First, the measured DC bus voltage V_{dc} is compared with the reference DC bus voltage V_{dc_ref} and the difference is sent to a proportional integration (PI) controller to get the current reference I_{ref} or total current I_{tot}. This total current is split into two parts. One is the battery current reference I_{ref_bat} which is obtained by applying a low pass filter (LPF) and a coefficient K to I_{ref}. The other one I_{ref_SC} is the difference between I_{ref} and I_{ref_bat} . By this, high frequency part of the DC bus disturbance will be mitigated by SC and the low frequency part of the disturbance is smoothed by battery. In shown control scheme, following parameters such as PI controller values and cut-off frequency has a great importance in terms of current distribution ratio and DC bus stability with respect to the given reference value.

The current references I_{ref_bat} and I_{ref_SC} will be further used for charging and discharging of battery and SC depending on converter operation, either buck mode or boost mode.

2.3 Local-level modelling and control

Hierarchical control structure has three control levels, i.e., primary control, secondary control, and tertiary control explained in Chapter 1. The first two levels deal with the converter-level local control such as current control and voltage control. The third level is for monitoring, control, and analysis of the overall system, which is referred to as system-level modeling. This section focus on local-level modelling with its control structure.

For the component tests, a separate battery and SC model were first developed under MATLAB/Simulink and tested at the local level. Subsequently, both elements were tested on the developed experimental platform. This part of the work allowed us to test each component separately to observe the charging

and discharging behavior of the battery and SC individually and together as HESS by using different methods such as constant current (CC), and constant voltage (CV) method, as described below.

2.3.1 Constant current (CC) charging

For charging, CC method is used to charge the battery and SC with a constant current reference ($I_{ref} = -1A$). The converter works in a buck mode by a control signal (M2) as shown in Figure 2.27 for battery, and in Figure 2.28 for SC respectively.

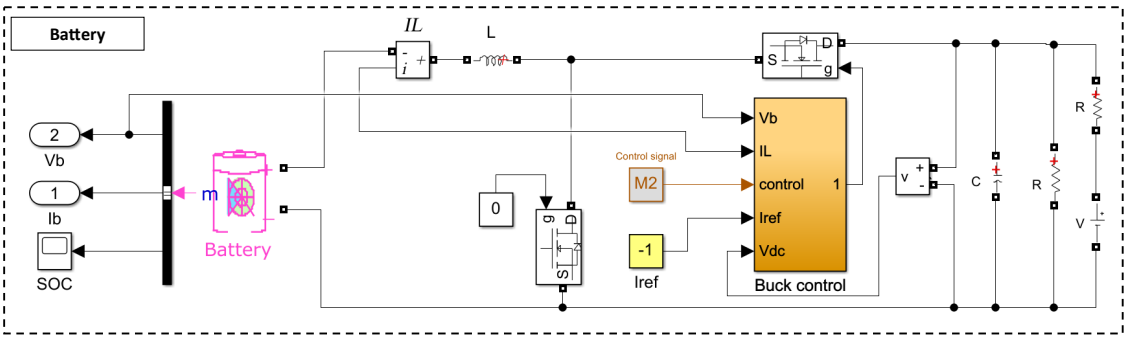

Figure 2.27: Battery charging model (CC).

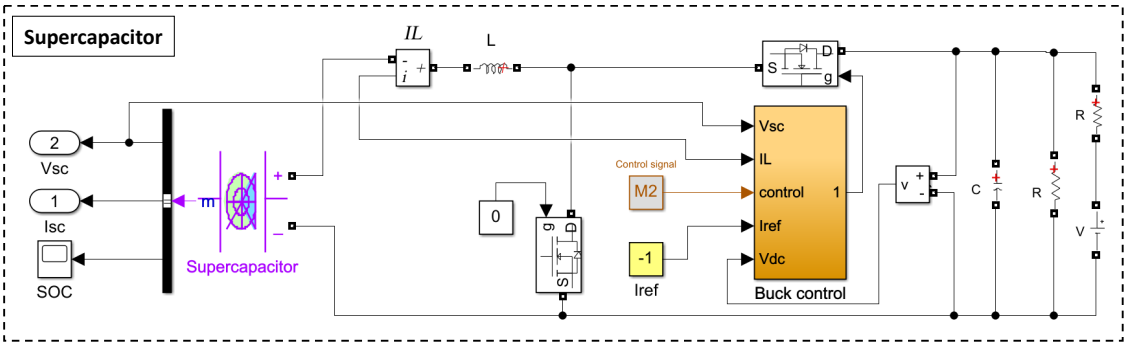

Figure 2.28: Supercapacitor charging model (CC).

A single battery (LiFOS-68) and SC (XLM-62) are integrated with a DC/DC converter that operates in step-down mode to charge the battery and SC separately. The initial voltage of the SC are set in a similar range of battery (i.e., $V_{bat} = 12.8$V, $V_{sc} = 13$V). The modeling parameters such as, PI controller values are set manually in the battery and SC models (i.e., $Kp/Ki = 10/1$). The load resistance is calculated according to the battery and SC voltage (i.e., $R_L = 50\Omega$). The DC voltage source is used as an input and the value is set higher than the battery voltage and SC voltage (i.e., $V_S = 30$V). In this case, the battery and SC will be charged by a constant current. The simulation and experimental results of battery and SC charging are shown in Figure 2.29.

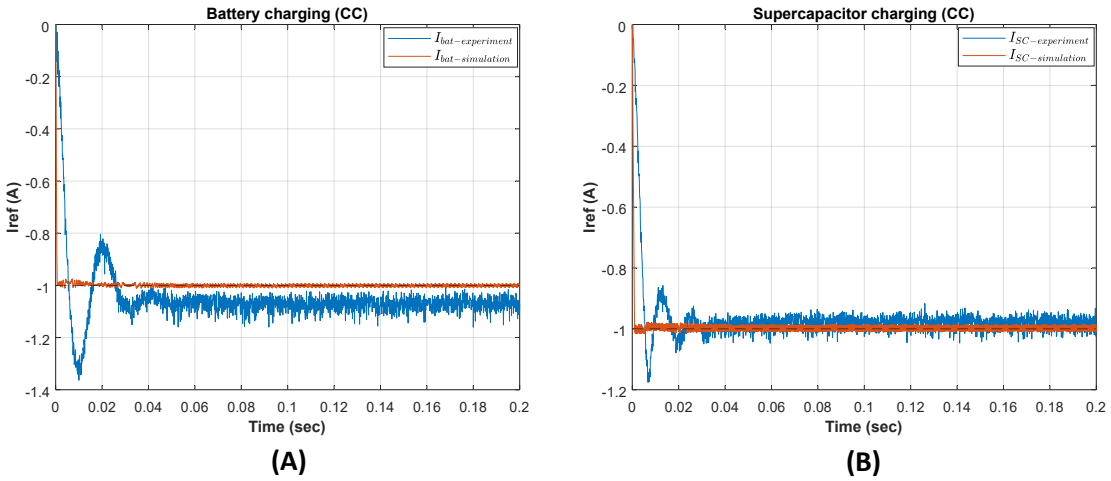

Figure 2.29: Charging comparison (CC).

As can be seen in sub-figure (A), simulation and experimental results for the battery are in close agreement in terms of rise time (i.e., 0.0050 s). Similarly sub-figure (B) shows the simulation and experimental results for SC with its shorter rise time (i.e., 0.0029 s). In both cases, the battery and SC reach the reference current (i.e., I_{ref} = -1A), but, as expected, in a shorter time for the SC compared to the battery. Here, the battery and SC current are negative ($I_{Batt} < 0, I_{SC} < 0$) , which means that the battery and SC are in charging mode.

2.3.2 Constant current (CC) discharging

As for the charging mode, a current closed-loop method is used to discharge the battery and SC for different values of reference current (I_{ref}). In this case, the converter work in a boost mode by a control signal (M1) as shown in control diagram for battery in Figure 2.30, and for SC in Figure 2.31 respectively.

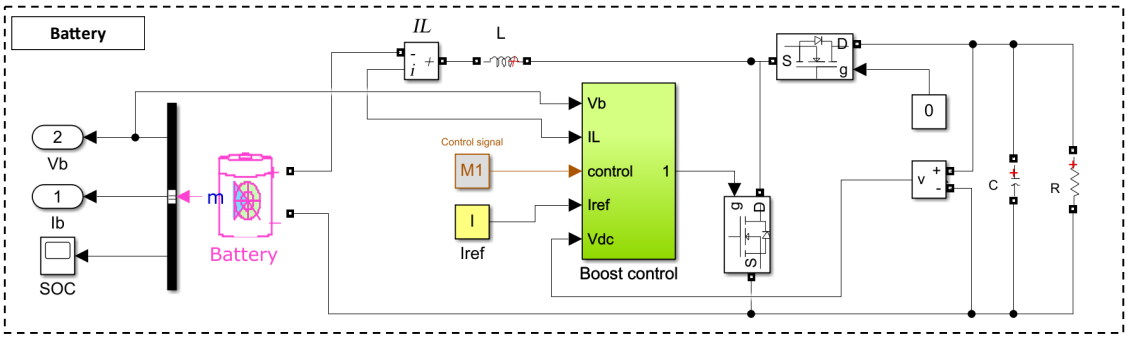

Figure 2.30: Battery discharging model (CC).

Battery and SC are integrated with a DC-DC converter that operates in step-up mode to discharge the battery and SC separately. Load resistance is calculated with respect to the given value of reference current and nominal voltage of each element (battery, SC).

The modeling parameters such as the values of the PI controller (Kp/Ki) are set manually in the battery and SC models for the various given values of the reference current (i.e., $I_{ref} = 5A, 10A, 15A, 20A$). The simulation and experimental results for battery are shown in Figure.2.32, and likewise for SC in Figure.2.33.

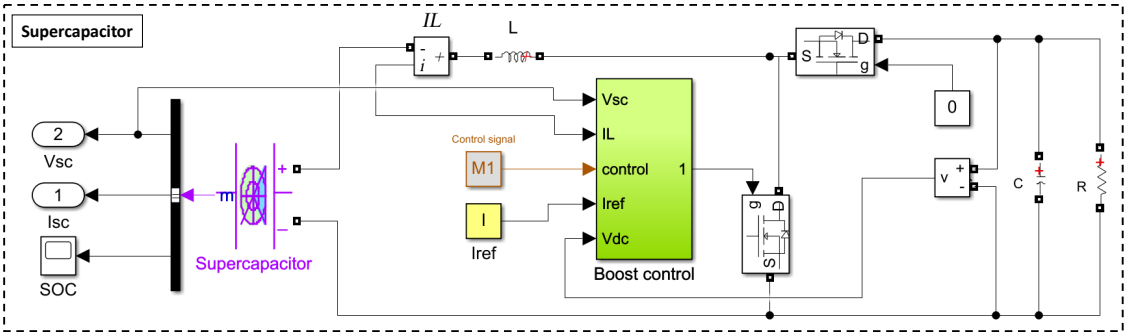

Figure 2.31: Supercapacitor discharging model (CC).

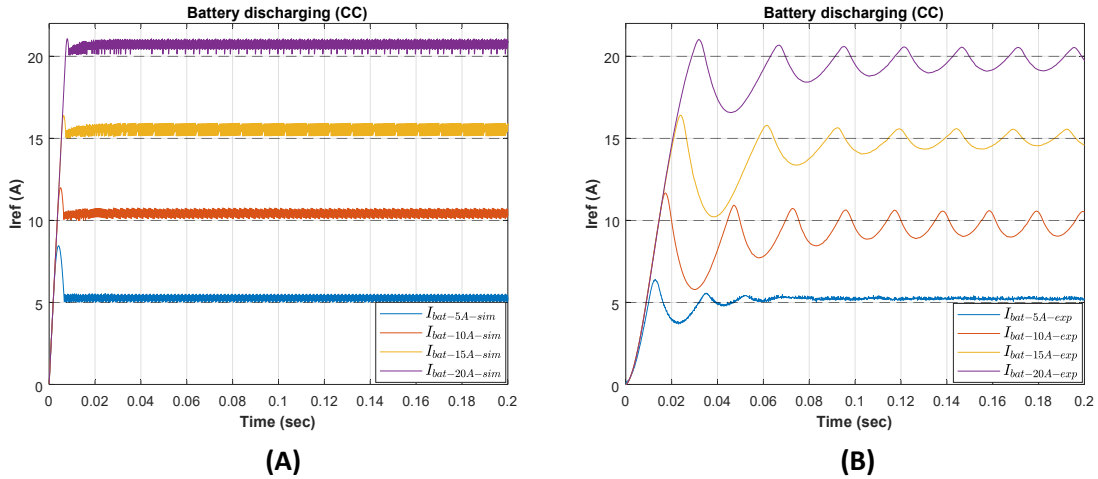

Figure 2.32: Battery discharging (CC).

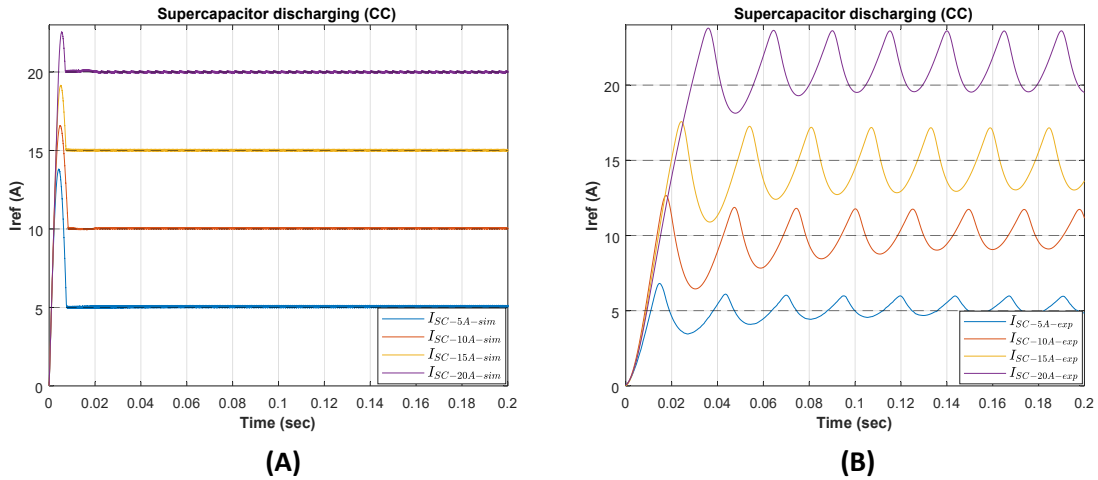

Figure 2.33: Supercapacitor discharging (CC).

The comparison of simulation and experimental results for the battery and SC at different discharge currents reveals the difference in their rise times. For example; For a discharge current of 5 A, the battery

has a rise time of (0.1195 s), while the SC has a rise time of (0.0159 s). At a discharge current of 10 A, the battery exhibits a rise time of (0.4242 s), whereas the SC demonstrates a rise time of (0.0045 s). For a discharge current of 15 A, the battery shows a rise time of (0.3024 s), while the SC exhibits a rise time of (0.0071 s). At a discharge current of 20 A, the battery has a rise time of (0.2505 s), whereas the SC has a rise time of (0.0303 s).

In all cases, both the battery and SC reach the reference current (i.e., $I_{ref} = 5A, 10A, 15A, 20A$). However, it is evident that the SC consistently achieves this reference current in a shorter time compared to the battery.

2.3.3 Constant Voltage (CV) discharging

Similar to the CC method for discharging, the voltage control loop method is used to discharge the battery and SC with different values of the reference voltage (V_{ref}). The operation of the boost converter is similar to the CC discharge method which is operated by a control signal (M1). The only difference is the addition of a PI controller in the outer loop to determine the value of the reference current. The boost control diagram for battery is shown in Figure. 2.34, and for SC in Figure. 2.35.

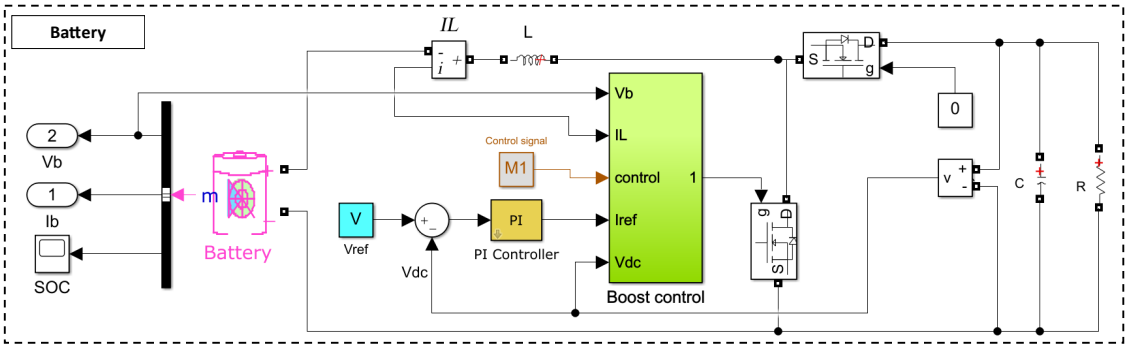

Figure 2.34: Battery discharging model (CV).

In case of battery, two values of reference voltage (i.e., $V_{ref} = 20V$, $V_{ref} = 30V$) are used to discharge the battery. The load resistance is calculated and set according to the given reference and battery voltages (i.e., $R_L = 50\Omega$).

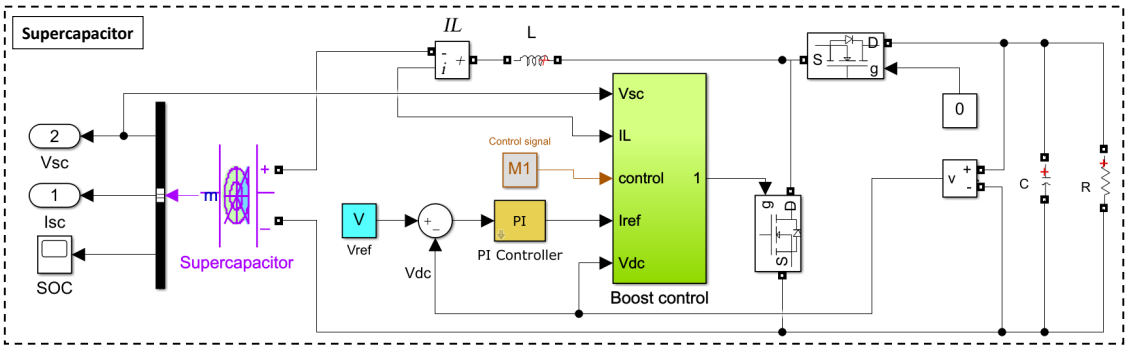

Figure 2.35: Supercapacitor discharging model (CV).

In case of SC, two values of reference voltage (i.e., $V_{ref} = 40V$, $V_{ref} = 48V$) are used to discharge the SC. The load resistance is recalculated and set according to the reference voltage and SC voltage (i.e., $R_L = 40\Omega$).

The modeling parameters such as the PI controller (Kp/Ki) values for inner and outer loops are set manually for each given value of reference voltage in both battery and SC model.

The comparison between battery simulation and experimental results are shown in Figure.2.36 for each reference value (i-e., $V_{ref} = 20V$, $V_{ref} = 30V$).

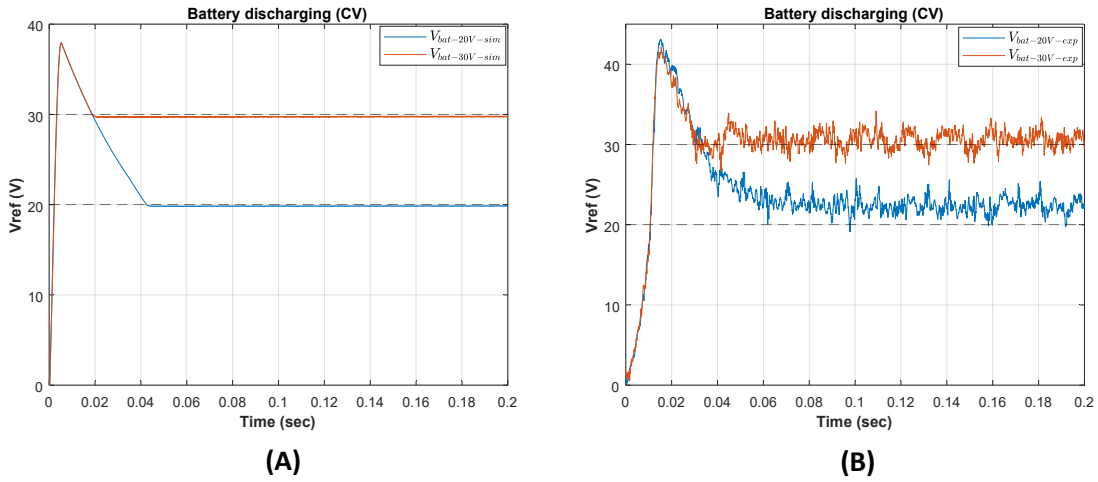

Figure 2.36: Battery discharging (CV).

In Figure.2.36, simulation and experimental results for the battery obtained for the reference voltages ($V_{ref} = 20V$, $V_{ref} = 30V$) are reported in sub-figure (A) and in sub-figure (B), respectively. The rise time for ($V_{ref} = 20V$) is recorded as (0.0675 s) and for ($V_{ref} = 30V$) as (0.1941 s) for both simulation and experimental results.

Likewise the comparison between the SC simulation and experimental results are shown in Figure. 2.37. for each reference voltage (i-e. $V_{ref} = 40V$, $V_{ref} = 48V$).

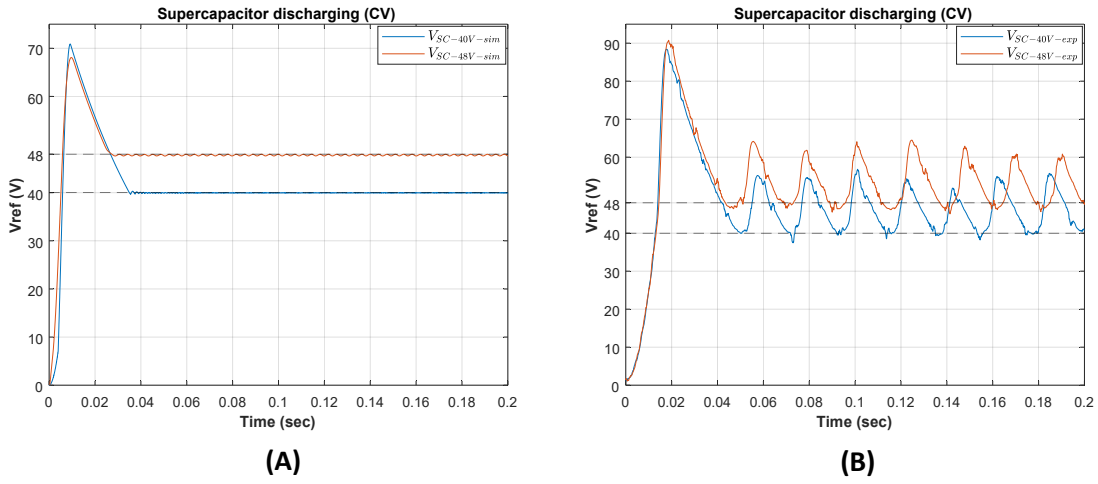

Figure 2.37: Supercapacitor discharging (CV).

In Figure.2.37, simulation and experimental results for the SC obtained for the reference voltages ($V_{ref} = 40V$, $V_{ref} = 48V$) are reported in sub-figure (A) and in sub-figure (B), respectively. The rise time for ($V_{ref} = 40V$) is recorded as (0.0454 s) and for ($V_{ref} = 48V$) as (0.3455 s) for both simulation and experimental results.

2.3.4 Constant voltage (CV) charging/discharging

For DCMG system, various DC bus voltage levels (i.e., $12V, 24V, 48V, 400V$) were found in the literature as discussed in chapter 1. In residential application, medium DC power devices use a $48V$ bus level. For this reason, the $48V$ DC bus level is considered for HESS local level testing. A voltage control loop method is used to test the HESS control in terms of charging and discharging.

Control diagram of HESS in buck and boost mode are shown in Figure 2.38, and Figure 2.39.

Three different tests (Test 1, Test 2, Test 3) were performed to observe and compare the dynamic behavior of the system and the DC bus stability. All tests were performed with the reference voltage, i.e., $V_{ref} = 48V$. The value of the load resistance is set as $R_L = 50\Omega$, which changes for each period to observe the system dynamic behavior.

The modeling parameters such as the PI controller (Kp/Ki) values for inner and outer loops of HESS model are set manually for different values of angular frequency, (i.e., $\omega = 10\ rad/s$, $50\ rad/s$, $250\ rad/s$) with the same reference voltage V_{ref}.

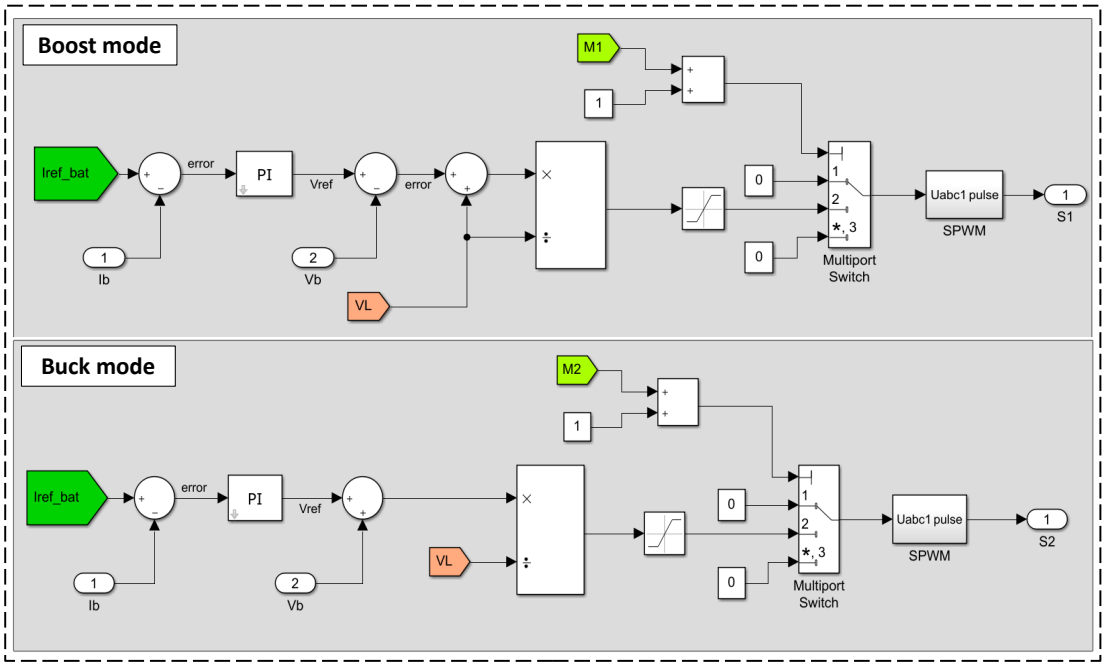

Figure 2.38: Buck-boost converter control diagram for battery.

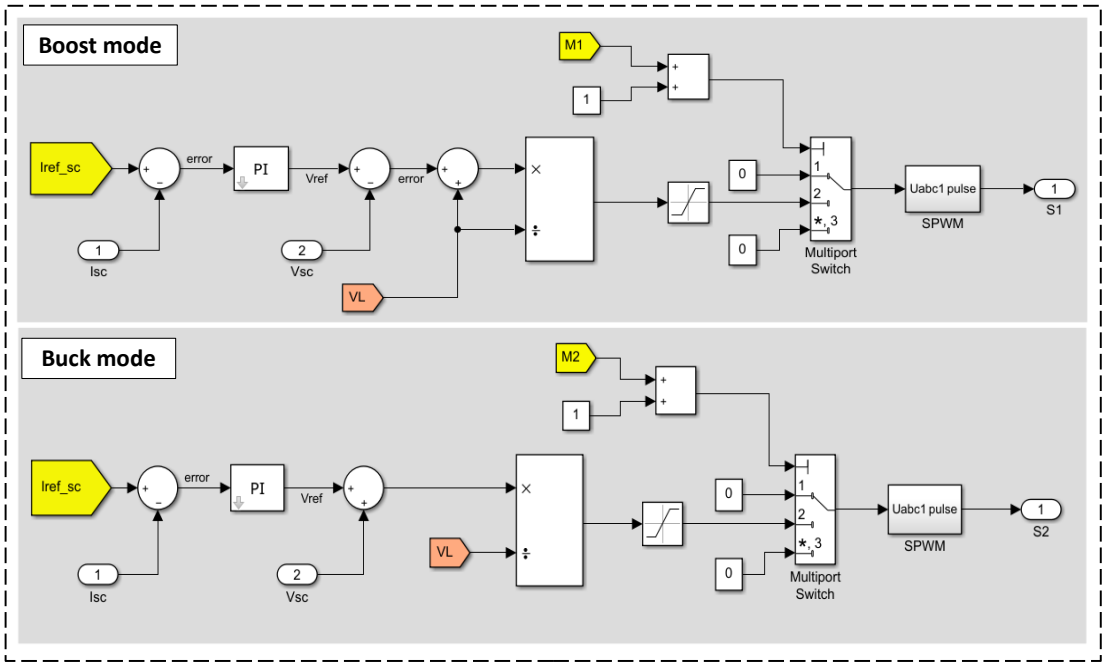

Figure 2.39: Buck-boost converter control diagram for supercapacitor.

Simulation and the experimental validation of the HESS are explained below with a separate presentation of the obtained results.

Simulation validation

For the simulation validation, two main actions were performed individually for two different time periods t1 and t2;

- **Change in Load** ΔL

  The load value is initially set to $R_L = 50\ \Omega$, which is then reduced to $R_L = 30\ \Omega$ for a period of time $t1$. During this time the boost mode is activated.

- **Change in Mode** ΔM

  The system started in boost mode and then switched to buck mode for a certain time $t2$. During this time the load value is the same $R_L = 30\ \Omega$.

Experimental validation

For experimental validation, the same two actions were performed individually for four different time periods t1, t2, t3, and t4 individually;

- **Change in Load** ΔL

  The initial load value is set to $R_L = 50\ \Omega$, which is then reduced to $R_L = 30\ \Omega$ for a period of time t1 and then increased again to $R_L = 50\ \Omega$ for a period of time t2. During this time the operating mode does not change.

- **Change in Mode** ΔM

  The system started in boost mode, switched to buck mode for a period of time t3, and then returned to boost mode for a period of time t4. During this mode change, the load is always the same $R_L = 50\ \Omega$.

In each period, a single action is performed, either the load or the operating mode changes. As a result, the dynamic behavior of each component (battery, SC) changes.

The dynamic behavior of the battery and SC in terms of charging/discharging mode and the control behavior in terms of current distribution between the HESS is similar in the simulation and experimental results. The only difference is in the time period and the actions performed during this time period such as ΔL and ΔM.

The comparison between simulation and experimental results for different values of ω are shown in Figure. 2.40, 2.41, 2.42.

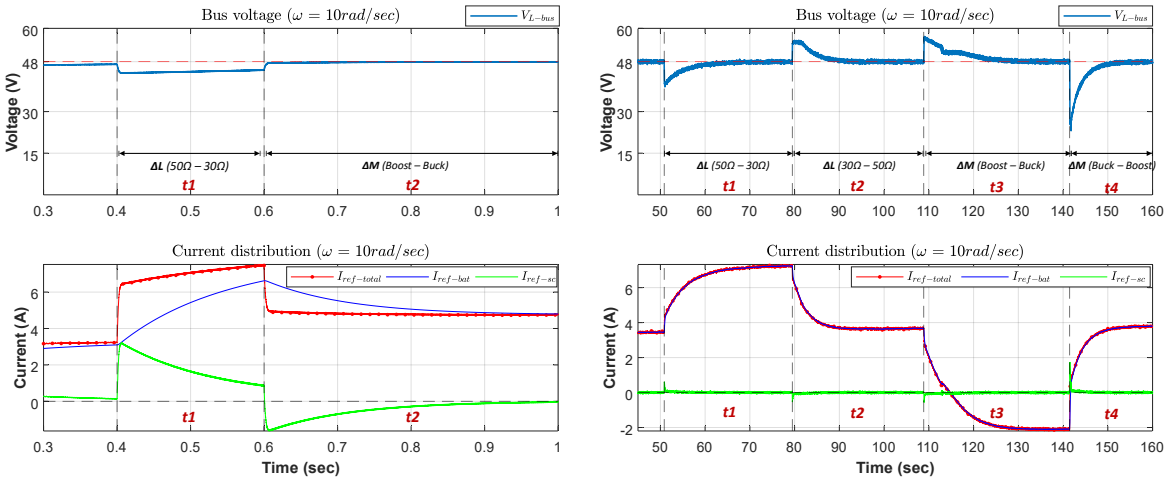

(a) *Simulation result* **(b)** *Experimental result*

Figure 2.40: LPF effect, $\omega = 10$ (rad/s).

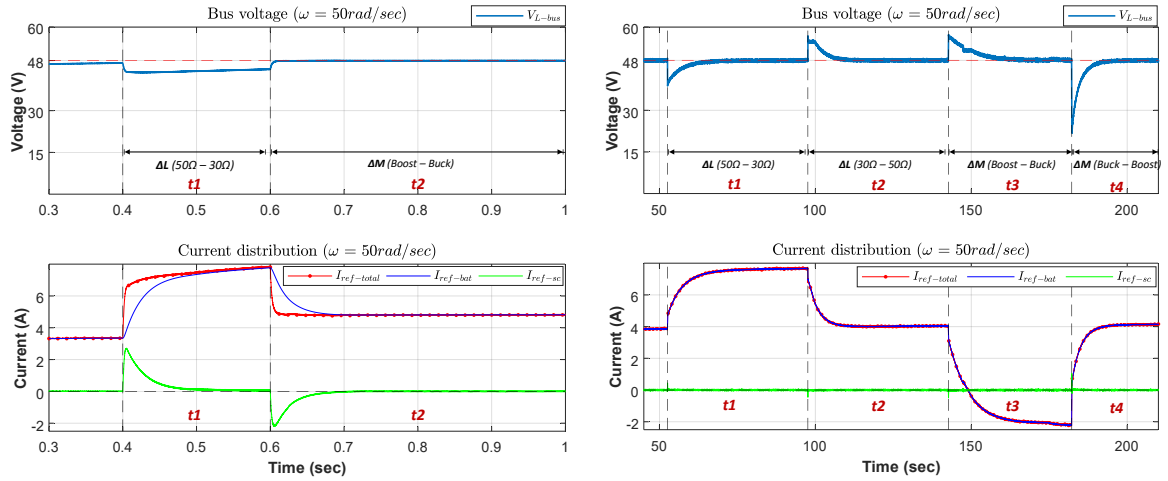

(a) *Simulation result* **(b)** *Experimental result*

Figure 2.41: LPF effect, $\omega = 50$ (rad/s).

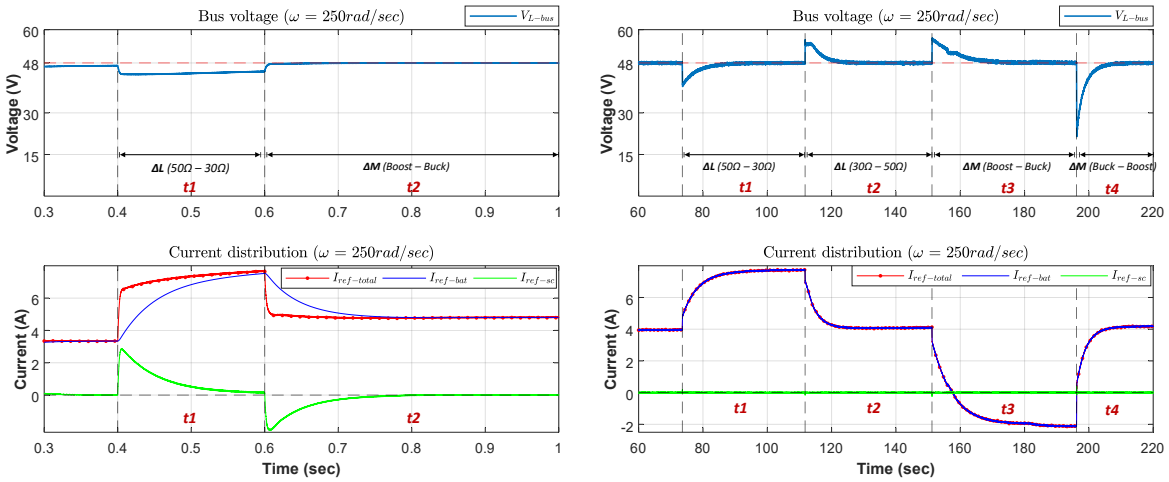

(a) *Simulation result* **(b)** *Experimental result*

Figure 2.42: LPF effect, $\omega = 250\ (rad/s)$.

The **simulation results** in Figure. 2.40a, 2.41a, 2.42a are divided into two time periods.

The period $t1$ shows the change in load, while $t2$ represents the change in operating mode. During the first period ($t1$), when the load decreases, the bus voltage decreases to a certain value and then starts to increase. During this period, the reference current is always positive, i.e., $I_{ref} > 0$, indicating discharging mode. After a time period, the boost mode changes to buck mode and the reference current starts to decrease and becomes negative, i.e., $I_{ref} < 0$, indicating charging mode. During the period $t2$, the bus voltage stabilizes to the reference voltage.

The **experimental results** in Figure. 2.40b, 2.41b, 2.42b are divided into four different time periods.

The first two periods $t1$ and $t2$ show the change in load, while the two other periods $t3$ and $t4$ show the change in operating mode. During the first period $t1$, when the load decreases, the bus voltage decreases to a certain value and then remains stable. During this period, the reference current increases until the load changes again. Even after the load increases, the reference current is always positive, i.e., $I_{ref} > 0$ during the periods $t1$ and $t2$, which represent the discharge action. Then the boost mode changes to buck mode and the reference current goes negative, i.e., $I_{ref} < 0$ during period $t3$, which represents the charge action. After some time, the buck mode changes back to the boost mode and the reference current starts to increase and goes to the positive region during period $t4$, which represents the discharge action.

As can be seen from the comparison results, the bus voltage increases and decreases with the change of the load or the change of the mode, but always remains stable with respect to the reference voltage V_{ref}.

In the following results, the 1st subplot shows the reference voltage V_{ref} and the DC bus voltage Vdc, while the 2nd subplot of each Figure shows the total reference current $Iref$ and the current distribution between $I_{ref_{.bat}}$ for the battery and $I_{ref_{.SC}}$ for the SC.

To see the influence of ω on the reference current I_{ref} and the current distribution between $I_{ref_{.bat}}$ for the battery and $I_{ref_{.SC}}$ for the SC, several points in the simulation and experimental results are highlighted, as shown in Figure. 2.43, and Figure 2.44, respectively.

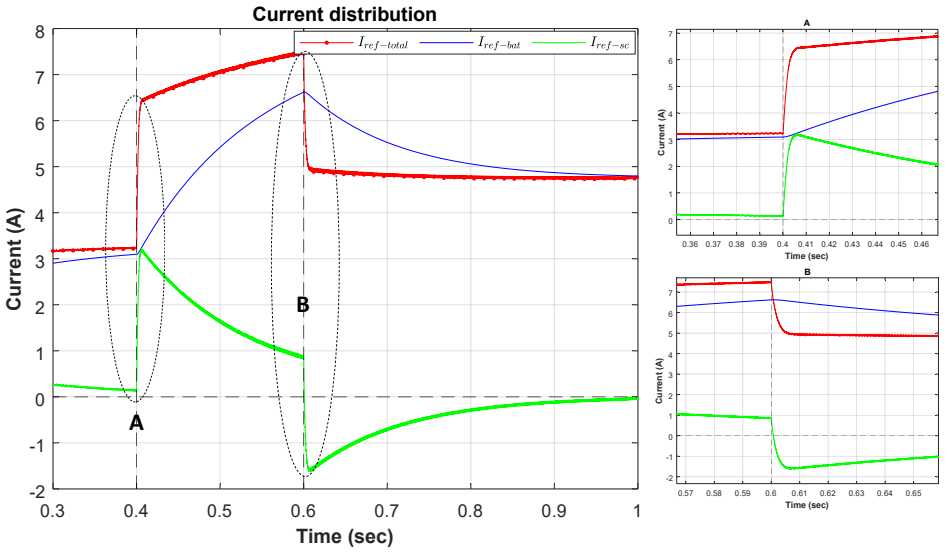

Figure 2.43: Simulation results: Influence of ω on current distribution, $\omega = 50\ (rad/s)$.

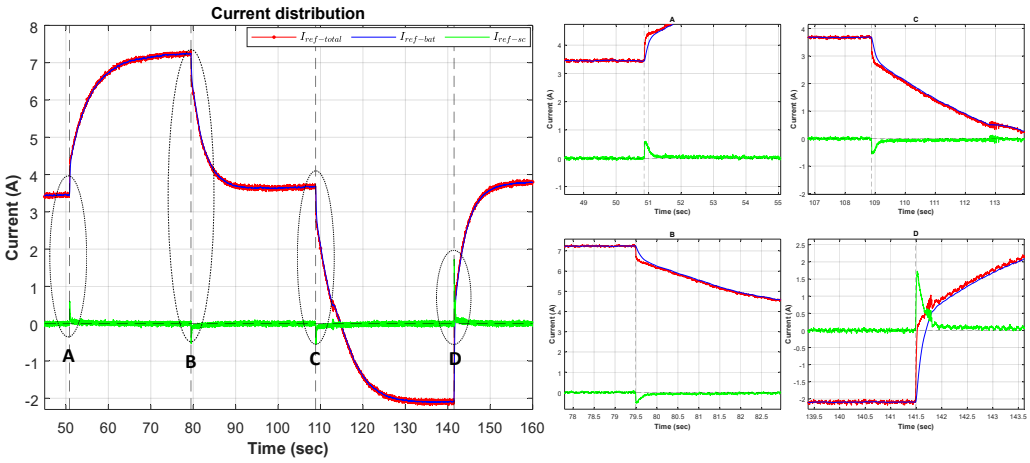

Figure 2.44: Experimental results: Influence of ω on current distribution, $\omega = 50\ (rad/s)$.

To illustrate the dynamic behavior of the battery and of SC during high peaks, two points A and B are highlighted in the simulation results and shown in Figure. 2.43 and four points A, B, C, and D in the experimental results are highlighted and shown in Figure. 2.44 . In both sub-Figures, it can be seen that the high dynamic response during the transition period is always compensated by SC.

The goal of testing different ω values is to compare the result of different dynamic behavior and choose the appropriate value of ω for LPF, which must ensure:

- Bus voltage stability.
- Current distribution between battery and SC.

To see the impact of ω on bus voltage stability and current control strategy, different time periods are considered to compare the results for simulation and experimental results separately.

Simulation results comparison

In the simulation results, the change in dynamic behavior was observed for two different periods $t1$ and $t2$. For each period, a comparison of the bus voltage, reference current, battery current, and SC current was performed for different values of (ω), as shown in the following figures.

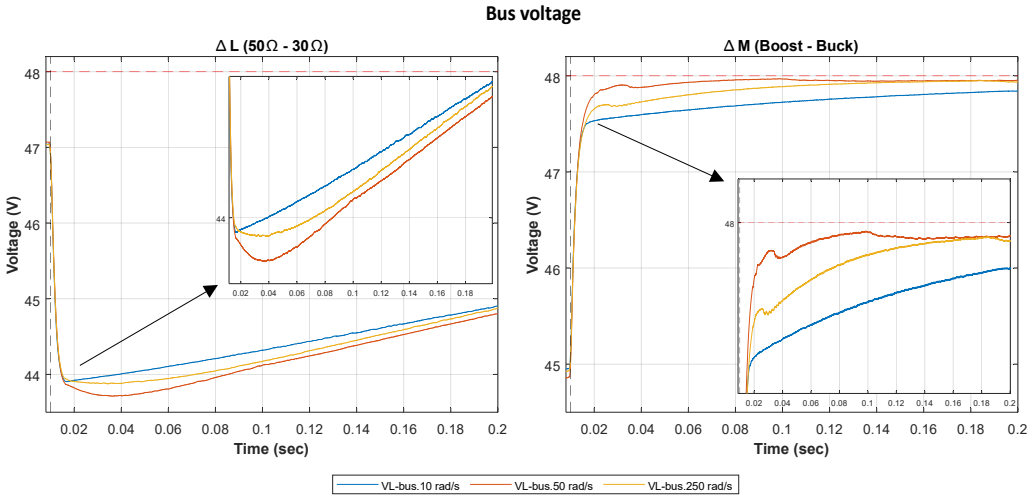

Figure 2.45: Simulation results: Bus voltage comparison.

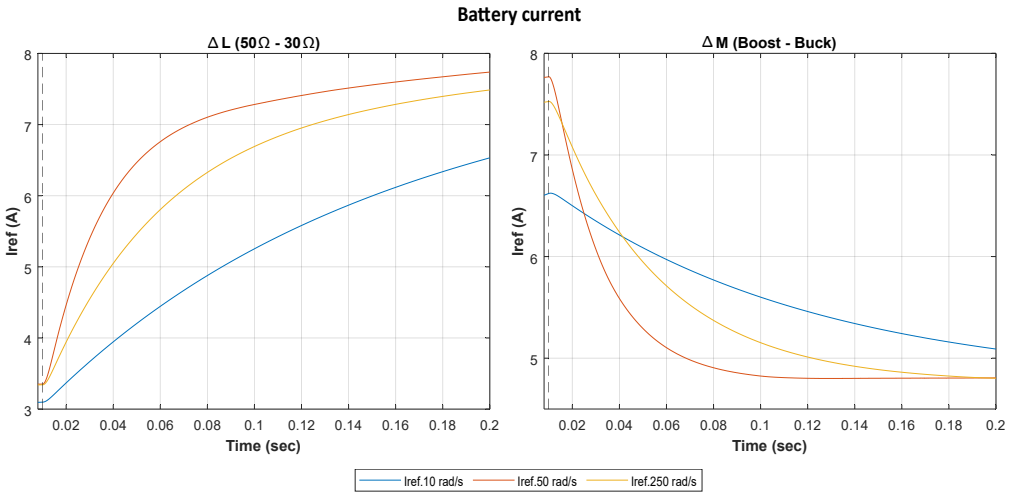

Figure 2.47: Simulation results: : Battery current comparison.

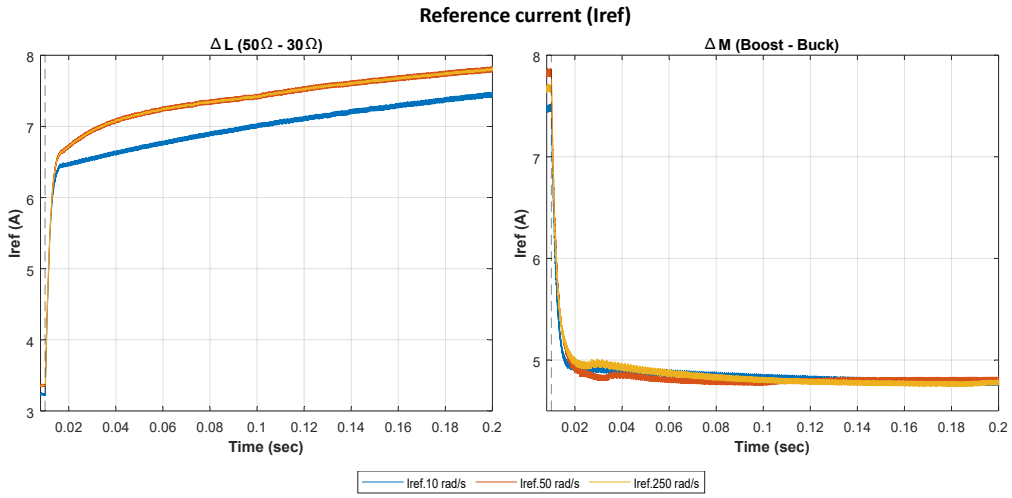

Figure 2.46: Simulation results: Reference current comparison.

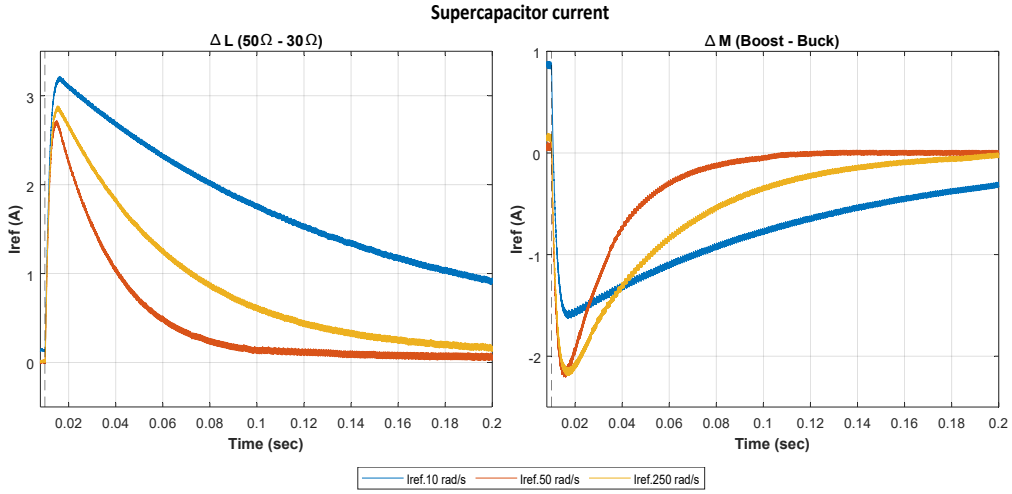

Figure 2.48: Simulation results: Supercapacitor current comparison.

Experimental results comparison

In the experimental results, the change in dynamic behavior was observed for the four different time periods $t1, t2, t3$ and $t4$. Just like the simulation results, a comparison of the bus voltage, reference current, battery current, and SC current was performed for different values of ω as shown in the following figures.

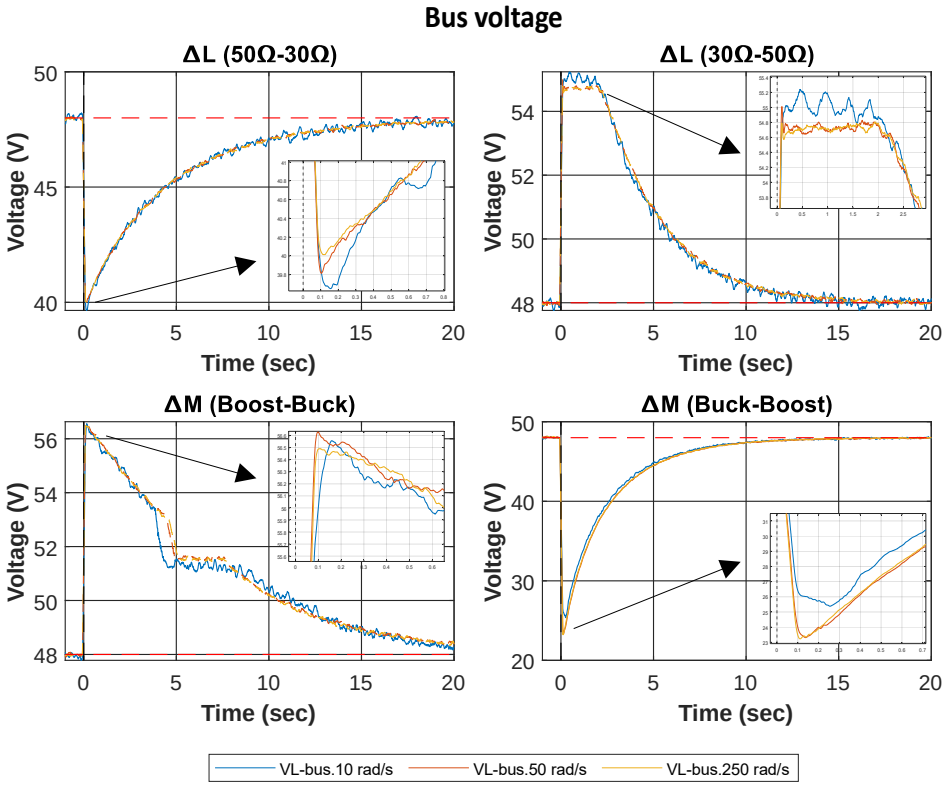

Figure 2.49: Experimental results: Bus voltage comparison.

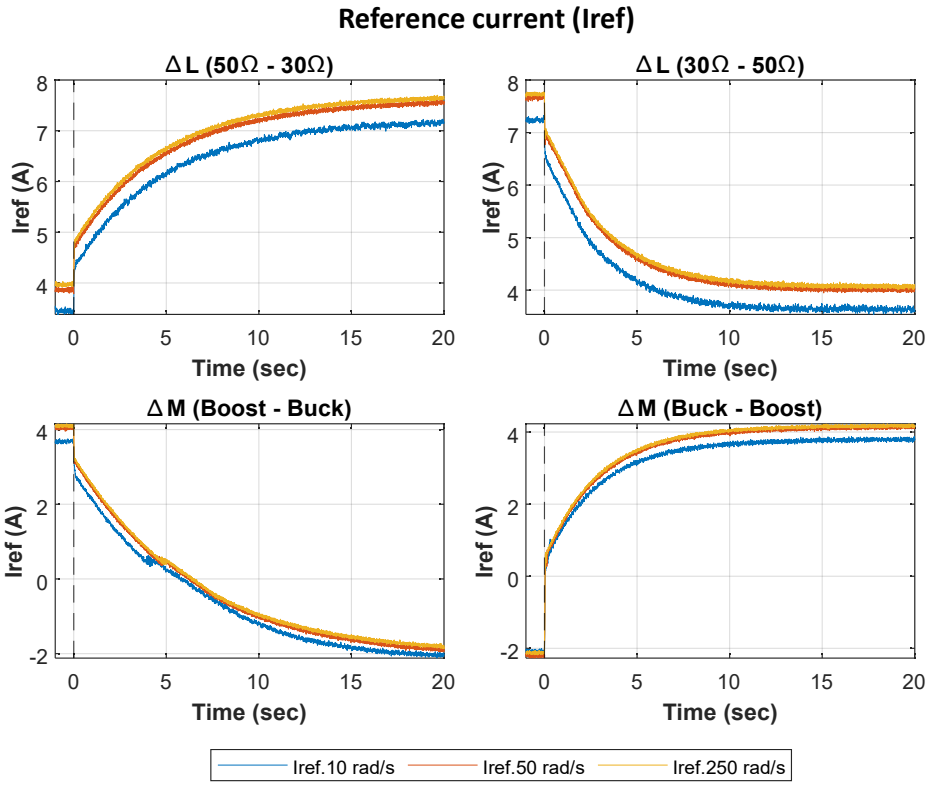

Figure 2.50: Experimental results: Reference current comparison.

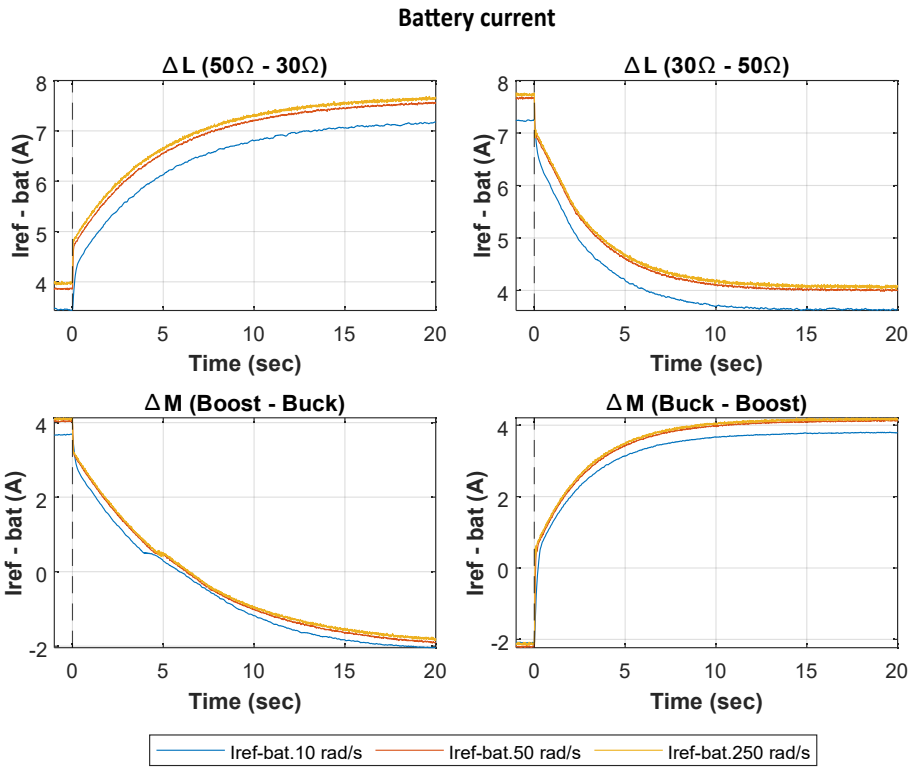

Figure 2.51: Experimental results: Battery current comparison.

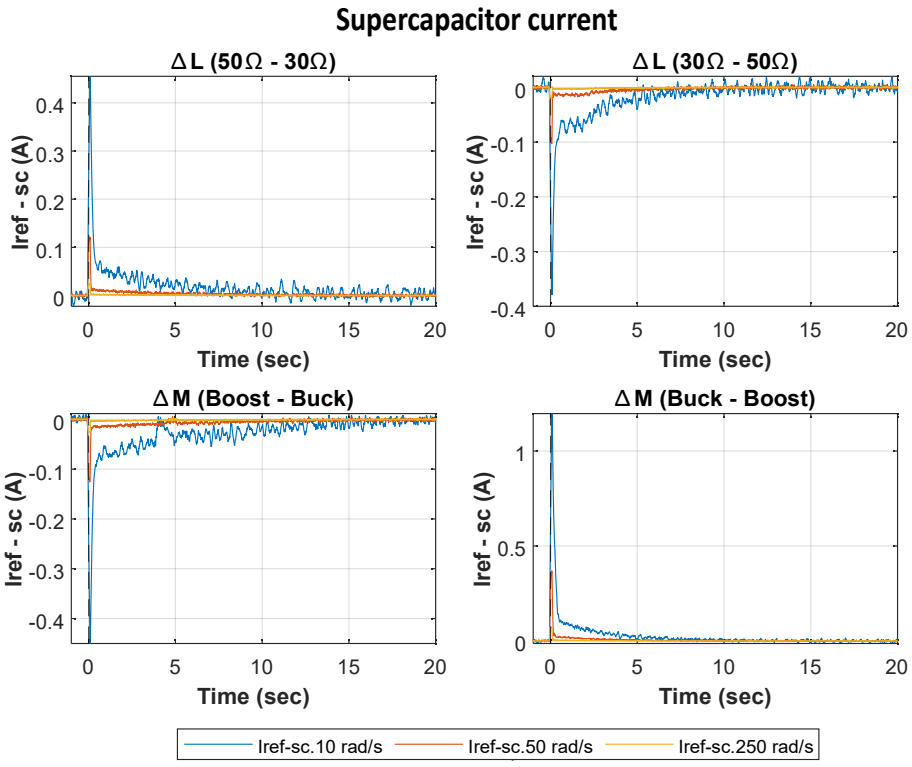

Figure 2.52: Experimental results: Supercapacitor current comparison.

The comparison of the simulation and experimental bus voltage in Figure. 2.45 and Figure 2.49 shows that a longer rise time exists for $\omega = 10\ rad/s$, compared to that for $\omega = 50\ rad/s$ and $\omega = 250\ rad/s$. However, the difference in rise time between $\omega = 50\ rad/s$ and $\omega = 250\ rad/s$ is not very large. Therefore, it does not make much difference in terms of bus voltage stability.

To see how ω affects the reference current I_{ref}, a comparison is made based on simulation and experimental results shown in Figure.2.46, and Figure 2.50. From the results, it can be noticed that the current behavior for $\omega = 50\ rad/sec$ and $\omega = 250\ rad/sec$ is similar and the difference between the $Iref$ values is not noticeable.

The battery current follows the reference current in both the simulation and experimental results, as shown in Figure. 2.47, 2.51, but SC reacts differently from the battery because of its properties. As shown in Fig. 2.48, 2.52, the high dynamics during the transition period is always compensated by SC.

The comparison of the simulation and experimental results showed that in the local control and single element tests, the angular frequency $\omega = 50\ rad/s$ and $\omega = 250\ rad/s$ do not have much difference in terms of bus voltage stability and current distribution between the battery and SC. However, they straightforwardly affect the sizing of SC. As a consequence, they ultimately increases the overall size and cost of the HESS, which respond to the system-level modeling and testing discussed in detail in the next chapter. Therefore, the angular frequency $\omega = 50\ rad/s$ is chosen as a suitable value for the designed system.

Conclusion

Chapter 2 introduces and explains the DC microgrid scheme developed in this thesis. The DC microgrid simulation platform is presented. It consists of a PV system, a HESS connected to the load via DC/DC converters.

PV panels connected to the DC bus via an MPPT controller and a DC/DC boost converter are used as the generation source. The HESS consists of a battery and SC, connected to the DC bus via a bidirectional DC/DC buck-boost converter. The DC load is connected via a DC/DC buck converter.

Local-level modeling with its control structure is briefly discussed. Maximum power point tracking (MPPT) control was implemented for the PV system. For the batteries and SC, different control modes such as current control and voltage control are developed and tested. In addition, a low pass filter (LPF) was applied to split the total HESS power into low and high frequency components for the batteries and SC, respectively. The influence of different angular frequencies ω of the LPF on the power sharing was also investigated. In the work developed in this study and presented in this chapter, our results obtained showed simulation and experimental results in good agreement.

Based on these simulation and experimental results, a comparison was made and analyzed as function of the cutting angular frequency ω of the LPF. We have found that $\omega = 50\ rad/s$ is a suitable value with the integration in the microgrid a battery and a supercapacitor having the specifications as described in this chapter.

Chapter 3

System-level EMS simulation platform

This chapter introduces the system-level simulation platform with its modeling and control. In a global energy management strategy control, especially for this work, in EMS system dedicated for DC microgrid (MG), system-level modeling is different than local-level modeling in terms of time complexity, memory problem, and especially control behavior. It requires an efficient EMS, which can analyze, monitor, and control the power generation, distribution, and load consumption at the system level. An overall view of the DCMG platform integrated with EMS is shown in Fig 3.1.

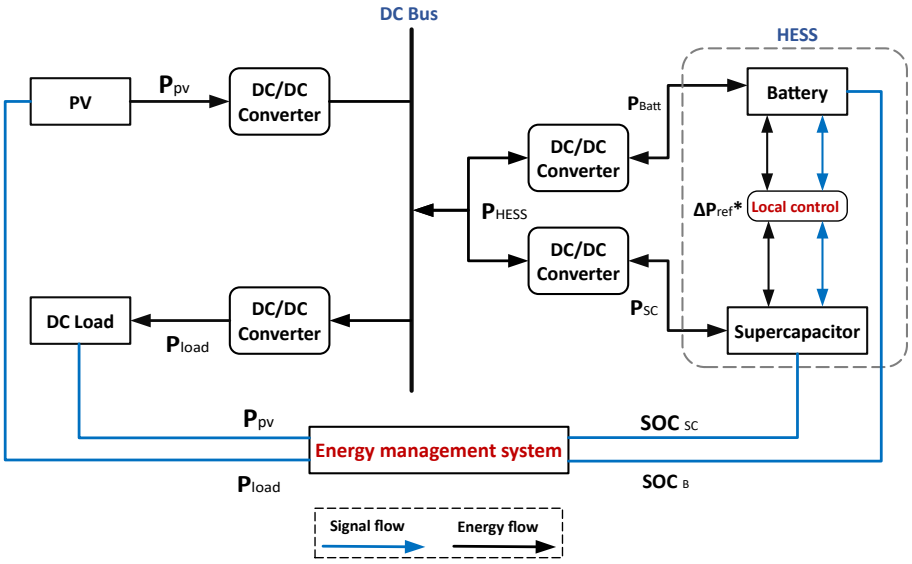

Figure 3.1: DC MG platform integrated with EMS.

EMS plays an important role in the operation, control, and the supervision of a DCMG at system level. In this system-level simulation platform, the local control behavior such as the switching behaviors of various DC/DC converters is ignored. In renewable-source integrated DCMG system, PV power (P_{pv}) is uncertain and unreliable. The same consideration can be given to the load power (P_{load}) as it varies according to user demand. Both of them have to be bounded and controlled, then managed by a proper EMS.

In Chapter 1, various EMS for DCMG system were described and discussed. In this chapter, we examine and analyze three of them, including: filtration-based EMS, rule-based EMS, and the combination of filtration-based EMS & rule-based EMS. Each strategy has its own advantages and disadvantages in terms of constraints, control and efficiency. In the next section, a general comparison between these three strategies is made and the most optimal strategy is selected for further validation. This will be explained in more detail in the following chapter. To validate the effectiveness of the proposed EMS, a universal EMS testbench evaluator with built-in cost functions developed to test the EMS under different operational scenarios.

3.1 The developed energy management strategy

A major challenge for a DCMG is to deal with stochastic renewable sources and volatile loads to achieve better operational performance. For this reason, an extensive literature survey on EMS role has been done and different strategies related to MG energy management are covered in chapter 1.

The primary goal of the energy management strategy for the DC MG is to ensure energy balance in the system, taking into account the degradation factor of the distributed generators and reducing system costs with several other control objectives.

In this context, three different methods have been applied to the designed system to achieve the following objectives:

- To maintain the stability of the DC bus voltage;
- To ensure the power balance control in HESS;
- To protect the battery & SC from deep discharge and overcharge;
- To protect the battery during high dynamics as much as possible;
- To ensure optimal sizing of the HESS with less cost.

Each method has its own limitations in terms of efficiency and control strategy. Therefore, not all objectives can be achieved by a single method.

For example, in **filtration-based EMS** a conventional control scheme is used to divide the current between battery and SC. At local level, this control strategy works well for the current sharing between HESS and the DC bus voltage level can also be achieved. But at the system level, this is not a good choice because there are no other control functions such as SOC control and power balance control between HESS. **Rule-based EMS** involves the use of a predefined set of instructions or rules. These rules are based on human knowledge or on information available in the literature. In this strategy, two different approaches are taken into account for HESS control. In the first approach, the battery has priority in charging and discharging operations, while in the second approach, this priority is devoted to SC. In each scenario, several cases are defined to perform the charging and discharging operations depending on several other factors such as SOC levels and the reference currents of battery and SC. In this strategy, the SOC of each element can be observed to perform the charging and discharging action within certain limits, but the power balance control can not be achieved properly. Moreover, the HESS sizing and cost function is not included in rule-based EMS.

The third strategy that we considered is the combination of the **filtration-based EMS** and the **rule-based EMS** which can bring a solution to ensure the power balance control in HESS. The HESS supplies the energy to the load by sharing power between SC and battery. If the energy stored in the battery and SC decreases below a limit, the power supplied to the load will be shedded (**load shedding**). If the energy stored in the battery and SC increases over a limit, the power supplied by the PV will be interrupted **(power curtailment)**. In addition, it protects the HESS from deep discharge and overcharge. The proposed EMS is explained below in detail.

3.1.1 Filtration - based EMS + Rule - based EMS

As introduced above, the proposed energy management strategy is a combination of filtration-based EMS and the rule-based EMS shown in Fig 3.2. This enhanced form of EMS differs in many ways from the previous two strategies.

The main focus of this EMS are listed below:

- To ensure the power balance control in HESS;
- High dynamics profile is always compensated by SC during the transition period;
- Power curtailment in case of overcharging and load shedding in case of undercharging battery and SC;
- Cost function evaluation for HESS and only-battery case.
- Combined sizing of HESS with EMS.

As shown in Figure 3.1, the main components which constitute the DC MG are:

PV array

The performance of PV systems is primarily influenced by solar radiation and operating temperature. To obtain the maximum power, an MPPT method is usually used to obtain the peak value of the available electrical power of the PV array but in the targeted DC MG scheme, the system-level references are strictly followed by assuming that the PV panels are working at maximum power point. At the same time, the overcharging of the battery and the supercapacitor must be controlled by limiting the PV production. For this reason, PV curtailment can be done during off-load peak hours presented in the EMS flowchart (Level-1) shown in Fig 3.2 .

Battery

In the proposed EMS design, Li-ion battery type is considered for the development of DC MG simulation platform. In order to protect the batteries from over-charging and over-discharging, SOC_B is limited between $SOC_{B.min}$ and $SOC_{B.max}$ as upper and lower limits as shown in equation 3.1 and computed by equation 3.2. Moreover, the charge-discharge rate of the batteries is controlled by current, and the batteries power can be controlled by giving corresponding current reference. Thus, the charging and discharging current I_B has to respect the limitations, $I_{B.max}$ and $I_{B.min}$, as in equation 3.3.

$$SOC_{B.min} \leq SOC_B(t) \leq SOC_{B.max} \tag{3.1}$$

$$SOC_{B(t)} = SOC_{B.initial} + \frac{1}{130 \times 3600 \times V_B} \int_0^t P_B(t).dt \tag{3.2}$$

$$I_{B.min} \leq I_B(t) \leq I_{B.max} \tag{3.3}$$

where $P_{B(t)}$ is the battery power, $SOC_{B.initial}$ is the initial SOC of battery, and V_B is the battery voltage [4].

Supercapacitor

The SC has a high-power density compared with battery which has a high energy density. Due to this characteristic, SC is most effective to bridge power gaps lasting from a few seconds to a few minutes. Due to the fact that SC has a greater power density than the battery, HESS is considered for DC MG simulation platform. The most attractive advantage of using SC with the battery is to compensate the domestic high-dynamic load profiles and fluctuated PV power generation especially in cloudy days. In HESS, battery is considered as an energy source while SC is considered as a power source due to its quick response. Same as batteries, SOC_{SC} is limited between $SOC_{SC.min}$ and $SOC_{SC.max}$ as upper and lower limits as shown in equation 3.4 and computed by equation 3.5.

$$SOC_{SC.min} \leq SOC_{SC}(t) \leq SOC_{SC.max} \tag{3.4}$$

$$SOC_{SC(t)} = \frac{E_{SC.stored}}{E_{SC.rated}} \times 100\% \tag{3.5}$$

The SC stored energy $E_{SC.stored}$, is decided by the SC voltage V_{SC} and the capacitance C_{SC};

$$E_{SC.stored} = \frac{1}{2} C_{SC} V_{SC}^2$$

$$E_{SC.rated} = \frac{1}{2} C_{SC} V_{SC.rated}^2$$

where $V_{SC.rated}$ is the rated voltage of the SC [4].

Over-charge and over-discharge are predictable, during charging and discharging processes, respectively. These over-limits will seriously affect the life of battery and SC. To avoid this situation, certain measures are taken into an account to protect the storage system in form of SOC limit of battery and SC presented in Figure 3.3.

Corresponding treatment to the power is done depending on the SOC of each element. The total charge-discharge power of batteries and SC can be controlled by corresponding reference power P_{ref} computed by equation 3.6, where P_{load} is the load power and P_{pv} is the power generated by PV panels.

$$P_{ref} = P_{load} - P_{pv} \tag{3.6}$$

Load

In this chapter, a domestic load profile has been utilized to test the developed EMS. In case of less PV generation, load power will be taken from the battery and SC while respecting the SOC limits. To keep the SOC of battery and SC in a proper operational limit, load shedding can be done during load peak hours as described and presented in the EMS flowchart (Level-1) shown in Figure 3.2 .

In DCMG system configuration, P_{pv} is uncertain and unreliable. The same for P_{load}, which is varying according to the user demand. But both of them can be limited and controlled by a proposed EMS. The main objective is to ensure the power balance control between battery and supercapacitor. In order to test the combined strategy, i.e., the combined sizing and EMS strategy, a very simple but computationally effective EMS is implemented on EMS simulation platform presented in the next section.

The aim of utilizing proposed EMS is to distribute and control the power balance between battery and SC. Battery power (P_{Batt}) and SC power (P_{sc}) are controlled within their physical limits, by giving corresponding power reference P_{ref}.

P_{pv} and P_{load} are always positive, P_{Batt} and P_{sc} can be positive or negative, which represent discharging power to the system and absorbing power from the system respectively. Here, power is considered as a negative power when HESS is charged, and power is considered as positive when HESS is discharged. A unique feature of designed EMS is the power exchange between battery and SC depending on the SOC of individual element.

Above-mentioned EMS is divided into two levels (Level-1, Level-2). In presentations below, the various considered cases are reported in Figure 3.2.

Level - 1

Level-1 is based on three different scenarios:

- P_{pv} is less than the required P_{load};
- P_{pv} is greater than the required P_{load};
- P_{pv} is equal to the required P_{load}.

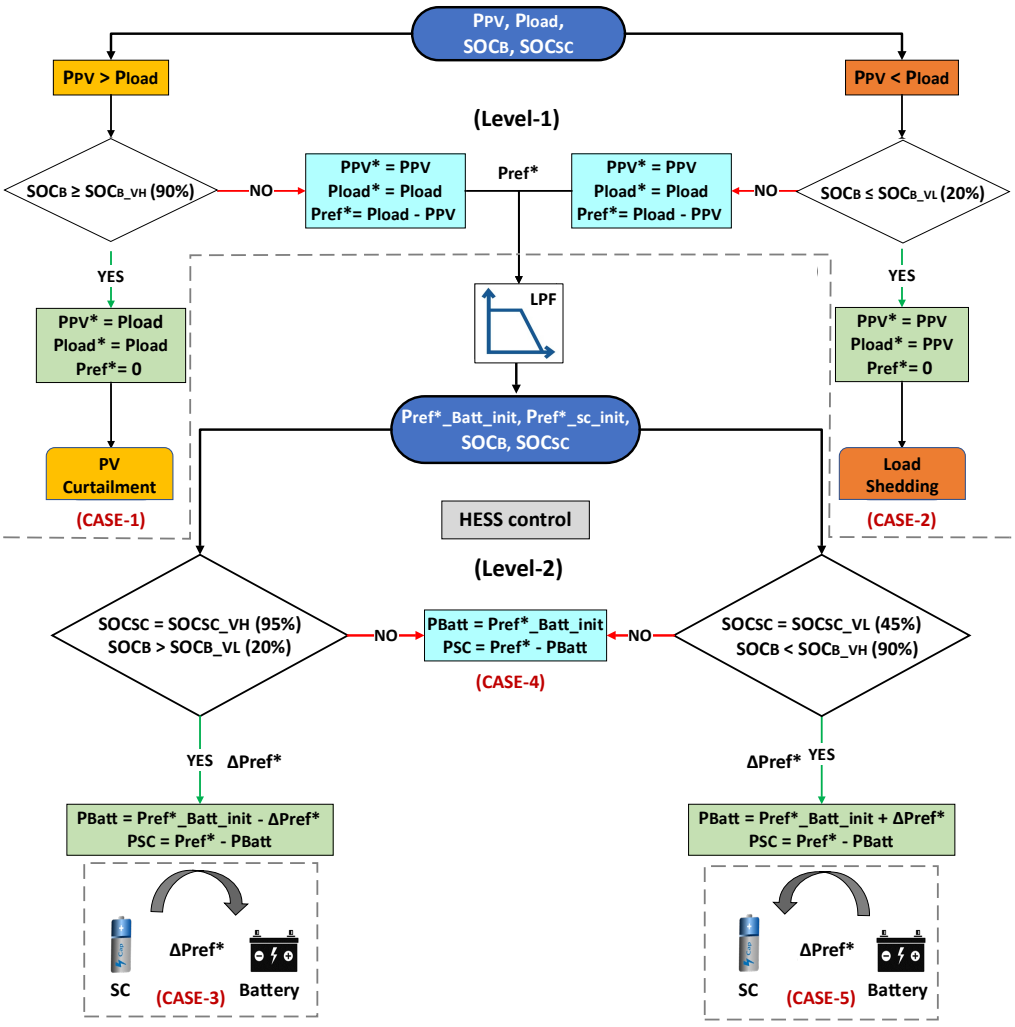

Figure 3.2: Energy management strategy : Filtration-based + Rule-based EMS.

In the 1^{st} **scenario**, P_{pv} is greater than required P_{load}, SOC_B and SOC_{sc} is set very high. No extra energy can be stored in battery and SC. Therefore, PV curtailment will be done, which corresponds to case 1.

In the 2^{nd} **scenario**, P_{pv} is less than required P_{load}, SOC_B and SOC_{sc} is set very low. No energy can be taken from the battery and SC. Therefore, load shedding case will be activated, which corresponds to case 2.

In the 3^{rd} **scenario**, P_{pv} is equal to the required P_{load}. In this case the load demand is totally accomplished by the PV array and no power is extracted from the batteries or SC. This is an ideal case that is not by a specific strategy as no intervention in the energy management is necessary.

At level-1, power curtailment and load shedding control have been done, corresponding to case 1 and case 2 respectively. As a result, $P_{ref}*$ signal can be generated and further utilized for the extension of other cases at level-2.

Level - 2

Level-2 is based on a low pass filter (LPF), which is about HESS control. A simple filtering approach is used to decouple the high and low frequency components of the required power. This decoupling of

power between battery and SC allows both ESS elements to operate at a wider range of SOC that can greatly improve the efficiency of HESS.

This power division among battery and SC relied on the angular frequency ω used in LPF parameters. A set of different ω values have been configured and tested in chapter 2 and $\omega = 50\ rad/sec$ is chosen as a suitable value for the designed system. This factor has a great influence on the sizing of HESS, it will be further analyzed and discussed in the sizing and cost calculation section.

After LPF processing, the power P_{HESS} is divided into low-frequency and high-frequency power. The high-frequency power is offered by the SC, the low-frequency power is smoothed by the battery.

At level-2, a unique feature has been included in the designed EMS, in which the power ΔP_{ref^*} is exchanged between the battery and SC. The interest of power exchange between HESS is to charge and discharge the SC when the SOC_{sc} level is lower and higher than a pre-set threshold. For this reason, SC SOC retaining strategy has been introduced in HESS control block shown in Figure 3.8.

In the literature, different SOC limits can be found for battery and SC depending on the application. For residential applications, SOC range for battery ($20\% \leq SOC_B \leq 90\%$) and for SC ($45\% \leq SOC_{SC} \leq 95\%$) are proposed by the authors in [4]. These limits can be different for each system which are based on the defined strategy. According to proposed EMS strategy, SOC of battery and SC are further divided into: SOC_{VL} – (very low), SOC_L – (Low), SOC_H – (High), SOC_{VH} – (very high) as shown in Figure 3.3.

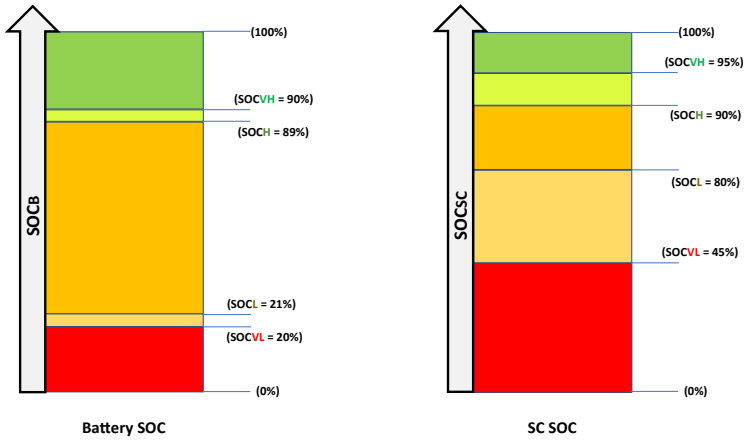

Figure 3.3: HESS SOC range [4].

SOC limits for batteries differ from SC due to the different charging and discharging behavior of the individual elements. The battery takes a long time (several minutes to hours) to charge and discharge, while SC takes a very short time (a few seconds to minutes) to charge and discharge. Since SC has a self-discharge current,it is obvious that the SOC_{sc} will drop after tens of seconds, resulting in shortened lifetime and performance due to frequent charging and discharging. This switching behavior of SC can be controlled by defining a wide range of SOC in terms of hysteresis control, which can prevent SC from frequent switching between different modes.

3.1.2 Design of EMS testbench evaluator

To test the developed EMS, a testbench evaluator was designed in the laboratory, as shown in Figure.3.4. The main interest is to evaluate and validate the EMS with less computational time.

A few assumptions has been made to test the EMS testbench evaluator:

- PV panels are working at maximum power point;
- Converter power losses are zero;

- System-level references are strictly followed;
- Load shedding start/stop thresholds and SOC limits are the parameters of the strategy that can be defined by optimization.

In general, the power curtailment, the start/stop thresholds for load shedding, and SOC limits are the parameters of the strategy that can be optimized by optimization methods. In this study, existing values from the literature were used for initial validation of the defined control strategy.

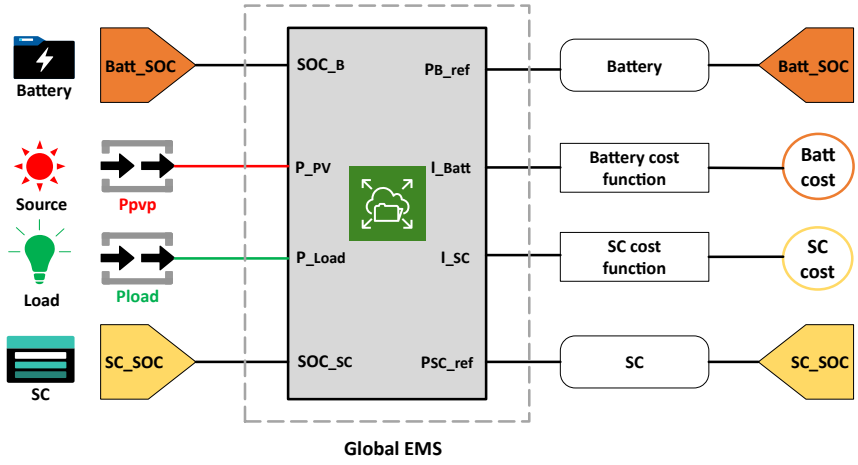

Figure 3.4: EMS testbench evaluator.

Testbench evaluator has a global EMS block consisting of three sub-blocks, as shown in Figure 3.5.

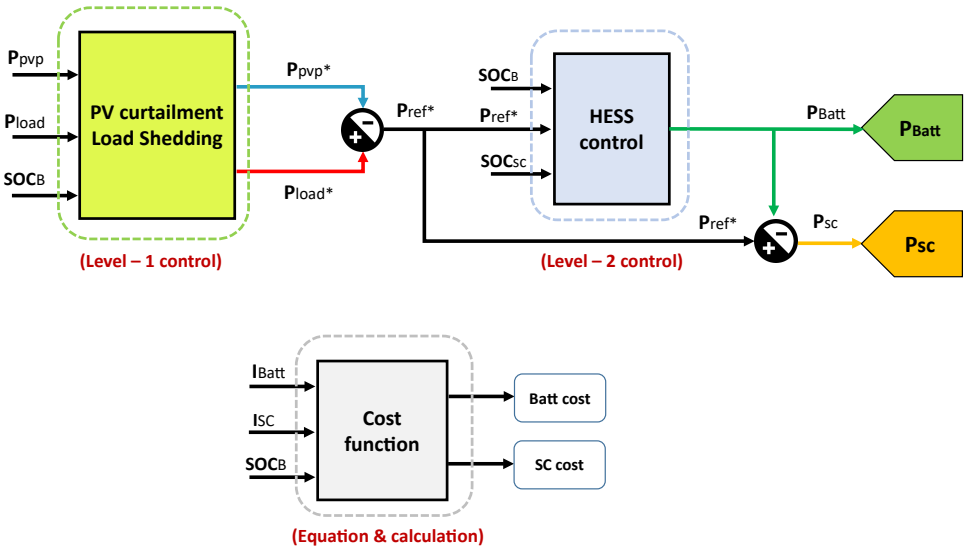

Figure 3.5: Global EMS.

Two sub-blocks refer to the local control of the system operate at level-1 and level-2, respectively according to the proposed EMS. Level-1 control deals with power curtailment and load shedding at the local-level EMS, which stop and deliver power to a load according to established rules while respecting SOC limits. Level-2 control is about HESS control. To make the best use of the battery and SC, the local HESS control is introduced, different from the conventional control. Indeed, in this part, a SOC retaining

control strategy for SC has been introduced to regulate its SOC. The third sub-block is about the cost function of HESS. The blocks are described and explained in more detail in the following subsections.

3.1.2.1 Power curtailment and load shedding control

Power curtailment and load shedding block are implemented at local-level EMS control, which stop and supply the energy to a load according to the defined rules while respecting the SOC limits. It has two main inputs (P_{pvp}) and (P_{load}), which are further analyzed and adapted by considering the battery SOC, providing two outputs, namely reference PV power ($P_{pvp}*$) and reference load power ($P_{load}*$), as shown in Figure 3.6 .

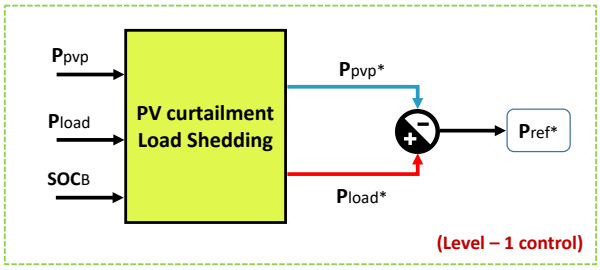

Figure 3.6: PV curtailment & load shedding control.

In both cases, P_{pvp} and P_{load} are further adapted according to the battery SOC. If the energy stored in the battery decreases below a limit, the power supplied to the load will be interrupted (Load shedding) and $P_{load}*$ will be injected to the system. If the energy stored in the battery increases over a limit, the power supplied by the PV will be interrupted (Power curtailment) and $P_{pvp}*$ will be injected to the system. Same as in equation 3.6, $P_{ref}*$ can be calculated by the difference of load power $P_{load}*$ and $P_{pvp}*$ computed in equation 3.7.

$$P_{ref}* = P_{load}* - P_{pvp}* \tag{3.7}$$

3.1.2.2 HESS control

In order to make the best use of battery and SC, HESS local control is introduced as shown in Figure 3.7 . The conventional LPF is used to distribute the energy/power between battery and SC. Besides, SC SOC retaining control block is established to store and supply an energy.

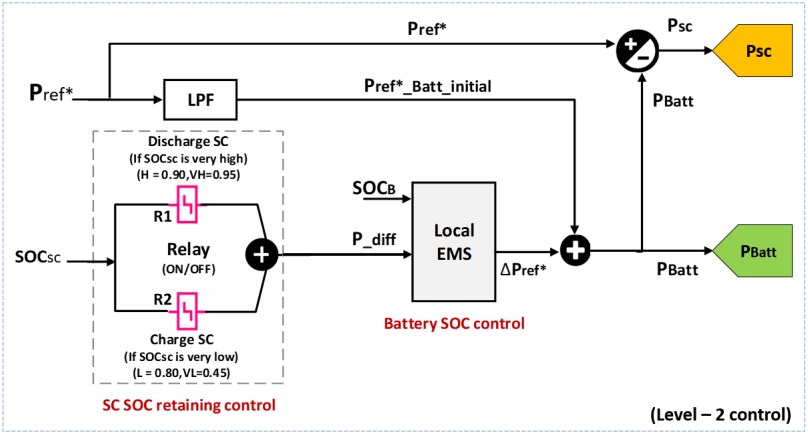

Figure 3.7: HESS control.

A simple SOC management scheme is implemented by combining two relays (R-1, R-2). R-1 deals with the discharging process while R-2 deals with the charging process of SC. A power sharing method is introduced here for which a specific amount of power is calculated (50% of peak reference power, i.e., $\pm\ P_{diff} = 200$W).

When SC SOC level is very high (V_H), R-1 turns ON to discharge the SC by supplying power ($-P_{diff}$) until SC SOC reaches to the high limit (H). At this specific point R-1 turns OFF to stop discharging of SC ($-P_{diff} = 0$). Likewise, when the SC SOC level is low (L), R-2 turns ON but no need to charge the SC until it come to the very low limit (V_L). At this specific point R-2 turns off and SC charge starts by taking power ($+P_{diff}$). The working principle of SC SOC retaining control block is shown in schema Figure 3.8.

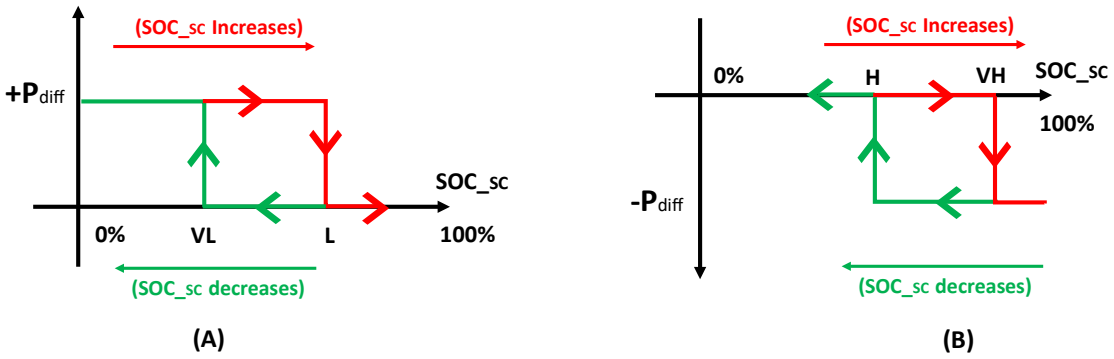

Figure 3.8: SC SOC retaining control.

In both cases, $\pm\ P_{diff}$ will enter into a battery SOC control block. In the next step, battery SOC is compared with the pre-set threshold ($SOC_B \leq 20\%$) to generate the power (ΔP^*_{ref}). The change in power (ΔP^*_{ref}) is further added to the battery initial reference power $P^*_{ref-Batt-initial}$ to get the corresponding reference power for battery (P_{Batt}) shown in equation (3.8) and SC power (P_{SC}) as shown in equation (3.9).

$$P_{Batt} = P^*_{ref-Batt-initial} - \Delta P^*_{ref} \tag{3.8}$$

$$P_{SC} = P^*_{ref} - P_{Batt} \tag{3.9}$$

3.1.2.3 Cost function

To evaluate the performance of developed EMS, a cost function has been defined herein. It comprises of capital cost (CAPEX) and operational cost (OPEX), which is expressed as:

$$J = CAPEX + OPEX$$

CAPEX is strongly related to the sizing of the system, which includes system elements such as PV panels, batteries and SC expressed as:

$$CAPEX = \sum_i C_i.N_i$$

where

i = PV panels, batteries, SC
C = Cost per unit
N = Number of elements

In the above expression, i represents the type of elements which we need to consider for the calculation, and N represents the number of these specific elements that need to be optimized for a known set of profiles. There are only discrete solutions for the size of the elements, and c is the unit cost, which is known and related to the market price. An upper bound $CAPEX < C_{max}$ should be considered to avoid economically infeasible solutions. In our study, for a given configuration, we considered only the battery and SC for the calculation of the cost function, which is supposed to be universal.

OPEX depends on the defined energy management strategy for charging and discharging of HESS. This cost is calculated by

$$OPEX = degradation + penalisation$$

It is associated with the degradation cost of each storage element and the penalization cost during system operation.

A. Degradation cost

The battery degradation function $\Delta B_{(t)}$ depends on the state of charge with $f(SOC_B)$ and power dynamics with $g(i_B)$ [146]. The lifetime of the battery is expected to be the half of the lifetime of the supercapacitors,(i.e., 15000 h) for 7.5 years. The battery degradation function $\Delta B_{(t)}$ is expressed by

$$\Delta B(t) = \frac{1}{3600 * 15 * 10^3 . Q_{B-rat}} \int_0^t f(SOC_B).g(i_B).i_B(t)dt \tag{3.10}$$

with Q_{B-rat} the rated capacity and i_B the current of the battery.

The operational cost of the battery can then be deduced from $\Delta B(t)$ computed by:

$$\epsilon.B(t) = E_{B-rat}.B_{cost}.\Delta B(t) \tag{3.11}$$

with E_{B-rat} the energy of the battery (kWh) and B_{cost} the battery cost per unit of energy (€/kWh).

One reference value for the cost per unit of energy given in literature is, for the battery about 200 €/kWh [147] and for SC about 250 €/kWh [148].

The SC degradation is computed by using the following equation:

$$\Delta SC(t) = \frac{t_{use}}{30 \times 10^3} \tag{3.12}$$

with the time used in hours and the expected lifetime of SC is considered for 15 years (i.e., 30000 h) [149] .

The operational cost of the supercapacitors can then be deduced from $\Delta SC(t)$:

$$\epsilon.SC(t) = E_{SC-rat}.SC_{cost}.\Delta SC(t) \tag{3.13}$$

with E_{SC-rat} the rated energy of the supercapacitors (kWh) and SC_{cost} is the supercapacitors cost per unit of energy (€/kWh).

B. Penalization cost

The penalty cost is related to curtailed power and load shedding power. In case of excessive generation, when the HESS is full and no charge can be further stored in the batteries and SC. The extra power is fed into the central grid. Taking as example the the PV feed-in grid tariff as given by EDF France, it is equal to 0.1814 €/kWh. Due to the unavailability of HESS, load shedding occurs. When SOC of the battery and SC are very low, the corresponding energy storage element cannot supply the deficit energy required by the load. In this case, the consumer must pay an additional amount during the period of power shortage. The cost of electricity for households in France, is given as 0.1740 €/kWh (global petrol price). This price is used to calculate the penalty costs, which are directly related to the amount of curtailed power and load shedding.

$$\epsilon.Penalty(t) = E_{pv-curt}.\epsilon_{pv-coff} + E_{load-shedd}.\epsilon_{load-coff} \tag{3.14}$$

where, $E_{pv-curt}$ and $E_{load-shedd}$ are measured PV curtailed energy and load shedded energy, $\epsilon_{pv-coff}$ and $\epsilon_{load-coff}$ are Pv feed-in grid tariff and the load shedding grid price. The cost function results are presented in the HESS cost evolution results section.

Input data

A dataset of a real PV system installed in the GECAD building (Zone-3) in Porto, Portugal, is considered to test the developed EMS. It contains 4 panels (250 W/Panel) with a peak generation of 1 kW [3]. A 24-hour residential profile (summer/winter) with a sampling time of 10 seconds is used as input to EMS testbench evaluator, as shown in Figure 3.9.

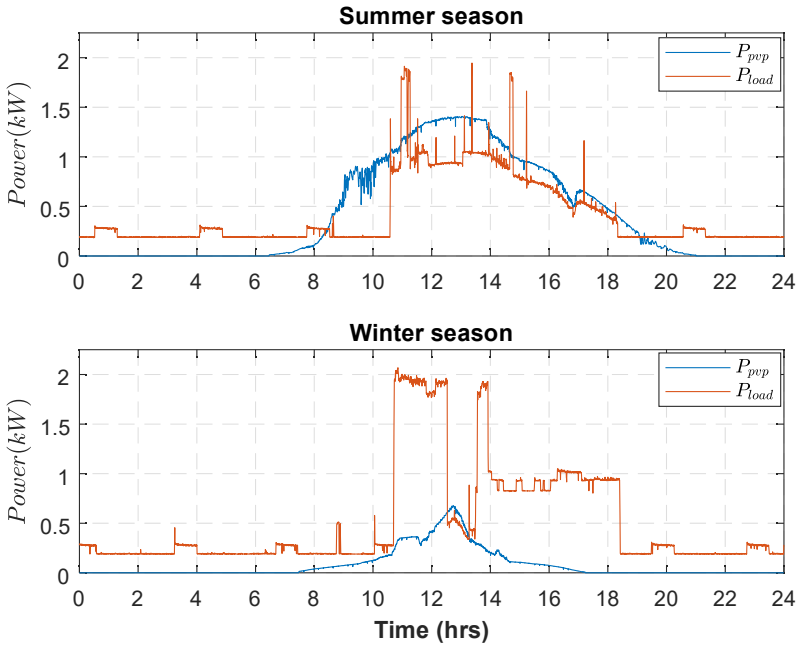

é

Figure 3.9: Power profile: (a) Summer season (b) Winter season.[3]

As can be seen in Figure 3.9. The difference between the generation power and the consumption power is small in the summer profile, but a larger dynamic is observed in the PV profile and in the load profile, due to the change of irradiance and the transient load effect. In the winter profile, the generation power is lower than the consumption power and a very large power difference between P_{pvp} and P_{load} is observed. This power difference is compensated by HESS, thanks to the local EMS control for the power balance in the HESS.

Hypothesis

Using the summer/winter profile as system input (i.e., power generation and load consumption), the following hypothesis is made to verify and evaluate the EMS.

A. Low pass filter parameters

For LPF, the angular frequency $\omega = 50$ rad/s is chosen for the power sharing between batteries and the supercapacitor. For vehicle applications this would be a very low frequency, but for residential applications it is quite a high frequency compared to the usual.

B. HESS initial parameters

The initial parameters such as SOC_B and SOC_{SC} have a great influence on the charging and discharging behavior of the battery and SC. To validate each case, the initial values for the battery & SC SOC are shown in Table 3.1.

At **level-1**, only SOC_B is considered to validate case 1 & case 2.

Table 3.1: HESS initial parameters.

Scenario	Actions	Battery initial SOC	SC initial SOC
Case 1	Power curtailment	90%	—
Case 2	Load shedding	20%	—
Case 3	Mutual charging (SC charge Battery)	20%	95%
Case 4	LPF control	$SOC_{VL} < SOC_B < SOC_{VH}$	$SOC_{VL} < SOC_{SC} < SOC_{VH}$
Case 5	Mutual charging (Battery charge SC)	90%	45%

Table 3.2: HESS sizing parameters.

	HESS	
Profile	**Battery**	**Supercapacitor**
Summer season	n = 2 (12.8V / 68Ah)	n = 1 (62.1V / 0.0043F)
Winter season	n = 8 (12.8V / 68Ah)	n = 1 (62.1V / 0.0043F)

In the case of power curtailment, the initial SOC_B is compared with the highest defined limit $SOC_{VH} = 90\%$ to realize the effect of power curtailment. If P_{pv} is greater than P_{load}, the power is curtailed.

In the case of load shedding, initial SOC_B is compared with the lowest defined limit $SOC_{VL} = 20\%$ to realize the effect of load shedding. When P_{pv} is less than P_{load}, load shedding is performed.

At **level 2**, initial SOC_B and SOC_{SC} are considered simultaneously to validate the remaining cases (case 3, case 4, case 5). Considering all these parameters, a comparison are made between the simulation results of the summer and winter profiles for a time horizon of 24 hours.

C. HESS sizing & cost parameters

An automatic optimization method has been developed to find an optimal size of the HESS. Automatic sizing is done in such a way that the HESS can store a maximum of energy with a minimum of surplus to provide the required energy whenever needed. To choose the right size of the HESS, battery sizing is done for a time horizon of 24 hours based on summer and winter profiles separately. SC sizing is done for a continuous high power demand as shown in Table 3.2.

Th input data-set (summer/winter) has different dynamics in terms of P_{pvp} and P_{load}. The difference between the generation power and the consumption power is small in the summer profile, while in the winter profile the generation power is lower than the consumption power and a very large power difference between P_{pvp} and P_{load} is observed. This power difference is compensated by HESS. Therefore, the number of batteries calculated for winter profile is more than summer profile which has a great impact on the cost function.

3.1.3 Simulation results based on EMS

The performance of the proposed EMS is verified by the self-developed system-level testbench evaluator for the 24-hour residential summer/winter profile. In order to validate each case, different time intervals were considered to represent the results in concentrated hours, as shown in the following subsections.

3.1.3.1 Case 1: PV curtailment

Case 1 deals with level-1 control, comparing P_{pvp} with P_{load}. For case 1, summer season profile is taken into an account for certain hours (11:30 hr – 15:00 hr) as shown in Figure 3.10.

In Figure 3.10, P_{pvp} and P_{load} are actual PV power and load power while P_{pvp*} and P_{load*} are regulated PV power and load power.

As can be seen in Figure 3.10, P_{pvp} is greater than P_{load}, SOC_B = 89.992% between (11:30 hr - t1), labeled as (A). During this time, the battery is in charging mode and SOC_B gradually increases until it reaches the highest limit (i.e., SOC_{VH} = 90%). At time t1, the battery has already reached its maximum limit, but the PV power is still higher than the load power. Therefore, the PV curtailment has been constrained to reduce the excessive PV power between (t1- t2), which is shown in the regulated power display. During the underlined time interval, the battery can not absorb further power. Therefore, excessive PV power must be curtailed until SOC_B is reduced to the normal range. After time t2, power reduction has stopped because SOC_B is below than the maximum value between (t2 - 15:00 hr) labeled as (B).

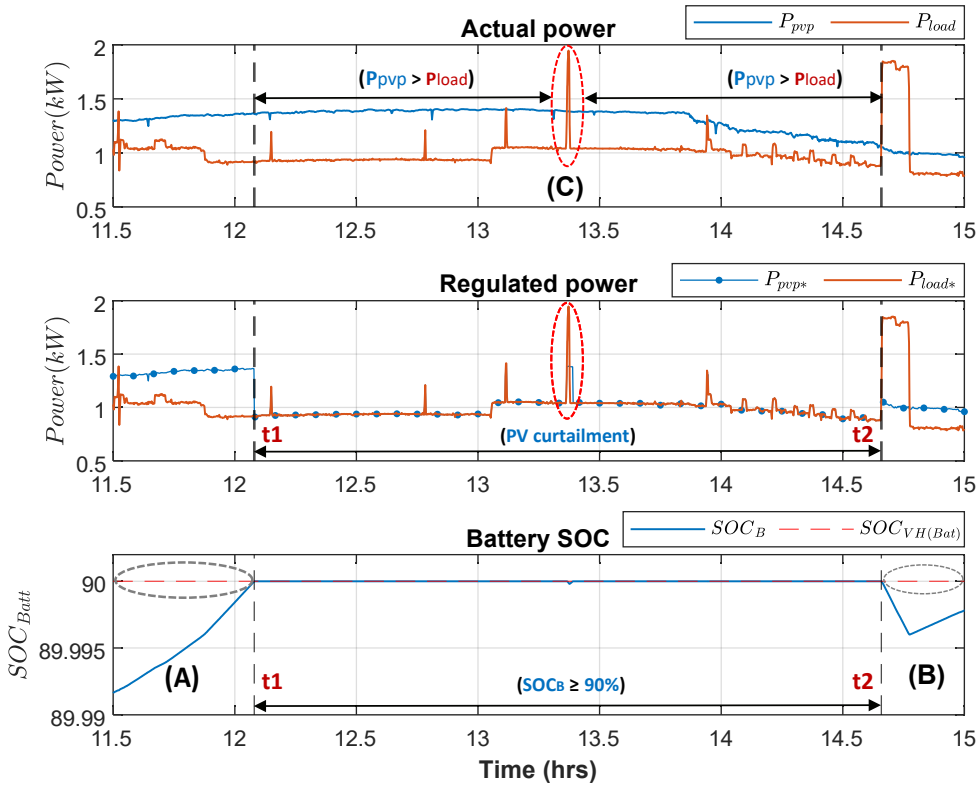

Figure 3.10: PV curtailment, case 1 (summer season).

In Figure 3.11, battery SOC is displayed to further illustrate the actual SOC_B at point (A) and (B). As can be observed in Figure 3.11, the battery is in charging mode between (11:30 hr - t1), and in discharging mode between (t2 - 15:00 hr). In both cases the SOC_B is less than the highest limit (i.e., SOC_{VH} = 90%), due to the fact that PV power is not regulated and curtailed during the time intervals (t1- t2). During the underlined time interval (t1- t2), the actual power displayed in Figure. 3.10 is labeled as (C), representing the highest peak in the summer season. The effect of this peak can be observed on battery SOC in Figure. 3.11.

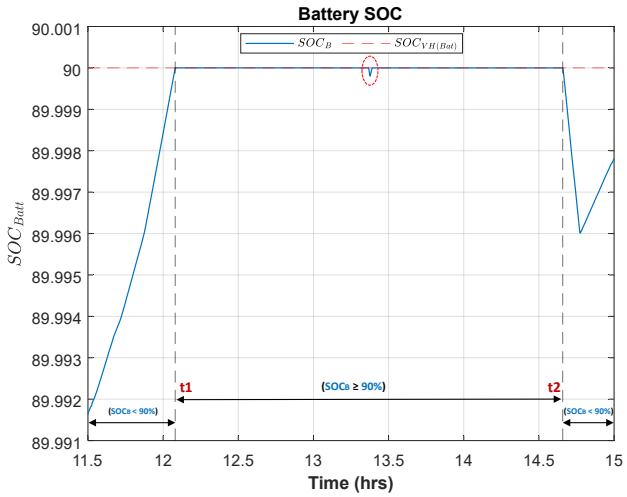

Figure 3.11: State of charge, case 1.

3.1.3.2 Case 2: Load shedding

Case 2 deals with level-1 control and compares P_{pvp} with P_{load}. For Case 2, the winter season profile is considered for certain hours (12:10 hr - 12:70 hr), as shown in Figure. 3.12.

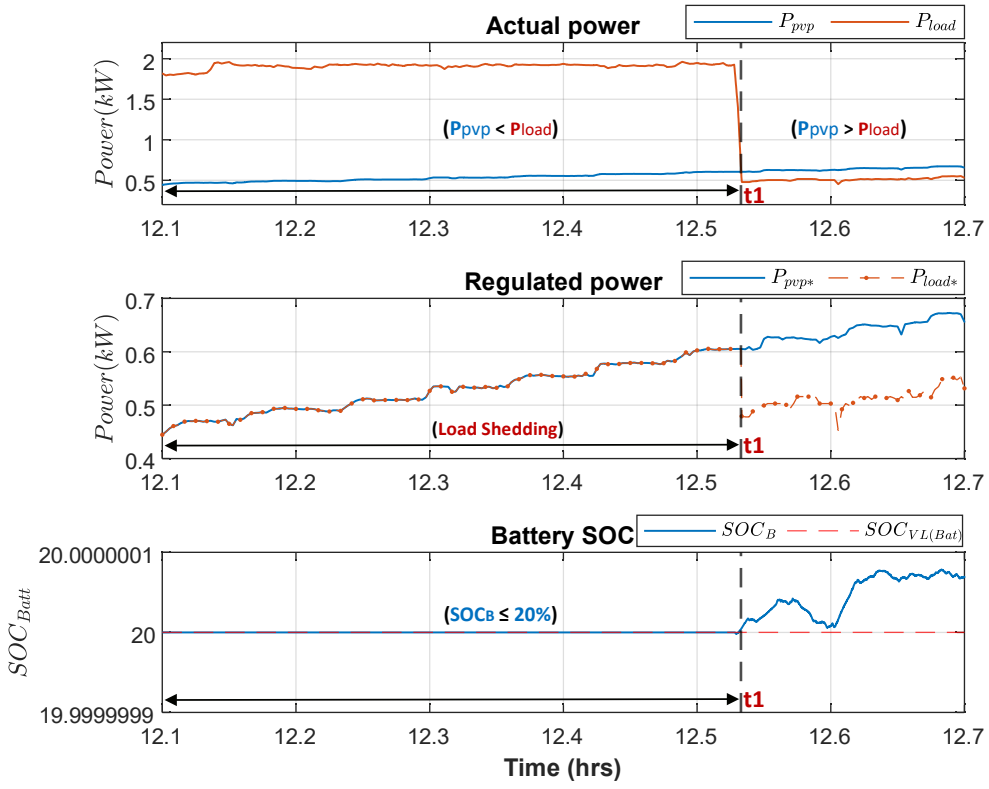

Figure 3.12: Load shedding, case 2 (winter season).

In Figure 3.12, P_{pvp} and P_{load} are the actual PV power and load power, while P_{pvp*} and P_{load*} are the regulated PV power and load power. As can be seen in Figure 3.12, P_{pvp} is initially smaller than P_{load} and $SOC_B = 20\%$ between (12:10 hr - t1). The battery is already at a very low level and cannot be discharged. Therefore, the only solution is to shut-down the load until the PV produces more power than the load needs, or SOC of the battery increased. For this reason, the load is reduced between (12:10 hr- t1) and follows the PV power shown in the regulated power display. Between the time (t1 - 12:70 hr), P_{pvp} is greater than P_{load}. There is no need to reduce the load, and the excess power is stored in the battery.

After time t1, the battery begins charging and battery SOC increases, as shown in Figure. 3.13.

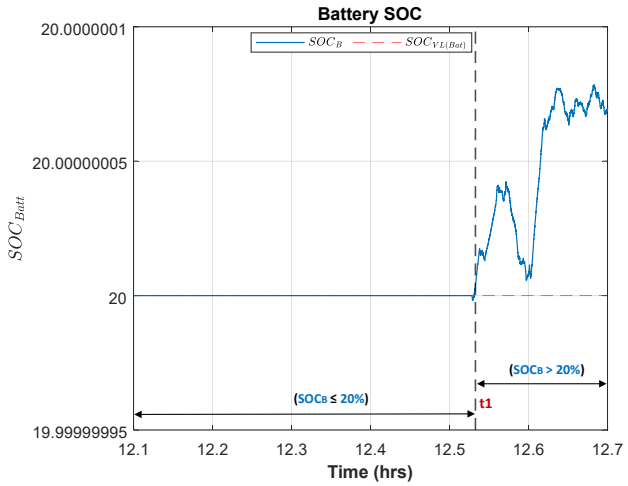

Figure 3.13: State of charge, case 2.

As can be observed in Figure 3.13, the battery SOC is at their lower charge limit by time t1 but after time t1 the battery is in charge mode because P_{pvp} is greater than P_{load} during this time.

3.1.3.3 Case 3 & 5: Mutual charging/discharging

Case 3 & 5 deals with level-2 control, which is about the mutual charging/discharging of the battery and SC. In both cases, HESS power distribution is performed to realize the power sharing between HESS according to the defined SOC limits as shown in Table 3.1.

The power distribution occurs to charge and discharge the battery and SC which is based on the reference power P_{ref} obtained by LPF.

In this process, the reference power (P_{ref}) can be positive or negative, which means;

- When P_{ref} is positive, it shows the discharge behavior of battery($+P_{ref}$).
- When P_{ref} is negative, it shows the charging behavior of battery ($-P_{ref}$).

In both cases, P_{ref} is compared with the initial power of HESS, and initial SOCs of HESS are compared with the defined SOC limits of the battery and SC simultaneously.

3.1.3.3.1 Case 3: SC charges battery To validate case 3, summer profile is taken into an account for specific hours between (8:30 hr – 11:00 hr) shown in Figure 3.14.

In case 3, the initial SOC of SC is set very high (i.e., $SOC_{VH} = 95\%$) and the battery SOC is comparatively low (i.e., $SOC_{VL} = 20\%$). At the beginning of the simulation, P_{Pvp} is lower than than P_{load} but by time t1 P_{Pvp} has increased by P_{load}. As a result, excessive power should be stored in battery and SC according to the defined conditions. In this case, SC is fully charged and can not absorb more power but release extra power to charge the battery. During the time interval (8:30 hr - t1), the HESS

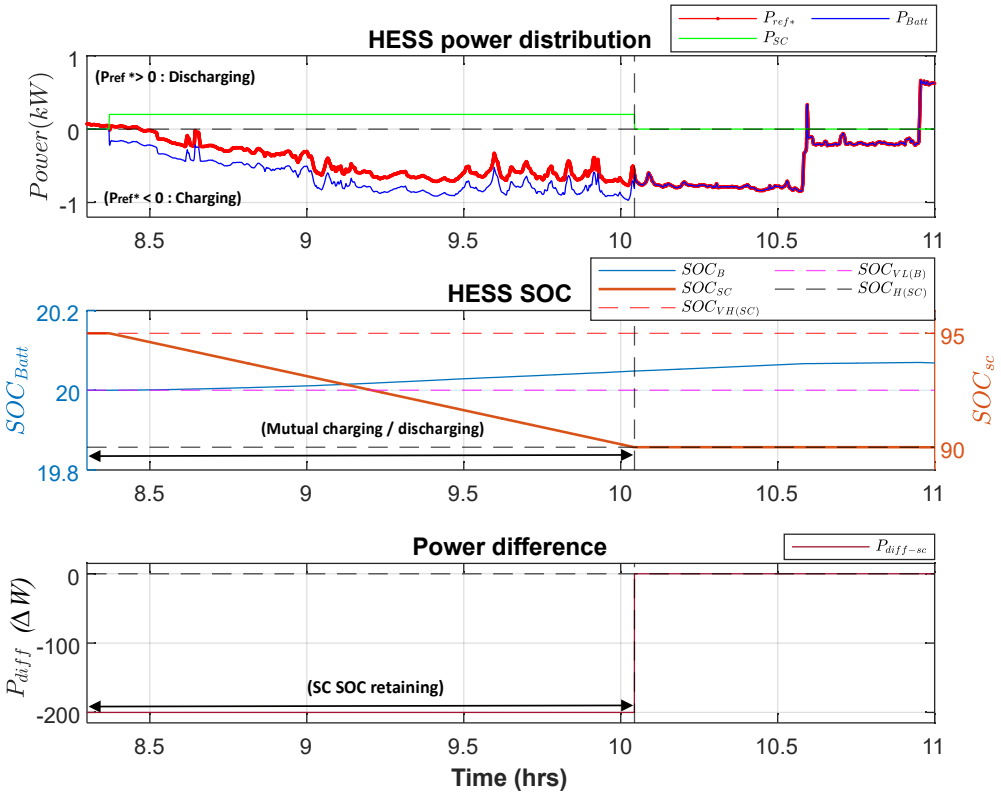

Figure 3.14: HESS power distribution, case 3 (summer season).

control strategy works which is based on the relay (R-1). As can be seen in HESS power distribution display, SC has started discharging and charges the battery until SC SOC reaches the high limit (i.e., $SOC_H = 90\%$).

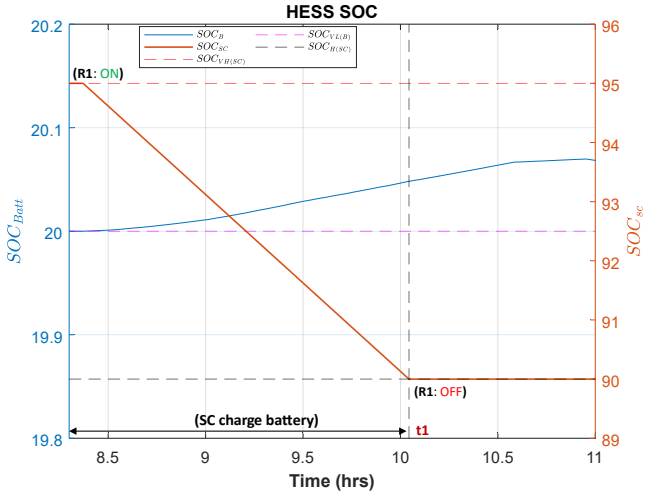

Figure 3.15: SC charges the battery

The mutual charging and discharging behaviour of HESS can be observed in Figure 3.15. At the start,

R-1 turns ON and power sharing strategy is activated to discharge the SC by supplying power ($-P_{diff}$) until SC SOC reaches to the high limit (i.e., $SOC_H = 90\%$). At time t1, R-1 turns OFF and power sharing strategy is terminated.

3.1.3.3.2 Case 5: Battery charges SC To verify case 5, winter profile is taken into an account for specific hours between (0:00 hr – 14:00 hr) shown in Figure 3.16.

In case 5, the initial SOC of battery is set very high (i.e., $SOC_{VH} = 90\%$) and the SC SOC is comparatively low (i.e., $SOC_{VL} = 45\%$). At the beginning of the simulation, P_{Pvp} is lower than than P_{load} and it gradually increases but is always less than the load power. In this case, battery is fully charged which is used to feed the load and also charge the SC at the same time until SC reaches the lower limit (i.e., $SOC_L = 80\%$). During the time interval (0:00 hr - t1), the HESS control strategy works, which is based on the relay (R-2). It works in ON/OFF mode which functions inversely to R-1. As can be seen in HESS power distribution display, battery has started discharging and charges the SC until SC SOC reaches the lower limit (i.e., $SOC_L = 80\%$).

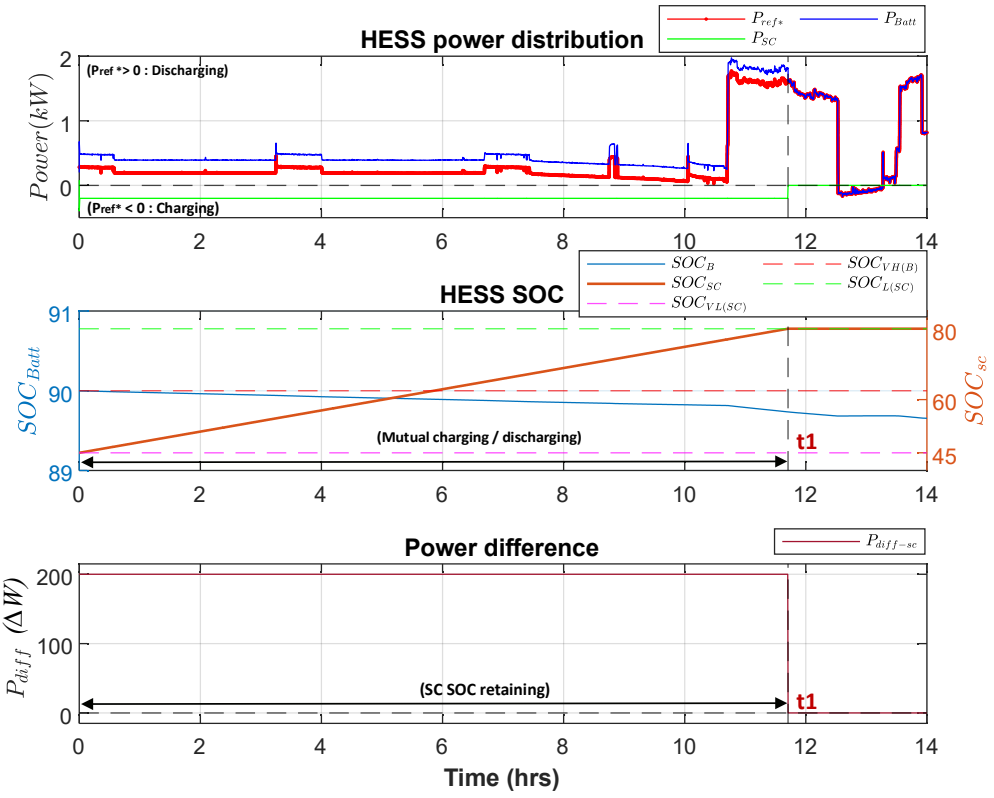

Figure 3.16: HESS power distribution, case 5 (winter season).

The mutual charging and discharging behaviour of HESS can be observed in Figure 3.17. At the start, R-2 is OFF and SC is continuously charged by taking power ($+P_{diff}$) and battery is discharged until SC SOC reaches to the lower limit (i.e., $SOC_L = 80\%$). At time t2, R-2 turns ON and power sharing strategy is terminated.

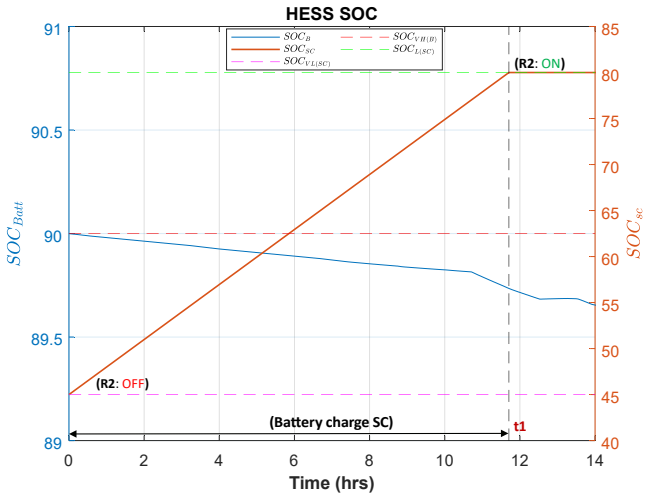

Figure 3.17: Battery charges the SC.

3.1.3.4 Case 4: LPF control

Case 4 can be verified when there is no mutual charging/discharging activated in case 3 & 5. This case is based on the LPF strategy. To study the effectiveness of LPF, HESS SOC must be in a normal range ($SOC_L < SOC_B < SOC_H$) & ($SOC_L < SOC_{SC} < SOC_H$).

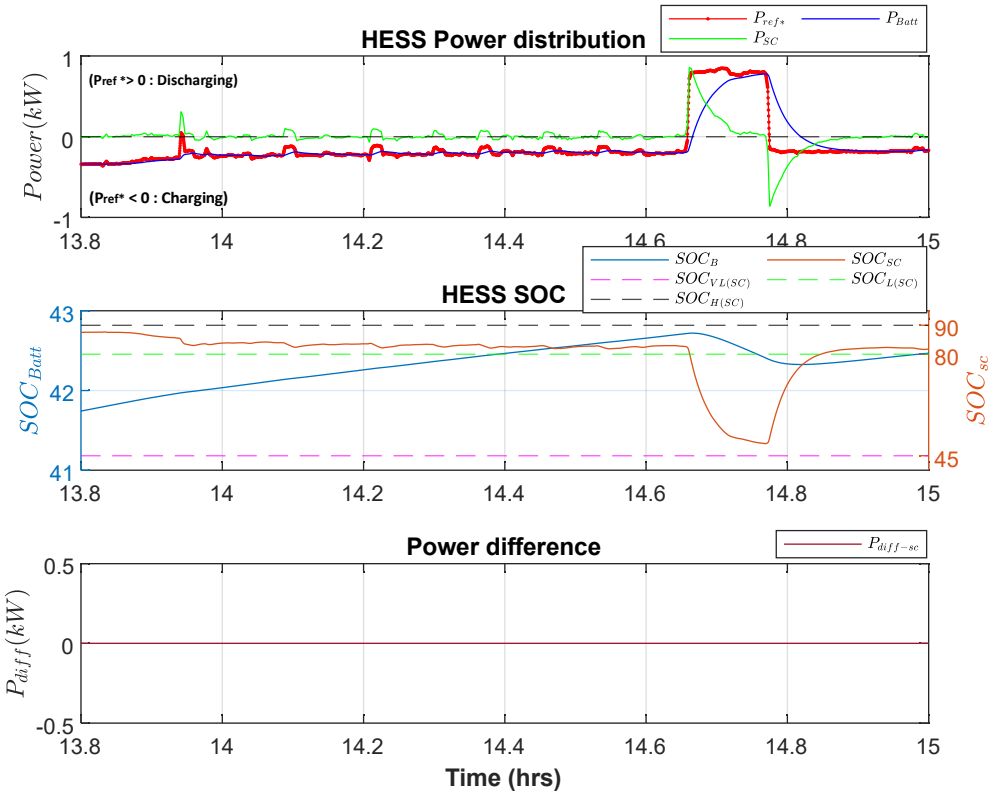

Figure 3.18: HESS power distribution, case 4 (summer season).

In case 4, the initial SOC of battery is set as (SOC_B = 40%) and initial SOC of SC is set as (SOC_{SC} = 80%). Based on the LPF method, the power distribution between battery and SC is realized between (13:80 hr – 15:00 hr) shown in Figure 3.18.

As can be observed from the HESS power distribution results, the reference power P_{ref} is divided into low-frequency and high-frequency parts. The high-frequency part is offered by the SC, and the low-frequency part is smoothed by the battery. In this case, the battery and SC are charged and discharged independently because both elements' SOC are in the normal range and case 4 works well without triggering a mutual charging/discharging process as shown in Figure 3.19.

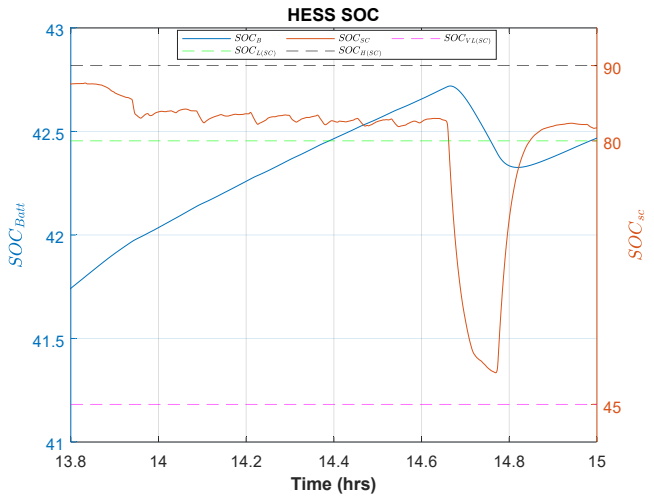

Figure 3.19: LPF effect on state of charge

Different values of angular frequency ω have been tested to study the effect of LPF on SOC variations of battery and SC. After comparison, an appropriate value for ω is chosen (i.e., ω = 50 rad/sec) . This allows both HESS elements to operate over a wider range of SOC, which can significantly reduce the size of the HESS and also improve its operating efficiency.

3.1.4 Cost function evaluation

The calculation of the cost function is performed for HESS and only-battery case. Few assumptions are made to evaluate the cost function, such as the choice of profile (summer, winter or summer + winter) and the initial SOC for battery and SC.

For the cost function evaluation, a 24-hour winter profile is chosen as shown in Figure.3.20.

In the winter season, the generation power is lower than the consumption power and a very large power difference between P_{pvp} and P_{load} is observed.

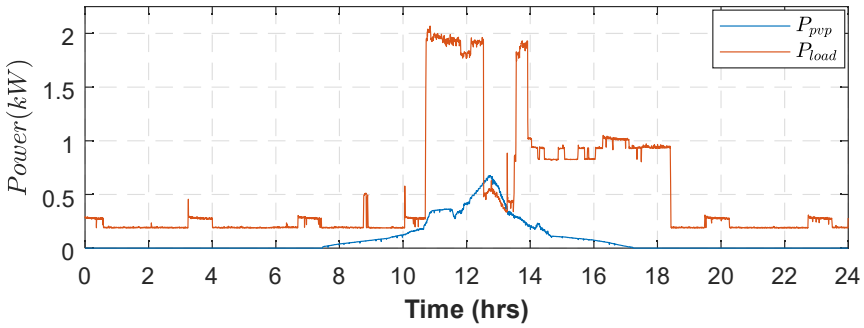

Figure 3.20: 24-hours winter profile

This power difference is compensated by the storage system (SS), which ultimately affects the cost of SS. For the cost calculation, two different scenarios with different cases are considered to evaluate the cost with respect to the following SOC limits given in the Table 3.3.

Table 3.3: Cost function evaluation parameters

Case	**only-battery**	**HESS**	
	SOC_B	SOC_B	SOC_{SC}
Scenario 1	VL = 20%	VL = 20%	VL = 45%
Scenario 2	VH = 90%	VH = 90%	VH = 95%
Scenario 3	Normal = 55%	Normal = 55%	Normal = 70%

For the selected profile, curtailed PV energy and shedded energy is evaluated separately, in the battery case and in the HESS case. In each case, the cost function is evaluated separately with respect to the initial SOC of the battery and SC as defined in the above Table 3.3.

A: Only-Battery case

In only-battery case, the curtailed energy and shedded energy are calculated according to the curtailed power and shedded power for different scenarios (Scenario 1, Scenario 2, Scenario 3) defined in Table 3.3.

In **scenario 1**, the SOC_B is set very low (VL = 20%). In this case, PV curtailment is always zero and no curtailed power or curtailed energy is recorded, but load shedding occurs when P_{load} is greater than P_{pvp} . As a result, the shedded power and the shedded energy is recorded, as shown in Figure. 3.21.

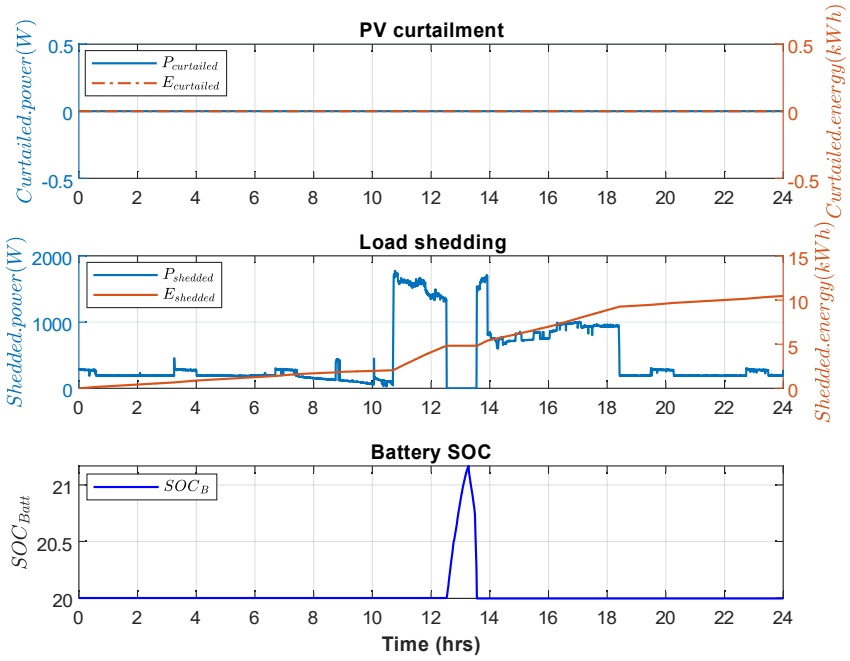

Figure 3.21: Curtailed PV energy & shedded energy, only-battery scenario 1.

In **scenario 2**, the SOC_B is set very high (VH = 90%). In this case, PV curtailment is zero because P_{load} is greater than P_{pvp} and the load is compensated by the battery. During this time no shedded energy or power is recorded but after 12:00 hrs the shedded power and energy is recorded because the SOC_B reach to its lower limit, as shown in Figure. 3.22.

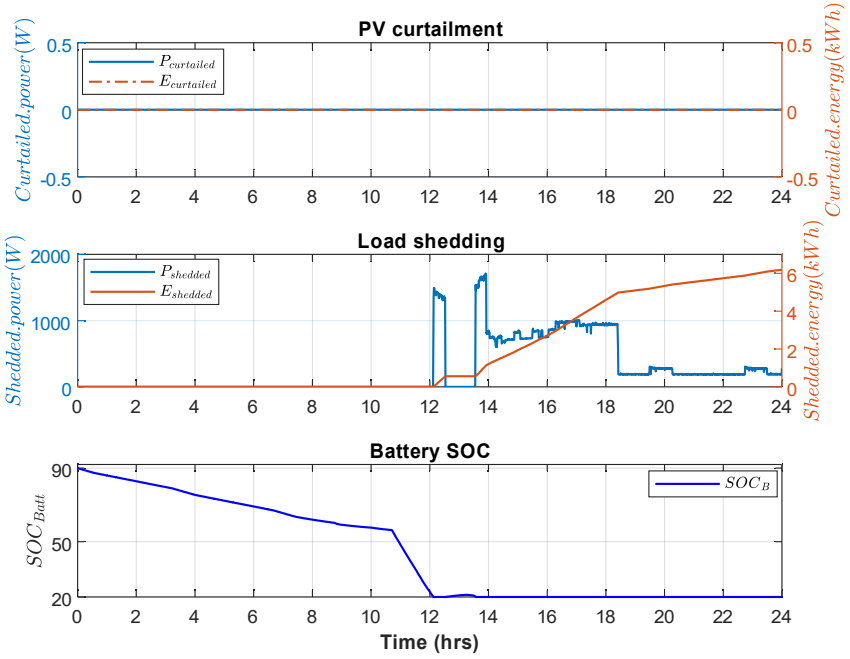

Figure 3.22: Curtailed PV energy & shedded energy, only-battery scenario 2.

Scenario 3 is quite similar to scenario 2 in terms of PV curtailment and load shedding. In this case, the SOC_B is set to a normal range (Normal = 55%) to realize the effect on curtailment power and load shedding. As shown in Figure. 3.23, the PV curtailment is always zero but load shedding is activated after 12:00 hrs when SOC_B reach to its lower limit. In this case shedded power and energy is recorded, just like in scenario 2.

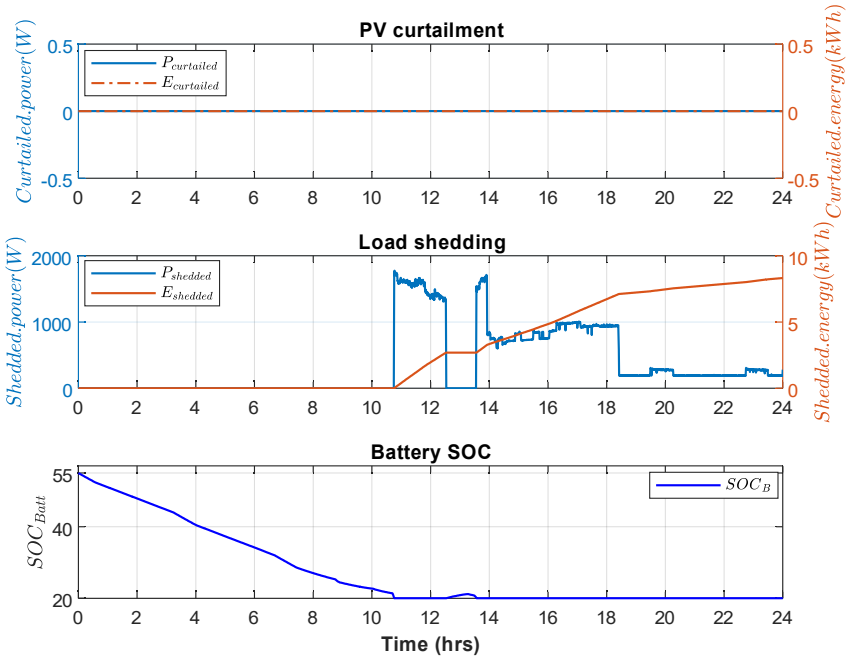

Figure 3.23: Curtailed PV energy & shedded energy, only-battery scenario 3.

B: HESS case

As in the case of only-battery, the curtailed energy and shedded energy are calculated according to the curtailed power and shedded power for different scenarios (Scenario 1, Scenario 2, Scenario 3) for HESS. In this case the initial SOC_B battery and SC are defined for each scenario shown in Table 3.3.

In **scenario 1**, the initial SOC_B battery and SC is set very low (SOC_B = 20%, SOC_{SC} = 45%). In this case, no curtailed power or curtailed energy is recorded, but load shedding occurs when P_{load} is greater than P_{pvp} . As a result, the shedded power and the shedded energy is recorded, as shown in Figure. 3.24.

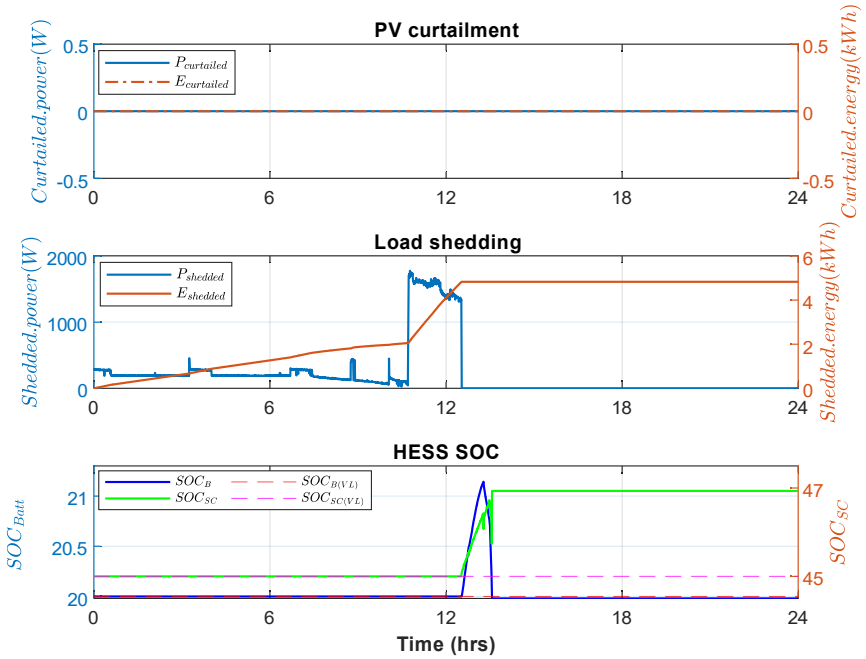

Figure 3.24: Curtailed PV energy & shedded energy, HESS scenario 1.

In **scenario 2**, the initial SOC_B battery and SC is set very high ($SOC_B = 90\%$, $SOC_{SC} = 95\%$). In this case, neither PV curtailment nor load shedding occurs. Because in the start of simulation, P_{load} is greater than P_{pvp} and the power difference is compensated by the battery and SC together. As can be seen in the results, the SOC of battery and SC is continuously declining.

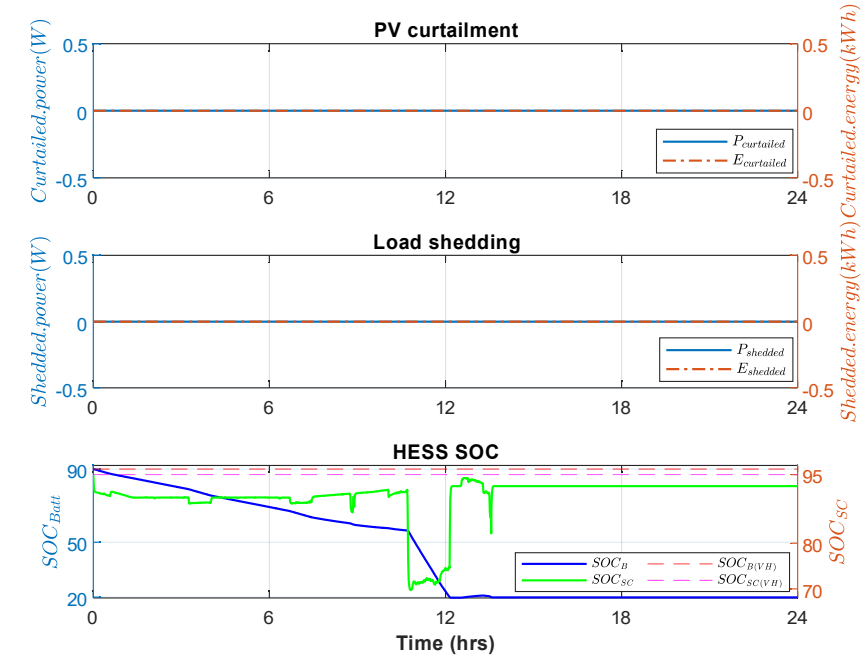

Figure 3.25: Curtailed PV energy & shedded energy, HESS scenario 2.

Scenario 3 is quite similar to scenario 2 in terms of PV curtailment and load shedding. In this case, the initial SOC_B battery and SC is set to a normal range ($SOC_B = 55\%$, $SOC_{SC} = 70\%$) to realize the effect on curtailment power and load shedding. As shown in Figure. 3.26, no PV curtailment or load shedding occurs in this case because when P_{load} is greater than P_{pvp} the SOC of HESS is in a normal range and the power difference is compensated by HESS. Similarly when P_{load} is less then than P_{pvp} the SOC of HESS is at their lower limits. In both situation,no power curtailment and no power shedding is recorded which means the battery and SC are continuously in charging and discharging mode by mutual charging/discharging process and this is the main interest of using HESS.

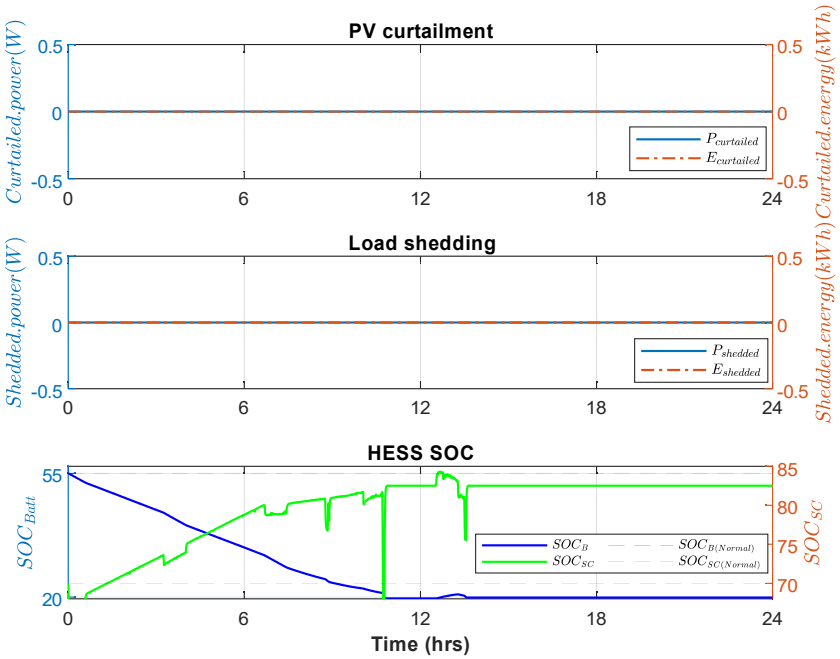

Figure 3.26: Curtailed PV energy & shedded energy, HESS scenario 3.

Based on the above results from both cases, it can be concluded that the initial SOC of each element has a large impact on the curtailed power/energy and shedded power/energy recorded in the PV curtailment and load shedding results in only-battery case or in HESS case. This also affects the PV curtailment cost and load shedding cost, which are analyzed in more detail in the next section.

3.1.4.1 Cost evaluation of the battery

In this case, only-battery configuration is considered for the cost evaluation with respect to three different value of initial SOC_B defined for each scenario respectively as shown in Figures 3.27 (A), 3.28 (A), 3.29 (A) only-battery case.

In following figure OPEX is evaluated for only-battery case, which is directly related to the penalization cost and degradation cost of the battery. As can be observed from the results, each scenario captures the penalty cost and degradation cost different than others due to the SOC_B .

A general comparison among three scenarios has been made to calculate OPEX as a function of penalty costs and degradation costs. Among these three scenarios, scenario 2 has less OPEX, which is due to the low penalty cost.

3.1.4.2 Cost evaluation of the HESS

In this case, HESS is considered for the cost evaluation with respect to initial SOC_B and SOC_{SC} defined for each scenario respectively. Same like only-battery case, OPEX is evaluated for HESS which is directly related to the penalization cost and degradation cost of the battery and SC together as shown in Figure Figures 3.27(B), 3.28(B), 3.29(B) HESS case.

In the case of HESS, the penalty cost is only recorded when the initial SOC_B and SOC_{SC} are very low, which corresponds to scenario 1. In scenario 2 & scenario 3, the penalty cost is zero because SOC limits of the battery and SC are above then the lower range. Due to the fact, neither PV curtailment nor load shedding occurs in this case.

A general comparison among three scenarios has been made to evaluate OPEX as a function of penalty costs and degradation costs. Among these three scenarios, scenario 3 recorded less OPEX in HESS case , which is due to the normal range of SOC of battery and SC.

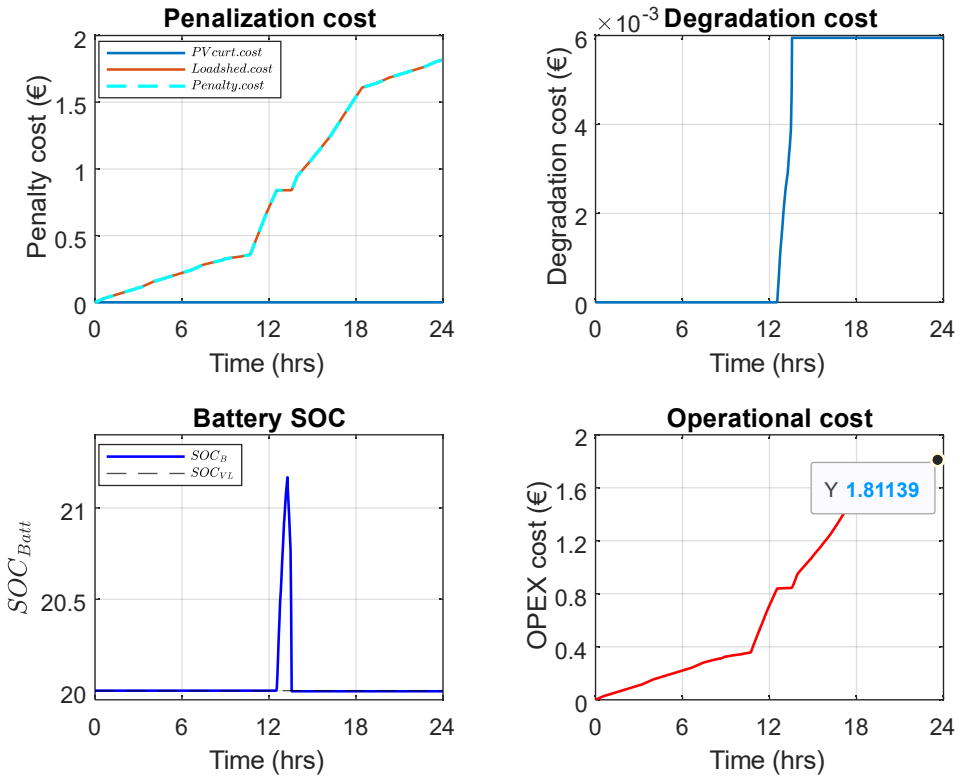

(A) *Only- battery, Scenario 1*

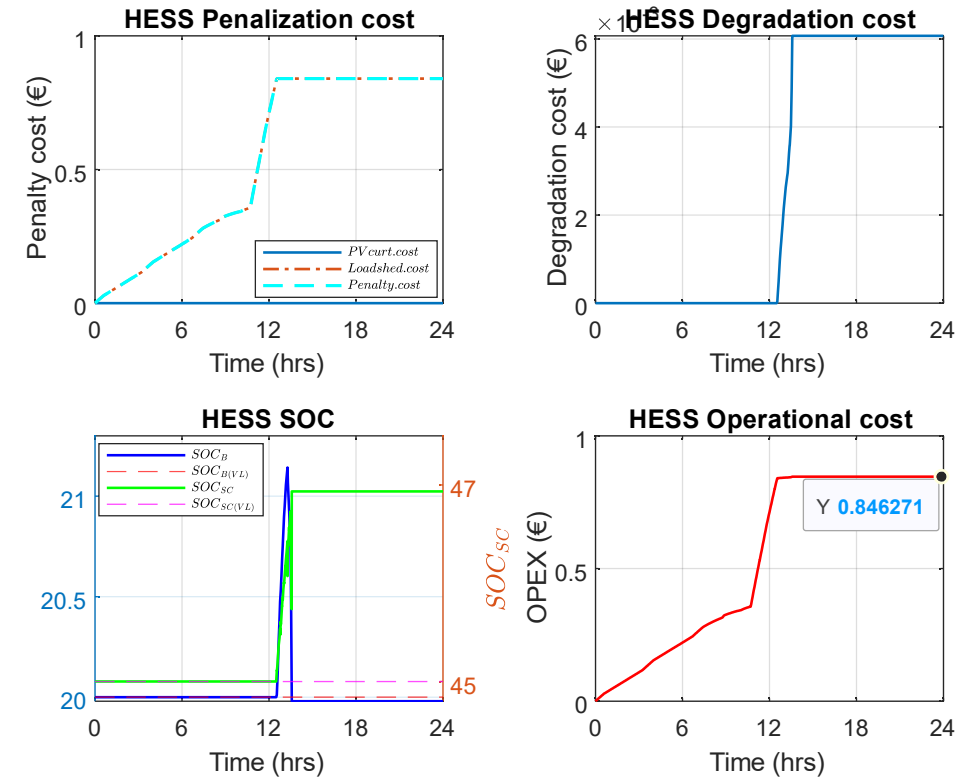

(B) *HESS, Scenario 1*

Figure 3.27: OPEX comparison (VL); **(A)** Only-battery case, **(B)** HESS case.

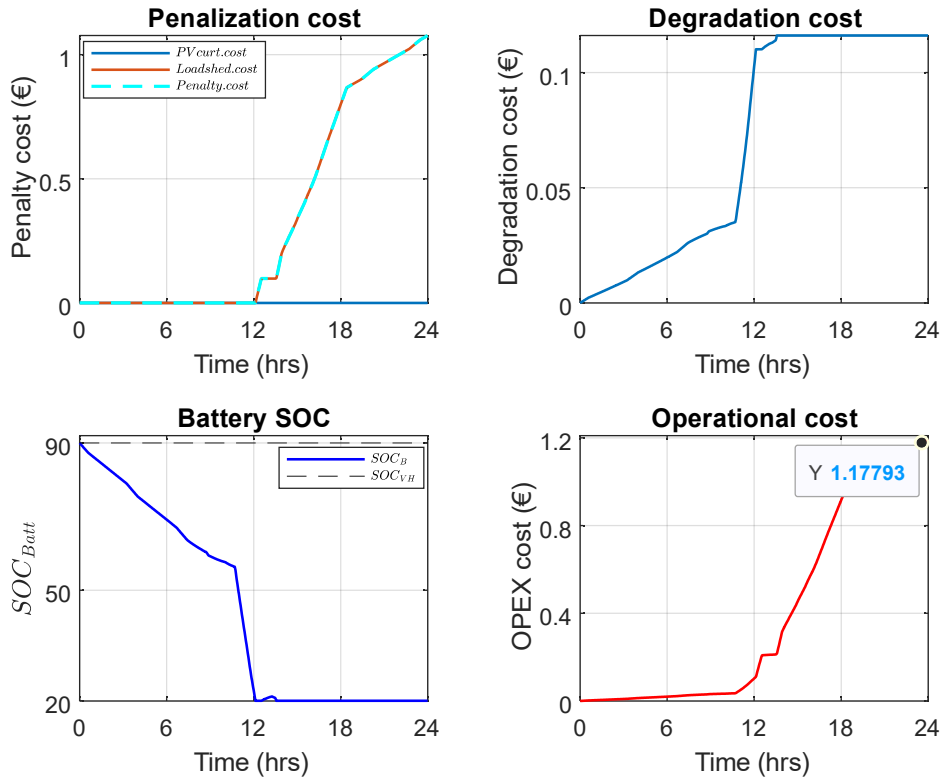

(A) Only- battery, Scenario 2

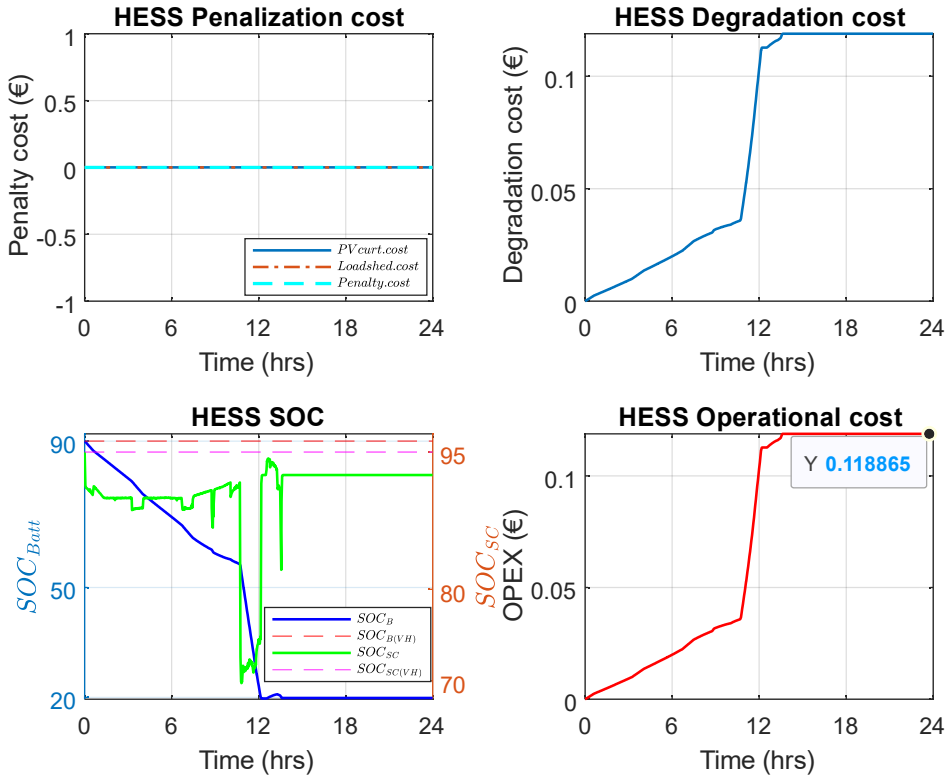

(B) HESS, Scenario 2

Figure 3.28: OPEX comparison (VH); **(A)** Only-battery case, **(B)** HESS case.

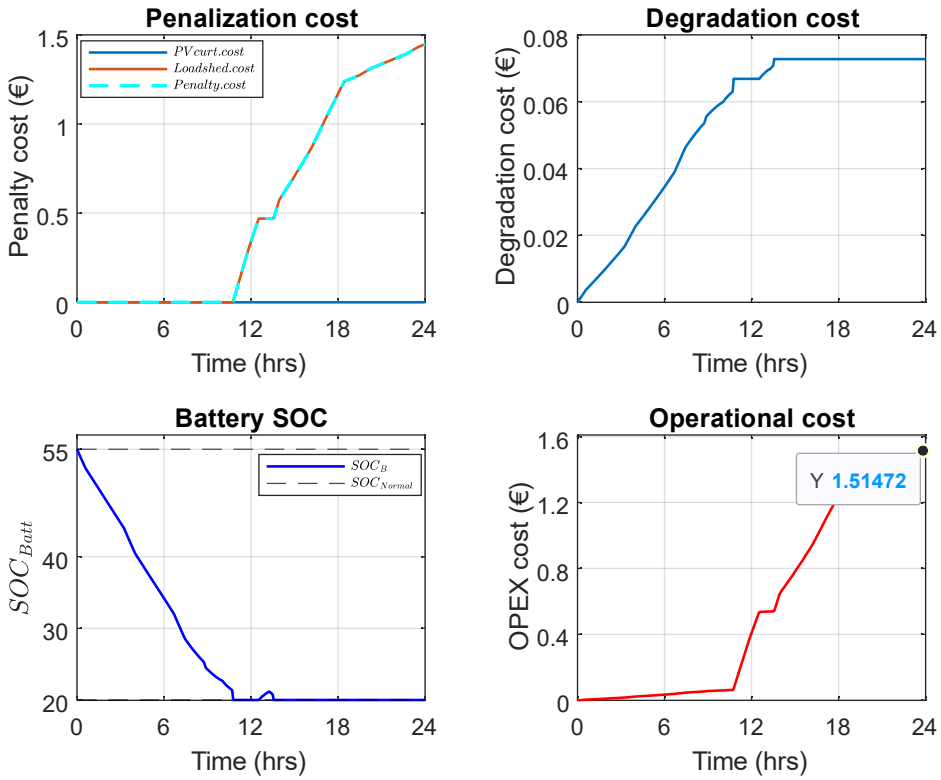

(A) *Only- battery, Scenario 3*

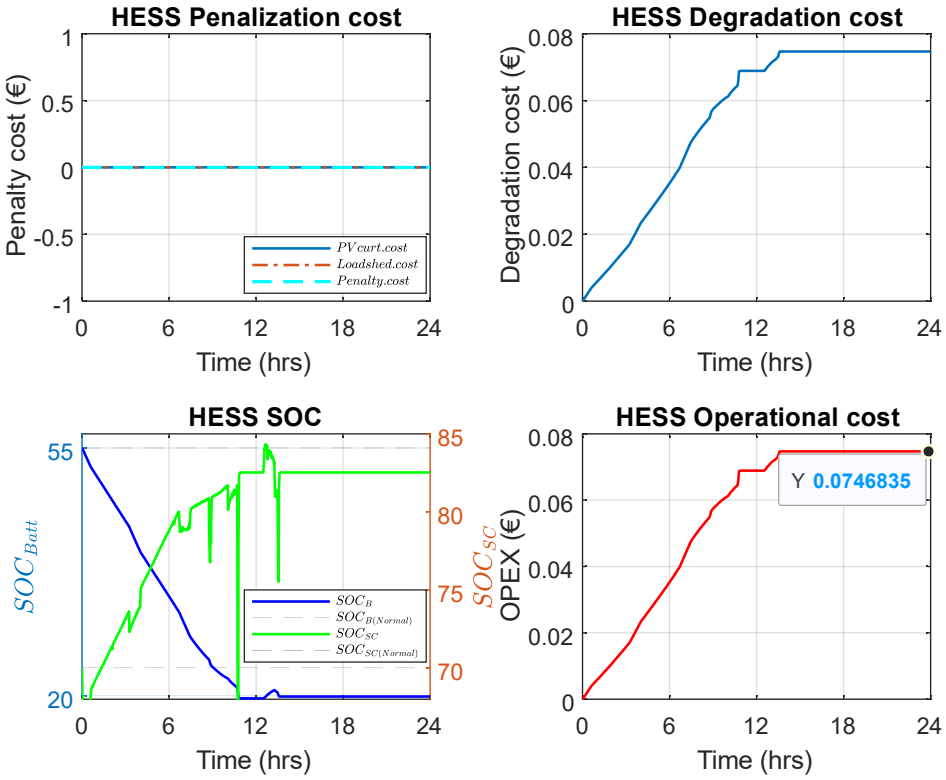

(B) *HESS, Scenario 3*

Figure 3.29: OPEX comparison (Normal); **(A)** Only-battery case, **(B)** HESS case.

Cost function comparison

As mentioned earlier, **OPEX** is related to the energy management of the system which is associated with the degradation costs and the penalty cost. OPEX comparison is made between only-battery case and HESS case and results of each scenario is presented in the form of histogram shown in Figure 3.30.

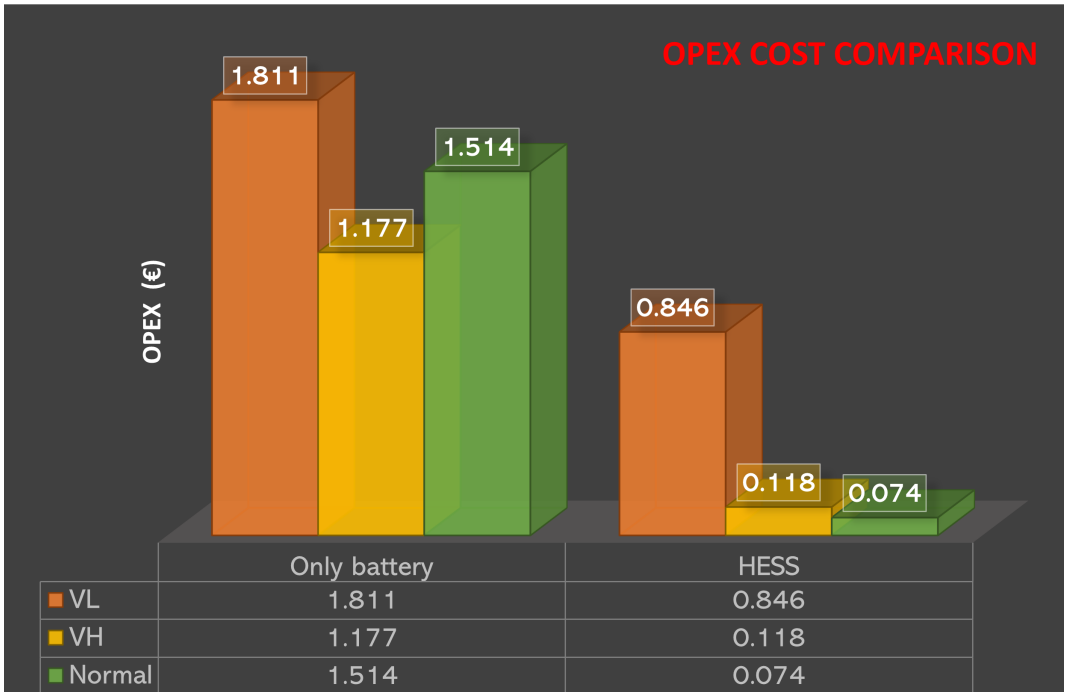

Figure 3.30: OPEX cost.

Based on the results presented above, the following analysis has been conducted in terms of percentage comparison between the only-battery case and the HESS case.

Scenario 1 (VL & VL):
only-battery (1.811 €) vs HESS (0.846 €) Only-battery has 1.4 times higher cost than HESS case.

Scenario 2 (VH & VH):
only-battery (1.177 €) vs HESS (0.118 €) Only-battery has 9 times higher cost than HESS case.

Scenario 3 (Normal & Normal):
only-battery (1.514 €) vs HESS (0.074 €) Only-battery has 20 times higher cost than HESS case.

CAPEX relates to the sizing of system and it has been deduced with respect to the calculated number of batteries and SC for a known set of profile. In this study 24 hours winter profile is considered and the capital cost is calculated while considering the number of batteries (n=8, 12V/68Ah) and SC (n=1, 62V/0.0043F), accordingly as shown in Table 3.4.

The hybrid energy storage system (HESS) case exhibits slightly higher capital expenditure (CAPEX) compared to the only-battery case due to the additional cost of the supercapacitor (SC). CAPEX isn't shown in the histogram charts because it's not on the same level as operating expenditure (OPEX). We calculate CAPEX by considering component lifespan from the literature, which is typically 20 years, and then calculate it cumulatively for 24 hours as shown in Table 3.4.

Table 3.4: CAPEX cost.

	only-battery	**HESS**
CAPEX (20 years)	1218 €	1235 €
CAPEX (24h)	0.167 €	0.281 €

Total cost
Total cost comprises of capital cost (CAPEX) and operational cost (OPEX), which is expressed as:

$$J = CAPEX + OPEX$$

Table 3.5: Total cost comparison.

	Only-battery		**HESS**	
Scenrio	**OPEX + CAPEX**	**Total €**	**OPEX + CAPEX**	**Total €**
VL	1.811 + 0.167	1.977	0.846 + 0.281	1.127
VH	1.177 + 0.167	1.343	0.118 + 0.281	0.399
Normal	1.514 + 0.167	1.680	0.074 + 0.281	0.355

In both cases, CAPEX remains constant, while OPEX varies depending on initial conditions like the state of charge (SOC) of the battery and SC.

A quantitative comparison has been conducted between the standalone battery case and the HESS. Upon comparing the costs in both scenarios, it's clear that the HESS case has lower operating costs compared to the standalone battery case. Consequently, the HESS is recommended as a more favorable solution when compared to using only a battery for storage.

Conclusion

Chapter 3 provides a global overview of the DC MG platform integrated with EMS. A simulation platform is developed that includes the bi-level control scheme for analyzing, monitoring, and controlling power generation, distribution, and load consumption at the system level.

An EMS testbench evaluator is introduced to validate the bi-level control strategy. An enhanced energy management strategy (Filtration-based EMS + Rule-based EMS) is explained and validated with the testbench evaluator. The testbench evaluator is very useful for system-level control at very low computation time. It works efficiently for both short-term and long-term simulations.

The proposed EMS consists of two levels (Level-1 & Level-2) with five different cases. Level-1 deals with PV curtailment and load shedding scenarios, while Level-2 is based on low-pass filter, which is very useful to distribute power between the battery and SC. By introducing a local EMS control for HESS, not only the SOC regulation is performed, but also the power is exchanged between battery and SC to get equilibrium charge and discharge of each element. A hysteresis SOC control strategy has been introduced to regulate the SOC of SC.

An automatic sizing method has been developed to determine the optimal sizes of the battery and SC in a hybrid energy storage system. The battery sizing is performed for a 24-hour time horizon using summer and winter profiles, while the SC is sized to meet continuous high power demand. It should be noted that the same LPF utilized in the EMS was utilized in the sizing phase to share the power difference between batteries and SC.

A cost function is then considered to calculate the OPEX and CAPEX of the HESS. The costs are compared with the only-battery case, taking into account degradation costs and penalty costs. In both cases, the CAPEX remains fixed, while the OPEX varies depending on the initial conditions, such as the SOC of the battery and SC. Upon comparing the costs of each scenario between the only-battery and HESS cases, it becomes evident that the HESS case incurs lower operating costs compared to the only-battery case. Therefore, the HESS is recommended as a more favorable solution, both economically and in terms of battery durability.

Chapter 4

Experimental validation of the developed EMS

This chapter introduces the experimental platform with its modeling and control. Developed EMS is tested and validated scenario by scenario on the designed experimental platform, which is explained in more detail below.

4.1 Development of an experimental platform

An experimental platform of the DC microgrid system has been developed in the laboratory. The platform consists of a programmable PV simulator power supply, an electronic load, HESS, corresponding DC/DC converters, and a real-time controller. This experimental setup allows the real-time validation of the different operating scenarios of the developed EMS. Figure 4.1 gives a general overview of the experimental platform. A more detailed platform schema with component connections is shown in Figure 4.2.

A programmable PV simulator (Chroma 62020H-150S) is used to emulate PV generation profiles. This simulator can easily program the parameters such as, $(V_{oc}, I_{sc}, V_{mp}, I_{mp})$ to simulate the $(I-V)$ characteristics of different solar cell materials with fast response time. This equipment can also be applied to simulate real weather conditions including different irradiance and temperature levels and partial shading effects. In this experimental setup, the analog programming interface (APG) mode was utilized to program the PV generation profiles.

In the experimental platform, an electronic load (Electro-Automatik EA-EL-9750-50) provides four typical operational modes, including constant current (CC), constant power (CP), constant resistance (CR) and constant voltage (CV). In this setup, an external control mode based on APG was configured and the CR mode was selected for easiness of system control.

The HESS contains a battery bank (consisting of 4 lithium-ion batteries connected in series) and a SC, which is connected in parallel with the battery bank by two individual buck-boost converters within a nominal operating voltage of 62 V.

A multi-function power converter stack (SEMIKRON SEMITEACH IGBT) serves as two bidirectional converters which connect the HESS to the integrated DC bus. It can either operate in boost mode (discharging) or buck mode (charging) depending on the control mode delivered by the EMS controller.

This controller included in the experimental platform is a dSPACE MicroLabBox real-time controller. The developed EMS was implemented herein together with a control interface. It collects voltage and current signals from the platform and generates control signals to the corresponding converters, the programmable PV simulator, and the electronic load.

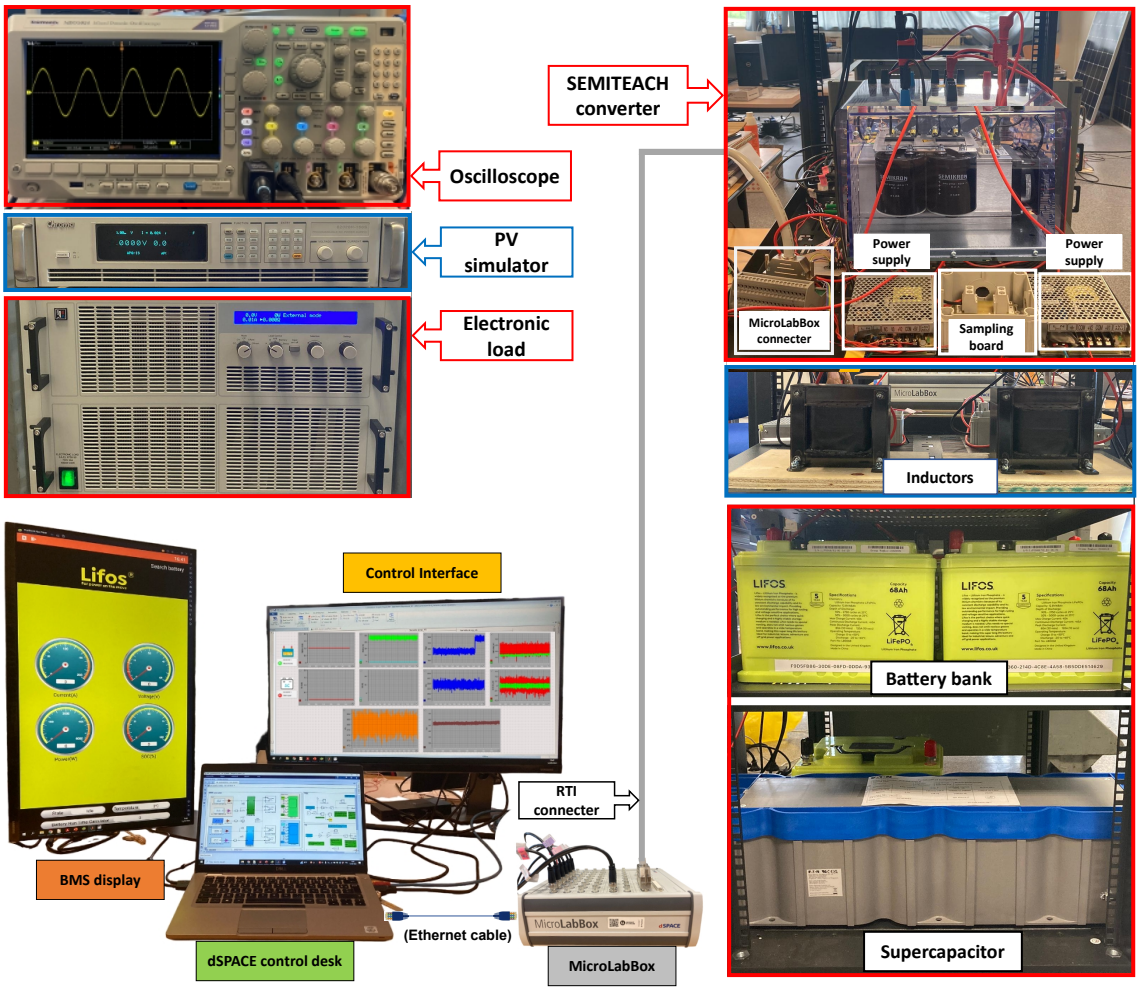

Figure 4.1: DC microgrid experimental platform

A real-time platform is based on the dSPACE MicroLabBox DS1202, which is used as a PWM generator to drive the converter by controlling IGBTs from top and bottom legs separately. A voltage shifter $(5V - 15V)$ was utilized to adapt the voltage levels between the MicroLabBox control signals and SEMITEACH converter driving signals. MicroLabBox consists of 100 channels for input/output signals that can be configured as analog, digital, or PWM signals. In the designed setup, two channels are used for digital to analogue **(DAC)** signals and five channels are used for analogue to digital **(ADC)** signals as shown in the hardware configuration, Figure 4.2.

In **DAC** signals, ch-1 is used for remote CR control of electronic load as indicated by (R_{com}) and ch-2 for remote CC control of programmable PV simulator as indicated by (I_{com}).

In **ADC** signals, ch-1, ch-2 are assigned for the battery measurement (I_b, V_b) , ch-3 are assigned for measuring the bus voltage (V_L), ch-4, ch-5 are assigned for SC measurement (I_{sc}, V_{sc}), with the help of corresponding sampling board (SB-1, SB-3 and SB-2)).

MicroLabBox DS1202 supports the Real-Time Interface (RTI), which allows fast and automatic generation of c-code, and has easy interaction with the developed the simulink procedure. The DS1202 is managed via control desk, software from dSPACE that collects, displays the acquired data, and delivers

the generation and load commands in real time, as shown in host computer connected via an ethernet cable. The HESS consists of a battery bank and SC connected to the converter stack. A separate inductor is used in series with the battery and SC.

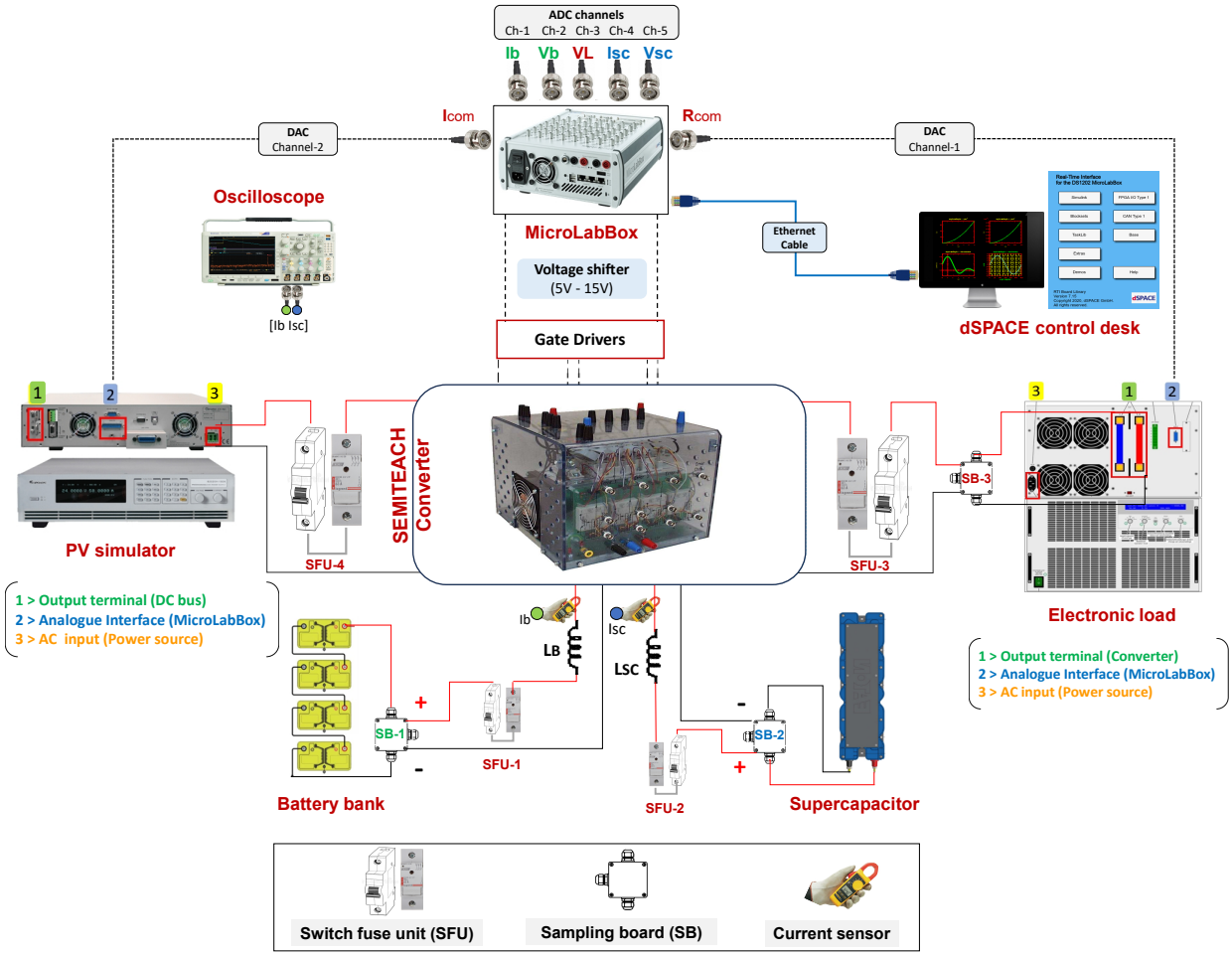

Figure 4.2: Hardware system configuration

Three sampling boards are used in the hardware configuration: (SB -1) between the battery and the converter, (SB -2) between SC and the converter, and (SB -3) between the electronic load and the converter. The purpose of using three sampling boards is to measure data from the battery (I_b, V_b), SC (I_{sc}, V_{sc}), and the load (V_L) via ADC channels connected to the MicroLabBox. Each element such as battery, SC, electronic load is protected by separate switch-fuse units (SFU-1, SFU-2, SFU-3). An additional SFU-4 is used between the PV simulator and the converter to control the generation part. The oscilloscope can't only measure the current but also measure the voltage of battery and SC using voltage probes and current sensors. In this setup, V_b is not measured by the oscilloscope, since it has relative small variations and the number is limited to 4 channels.

Table 4.1: Hardware system parameters

Element	Description	Technical specification
PV simulator	Chroma 62020H-150S	Output current: 40A max Output voltage: 150V max Output power: 2kW max
Electronic load	Electro-Automatik EL-9750-50	Input voltage: 750V max Input current: 50A max Nominal power: 4.8 kW max
MicroLabbox	dSPACE DS1202	Input/output voltage: -10-10V Output current: ± 8mA
SEMITEACH IGBT	SEMIKRON	Input/output current: 30A max DC bus voltage: 750V max
Battery	LiFOS - 68	Nominal voltage: 12.8V Nominal capacity: 68Ah
Supercapacitor	XLM - 62R1137A	Nominal voltage: 62.1V Nominal capacity: 130F

4.2 EMS experimental validation based on a 48V DC bus

The proposed EMS has been initially verified in the testbench evaluator developed under MATLAB/simulink and simulation results were introduced and analyzed in chapter 3. In this chapter the same EMS is validated on the real experimental platform (only one of the four batteries is connected) based on the following initial SOC levels shown in Table 4.1.

Table 4.2: HESS initial SOC configurations

Scenario	Actions	Battery SOC	SC SOC
Case 1	Power curtailment	25 % (self-defined for accelerated test)	—
Case 2	Load shedding	22 % (self-defined for accelerated test)	—
Case 3	Mutual charging (SC charge Battery)	$SOC_B < SOC_{SC}$	$SOC_H = 70\%$ $SOC_{VH} = 90\%$
Case 4	LPF control	$SOC_{VL} < SOC_B < SOC_{VH}$	$SOC_{VL} < SOC_{SC} < SOC_{VH}$
Case 5	Mutual charging (Battery charge SC)	$SOC_B > SOC_{SC}$	$SOC_L = 50\%$ $SOC_{VL} = 30\%$

The HESS initial SOC levels for experimentation validation was configured slightly different than the simulation validation in terms of SOC limits for HESS. The consideration is to facilitate an accelerated test of different operating scenarios and a switch between them. The bus voltage for the experimental validation was initially set to be $V_{ref} = 48V$, with a single battery and a SC as HESS.

At **level-1**, only SOC_B is considered to validate case 1 & case 2.

In the case of power curtailment , actual SOC_B is compared with the highest defined limit $SOC_{VH} = 25\%$ to realize the effect of power curtailment. When P_{pv} is greater than P_{load} , the power is curtailed.

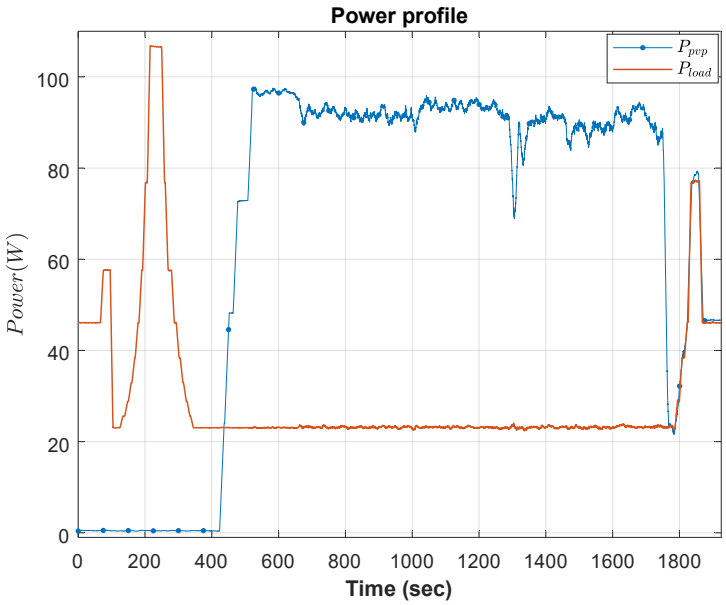

Figure 4.3: Self-defined power profile.

In the case of load shedding, actual SOC_B is compared with the lowest defined limit $SOC_{VL} = 22\%$ to realize the effect of load shedding. When P_{pv} is less than P_{load}, load shedding is performed.

At **level-2**, the actual SOC_B and SOC_{SC} are considered simultaneously to validate the other three cases (case 3, case 4, case 5).

Considering all these initial SOC settings, EMS was validated on the experimental setup and the results for each case are presented in the following subsections.

4.2.1 Case 1: PV curtailment

The validation of case 1 on the experimental setup is done by comparing the PV power (P_{pvp}) determined by the PV simulator and load profiles (P_{load}) determined by the controllable electronic load as shown in Figure 4.3.

In case 1, the SOC_B is compared with the highest defined limit (i.e., $SOC_{VH} = 25\%$). To observe the change in power profile with respect to the battery SOC , a specific time period ($1700sec - 1800sec$) is selected, as shown in Figure.4.4.

In the chosen time period, P_{pvp} is greater than P_{load} and $SOC_B < 25\%$ until time t1. During this time, the battery is in charging mode and SOC_B gradually increases until it reaches the highest limit. At time t1, the battery has already reached its maximum limit, but the PV power is still higher than the load power. Therefore, the PV curtailment occurs and P_{pvp} follows P_{load} to reduce the excessive power between ($t1 - 1900sec$). During the underlined time interval, the battery can not absorb more power. Therefore, excessive PV power must be curtailed until SOC_B is reduced to the normal range.

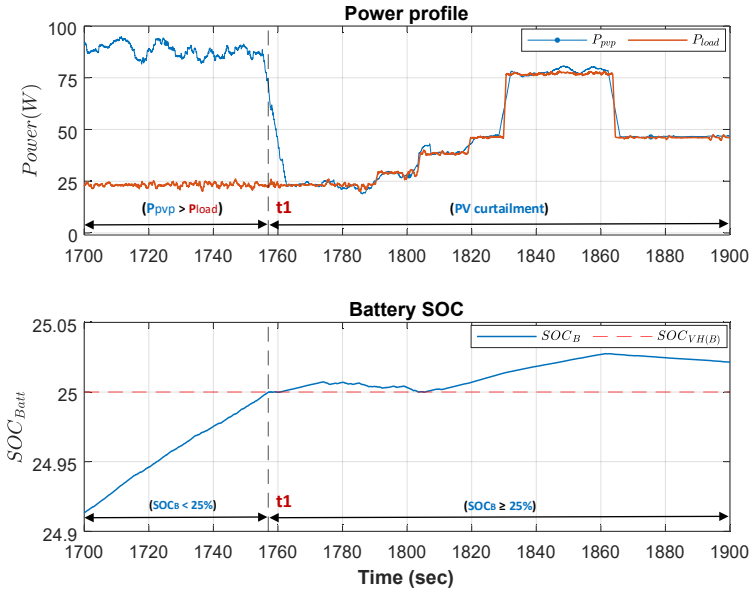

Figure 4.4: PV curtailment, case 1.

4.2.2 Case 2: Load shedding

As in case 1, case 2 is validated by comparing the PV power (P_{pvp}) determined by the PV simulator with the load profiles (P_{load}) determined by the controllable electronic load, which behave dynamically differently from case 1, as shown in Figure. 4.5.

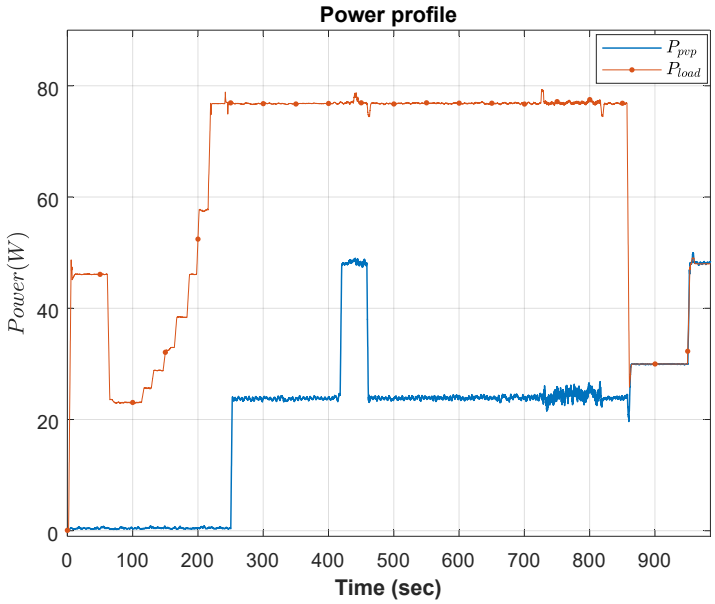

Figure 4.5: Self-defined power profile.

To validate case 2, the SOC_B is compared with the lowest defined limit (i.e., $SOC_{VL} = 22\%$). To observe the change in power profile with respect to the battery SOC , a specific time period ($800sec - 985sec$) is selected, as shown in Figure.4.6.

As can be seen in Figure. 4.6, P_{pvp} is initially smaller than P_{load} and $SOC_B > 22\%$ until time t1. During this time, the battery is in discharging mode and SOC_B gradually decreases until it reaches the lowest limit. At time t1, the battery has already reached at very low level and cannot be discharged. Therefore, the only solution is to shut-down the load until the PV produces more power than the load needs, or SOC of the battery increases. For this reason, the load is reduced between $(t1 - 985sec)$ and follows the PV power shown in Figure. 4.6.

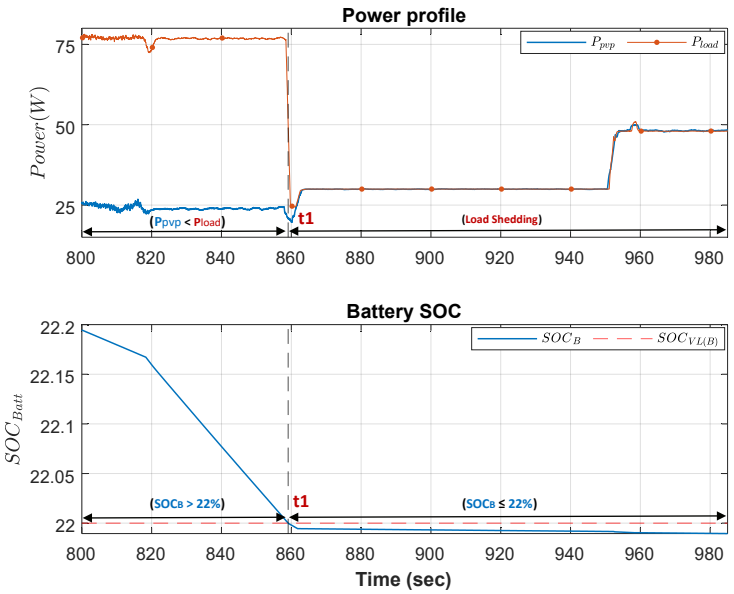

Figure 4.6: Load shedding, case 2.

4.2.3 Cases 3 & 5: Mutual charging/discharging

Case 3 & 5 are about mutual charging/discharging between battery and SC. In both cases, the current distribution between the battery and SC was done according to the SOC limits defined in Table 4.1.

The charging/discharging of the battery and SC is based on the reference current (I_{ref}) determined by **LPF**, which is further distributed as the battery current reference $I_{Batt.ref}$ and SC current reference $I_{SC.ref}$.

In this process, the reference current (I_{ref}) can be positive or negative, which means;

- When I_{ref} is positive, it shows the discharge behavior ($+I_{ref}$).
- When I_{ref} is negative, it shows the charging behavior ($-I_{ref}$).

In both cases, I_{ref} is compared with the initial current and the actual SOC of HESS is compared with the defined SOC limits of the battery and SC simultaneously.

4.2.3.1 Case 3: SC charges battery

To validate the case 3, two dynamic power profiles of P_{pvp} and P_{load} are configured, as shown in the Figure 4.7.

The dynamic behaviors of the power generation and load consumption profiles are achieved by programming different values of power supply current command (I_{comm}) and load command (R_{comm}). To observe the influence of the individual inputs on the power profile and the bus voltage, a specific time period $(10sec - 82sec)$ is selected, as shown in Figure. 4.8.

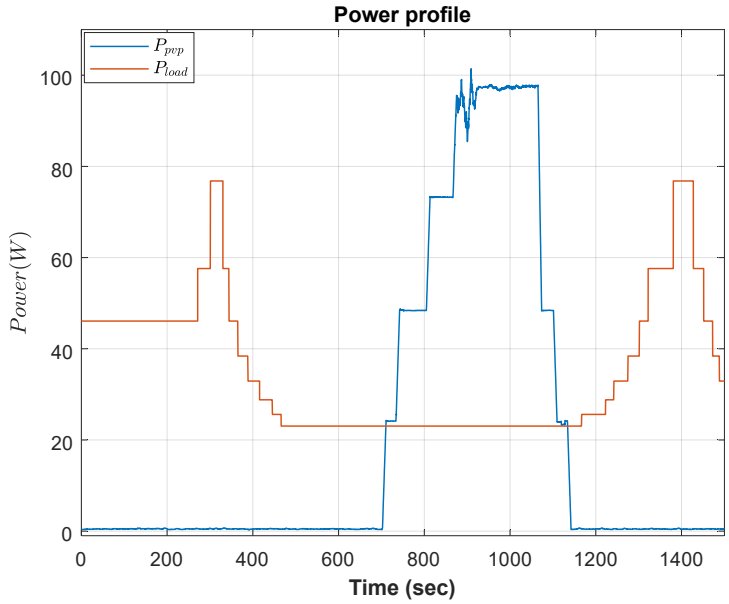

Figure 4.7: Self-defined power profile.

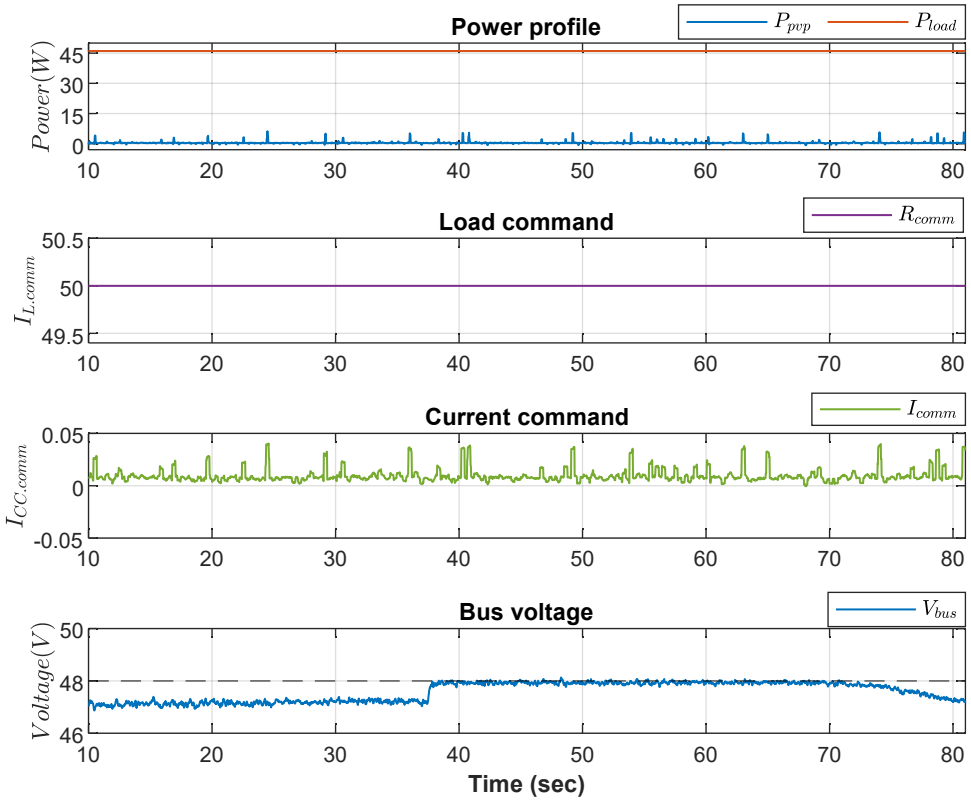

Figure 4.8: Power profile & bus voltage, case 3.

As can be seen in the results, a constant load was set during this time ($R_{comm} = 50\Omega$) and the power

supply current was also set to zero ($I_{comm} = 0A$). Therefore, there is a constant positive power difference between P_{load} and P_{pvp}. As for the DC bus voltage, it follows the reference voltage with a quick dynamic and high tracking precision (around 1V deviation) despite the switch of the operating scenarios during the selected time period.

The current distribution between battery and SC with their SOC levels, together with the retaining control of SC SOC are displayed in Figure 4.9. In case 3, SC SOC is set higher than the battery SOC and SC SOC limits are defined as ($SOC_H = 70\%, SOC_{VH} = 90\%$) which is useful to activate the SOC retaining control strategy by delivering the power difference (P_{diff}).

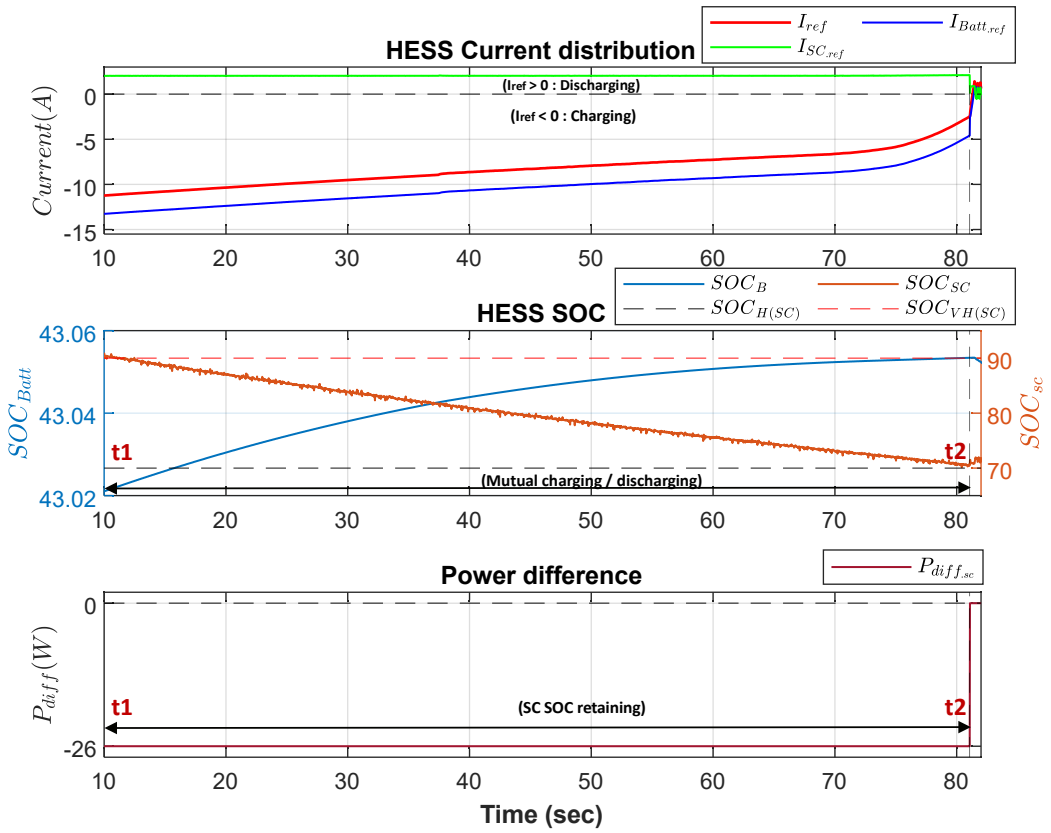

Figure 4.9: HESS current distribution, case 3.

In Figure 4.10, the charging and discharging behavior of battery and SC can be observed within the time period ($t1 - t2$). In the HESS current distribution display, the reference current (I_{ref}) is distributed between battery $I_{Batt,ref}$ and $I_{SC,ref}$. During this time period, SC current reference $I_{SC,ref}$ is positive while the battery current reference $I_{Batt,ref}$ is negative. This means that SC is in discharging mode while the battery is in charging mode. In this case, SC charges the battery with the mutual charge/discharge process. During the time period ($t1 - t2$), SC SOC retaining control strategy is activated, relay ($R - 1$) turns **ON** to discharge SC by supplying power ($P_{diff} = -26W$) until SC SOC reaches its lower limit ($SOC_H = 70\%$). Following SC SOC retaining control scheme, the specific amount of power is calculated (20% of total battery power ; i-e. $P_{diff} = -26W$). At time ($t2$), the relay ($R - 1$) turns **OFF** and the power sharing strategy is terminated shown in Figure 4.10.

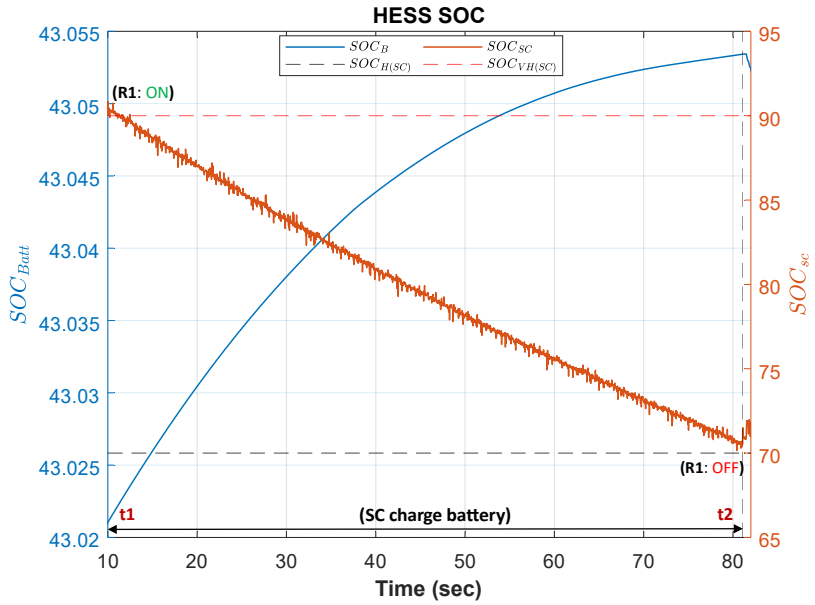

Figure 4.10: SC charges the battery.

4.2.3.2 Case 5: Battery charges SC

As in case 3, a self-defined power profiles (P_{pvp}, P_{load}) are utilized to validate the case 5, as shown in Figure 4.11.

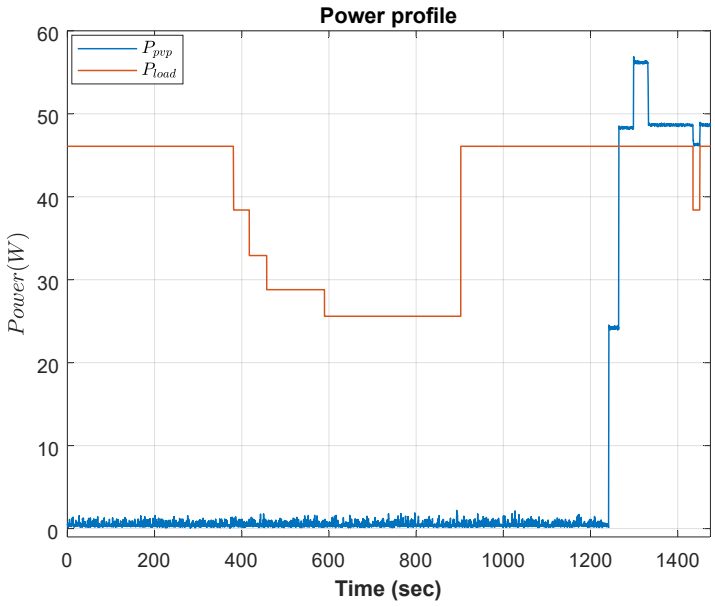

Figure 4.11: Self-defined power profile.

The dynamic behavior of the power profile is different in case 5, as the values of power supply current command (I_{comm}) and the electronic load command (R_{comm}) are set differently to cover more dynamic changes. In the following power profile, a certain time period ($350sec - 760sec$) is selected to study the effect of load and current on bus voltage stability shown in Figure 4.12.

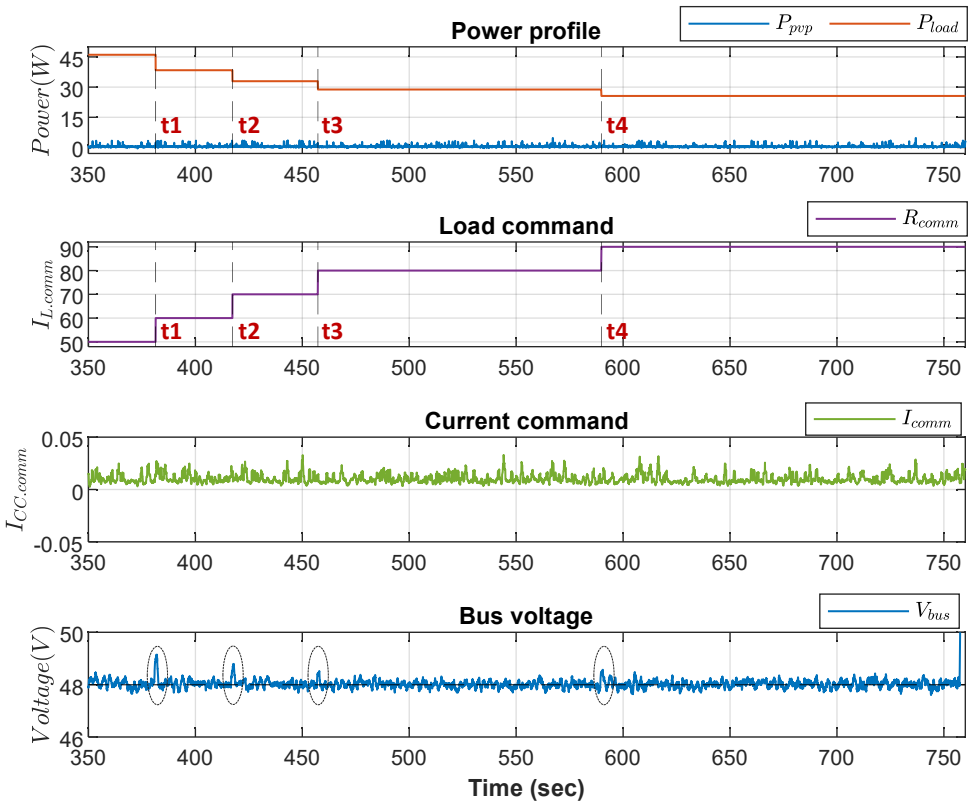

Figure 4.12: Power profile & bus voltage, case 5.

In the chosen time period, the change in load power (P_{load}) at different time points ($t1, t2, t3, t4$) can be observed, shown in Figure. 4.12. The change in (P_{load}) is due to the different input values of (R_{comm}) at certain time points. This change also affects the bus voltage at a the specific time points , which is circled in the bus voltage display, but is always in a stable range.

Based on the following power profile, the dynamic behavior of the battery and SC also changes in terms of charging and discharging. Figure 4.13 shows the current distribution between the battery and SC with the mutual charging/discharging process of the HESS. The whole process is based on the SOC retaining control strategy controlled by relay (R-2), respecting the SC SOC limits defined in case 5 ($SOC_L = 50\%, SOC_{VL} = 30\%$).

In Figure 4.14, time period ($t1 - t2$) is enlarged to observe the mutual charging and discharging behavior between the battery and SC. In the HESS current distribution display, the reference current (I_{ref}) is distributed between battery current reference $I_{Batt.ref}$ and SC current reference $I_{SC.ref}$. During this time period, SC current reference $I_{SC.ref}$ is negative and the battery current reference $I_{Batt.ref}$ is positive. This means that SC is in charging mode while the battery is in discharging mode. In case 5, SC SOC is set lower than the battery SOC and SC SOC limits are defined as ($SOC_L = 50\%$, $SOC_{VL} = 30\%$) which is configured to activate the SOC retaining control strategy by delivering the power difference (P_{diff}). During the time (t1 - t2) SC SOC retaining control strategy works, relay (R-2) turns **ON** to discharge battery by supplying power ($P_{diff} = +26W$) until SC SOC reaches the lower limit ($SOC_L = 50\%$). At time ($t2$), the relay ($R-2$) turns **OFF** and the power sharing strategy is terminated as shown in Figure 4.10.

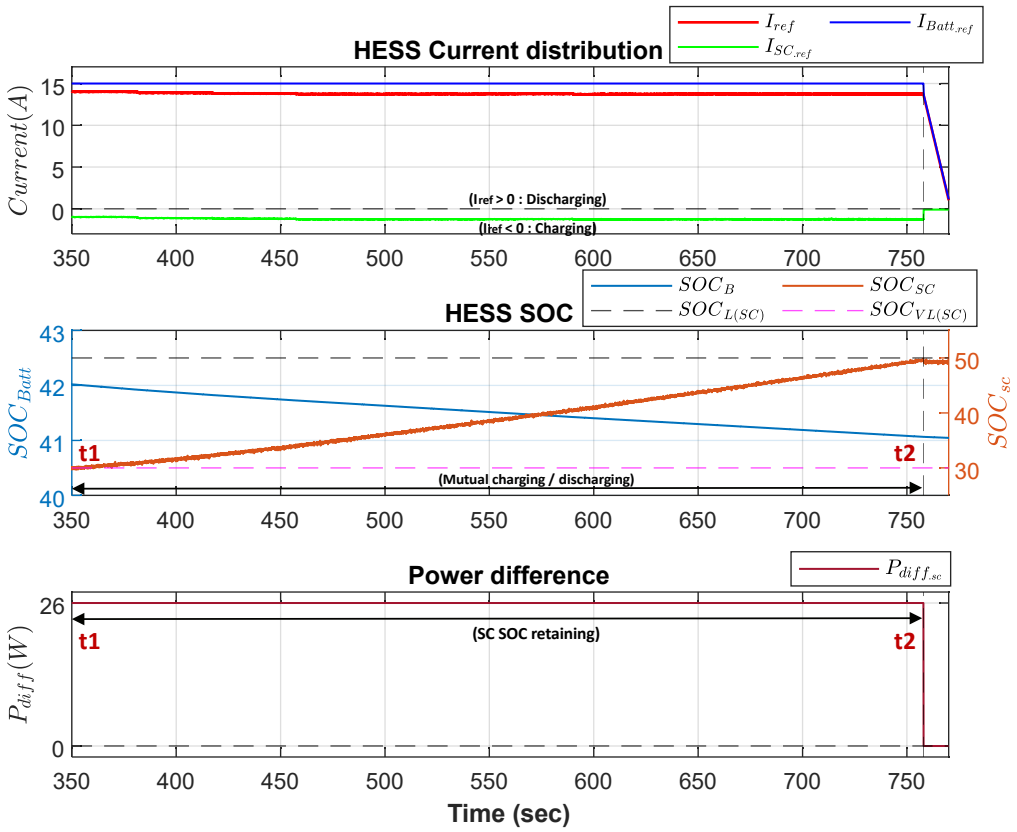

Figure 4.13: HESS current distribution, case 5.

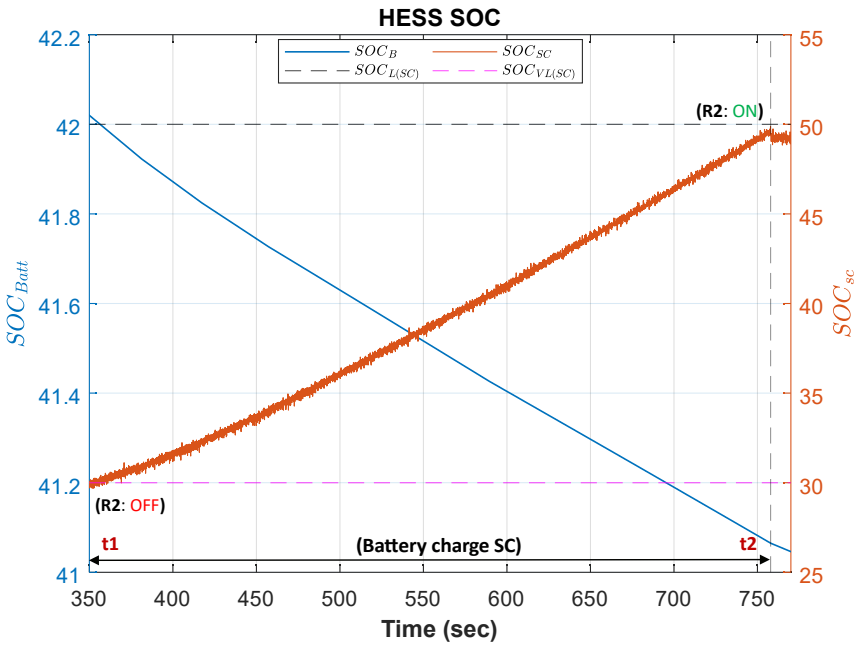

Figure 4.14: Battery charges the SC.

4.2.4 Case 4: LPF control

The effectiveness of the LPF on the HESS current distribution between the battery and SC can be determined at the system level as well as at the local level. LPF parameters are set the same as in chapter 2. Case 4 is justified if case 3 & case 5 are not applicable. To study the effects of load and current command on bus voltage stability, a specific time period ($220sec - 400sec$) is selected, shown in Figure. 4.15.

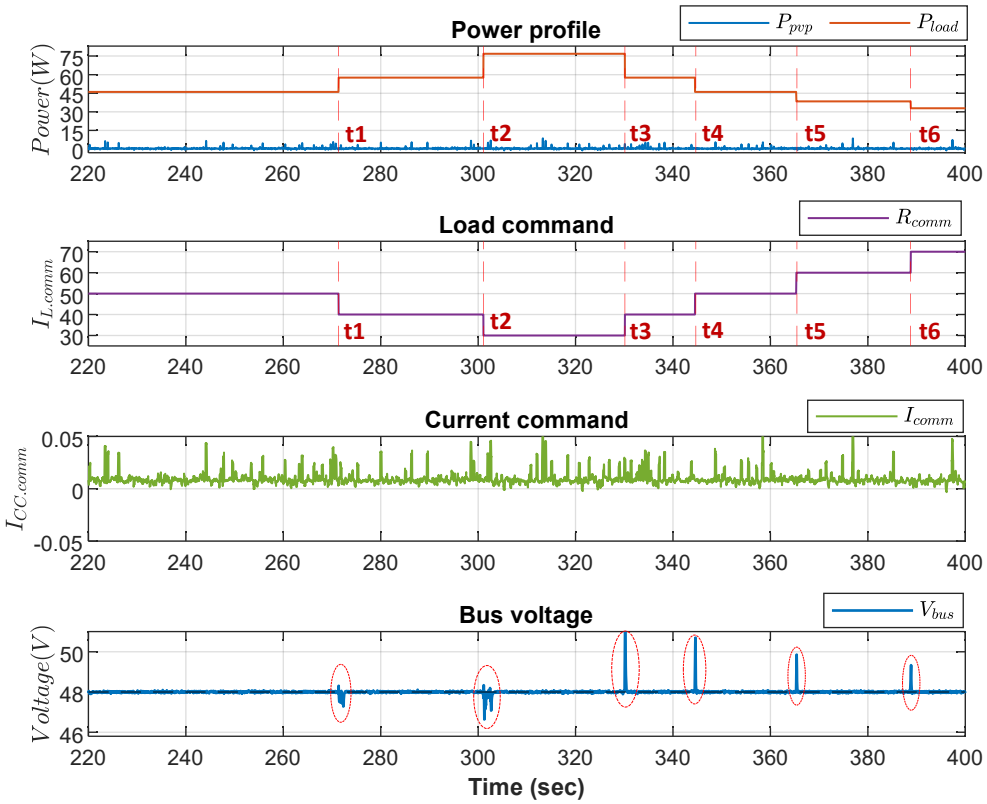

Figure 4.15: Power profile & bus voltage, case 4.

In this case, I_{comm} changes continuously with time and affects the power profile P_{pvp} at different time points $(t1, t2, t3, t4, t5, t6)$, as shown in Figure 4.15. The change in P_{pvp} also affects the bus voltage at a particular time, which is circled in the bus voltage display. Due to this change, there are small spikes in V_{bus} at time points $(t1, t2, t3, t4, t5, t6)$ can be observed but always in a stable range.

Figure 4.16 shows the current distribution between the battery and SC. As can be seen from the HESS current distribution results, the reference current I_{ref} is divided into high and low frequency parts. The high-frequency part is supplied by the SC, and the low-frequency part is smoothed by the battery, which reduces the electrical stress on the batteries. In this case, the battery and SC charge and discharge independently because both elements' SOC are in the normal range and case 4 works well without triggering a mutual charge/discharge process as shown in Figure 4.17.

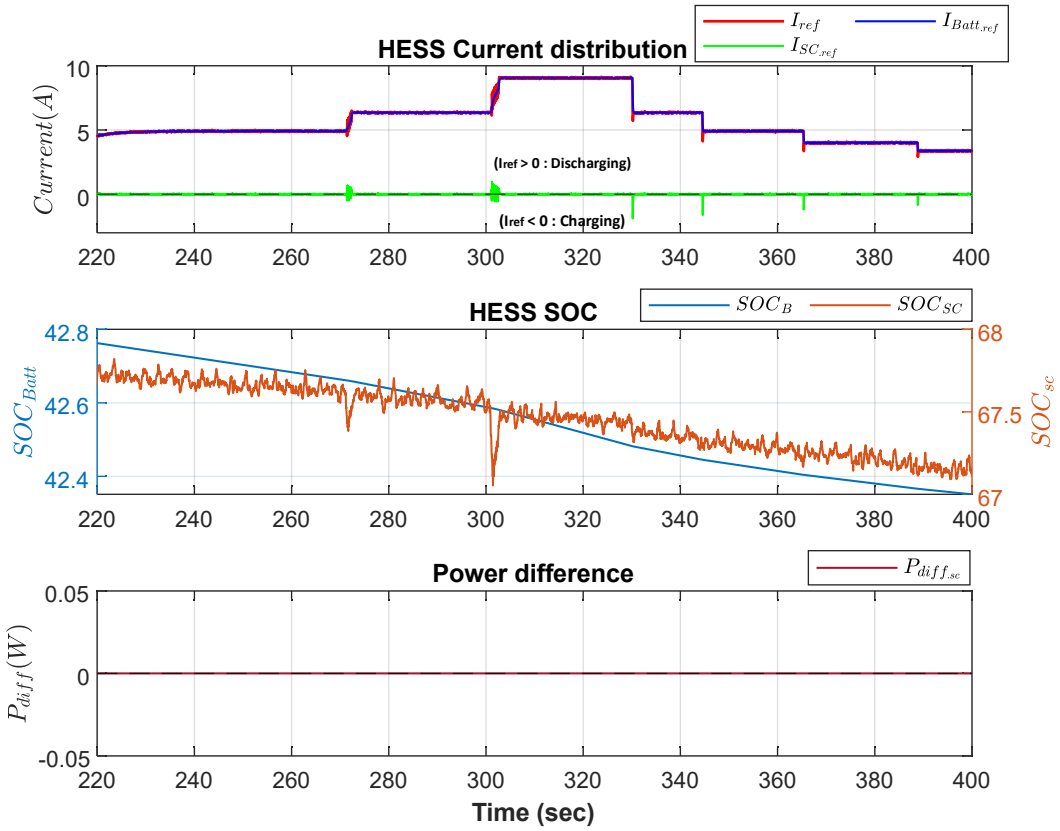

Figure 4.16: HESS current distribution, case 4.

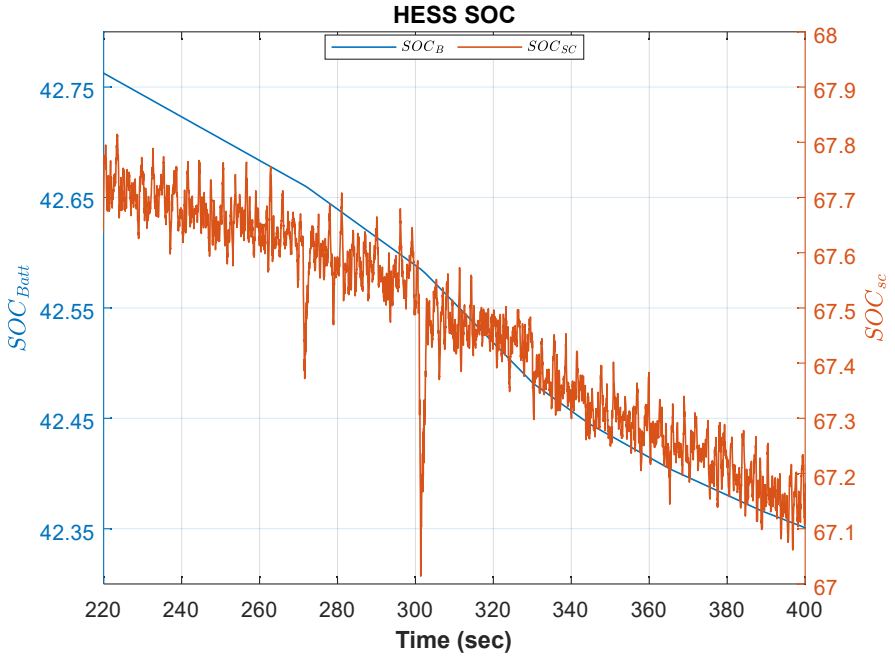

Figure 4.17: LPF effect on HESS SOC, case 4

Conclusion

Chapter 4 provides an overview of the experimental results obtained through a self-developed experimental platform. Before delving into the results, this platform which focuses on a DC microgrid, is introduced and presented. It encompasses various components, including a programmable PV simulator power supply, an electronic load, a HESS consisting of a battery bank and a SC connected to a multi-function power converter stack, and a real-time controller (dSPACE/MicroLabBox).

The proposed EMS consists of two levels, namely Level-1 & Level-2. To validate its performance, five different cases were thoroughly tested and validated, scenario by scenario, on the designed real-time experimental platform. In order to emulate PV generation profiles, a programmable PV simulator (Chroma 62020H-150S) was utilized, employing the analog programming interface (APG) mode for precise control over the PV generation profiles. Similarly, for the load profile, an electronic load (Electro-Automatik EA-EL-9750-50) was employed, configured in constant resistance (CR) mode to facilitate system control. The Hybrid Energy Storage System (HESS) consists of a battery bank, comprising four lithium-ion batteries connected in series, and a supercapacitor (SC) connected in parallel to the battery bank through a multi-function power converter stack (SEMIKRON SEMITEACH IGBT). This configuration facilitates the connection of the HESS to the DC bus.

Accelerated tests were conducted to verify the proposed EMS under various operating scenarios. Real PV generation and load consumption power profiles were integrated into a programmable DC supply and load. To control the system, a real-time controller (dSPACE/MicroLabBox) was employed. This controller collects voltage and current signals from the experimental platform and generates control signals for the corresponding converters, the programmable PV simulator, and the electronic load.

The proposed EMS was initially validated using a testbench evaluator developed in MATLAB/Simulink, and the simulation results were presented and analyzed in Chapter 3. In this chapter, the same EMS is further validated on a real experimental platform, and the results closely align with the simulation findings. The developed DC microgrid experimental platform has the potential to be utilized for the verification and evaluation of various other EMS, making it a versatile tool for future research and development in the field.

Conclusions and perspectives

General conclusions

According to the results and analysis presented in the four chapters, the main contributions of this work can be concluded as below.

Chapter 1 is based on the literature review, which summarized several critical aspects of DC microgrids (DCMG) for residential applications, including architecture, control structure, and EMS classification.

- Concerning its architecture, following elements are chosen for the formation of DCMG, i.e., Distributed Generators (DG) (PV panels), Storage Systems (SS) (Battery & SC), Bi-directional DC/DC converter and DC load.
- For the control aspect, special attention has been given to EMS issues in the tertiary level specifically for residential applications. A comprehensive analysis has been conducted, categorizing control methods into two main groups: classical methods and artificial intelligence (AI) techniques. Through this analysis, it has been recognized that no single method can fully meet all the requirements imposed by the multi-objective functions inherent in EMS. By combining different control approaches, hybrid methods offer the potential to optimize the performance of the EMS and effectively handle the diverse objectives and constraints associated with energy management in residential applications.
- In this review, various voltage levels (5V, 12V, 24V, 48V, 380-400V) have been examined to determine the most suitable voltage level for the proposed DCMG system designed for residential applications. After careful consideration, the DC bus level of 48V has been selected in our study as an appropriate voltage level. This selection is based on several factors, including compatibility with residential appliances and equipment, availability of components and converters, and overall system efficiency. By adapting a 48V DC bus level, the proposed DCMG system is well-suited to meet the specific requirements and operational characteristics of residential applications.
- Several software tools and hardware components that are highly beneficial for residential end users have been introduced. These tools and components include HOMER, i-HOGA, TRNSYS, OPAL-RT, Typhoon, and dSPACE.

It should be noted that this work has given rise to an international publication:

S. Ali, Z. Zheng, M. Aillerie, J.-P. Sawicki, M.-C. Péra, D. Hissel, « A Review of DC Microgrid Energy Management Systems Dedicated to Residential Applications ».
Energies 2021, 14, 4308. doi.org/10.3390/en14144308

having received the First Prize for a journal article in June 2023:

The First Prize: (CHF 1000 + one free publication + a certificate) A Review of DC Microgrid Energy Management Systems Dedicated to Residential Applications By Sadaqat Ali et al.

In Chapter 2, the main motivation is the introduction of the DC microgrid simulation platform, the fundamental principles and the modeling of DC microgrid at the local level.

- The first part of this chapter is about the construction and the development of multi-source DCMG scheme used in this study. The investigated DCMG system is established in MATLAB/Simulink environment, which consists of various element. Photovoltaic (PV) panels are considered as the main generation source, with batteries and SC as the storage system connected with a DC load via independent DC/DC power converters.
- In the second part of the chapter, local-level modeling with its control structure is briefly discussed. MPPT control was implemented for the PV system. For the batteries and SC, different control modes such as current control and voltage control are developed and tested. In addition, a LPF was applied to split the total HESS power into low and high frequency components for the batteries and SC, respectively. In addition, the influence of different angular frequencies ω of the LPF on the power sharing was also investigated and it was found that $\omega = 50 rad/s$ is a suitable value for the conventional control scheme based on the selected battery and SC types.

Chapter 3 provides a global overview of the DCMG simulation platform integrated with EMS. Different important aspects relating to controlling power generation, distribution, and load consumption at the system level is discussed.

- An enhanced hybrid energy management strategy (Filtration-based EMS + Rule-based EMS) is developed explained, which consists of two levels (Level-1 & Level-2) with five different cases.
- An EMS testbench evaluator is introduced to validate the bi-level control strategy at the system level.
- A local EMS control for HESS is introduced, not only for the SOC regulation, but also the power is exchanged between battery and SC to get equilibrium charge and discharge of each element. A new concept of SC SOC retaining control has been introduced to regulate the SOC of SC.
- An automatic sizing method has been developed, where battery sizing is performed for a 24-hour time horizon based on summer and winter profiles and SC for continuous high power demand.
- A cost function is also considered to calculate the Operating Expenditure & Capital Expenditure (OPEX & CAPEX) of HESS and compare it with battery case based on degradation costs and penalty costs. Upon conducting a cost comparison between the only-battery case and HESS case, it becomes evident that the HESS represents the superior choice, both economically and in terms of battery durability.

In Chapter 4, self-developed experimental platform is introduced and presented.

- In the first section, the developed platform is presented with the hardware configuration and system parameters. It consists of various components, including a programmable PV simulator power supply, an electronic load, a HESS consisting of a battery bank and a SC connected to a multi-function power converter stack, and a real-time controller (dSPACE/MicroLabBox).
- The second part is about the EMS validation on the experimental prototype. The proposed EMS was initially validated using a testbench evaluator developed in MATLAB/Simulink, and then was validated on the developed experimental platform.
- Accelerated tests were conducted to verify the proposed EMS under various operating scenarios and all the cases have been validated step by step.

Major contributions

The major contributions of this work can be summarized as follows:

- Modeling of a hierarchical DC microgrid simulation platform at both local and system levels under MATLAB/Simulink environment. At the local level, PV panels, batteries, supercondensators (SC) and DC/DC converters were modeled separately. At the system level, an Energy Management System (EMS) testbench evaluator was developed with designed cost functions for EMS evaluation uses.
- Development of two corresponding control layers, with a local-level control layer for component controls (e.g., MPPT control, constant-current control, and constant-voltage control) at a faster timescale (seconds to minutes) due to converter switching behaviors, and a system-level control layer for long-term EMS validation and performance evaluation (days to months).
- Proposition and development of a combined automatic sizing with bi-level hybrid EMS for the targeted multi-source DC microgrid. The hybrid EMS is an integration of filtration-based and rule-based EMS, which takes advantages of both. An accelerated test was conducted on the developed simulation performance under different operating scenarios. A comparison of cost functions was made between one Hybrid Energy Storage System (HESS) case and one only-battery case which demonstrated the advantage of the HESS solution.
- Development of an experimental multi-source DC microgrid prototype (at 5 kW level), which can serve as a universal test bench for evaluation and comparison of other existing EMS in the near future.

Perspectives

- The applications of this thesis revolve around the modeling of DC microgrid systems, incorporating an EMS specifically tailored for residential applications. This study is an integral part of a research-based project aimed at providing practical solutions for the implementation of DC microgrid systems. These systems can be employed either for individual households or for smaller communities in the form of nano-grids. The findings and insights from this research project will contribute to the real-life installation and operation of efficient DC microgrid systems, offering tangible benefits to end-users and promoting sustainable energy solutions at a local level.
- Developed EMS needs to be further improved by using AI techniques. By utilizing AI techniques, such as machine learning and neural networks, the EMS can be further refined to optimize energy management decisions, improve system efficiency, and adapt to dynamic operational conditions. A comprehensive comparison of the developed EMS with other existing EMS is necessary as well.
- EMS testbench evaluator can be further improved by integrating other objective functions. Expanding the objective functions of the EMS testbench evaluator would enhance its value as a tool for testing and validating different EMS strategies and facilitating the advancement of energy management solutions.
- To enhance the accuracy and realism of the experimental setup, it is recommended to replace the PV simulator with actual PV panels in order to extract the real-time maximum power output. Similarly, integrating a real DC load into the system would further validate the performance of the EMS. By integrating with PV panels and residential loads, the experimental platform would closely simulate the operational conditions and challenges faced in practical applications. This would enable a more reliable evaluation of the EMS and provide valuable insights for its further development and optimization.
- Finally, it would be beneficial to conduct a more comprehensive investigation of CAPEX associated with PV panels. This would enable the calculation of the total cost of the designed system, considering the expenses related to these components.

Bibliography

[1] "Electricity market report 2023,"

[2] "Accueil | ministères Écologie Énergie territoires,"

[3] L. Gomes, Z. Vale, and J. M. Corchado, "Microgrid management system based on a multi-agent approach: An office building pilot," *Measurement*, vol. 154, p. 107427, 2020.

[4] C. Yin, H. Wu, F. Locment, and M. Sechilariu, "Energy management of dc microgrid based on photovoltaic combined with diesel generator and supercapacitor," *Energy Conversion and Management*, vol. 132, pp. 14–27, 1 2017.

[5] rd Year and A. Professor, "Smart grid-the upcoming era," 2018.

[6] D. Kumar, F. Zare, and A. Ghosh, "Dc microgrid technology: System architectures, ac grid interfaces, grounding schemes, power quality, communication networks, applications, and standardizations aspects," *IEEE Access*, vol. 5, pp. 12230–12256, 6 2017.

[7] X. Yu, C. Cecati, T. Dillon, and M. G. Simes, "The new frontier of smart grids," *IEEE Industrial Electronics Magazine*, vol. 5, pp. 49–63, 9 2011.

[8] D. E. Olivares, A. Mehrizi-Sani, A. H. Etemadi, C. A. Canizares, R. Iravani, M. Kazerani, A. H. Hajimiragha, O. Gomis-Bellmunt, M. Saeedifard, R. Palma-Behnke, G. A. Jimenez-Estevez, and N. D. Hatziargyriou, "Trends in microgrid control," *IEEE Transactions on Smart Grid*, vol. 5, pp. 1905–1919, 7 2014.

[9] F. Martin-Martínez, A. Sánchez-Miralles, and M. Rivier, "A literature review of microgrids: A functional layer based classification," *Renewable and Sustainable Energy Reviews*, vol. 62, pp. 1133–1153, 9 2016.

[10] D. T. Ton and M. A. Smith, "The u.s. department of energy's microgrid initiative," *The Electricity Journal*, vol. 25, pp. 84–94, 10 2012.

[11] S. Choudhury, "A comprehensive review on issues, investigations, control and protection trends, technical challenges and future directions for microgrid technology," *International Transactions on Electrical Energy Systems*, vol. 30, p. e12446, 9 2020.

[12] S. Ali, Z. Zheng, M. Aillerie, J. P. Sawicki, M. C. Péra, and D. Hissel, "A review of dc microgrid energy management systems dedicated to residential applications," *Energies 2021, Vol. 14, Page 4308*, vol. 14, p. 4308, 7 2021.

[13] N. W. Lidula and A. D. Rajapakse, "Microgrids research: A review of experimental microgrids and test systems," *Renewable and Sustainable Energy Reviews*, vol. 15, pp. 186–202, 1 2011.

[14] K. W. Beard and T. B. Reddy, *Linden's Handbook of Batteries*. McGraw-Hill Education, 2019.

[15] A. González, E. Goikolea, J. A. Barrena, and R. Mysyk, "Review on supercapacitors: Technologies and materials," *Renewable and Sustainable Energy Reviews*, vol. 58, pp. 1189–1206, 2016.

[16] E. Hossain, E. Kabalci, R. Bayindir, and R. Perez, "Microgrid testbeds around the world: State of art," *Energy Conversion and Management*, vol. 86, pp. 132–153, 2014.

[17] Y. Yoldaş, A. Önen, S. Muyeen, A. V. Vasilakos, and İrfan Alan, "Enhancing smart grid with microgrids: Challenges and opportunities," *Renewable and Sustainable Energy Reviews*, vol. 72, pp. 205–214, 2017.

[18] M. . Abbasi, E. . Li, L. . Aguilera, R. P. . Lu, D. . Wang, Q. Xiao, Y. Liu, J. Zeng, F. Gao, M. Abbasi, E. Abbasi, L. Li, R. P. Aguilera, D. Lu, and F. Wang, "Review on the microgrid concept, structures, components, communication systems, and control methods," *Energies 2023, Vol. 16, Page 484*, vol. 16, p. 484, 1 2023.

[19] E. Planas, J. Andreu, J. I. Gárate, I. Martínez de Alegría, and E. Ibarra, "Ac and dc technology in microgrids: A review," *Renewable and Sustainable Energy Reviews*, vol. 43, pp. 726–749, 2015.

[20] G. Ding, F. Gao, S. Zhang, P. C. Loh, and F. Blaabjerg, "Control of hybrid ac/dc microgrid under islanding operational conditions," *Journal of Modern Power Systems and Clean Energy*, vol. 2, no. 3, pp. 223–232, 2014.

[21] M. N. Ambia, H. M. Hasanien, A. Al-Durra, and S. M. Muyeen, "Harmony search algorithm-based controller parameters optimization for a distributed-generation system," *IEEE Transactions on Power Delivery*, vol. 30, no. 1, pp. 246–255, 2015.

[22] E. Unamuno and J. A. Barrena, "Hybrid ac/dc microgrids—part ii: Review and classification of control strategies," *Renewable and Sustainable Energy Reviews*, vol. 52, pp. 1123–1134, 2015.

[23] X. Zhu, X. qing Han, W. ping Qin, and P. Wang, "Past, today and future development of micro-grids in china," *Renewable and Sustainable Energy Reviews*, vol. 42, pp. 1453–1463, 2015.

[24] M. A. Tavakkoli, A. Radan, and H. Hassibi, "Simulation and analysis of a compact electronic infrastructure for dc micro-grid: Necessity and challenges," *Smart Grid and Renewable Energy*, vol. 03, pp. 73–82, 2012.

[25] B. Sahoo, S. K. Routray, and P. K. Rout, "Ac, dc, and hybrid control strategies for smart microgrid application: A review," *International Transactions on Electrical Energy Systems*, vol. 31, p. e12683, 1 2021.

[26] A. Calpbinici, E. Irmak, E. Kabalci, and R. Bayindir, "Design of an energy management system for ac/dc microgrid," *Proceedings - 2021 IEEE 3rd Global Power, Energy and Communication Conference, GPECOM 2021*, pp. 184–189, 10 2021.

[27] S. Moussa, M. J.-B. Ghorbal, and I. Slama-Belkhodja, "Bus voltage level choice for standalone residential dc nanogrid," *Sustainable Cities and Society*, 2019.

[28] G. Manavalan, H. Tania, J. Patra, M. Poongothai, and S. Prema, "A closed loop system to stabilize a 24v solar dc nano grid," pp. 177–182, 08 2017.

[29] T. S. M. A. F. S.-E. e. a. I. o. s. l. Bachirou Bogno, Jean-Paul Sawicki and . . p. . .-erformance of lead acid battery in off-grid PV systems. International Journal of Hydrogen Energy, 2017

[30] M. Noritake, K. Yuasa, T. Takeda, K. Shimomachi, R. Hara, H. Kita, and T. Matsumura, "Experimental study of a 400 v class dc microgrid for commercial buildings," *2015 9th International Conference on Power Electronics and ECCE Asia (ICPE-ECCE Asia)*, pp. 1730–1735, 2015.

[31] X.-f. Lin, Y.-z. Xue, C.-n. Song, S.-j. Song, and L. Bin, "An experiment and research platform for dc micro-grid," in *2016 35th Chinese Control Conference (CCC)*, pp. 8588–8595, 2016.

[32] Anupam, M. Kumar, and S. Bhowmick, "Study and power flow management of dc bus for household loads," pp. 1–2, 2022.

[33] R. Wandhare, V. Randive, and S. Thale, "Design of a pv fed hybrid dc bus power supply with the high voltage ride through capability," pp. 2743–2750, 2020.

[34] N. Lidula and A. Rajapakse, "Microgrids research: A review of experimental microgrids and test systems," *Renewable and Sustainable Energy Reviews*, vol. 15, no. 1, pp. 186–202, 2011.

[35] "Title european energy storage technology development roadmap towards 2030 joint ease/eera recommendations for a,"

[36] D. Linden, T. B. R. Editor, N. York, C. San, F. Lisbon, L. Madrid, M. City, M. New, D. San, and J. Seoul, "Handbook of batteries," 2002.

[37] E. Hossain, E. Kabalci, R. Bayindir, and R. Perez, "A comprehensive study on microgrid technology," 2014.

[38] W. H. Danial, "Power electronics daniels," p. 477, 2010.

[39] U. Nasir, M. Rivera, S. Toledo, A. Costabeber, and P. Wheeler, "A review of power converter topologies with medium/high frequency transformers for grid interconnection systems."

[40] B. Singh, S. Gairola, B. N. Singh, A. Chandra, and K. Al-Haddad, "Multipulse ac-dc converters for improving power quality: A review," *IEEE Transactions on Power Electronics*, vol. 23, pp. 260–281, 1 2008.

[41] M. Shahbazi and A. Khorsandi, "Power electronic converters in microgrid applications," *Microgrid: Advanced Control Methods and Renewable Energy System Integration*, pp. 281–309, 1 2017.

[42] P. Singh, P. Paliwal, and A. Arya, "A review on challenges and techniques for secondary control of microgrid," *IOP Conference Series: Materials Science and Engineering*, vol. 561, p. 012075, oct 2019.

[43] W. Huang, M. Lu, and L. Zhang, "Survey on microgrid control strategies," *Energy Procedia*, vol. 12, pp. 206–212, 2011. The Proceedings of International Conference on Smart Grid and Clean Energy Technologies (ICSGCE 2011.

[44] J. Justo, F. Mwasilu, J. Lee, and J.-W. Jung, "Ac-microgrids versus dc-microgrids with distributed energy resources: A review," *Renewable and Sustainable Energy Reviews*, vol. 24, pp. 387–405, 08 2013.

[45] T. L. Nguyen, Q. T. Tran, R. Caire, C. Gavriluta, and V. H. Nguyen, "Agent based distributed control of islanded microgrid — real-time cyber-physical implementation," *2017 IEEE PES Innovative Smart Grid Technologies Conference Europe (ISGT-Europe)*, pp. 1–6, 2017.

[46] L. Meng, A. Luna Hernandez, E. Rodriguez-Diaz, S. Bo, T. Dragicevic, M. Savaghebi, J. C. Vasquez, J. Guerrero, M. Graells, and F. Andrade, "Flexible system integration and advanced hierarchical control architectures in the microgrid research laboratory of aalborg university," *IEEE Transactions on Industry Applications*, pp. 1–1, 01 2015.

[47] J. M. Guerrero, J. C. Vasquez, J. Matas, L. G. de Vicuna, and M. Castilla, "Hierarchical control of droop-controlled ac and dc microgrids—a general approach toward standardization," *IEEE Transactions on Industrial Electronics*, vol. 58, no. 1, pp. 158–172, 2011.

[48] P. García, J. P. Torreglosa, L. M. Fernández, and F. Jurado, "Optimal energy management system for stand-alone wind turbine/photovoltaic/hydrogen/battery hybrid system with supervisory control based on fuzzy logic," *International Journal of Hydrogen Energy*, vol. 38, no. 33, pp. 14146–14158, 2013.

[49] Y. Wang, C. Chen, J. Wang, and R. Baldick, "Research on resilience of power systems under natural disasters—a review," *IEEE Transactions on Power Systems*, vol. 31, no. 2, pp. 1604–1613, 2016.

[50] A. Hirsch, Y. Parag, and J. Guerrero, "Microgrids: A review of technologies, key drivers, and outstanding issues," *Renewable and Sustainable Energy Reviews*, vol. 90, pp. 402–411, 2018.

[51] L. Meng, E. R. Sanseverino, A. Luna, T. Dragicevic, J. C. Vasquez, and J. M. Guerrero, "Microgrid supervisory controllers and energy management systems: A literature review," *Renewable and Sustainable Energy Reviews*, vol. 60, no. C, pp. 1263–1273, 2016.

[52] A. Ahmad Khan, M. Naeem, M. Iqbal, S. Qaisar, and A. Anpalagan, "A compendium of optimization objectives, constraints, tools and algorithms for energy management in microgrids," *Renewable and Sustainable Energy Reviews*, vol. 58, no. C, pp. 1664–1683, 2016.

[53] X. Feng, A. Shekhar, F. Yang, R. Hebner, and P. Bauer, "Comparison of hierarchical control and distributed control for microgrid," *Electric Power Components and Systems*, vol. 45, pp. 1043–1056, 06 2017.

[54] L. I. Minchala-Avila, L. E. Garza-Castañón, A. Vargas-Martínez, and Y. Zhang, "A review of optimal control techniques applied to the energy management and control of microgrids," *Procedia Computer Science*, vol. 52, pp. 780–787, 2015. The 6th International Conference on Ambient Systems, Networks and Technologies (ANT-2015), the 5th International Conference on Sustainable Energy Information Technology (SEIT-2015).

[55] Y. R. Li and F. Nejabatkhah, "Overview of control, integration and energy management of microgrids," *Journal of Modern Power Systems and Clean Energy*, vol. 2, pp. 212–222, 08 2014.

[56] M. F. Zia, E. Elbouchikhi, and M. Benbouzid, "Microgrids energy management systems: A critical review on methods, solutions, and prospects," *Applied Energy*, vol. 222, no. C, pp. 1033–1055, 2018.

[57] S. El Alimi, T. Maatallah, and S. Ben Nasrallah, "Break-even analysis and optimization of a standalone hybrid system with battery storage for residential load consumption—a case study," *Renewable and Sustainable Energy Reviews*, vol. 37, p. 408–423, 09 2014.

[58] Y. Zhang, H. Jia, and L. Guo, "Energy management strategy of islanded microgrid based on power flow control," *2012 IEEE PES Innovative Smart Grid Technologies (ISGT)*, pp. 1–8, 2012.

[59] L. Xu, X. Ruan, C. Mao, B. Zhang, and Y. Luo, "An improved optimal sizing method for wind-solar-battery hybrid power system," *Sustainable Energy, IEEE Transactions on*, vol. 4, pp. 774–785, 07 2013.

[60] G. Bruni, S. Cordiner, V. Mulone, V. Rocco, and F. Spagnolo, "A study on the energy management in domestic micro-grids based on model predictive control strategies," *Energy Conversion and Management*, vol. 102, pp. 50–58, 2015.

[61] J. P. Torreglosa, P. García-Triviño, L. M. Fernández-Ramirez, and F. Jurado, "Control based on techno-economic optimization of renewable hybrid energy system for stand-alone applications," *Expert Systems with Applications*, vol. 51, pp. 59–75, 2016.

[62] R. Hosseinalizadeh, H. Shakouri G, M. S. Amalnick, and P. Taghipour, "Economic sizing of a hybrid (PV–WT–FC) renewable energy system (HRES) for stand-alone usages by an optimization-simulation model: Case study of Iran," *Renewable and Sustainable Energy Reviews*, vol. 54, no. C, pp. 139–150, 2016.

[63] F. A. Bhuiyan, A. Yazdani, and S. Primak, "Optimal sizing approach for islanded microgrids," *Iet Renewable Power Generation*, vol. 9, pp. 166–175, 2015.

[64] C. Nogueira, M. Vidotto, R. Niedzialkoski, N. Souza, L. Chaves, T. Edwiges, D. Santos, and I. Werncke, "Sizing and simulation of a photovoltaic-wind energy system using batteries, applied for a small rural property located in the south of brazil," *Renewable and Sustainable Energy Reviews*, vol. 29, pp. 151–157, 01 2014.

[65] V. Dash and P. Bajpai, "Power management control strategy for a stand-alone solar photovoltaic-fuel cell–battery hybrid system," *Sustainable Energy Technologies and Assessments*, vol. 9, pp. 68–80, 2015.

[66] B. Rani, G. Ilango, and N. Chilakapati, "Control strategy for power flow management in a pv system supplying dc loads," *Industrial Electronics, IEEE Transactions on*, vol. 60, pp. 3185–3194, 08 2013.

[67] C. Battistelli, L. Baringo, and A. Conejo, "Optimal energy management of small electric energy systems including v2g facilities and renewable energy sources," *Electric Power Systems Research*, vol. 92, pp. 50–59, 2012.

[68] N. Karami, N. Moubayed, and R. Outbib, "Energy management for a pemfc–pv hybrid system," *Energy Conversion and Management*, vol. 82, pp. 154–168, 2014.

[69] J. Pascual, J. Barricarte, P. Sanchis, and L. Marroyo, "Energy management strategy for a renewable-based residential microgrid with generation and demand forecasting," *Applied Energy*, vol. 158, p. 12, 11 2015.

[70] S. Sukumar, H. Mokhlis, S. Mekhilef, K. Naidu, and M. Karimi, "Mix-mode energy management strategy and battery sizing for economic operation of grid-tied microgrid," *Energy*, vol. 118, no. C, pp. 1322–1333, 2017.

[71] G. Comodi, A. Giantomassi, M. Severini, S. Squartini, F. Ferracuti, A. Fonti, D. Nardi Cesarini, M. Morodo, and F. Polonara, "Multi-apartment residential microgrid with electrical and thermal storage devices: Experimental analysis and simulation of energy management strategies," *Applied Energy*, vol. 137, no. C, pp. 854–866, 2015.

[72] L. Igualada, C. Corchero, M. Cruz-Zambrano, and F.-J. Heredia, "Optimal energy management for a residential microgrid including a vehicle-to-grid system," *Smart Grid, IEEE Transactions on*, vol. 5, pp. 2163–2172, 07 2014.

[73] P. T. Baboli, M. Shahparasti, M. P. Moghaddam, M. R. Haghifam, and M. Mohamadian, "Energy management and operation modelling of hybrid ac–dc microgrid," *IET Generation, Transmission Distribution*, vol. 8, pp. 1700–1711, 10 2014.

[74] M.-C. Hu, S.-Y. Lu, and Y.-H. Chen, "Stochastic programming and market equilibrium analysis of microgrids energy management systems," *Energy*, vol. 113, no. C, pp. 662–670, 2016.

[75] B. V. Solanki, A. Raghurajan, K. Bhattacharya, and C. A. Cañizares, "Including smart loads for optimal demand response in integrated energy management systems for isolated microgrids," *IEEE Transactions on Smart Grid*, vol. 8, no. 4, pp. 1739–1748, 2017.

[76] I. Prodan and E. Zio, "A model predictive control framework for reliable microgrid energy management," *International Journal of Electrical Power Energy Systems*, vol. 61, pp. 399–409, 2014.

[77] M. N. Akter, M. A. Mahmud, and A. M. T. Oo, "A hierarchical transactive energy management system for energy sharing in residential microgrids," *Energies*, vol. 10, no. 12, 2017.

[78] Y.-K. Chen, Y.-C. Wu, C.-C. Song, and Y.-S. Chen, "Design and implementation of energy management system with fuzzy control for dc microgrid systems," *Power Electronics, IEEE Transactions on*, vol. 28, pp. 1563–1570, 04 2013.

[79] O. Erdinc, O. Elma, M. Uzunoglu, U. Selamogullari, B. Vural, E. Ugur, A. Boynuegri, and S. Dusmez, "experimental performance assessment of an online energy management strategy for varying renewable power production suppression," 04 2014.

[80] G. K. Venayagamoorthy, R. K. Sharma, P. K. Gautam, and A. Ahmadi, "Dynamic energy management system for a smart microgrid," *IEEE Transactions on Neural Networks and Learning Systems*, vol. 27, no. 8, pp. 1643–1656, 2016.

[81] A. L. Jifang, B. T. Tianhao, and C. H. Jingang, "A neural network control strategy for multi-energy common dc bus hybrid power supply," in *SPEEDAM 2010*, pp. 1827–1831, 2010.

[82] A. Ogunjuyigbe, T. Ayodele, and O. Akinola, "Optimal allocation and sizing of pv/wind/split-diesel/battery hybrid energy system for minimizing life cycle cost, carbon emission and dump energy of remote residential building," *Applied Energy*, vol. 171, pp. 153–171, 2016.

[83] S. Rajanna and R. Saini, "Development of optimal integrated renewable energy model with battery storage for a remote indian area," *Energy*, vol. 111, pp. 803–817, 2016.

[84] A. Kamjoo, A. Maheri, A. M. Dizqah, and G. A. Putrus, "Multi-objective design under uncertainties of hybrid renewable energy system using nsga-ii and chance constrained programming," *International Journal of Electrical Power Energy Systems*, vol. 74, pp. 187–194, 2016.

[85] W. Sheng, K. yan Liu, X. Meng, X. Ye, and Y. Liu, "Research and practice on typical modes and optimal allocation method for pv-wind-es in microgrid," *Electric Power Systems Research*, vol. 120, pp. 242–255, 2015.

[86] s. rangnekar, A. Khare, A. Mittal, and p. suhane, "Sizing and performance analysis of standalone wind-pv based hybrid energy system using ant colony optimization," *IET Renewable Power Generation*, vol. 10, 02 2016.

[87] J. Zhao and X. Yuan, "Multi-objective optimization of stand-alone hybrid pv-wind-diesel-battery system using improved fruit fly optimization algorithm," *Soft Computing*, vol. 20, no. 7, pp. 2841–2853, 2015.

[88] A. Anvari-Moghaddam, A. Rahimi-Kian, M. S. Mirian, and J. M. Guerrero, "A multi-agent based energy management solution for integrated buildings and microgrid system," *Applied Energy*, vol. 203, pp. 41–56, 2017.

[89] U. Sureshkumar, P. Manoharan, and A. Ramalakshmi, "Economic cost analysis of hybrid renewable energy system using homer," in *IEEE-International Conference On Advances In Engineering, Science And Management (ICAESM -2012)*, pp. 94–99, 2012.

[90] A. Mahesh and K. S. Sandhu, "Hybrid wind/photovoltaic energy system developments: Critical review and findings," *Renewable and Sustainable Energy Reviews*, vol. 52, pp. 1135–1147, 2015.

[91] M. S. Behzadi and M. Niasati, "Comparative performance analysis of a hybrid pv/fc/battery stand-alone system using different power management strategies and sizing approaches," *International Journal of Hydrogen Energy*, vol. 40, no. 1, pp. 538–548, 2015.

[92] C. Vargas-Salgado, J. Aguila-Leon, C. Chiñas-Palacios, and E. Hurtado-Perez, "Low-cost web-based supervisory control and data acquisition system for a microgrid testbed: A case study in design and implementation for academic and research applications," *Heliyon*, vol. 5, no. 9, p. e02474, 2019.

[93] T. Lambert, P. Gilman, and P. Lilienthal, "Micropower system modeling with homer,"

[94] S. Bhakta, V. Mukherjee, and B. Shaw, "Techno-economic analysis and performance assessment of standalone photovoltaic/wind/hybrid power system in lakshadweep islands of india," *Journal of Renewable and Sustainable Energy*, vol. 7, p. 063117, 12 2015.

[95] H. S. Das, A. Dey, T. C. Wei, and A. H. Yatim, "Feasibility analysis of standalone pv/wind/battery hybrid energy system for rural bangladesh," *International Journal of Renewable Energy Research*, vol. 6, pp. 402–412, 2016.

[96] E. Giannoulis and D. Haralambopoulos, "Distributed generation in an isolated grid: Methodology of case study for lesvos – greece," *Applied Energy*, vol. 88, no. 7, pp. 2530–2540, 2011.

[97] A. Al-Karaghouli and L. Kazmerski, "Optimization and life-cycle cost of health clinic pv system for a rural area in southern iraq using homer software," *Solar Energy*, vol. 84, no. 4, pp. 710–714, 2010. International Conference CISBAT 2007.

[98] G. Bekele and B. Palm, "Feasibility study for a standalone solar–wind-based hybrid energy system for application in ethiopia," *Applied Energy*, vol. 87, no. 2, pp. 487–495, 2010.

[99] T. Ma, H. Yang, and L. Lu, "Study on stand-alone power supply options for an isolated community," *International Journal of Electrical Power Energy Systems*, vol. 65, pp. 1–11, 2015.

[100] M. S. Adaramola, M. Agelin-Chaab, and S. S. Paul, "Analysis of hybrid energy systems for application in southern ghana," *Energy Conversion and Management*, vol. 88, pp. 284–295, 2014.

[101] L. Olatomiwa, S. Mekhilef, A. Huda, and O. S. Ohunakin, "Economic evaluation of hybrid energy systems for rural electrification in six geo-political zones of nigeria," *Renewable Energy*, vol. 83, pp. 435–446, 2015.

[102] S. K. Nandi and H. R. Ghosh, "Prospect of wind–pv-battery hybrid power system as an alternative to grid extension in bangladesh," *Energy*, vol. 35, no. 7, pp. 3040–3047, 2010.

[103] R. Sen and S. C. Bhattacharyya, "Off-grid electricity generation with renewable energy technologies in india: An application of homer," *Renewable Energy*, vol. 62, pp. 388–398, 2014.

[104] K. Lau, M. Yousof, S. Arshad, M. Anwari, and A. Yatim, "Performance analysis of hybrid photovoltaic/diesel energy system under malaysian conditions," *Energy*, vol. 35, no. 8, pp. 3245–3255, 2010.

[105] O. H. Mohammed, Y. Amirat, M. E. Benbouzid, and G. Feld, "Optimal design and energy management of a hybrid power generation system based on wind/tidal/pv sources: Case study for the ouessant french island," *Green Energy and Technology*, vol. 0, pp. 381–413, 2017.

[106] M. Fadaeenejad, M. Radzi, M. AbKadir, and H. Hizam, "Assessment of hybrid renewable power sources for rural electrification in malaysia," *Renewable and Sustainable Energy Reviews*, vol. 30, pp. 299–305, 2014.

[107] S. Nasri, B. S. Sami, and A. Cherif, "Power management strategy for hybrid autonomous power system using hydrogen storage," *International Journal of Hydrogen Energy*, vol. 41, no. 2, pp. 857–865, 2016.

[108] L. K. Gan, J. K. Shek, and M. A. Mueller, "Hybrid wind–photovoltaic–diesel–battery system sizing tool development using empirical approach, life-cycle cost and performance analysis: A case study in scotland," *Energy Conversion and Management*, vol. 106, pp. 479–494, 2015.

[109] L. Raju, A. A. Morais, V. Balaji, and S. Keerthivasan, "Multi agent systems and arduino based smart micro-grid test bed," *AIP Conference Proceedings*, vol. 2161, p. 020032, 10 2019.

[110] A. Kirubakaran, S. Jain, and R. K. Nema, "Dsp-controlled power electronic interface for fuel-cell-based distributed generation," *IEEE TRANSACTIONS ON POWER ELECTRONICS*, vol. 26, 2011.

[111] B. Belvedere, M. Bianchi, A. Borghetti, A. D. Pascale, M. D. Silvestro, and M. Paolone, "Dsp-controlled test set-up for the performance assessment of an autonomous power unit equipped with a pem fuel cell," *2007 International Conference on Clean Electrical Power, ICCEP '07*, pp. 468–473, 2007.

[112] I. Sheikh, "Hybrid energy management system for microgrid applications," *2016 International Conference on Energy Efficient Technologies for Sustainability, ICEETS 2016*, pp. 361–365, 10 2016.

[113] M. Kermani, B. Adelmanesh, E. Shirdare, C. A. Sima, D. L. Carnì, and L. Martirano, "Intelligent energy management based on SCADA system in a real Microgrid for smart building applications," *Renewable Energy*, vol. 171, no. C, pp. 1115–1127, 2021.

[114] A. Merabet, K. Tawfique Ahmed, H. Ibrahim, R. Beguenane, and A. M. Y. M. Ghias, "Energy management and control system for laboratory scale microgrid based wind-pv-battery," *IEEE Transactions on Sustainable Energy*, vol. 8, no. 1, pp. 145–154, 2017.

[115] A. Chaouachi, R. M. Kamel, R. Andoulsi, and K. Nagasaka, "Multiobjective intelligent energy management for a microgrid," *IEEE Transactions on Industrial Electronics*, vol. 60, no. 4, pp. 1688–1699, 2013.

[116] T. Bogaraj, J. Kanakaraj, and J. Chelladurai, "Modeling and simulation of stand-alone hybrid power system with fuzzy mppt for remote load application," *Archives of Electrical Engineering*, vol. Vol. 64, pp. 487–504, 9 2015.

[117] D. Rekioua and E. Matagne, "Optimization of photovoltaic power systems: Modelization, simulation and control," *Green Energy and Technology*, vol. 102, 2012.

[118] J. A. R. Hernanz, J. J. C. Martín, I. Z. Belver, J. L. Lesaka, E. Z. Guerrero, and E. P. Pérez, "Modelling of photovoltaic module," *Renewable Energy and Power Quality Journal*, vol. 1, pp. 1186–1190, 4 2010.

[119] H. Tian, F. Mancilla-David, K. Ellis, E. Muljadi, and P. Jenkins, "A cell-to-module-to-array detailed model for photovoltaic panels," *Solar Energy*, vol. 86, pp. 2695–2706, 9 2012.

[120] V. J. Chin, Z. Salam, and K. Ishaque, "Cell modelling and model parameters estimation techniques for photovoltaic simulator application: A review," *Applied Energy*, vol. 154, pp. 500–519, 9 2015.

[121] J. P. Charles, M. Abdelkrim, Y. H. Muoy, and P. Mialhe, "A practical method of analysis of the current-voltage characteristics of solar cells," *Solar Cells*, vol. 4, pp. 169–178, 1981.

[122] Z. Ouennoughi and M. Chegaar, "A simpler method for extracting solar cell parameters using the conductance method," *Solid-State Electronics*, vol. 43, pp. 1985–1988, 11 1999.

[123] M. Chegaar, Z. Ouennoughi, and A. Hoffmann, "A new method for evaluating illuminated solar cell parameters," *Solid-State Electronics*, vol. 45, pp. 293–296, 2 2001.

[124] G. R. Walker, "Evaluating mppt converter topologies using a matlab pv model," 2000.

[125] S. Aissou, D. Rekioua, N. Mezzai, T. Rekioua, and S. Bacha, "Modeling and control of hybrid photovoltaic wind power system with battery storage," *Energy Conversion and Management*, vol. 89, pp. 615–625, 1 2015.

[126] L. Lam, P. Bauer, and E. Kelder, "A practical circuit-based model for li-ion battery cells in electric vehicle applications," *INTELEC, International Telecommunications Energy Conference (Proceedings)*, 2011.

[127] H. E. S. A. Ibrahim, F. F. Houssiny, H. M. Z. El-Din, and M. A. El-Shibini, "Microcomputer controlled buck regulator for maximum power point tracker for dc pumping system operates from photovoltaic system," *FUZZ-IEEE'99. 1999 IEEE International Fuzzy Systems. Conference Proceedings (Cat. No.99CH36315)*, vol. 1, 1999.

[128] K. Nishioka, N. Sakitani, K. I. Kurobe, Y. Yamamoto, Y. Ishikawa, Y. Uraoka, and T. Fuyuki, "Analysis of the temperature characteristics in polycrystalline si solar cells using modified equivalent circuit model," *Japanese Journal of Applied Physics, Part 1: Regular Papers and Short Notes and Review Papers*, vol. 42, pp. 7175–7179, 2003.

[129] J. L. Santos, F. Antunes, A. Chehab, and C. Cruz, "A maximum power point tracker for pv systems using a high performance boost converter," *Solar Energy*, vol. 80, pp. 772–778, 7 2006.

[130] Z. Zheng, X. Wang, and Y. Li, "A control method for grid-friendly photovoltaic systems with hybrid energy storage units," *DRPT 2011 - 2011 4th International Conference on Electric Utility Deregulation and Restructuring and Power Technologies*, pp. 1437–1440, 2011.

[131] O. M. Toledo, D. O. Filho, and A. S. A. C. Diniz, "Distributed photovoltaic generation and energy storage systems: A review," *Renewable and Sustainable Energy Reviews*, vol. 14, pp. 506–511, 2010.

[132] M. Kalantar, S. M. G., M. Kalantar, and S. M. G., "Dynamic behavior of a stand-alone hybrid power generation system of wind turbine, microturbine, solar array and battery storage," *Applied Energy*, vol. 87, pp. 3051–3064, 2010.

[133] S. Barcellona and L. Piegari, "Lithium ion battery models and parameter identification techniques," *Energies 2017, Vol. 10, Page 2007*, vol. 10, p. 2007, 12 2017.

[134] S. M. M. G. and M. Nikdel, "Various battery models for various simulation studies and applications," *Renewable and Sustainable Energy Reviews*, vol. 32, pp. 477–485, 4 2014.

[135] F. Eltoumi, A. Badji, M. Becherif, and H. S. Ramadan, "Experimental identification using equivalent circuit model for lithium-ion battery," *International Journal of Emerging Electric Power Systems*, vol. 19, 6 2018.

[136] J. M. Miller, "Chapter 1 types of ultracapacitors," *Ultracapacitor Applications (IET Power and Energy Series)*, p. 363, 2011.

[137] Z. Cabrane, M. Ouassaid, and M. Maaroufi, "Battery and supercapacitor for photovoltaic energy storage: a fuzzy logic management," *IET Renewable Power Generation*, vol. 11, pp. 1157–1165, 6 2017.

[138] X. Cheng, D. Zhang, X. Liu, D. Cao, and G. Wang, "Influence of ctab on morphology, structure, and supercapacitance of -ni(oh)2," *Ionics*, vol. 21, pp. 533–540, 2 2015.

[139] Z. Cabrane and S. H. Lee, "Electrical and mathematical modeling of supercapacitors: Comparison," *Energies 2022, Vol. 15, Page 693*, vol. 15, p. 693, 1 2022.

[140] S. J. Choi and S. H. Lim, "Fluctuation suppression of dc-link voltage using control of converters connected with dc distributed generation," *Energies 2020, Vol. 13, Page 5832*, vol. 13, p. 5832, 11 2020.

[141] "Mohan, undeland, robbins: Power electronics: Converters, applications, and design, 3rd edition - instructor companion site,"

[142] S. S. Ang and A. Oliva, "Power-switching converters," p. 619.

[143] R. D. Middlebrook and S. Cuk, "A general unified approach to modelling switching-converter power stages," pp. 18–34, 4 2015.

[144] K. B. Liu, C. Y. Liu, Y. H. Liu, Y. C. Chien, B. S. Wang, and Y. S. Wong, "Analysis and controller design of a universal bidirectional dc-dc converter," *Energies 2016, Vol. 9, Page 501*, vol. 9, p. 501, 6 2016.

[145] S. Punna and U. B. Manthati, "Optimum design and analysis of a dynamic energy management scheme for hess in renewable power generation applications," *SN Applied Sciences*, vol. 2, pp. 1–13, 3 2020.

[146] C. Depature, S. Jemei, L. Boulon, A. Bouscayrol, N. Marx, S. Morando, and A. Castaings, "Energy management in fuel-cellbattery vehicles: Key issues identified in the ieee vehicular technology society motor vehicle challenge 2017," *IEEE Vehicular Technology Magazine*, vol. 13, pp. 144–151, 9 2018.

[147] B. Nykvist and M. Nilsson, "Rapidly falling costs of battery packs for electric vehicles," *Nature Climate Change*, vol. 5, pp. 329–332, 3 2015.

[148] P. K. S. Roy, H. B. Karayaka, Y. Yan, and Y. Alqudah, "Investigations into best cost battery-supercapacitor hybrid energy storage system for a utility scale pv array," *Journal of Energy Storage*, vol. 22, pp. 50–59, 4 2019.

[149] J. Solano, S. Jemei, L. Boulon, L. Silva, D. Hissel, and M. C. Pera, "Ieee vts motor vehicles challenge 2020 - energy management of a fuel cell/ultracapacitor/lead-acid battery hybrid electric vehicle," *2019 IEEE Vehicle Power and Propulsion Conference, VPPC 2019 - Proceedings*, 10 2019.

Appendix

Energy management strategy

EMS has 5 different cases. Each case was validated separately with the following conditions;

```
Case-1: (Ppvp > Pload)

if SOC_B >= SOC_B(VH)
        Ppvp = Pload;
        Pload = Pload;
        Pref = 0;
else
        Ppvp_curt = 0;
        Pload_shed = 0;

        Ppvp = Ppvp;
        Pload = Pload;
        Pref = Pload - Ppvp;
end
```

```
Case-2: (Ppvp < Pload)

if SOC_B <= SOC_B(VL)
        Ppvp = Ppvp;
        Pload = Ppvp;
        Pref = 0;
else
        Pload_shed = 0;
        Ppvp_curt = 0;

        Ppvp = Ppvp;
        Pload = Pload;
        Pref = Pload - Ppvp;
end
```

```
Case-3: (SC charge battery)

if SOC_sc = SOC_sc(VH)  &&  SOC_B > SOC_B(VL)

        PBatt = Pref*_Batt_init + Δ Pref*;
        Psc = Pref* - PBatt;

    else

        PBatt = Pref*_Batt_init;
        Psc = Pref* - PBatt;
end
```

```
Case-5: (Battery charge SC)

if SOC_sc = SOC_sc(VL)  &&  SOC_B < SOC_B(VH)

        PBatt = Pref*_Batt_init + Δ Pref*;
        Psc = Pref* - PBatt;

    else

        PBatt = Pref*_Batt_init;
        Psc = Pref* - PBatt;
end
```

Case 4 is justified if case 3 & 5 are untrue. This case is based on LPF theory, therefore the current and power between the battery and SC are normally distributed with no specific rules defined.

www.dspace.com

MicroLabBox

- Compact all-in-one development system for the laboratory
- More than 100 high-performance I/O channels with easy access
- Comprehensive support for electric motor control
- Three connector panel variants available

dSPACE

Technical Details

Parameter		Specification		
MicroLabBox		**Front Panel Variant**	**Top Panel Variant with BNC Connectors**	**Top Panel Variant with Spring-Cage Terminal Blocks**
Processor	Real-time processor	■ NXP (Freescale) QorIQ P5020, dual-core, 2 GHz ■ 32 KB L1 data cache per core, 32 KB L1 instruction cache per core, 512 KB L2 cache per core, 2 MB L3 cache total		
	Host communication co-processor	■ NXP (Freescale) QorIQ P1011 800 MHz for communication with host PC		
Memory		■ 1 GB DRAM ■ 128 MB flash memory		
Boot time		■ Autonomous booting of applications from flash (depending on application size), ~5 s for a 5 MB application		
Interfaces	Host interface	■ Integrated Gigabit Ethernet host interface		
	Ethernet real-time I/O interface	■ Integrated low-latency Gigabit Ethernet I/O interface		
	USB interface	■ USB 2.0 interface for data logging ("flight recorder") and booting applications via USB mass storage device (max. 32 GB supported)		
	CAN interface	■ 2 CAN channels (partial networking supported)		
	Serial interface	■ 2 x UART (RS232/422/485) interface		
	LVDS interface	■ 1 x LVDS interface to connect with the Programmable Generic Interface PGI1		
Programmable FPGA[1]		■ Xilinx® Kintex®-7 XC7K325T FPGA		
Analog input	Resolution and type	■ 8 14-bit channels, 10 Msps, differential; functionality: free running mode ■ 24 16-bit channels, 1 Msps, differential; functionality: single conversion and burst conversion mode with different trigger and interrupt options		
	Input voltage range	■ -10 ... 10 V		
Analog output	Resolution and type	■ 16 16-bit channels, 1 Msps, settling time: 1 µs		
	Output voltage range	■ -10 ... 10 V		
	Output current	■ ± 8 mA		
Digital I/O		■ 48 bidirectional channels, 2.5/3.3/5 V (single-ended); functionality: bit I/O, PWM generation and measurement (10 ns resolution), pulse generation and measurement (10 ns resolution), 4 x SPI Master ■ 12 bidirectional channels (RS422/485 type) to connect sensors with differential interfaces		
Electric motor control I/O functionality	Separate interfaces	■ 2 x Resolver interface		
	Functionality on digital I/O channels	■ 6 x Encoder sensor input ■ 2 x Hall sensor input ■ 2 x EnDat interface ■ 2 x SSI interface ■ Synchronous multi-channel PWM ■ Block commutational PWM		
Sensor supply		■ 1 x 12 V, max. 3 W/250 mA (fixed) ■ 1 x 2 ... 20 V, max. 1 W/200 mA (variable)		
Feedback elements		■ Programmable buzzer ■ Programmable status LEDs		
Theft protection		■ Kensington® lock		
Cooling		■ Active cooling (temperature-controlled fan)		
Physical connections		■ 4 x Sub-D 50 I/O connectors ■ 4 x Sub-D 9 I/O connectors	■ 2 x Sub-D 50 I/O connectors ■ 48 x BNC I/O connectors ■ 4 x Sub-D 9 I/O connectors	■ 2 x Sub-D 9 I/O connectors ■ 27 x spring-cage terminal block connectors with 8 pins each
		■ 3 x RJ45 for Ethernet (host and I/O) ■ USB Type A (for data logging) ■ 2 x 2 banana connectors for sensor supply ■ Power supply		

[1] *User-programmable via RTI FPGA Programming Blockset. Using the RTI FPGA Programming Blockset requires additional software.*

Elektro-Automatik

Bedienungsanleitung
Instruction Manual

EL 9000 HP
Electronic DC Load
4800 W

CE

EL 9080-400 HP	33 200 241
EL 9160-200 HP	33 200 243
EL 9400-100 HP	33 200 245
EL 9750-50 HP	33 200 250

Doc ID: EL9H4
Revision: 10
Date: 05/2015

2.2 Device specific data

	EL9080-400 HP	EL 9160-200 HP	EL9400-100 HP	EL9750-50 HP
Mains input				
Mains voltage	115V/230V ±10%, selectable			
Mains frequency	50/60Hz			
Mains fuse	T2,5A			
DC input				
Input voltage U_{nom}	80V	160V	400V	750V
Input power P_{nom}	4800W, with temperature related derating			
- permanent power	4800W at 40°C ambient temp.			
Input current I_{nom}	400A	200A	100A	50A
Overvoltage protection threshold	1.1 * U_{nom}			
Min. input voltage for max. current	approx. 1V	approx. 0.7V	approx. 0.5V	approx. 0.5V
Max. allowed input voltage	100V	180V	460V	850V
Voltage control				
Adjustment range	0…80V	0…160V	0…400V	0…750V
Display resolution	100mV	100mV	100mV	100mV
Accuracy**	<0.1% of U_{nom}			<0.2% of U_{nom}
Current control				
Adjustment range	0…400A	0…200A	0…100A	0…50A
Display resolution	100mA	100mA	100mA	10mA
Accuracy**	<0.2% of I_{nom}			
Power control				
Adjustment range	0…4800W	0…4800W	0…4800W	0…4800W
Display resolution	1W	1W	1W	1W
Accuracy**	<2% of P_{nom}			
Resistance control				
Adjustment range 1	0…2.5Ω	0…5Ω	0…5Ω	0…20Ω
Display resolution	1mΩ	10mΩ	10mΩ	10mΩ
Adjustment range 2	0…50Ω	0…100Ω	0…200Ω	0…400Ω
Display resolution	100mΩ	100mΩ	100mΩ	100mΩ
Accuracy**	<2% of the selected resistance range, 0,3% of the maximum input current			
Dynamic values				
Current rise and fall time***	0			
Level	2 adjustable levels per control mode			
Times (pulsed operation)	2 adjustable, 50us..100s			
Rise/fall time	adjustable, 30us…200ms			
Accuracy**	einstellbar, 30us…200ms			
Trigger input*	yes, for external level switching			
Battery test feature				
Modes	current / resistance / power			
Battery protection	final discharging voltage adjustable			
Display	time and consumed battery capacity			
Display	2 x 40 characters, illuminated			
Analogue interface*				
Set value inputs	0...10V for U / I / P / R (0...100% set value)			
Monitor outputs	0...10V for U / I (0...100% actual value)			
Control signals	internal/external, input on/off, R range 1 or 2			
Error signals	overvoltage / overtemperature			
Outputs	reference voltage			
Cooling				
Type	temperature controlled fans			
Ambient temperature	0…50°C			
Terminals				
Load input	rear side, M8 screw terminal			
System Bus	rear side, 7 pole screw clamp			
Analogue interface	rear side, 15 pole Sub-D socket			
Dimensions W x H x D	19" x 6U x 460mm			
Weight	35kg			
Supported interface cards	CAN, USB, RS232, GPIB, Ethernet			
Article number	33 200 241	33 200 243	33 200 245	33 200 250

* for technical specification see section "Analogue interface"

** Accuracy is defined as the max. allowed difference between actual value and set value, always related to the nominal value.
Example: nom. value is 400A and accuracy is given with 0.2%. A set value of 20A may thus result in an actual value of 19.2A...20.8A.

*** Rise and fall time are defined at 10%...90% and 90%...10% of the nominal value

All single values, which specify a tolerance are typical values

Chroma

dataTec
Mess- und Prüftechnik. Die Experten.

PROGRAMMABLE DC POWER SUPPLY (SOLAR ARRAY SIMULATION) MODEL 62000H-S SERIES

The latest programmable solar array simulator power supply 62000H-S Series released by Chroma provide simulation of Voc (open circuit voltage) up to 1800V and Isc (short circuit current) up to 30A. The 62000H-S provides an industry leading power density in a small 3U high package. The solar array simulator is highly stable and has a fast transient response design, which are both advantageos to MPPT performance evaluation on PV inverter devices.

The 62000H-S Series has many unique advantages including high speed & precision digitizing measurement circuits with a 100kHz A/D, 25kHz D/A controlled I-V curve and a digital filter mechanism. It can simulate an I-V curve accurately and response the mains ripple effect from the PV inverter. In addition, the built-in EN50530/Sandia SAS I-V model in the standalone unit can easily program the Voc, Isc, Vmp, and Imp parameters for I-V curve simulation, without a PC controller.

The real solar array is influenced by various weather conditions such as irradiation, temperature, rain and shade by trees or clouds, which will affect the I-V curve output. The 62000H-S Series is capable of storing up to 100 I-V curves into the simulator memory, with a programmed time interval range of 1-15,000 seconds. It can simulate the I-V curve from the early morning to nightfall for PV inverter testing or dynamic I-V curve transient testing.

The 62000H-S Series has a built-in 16 bit digital control and precision voltage & current measurement circuits with a voltage accuracy of 0.05% + 0.05% F.S. and a current accuracy of 0.1% + 0.1% F.S. It is ideal for real time MPPT analysis and tracking monitoring for PV inverters through our softpanel. The user can also enable the data recording function on the softpanel during the static MPPT performance test.

When high power solar array simulation is required, it is common to connect two or more power modules in parallel. The 62000H-S Series with a current range up to 30A and a voltage range up to 1800V offers a high power density envelope maximum of 18kW in a 3U package. It can easily parallel up to 16 units in a Master/Slave configuration to provide 288kW with current sharing and synchronized control signals for commercial utility PV inverter (10kW~100kW) testing. The 62000H-S Series supplies have a smart Master/Slave control mode that makes the parallel operation fast and simple. In this mode, the master scales values and downloads data to slave units so that the programming is as simple as using a standalone unit.

The 62000H-S Series DC power supplies are very easy to operate from the front panel keypad or from the remote controller via Ethernet/USB/RS232/RS485/GPIB/APG. Its compact size (3U) makes it ideal for both benchtop and standard racking.

Ethernet USB RS-485 RS-232 GPIB APG CE RoHS2 Compliant

MODEL 62000H-S SERIES

KEY FEATURES

- Voltage range : 0 ~150V/600V/1000V/1800V
- AC input voltage range : 200/220Vac, 380/400Vac , 440/480Vac
- 3U/18kW high power density module with easy master/slave parallel operation
- Fast transient response solar array simulation
- Simulation of multiple solar cell material I-V characteristic (fill factor)
- Simulation of dynamic irradiation intensity and temperature level from clear day to cloud cover conditions
- Shadowed I-V curve output simulation (up to 4096 data points)
- Low leakage current (< 3mA)
- Precision V & I measurements
- Auto I-V program: 100 I-V curves & Dwell time 1-15,000s
- Static & dynamic MPPT efficiency test (accumulated energy methods)
- Data recorded via softpanel
- Support Ethernet / USB / RS232 / RS485 / GPIB / APG interfaces
- Real time analysis of PV inverter's MPPT tracking via softpanel
- Free graphic user interface - softpanel for operation
- Real world weather simulation fast I-V curve update rate : 1s
- Support up to ten-channel SAS control for multi-MPPT testing
- Built-in dynamic MPPT test profile of EN50530, Sandia, CGC/GF004, CGC/GF035 and NB/T 32004

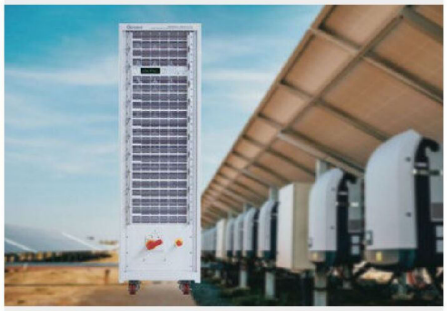

ELECTRICAL SPECIFICATIONS-WITH SOLAR ARRAY SIMULATION

Model	62020H-150S	62050H-600S	62100H-600S	62150H-600S	62150H-1000S	62180H-1800S
Output Ratings						
Output Voltage	0 ~ 150V	0 ~ 600V	0 ~ 600V	0 ~ 600V	0 ~ 1000V	0 ~ 1800V *5
Output Current	0 ~ 40A	0 ~ 8.5A	0 ~ 17A	0 ~ 25A	0 ~ 15A	0 ~ 30A
Output Power	2000W	5000W	10000W	15000W	15000W	18000W
Line Regulation						
Voltage	± 0.01% F.S.					± 0.01% F.S.
Current	± 0.05% F.S.					± 0.05% F.S.
Load Regulation						
Voltage	± 0.05% F.S.					± 0.05% F.S.
Current	± 0.1% F.S.					± 0.2% F.S.
Voltage Measurement						
Range	60V / 150V	120V / 600V	120V / 600V	120V / 600V	200V / 1000V	1100V / 1800V
Accuracy	0.05% + 0.05%F.S.					
Current Measurement						
Range	16A / 40A	3.4A / 8.5A	6.8A / 17A	10A / 25A	6A / 15A	15A / 30A
Accuracy	0.1% + 0.1%F.S.					
Output Noise&Ripple						
Voltage Noise(P-P)	450 mV	1500 mV	1500 mV	1500 mV	2550 mV	3500 mV
Voltage Ripple(rms)	65 mV	650 mV	650 mV	650 mV	1950 mV	750 mV
Current Ripple(rms)	80 mA	150 mA	300 mA	450 mA	270mA	250mA
OVP Adjustment Range						
Range	0 ~ 110% programmable from front panel, remote digital inputs.					
Accuracy	±1% of full-scale output					
Programming Response Time						
Rise Time: 50%F.S. CC Load	10ms (6.66A loading)	30ms	30ms	30ms	25ms	90ms
Rise Time: No Load	10ms	30ms	30ms	30ms	25ms	90ms
Fall Time: 50%F.S. CC Load	10ms (6.66A loading)	30ms	30ms	30ms	25ms	90ms
Fall Time: 10%F.S. CC Load	83ms (1.33A loading)	100ms	100ms	100ms	80ms	625ms
Fall Time: No Load	300ms	1.2s	1.2s	1.2s	3s	2.5s
Slew Rate Control						
Voltage Slew Rate Range	0.001V/ms ~ 15V/ms	0.001V/ms ~ 20V/ms	0.001V/ms ~ 20V/ms	0.001V/ms ~ 20V/ms	0.001V/ms ~ 40V/ms	0.001V/ms ~ 20V/ms
Current Slew Rate Range	0.001A/ms ~ 1A/ms, or INF	0.001A/ms ~ 0.1A/ms, or INF	0.001A/ms ~ 0.1A/ms, or INF	0.001A/ms ~ 0.1A/ms, or INF	0.001A/ms ~ 0.1A/ms, or INF	0.001A/ms ~ 0.1A/ms, or INF
Minimum Transition Time	0.5ms					
Transient response time	Recovers within 1ms to ± 0.75% of steady-state output for a 50% to 100% or 100% to 50% load change (1A/us)					1.5ms *4
Efficiency	0.77(Typical)	0.87(Typical)				0.9(Typical)
Programming & Measurement Resolution						
Voltage (Front Panel)	10 mV	10 mV	10 mV	10 mV	100mV	100mV
Current (Front Panel)	1mA	1mA	1mA	1mA	1mA	10mA
Voltage (Digital Interface)	0.002% of Vmax					
Current (Digital Interface)	0.002% of Imax					
Voltage (Analog Interface)	0.04% of Vmax					
Current (Analog Interface)	0.04% of Imax					
Programming Accuracy						
Voltage (Front Panel and Digital Interface)	0.1% of Vmax					
Current (Front Panel and Digital Interface)	0.3% of Imax					0.2% of Imax
Voltage (Analog Interface)	0.2% of Vmax					
Current (Analog Interface)	0.3% of Imax					
Parallel Operation*2	Master / Slave control via CAN for 10 units up to 150kW *1 (Parallel: ten units)					up to 288kW *3
Auto Sequencing (I-V program)						
Number of program	10					
Number of sequence	100					
Dwell time Range	1s ~ 15,000S					
Trig. Source	Manual / Auto					

Note*1 : Max. Power is 20kW for 62020H-150S.
Note*2 : There is parallel mode for DC power supply when the I-V curve function is enabled.
Note*3 : For higher power > 288kW, please call for availability.
Note*4 : Recovers within 1.5ms to ±1.5% of steady-state output for a 50% to 75% or 75% to 50% load change (0.1A/ms)
Note*5 : The high voltage wide-range output design is suitable for 1500V string PV inverter testing.

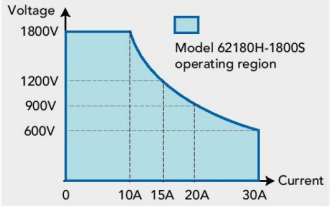

Chroma

dataTec
Mess- und Prüftechnik. Die Experten.

GENERAL SPECIFICATIONS

Model		62020H-150S	62050H-600S	62100H-600S	62150H-600S	62150H-1000S	62180H-1800S
Remote Interface							
Analog programming		Standard					
USB		Standard					
RS232		Standard					
RS485		Standard					
GPIB		Optional					
System bus(CAN)		Standard for master/slave control					
Ethernet		Optional					Standard
GPIB Command Response Time							
Vout setting		GPIB send command to DC source receiver <20ms					
Measure V&I		Under GPIB command using Measure <25ms					
Analog Interface (I/O) *							
Voltage and Current Programming Inputs (I/P)		0-10Vdc / 0 ~ 5Vdc / 0 ~ 5k ohm / 4 ~ 20 mA of F.S.					
Voltage and Current monitor output (O/P)		0 ~ 10Vdc / 0 ~ 5Vdc / 4 ~ 20mA of F.S.					
External ON/OFF (I/P)		TTL : Active Low or High (Selective)					
DC_ON Signal (O/P)		Level by user define (Time delay = 1 ms at voltage slew rate of 10V/ms.)					
CV or CC mode Indicator (O/P)		TTL Level High=CV mode ; TTL Level Low= CC mode					
OTP Indicator (O/P)		TTL : Active Low					
System Fault indicator(O/P)		TTL : Active Low					
Auxiliary power supply(O/P)		Nominal supply voltage : 12Vdc / Maximum current sink capability : 10mA					
Safety interlock(I/P)		Time accuracy: <100ms					
Remote inhibit(I/P)		TTL : Active Low					
Auto Sequencing(List Mode)							
Number of program		10					
Number of sequence		100					
Dwell time Range		5ms ~ 15000S					1ms ~ 15000S
Trig. Source		Manual / Auto / External					
Auto Sequencing (Step Mode)							
Start voltage		0 to Full scale					
End voltage		0 to Full scale					
Run time		10ms ~ 99hours					1ms ~ 99hours
Input Specification							
AC Input Volatage 3Phase, 3Wire+Ground		1Ø 200~220Vac ± 10% V_{LN}	3Ø 200~220Vac ± 10% V_{LL} ; 3Ø 380~400Vac ± 10% V_{LL} ; 3Ø 440~480Vac ± 10% V_{LL}				3Ø 380~400Vac ± 10% V_{LL}
AC Frequency range		47 ~ 63Hz					
Max Current (each phase)	200/220Vac	15.2A	39A	69A	93A	93A	--
	380/400Vac	--	22A	37A	50A	50A	37A
	440/480Vac	--	19A	32A	44A	44A	--
General Specification							
Maximum Remote Sense Line Drop Compensation		2% of full scale voltage per line (4% total)					1% of full scale voltage per line (2% total)
Operating Temperature Range		0°C ~ 40°C					
Storage Temperature Range		-40°C ~ +85°C					-25°C~+70°C
Dimension (HxWxD)		89x428x465 mm/ 3.5x16.85x16.73 inch	132.8 x 428 x 610 mm / 5.23 x 16.85 x 24.02 inch				132.8x428x660 mm/ 5.23x16.85x25.99 inch
Weight		Approx. 17 kg/37.44 lbs	Approx. 23 kg/55.70 lbs	Approx. 29 kg/63.88 lbs	Approx. 35 kg/77.09 lbs	Approx. 35 kg/77.09 lbs	Approx. 40 kg/88.19 lbs
Approval		CE					

All specifications are subject to change without notice.
Note * : None APG interface for A620027/A620028

CLIPSOL

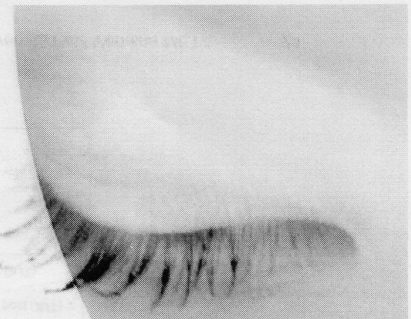

MODULE SOLAIRE PHOTOVOLTAÏQUE

CLIPSOL PV-175

Le module photovoltaique monocristallin utilise les dernieres générations de cellules monocristalline de haute performance. Ces cellules bénéficient d'un traitement anti-reflet SiN4 offrant un ratio performance/coût optimal. Les modules sont produits à partir de matériaux rigoureusement testés et conformes aux plus strictes standards de l'industrie, garantissant de hautes performances pendant plus de 25 ans.

Caractéristiques

Puissance nominale (Pmax)	175 W
Tolérance	+/- 3 %
Efficacité	16 %
Voltage Nominal	36 V
Conditions de garanties	5 ans de garantie complète Efficacité à 10 ans: 90% Efficacité à 25 ans: 80%

Configuration

Laminé livré avec câbles de sortie et connecteurs polarisés type MC3

Contraintes Physiques

Températures de fonctionnement et de stockage	de -40°C à +80°C
Poids maximum (ex: neige)	200Kg/m²
Résistance à l'impact	Bille d'acier de 270grs lachée à 1 mètre

Normes qualité & securité

* Ce module est strictement conforme aux normes CE, et IEC 61215 (laboratoires ASU, Intertek)
* Certifié ISO 9001

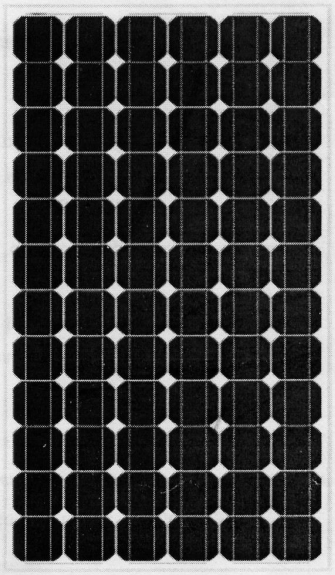

M175WU-5 Scale: 1/14

IEC CE ASU

Le soleil, votre énergie à vie

CLIPSOL

MODULE SOLAIRE PHOTOVOLTAÏQUE

CLIPSOL PV-175

Dimensions

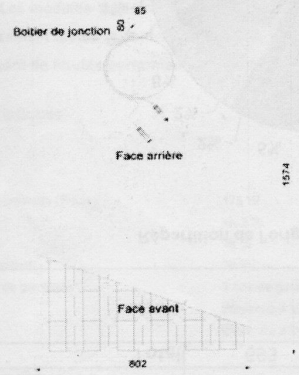

Délai de production	30 jours (moy.)
Commande minimum	1X20FT
Conditionnement	2 pcs par carton
Design de l'emballage	Optionel
Marquage	Optionel
Code barre	Optionel
Quantité par 20FT	225 pcs
Quantité par 40FT	440 pcs
Quantité par 40'HC	530 pcs

Spécifications électriques

Puissance nominale (Pmax)	175W
Voltage à Pmax (Vmp)	36.45V
Courrant à Pmax (Imp)	4.81A
Intensite de court-circuit (Isc)	5.1A
Voltage de circuit ouvert (Voc)	43.7V
Coëfficient de température à Isc	0.017%/°C
Coëfficient de température à Voc	-0.38%/ °C
Coëfficient de température à Pvoc	-0.47%/°C
Boitier de jonction	IP65
Voltage maximum admissible	1000V
NOCT (Air 20°C; Irradiation 0,8Kw/m² vitesse du vent 1m/s)	47°C +/- 2°C

Conditions Standard de Test (STC) - irradiation (1000W/m²), spectre de luminosité (AM 1.5G), température (25°C)

Spécifications mécaniques

Dimensions (mm)	1574x802x4
Poids net (Kg)	12,5
Cellules	72 cellules (125 x 125 mm) connectées en séries
Câbles de sortie	Cables de 4 mm² de diametre munis de connecteurs compatible MC3 polarisés et resistants aux conditions extérieures. Longueur 900 mm (-) et 900 mm (+)
Diodes	3 by-pass
Construction	Face avant: Verre trempé à faible teneur en fer Face arrière: TPT blanc

SEMITEACH IGBT

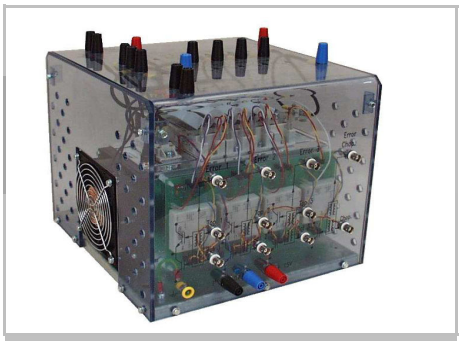

IGBT Module stack

SEMITEACH - IGBT

3-phase retifier + IGBT inverter + brake chopper

datasheet

Ordering No. 08753450
Description SEMITEACH IGBT
SKM50GB12T4, SKHI22A, SKD51/14

Features

- Multi-function IGBT converter
- IP2x protection for safety hazards
- Transparent enclosure to allow visualisation of internal part
- External connector for easy wiring
- Built in isolated IGBT driver and IGBT protection
- Forced-air cooled heatsink

Typical Applications

- Education : various converter configuration possible :

- 3-phase inverter+brake chopper
- Buck or boost converter
- single phase inverter
- single or 3-phase rectifier

Footnotes

1) The user shall ensure air ventilation for proper cooling

Remarks

This technical information specifies semiconductor devices but promises no characteristics. No warranty or guarantee, expressed or implied is made regarding delivery, performance or suitability.

Absolute maximum ratings			
Symbol	**Conditions**	**Values**	**Unit**
$I_{OUT\ MAX}$	Maximum permanent output current	**30**	A_{RMS}
$I_{IN\ MAX}$	Maximum permanent input current	**30**	A_{DC}
$V_{OUT\ MAX}$	Maximum output voltage	**400**	V_{AC}
$V_{BUS\ MAX}$	Maximum DC bus voltage	**750**	V_{DC}
f_{OUT}	Maximum inverter output frequency	**500**	Hz
f_{SW}	Maximum switching frequency	**50**	kHz

Electrical characteristics / Typical application			*$T_{AIR\ COOLING\ 1)}$ = 30°C unless otherwise specified*			
Symbol	**Conditions**		**min**	**typ**	**max**	**Unit**
Ratings						
$I_{OUT\ RATED}$	Rated output current	No overload, tamb = 30°C Chip junction T° < 150°C, (Max junction temperature = 175°C) With SEMIKRON axial fan assembly		**30**		A_{RMS}
V_{OUT}	Rated output voltage			**400**		V_{AC}
PF	Power factor			**1**		-
P_{OUT}	Rated output power			**20**		kW
f_{SW}	Inverter switching frequency			**5**		kHz
f_{OUT}	Output frequency			**50**		Hz
V_{BUS}	Rated DC voltage			**750**		V_{DC}
$P_{LOSS\ INV}$	Total power losses			**700**		W
η	Inverter efficiency			**-**		%

Protection & measurement					
Symbol	**Conditions**	**min**	**typ**	**max**	**Unit**
Thermal trip	Temperature trip level (Normally Open type: NO)		**71**		°C
Temperature sensing $T_{analogue\ OUT}$	Scaling over 30°C…110°C temperature range				$mV.°C^{-1}$
	Linear temperature range	**30**		**110**	°C
	Accuracy of analogue signal over 65°C…110°C range	**-1,5**		**1,5**	°C
	Max. output current			**5**	mA
	Max. voltage range	**0**		**10**	V_{DC}

Axial fan data					
Heatsink fans	V_{SUPPLY}	Heatsink fan DC voltage supply		**230**	Vac
	P_{FAN}	Rated power at V_{SUPPLY} per fan, PWM 100%		**15**	W

Filtering characteristics					
V_{BUS}	Rated DC voltage applied to the caps bank with switching		**540**	**700**	V_{DC}
$V_{DC\ CAP}$	Max DC voltage applied to the caps bank without switching			**800**	V_{DC}
$\tau_{d5\%}$	Discharge time of the capacitors (5%)		**-**		s
C_{DC}	Capacitor bank capacity	**0,88**		**1,32**	mF
LTE	Calculated LTE of the caps with forced air cooling		**-**		kH

Stack Insulation			
V_{ISOL}	Frame / Power stage AC/DC (insulation test voltage AC, 60s)	**1 500**	V

Driver Characteristcs					
Symbol	**Conditions**	**min**	**typ**	**max**	**Unit**
Driver board data					
V_S	Supply voltage	**14,4**	**15**	**15,6**	V_{DC}
$I_{VP,\ IDLE}$	Supply primary current (no load)		**20**		mA
$I_{VP,\ LOAD}$	Max. supply primary current			**290**	mA
ViT+	input threshold voltage HIGH			**12,5**	V_{DC}
ViT-	input threshold voltage LOW	**4,5**			V_{DC}
R_{IN}	Input resistance		**10**		kΩ

Weight	3-phase IGBT inverter	**13,3**	kg
	3-phase IGBT inverter including fan assembly	**14,9**	

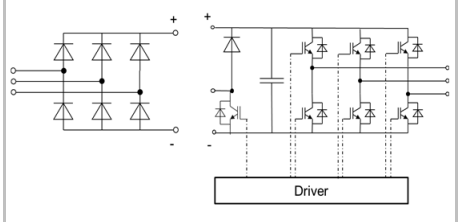

B6U + B6CI + E1CIKF

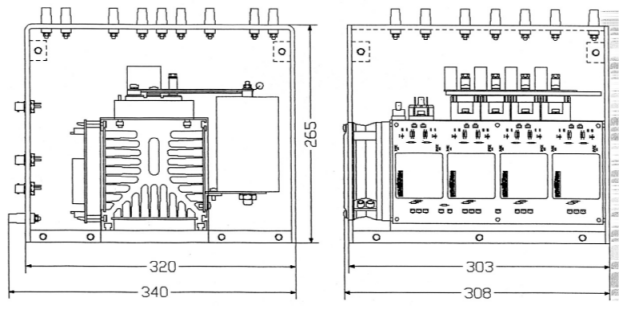

General dimensions

LITHIUM IRON PHOSPHATE BATTERY

LiFOS
ADVANCED LITHIUM POWER

Technical Data Sheet for Lifos 68

ELECTRICAL SPECIFICATIONS	
Nominal Voltage	12.8V
Nominal Capacity	68Ah
Energy	870Wh
Resistance	≤25mΩ
Efficiency	≥90%
Self Discharge	≤3% per month
Maximum Batteries in Series	N/A
Maximum Batteries in Parallel	2PCS

MECHANICAL SPECIFICATIONS	
Dimensions inc terminals (LxWxH)	257.5 x 175 x 200mm
Dimensions without terminals (LxWxH)	257.5 x 175 x 190mm
Weight	7.8kg
Terminal Type	Copper pole, M8
Terminal Torque	22～30 N.m
Case Material	ABS + PC
Enclosure Protection (IP rating)	IP54
Cell type - chemistry	LiFePO4

DISCHARGE SPECIFICATIONS	
Max Continuous Discharge Current	≤60A
Peak Discharge Current	80A-120A (under 10sec)
PCM Discharge Current Cut Off	100A±5A
PCM High Temperature Cut Off	50°C Charge/60°C Discharge
Recommended Low Voltage Disconnect	≥11.6V
Reconnect Voltage	≥12.8V
Short Circuit Protection	≥800A

CHARGE SPECIFICATIONS	
Recommended Charge Current	10-30A
Maximum Charge Current	40A
PCM Charge Current Cut Off	40A
Recommended Charge Voltage	14.4v
PCM Charge Voltage Cut Off	3.65V±0.025V/cell
Reconnect Voltage	3.0V±0.1V/cell
Balancing Voltage	3.4V/cell

TEMPERATURE SPECIFICATIONS	
Discharge Temperature	-20～60°C
Charge Temperature	0～50°C
Storage Temperature	-20～40°C
PCM High Temperature Cut-Off	85°C±5°C

COMPLIANCE SPECIFICATIONS - CERTIFICATION		
Certifications	CE Rohs	TUV TUV
Shipping Classification	MSDS	

DIMENSIONAL SPECIFICATIONS

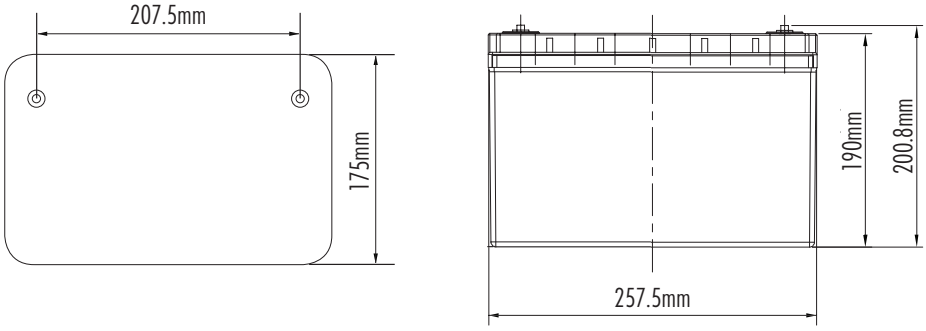

PERFORMANCE CHARACTERISTICS

5°C 14A Charging Curve

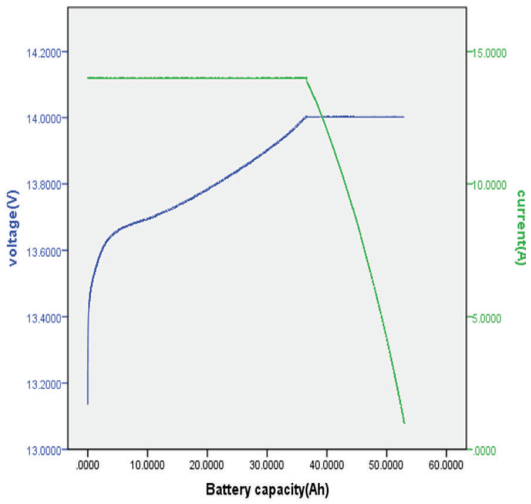

5°C 30A Discharging Curve

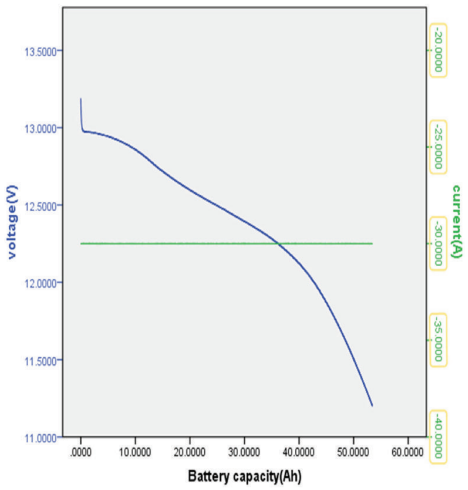

25°C 14A Discharging Curve

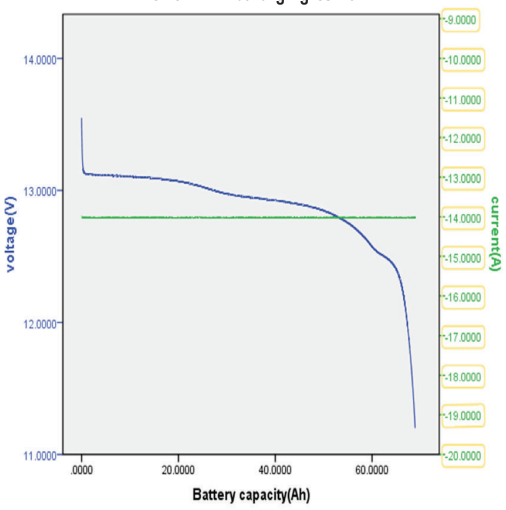

15°C 30A Discharging Curve

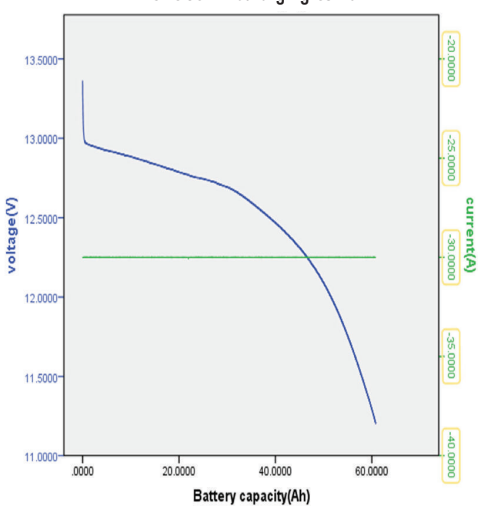

25°C 30A Discharging Curve

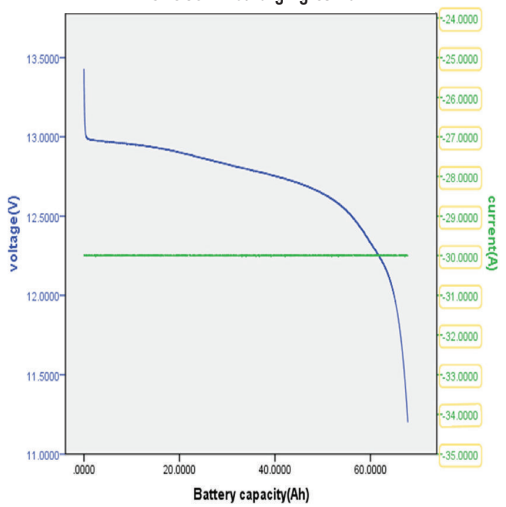

35°C 30A Discharging Curve

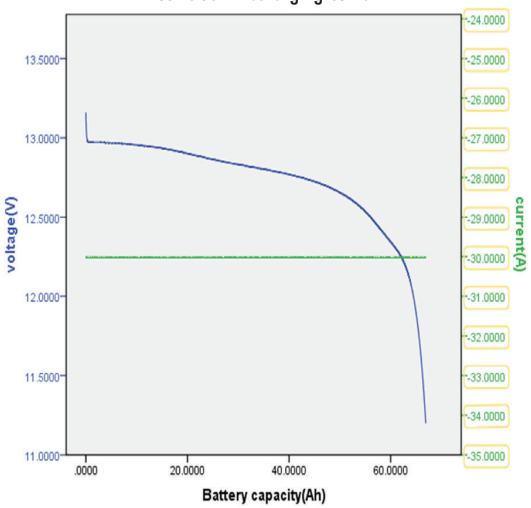

PERFORMANCE CHARACTERISTICS

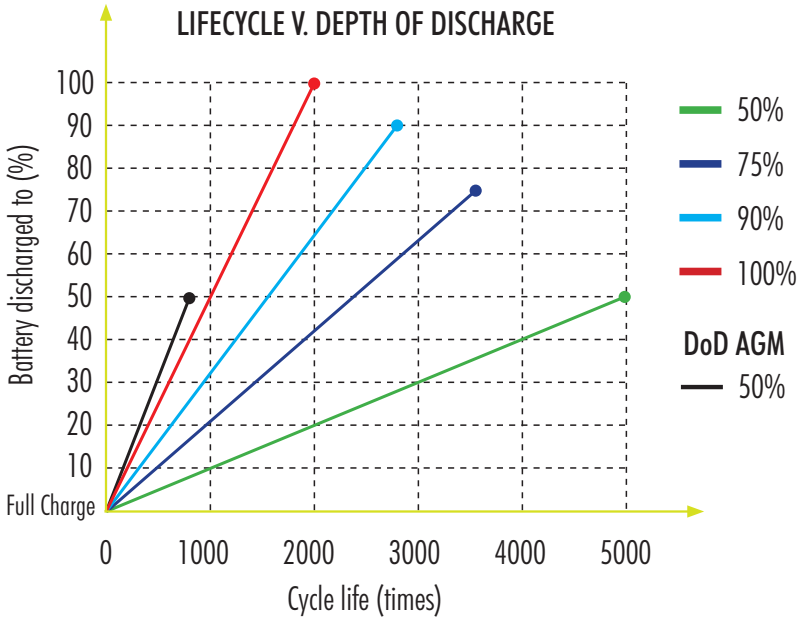

Depth of Discharge	100% DOD	90% DOD	75% DOD	50% DOD
Cycle life (times)	2000	2750	3500	5000

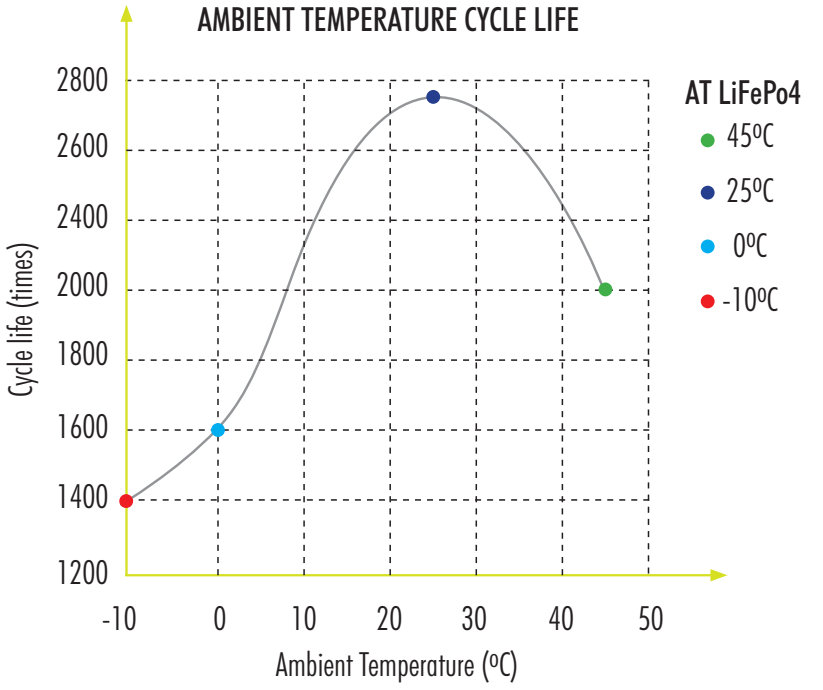

Ambient Temperature	-10ºC	0ºC	25ºC	45ºC
Cycle life (times)	1400	1600	2750	2000

Solar Technology International Ltd. Unit 6, Station Drive, Bredon, Gloucestershire GL20 7HH, United Kingdom
Tel: 01684 774000 Fax: 01684 773000 Email: support@solartechnology.co.uk www.solartechnology.co.uk

XLM-62R1137A-R Supercapacitors

62 V Module

Description

Eaton supercapacitors are high reliability, high power, ultra-high capacitance energy storage devices utilizing electrochemical double layer capacitor (EDLC) construction combined with proprietary materials and processes. This combination of advanced technologies allows Eaton to offer a wide variety of capacitor solutions tailored to applications for backup power, pulse power and hybrid power systems. They can be applied as the sole energy storage or in combination with batteries to optimize cost, life time and run time. System requirements can range from a few microwatts to megawatts. All products feature low ESR for high power density with environmentally friendly materials for a green power solution. Eaton supercapacitors are maintenance-free with design lifetimes up to 20 years and operating temperatures down to -40 °C and up to +85 °C.

Features

- Up to 20-year operating life
- Low ESR for high power density
- Long cycle life
- RoHS compliant
- Passive balancing to maximize lifetime
- Typical efficiency >98%
- Maintenance free
- Easy rack mounting

Applications

- Datacenter UPS
- Bridge power
- Hospital UPS
- Hybrid power system with fuel cells
- Grid storage
- Semiconductor equipment (SEMI F47 compliant)

Powering Business Worldwide

Ratings

Capacitance	130 F
Maximum working voltage	62.1 V
Capacitance tolerance	0% to +20% (+20 °C)
Operating temperature range	-40 °C to +65 °C

Specifications

Capacitance (F)	Part Number	Initial Maximum DC ESR[1] (mΩ)	Standby current[1] (mA) @ +20 °C 72 Hour	Maximum current[5] (A)	Peak power[2] (kW)	Total stored energy[3] (Wh)	Usable power[4] (kW)
130	XLM-62R1137A-R	6.7	128	2000	140	69.6	69.1

1. Measured according to IEC 62391 @ 62.1 V
2. Power = $Vrated^2/4/DC\ ESR$
3. Energy = $½C*Vrated^2/3600$
4. Usable power = $0.12*Vrated^2/DC\ ESR$
5. Maximum current, 1 second discharge = 1/2C*V/(1 + DC ESR*C)

Performance

Parameter (F)	Capacitance change (% of initial value)	ESR (% of maximum initial value)
Life (1500 hours @ +65 °C/62.1 Vdc)	≤ 20%	≤ 200%
Life (10 years @ +25 °C/62.1 Vdc)	≤ 20%	≤ 200%
Cycling (1M cycles +25 °C)[1]	≤ 20%	≤ 200%
Storage – 3 years (uncharged, +30 °C)	≤ 3%	≤ 10%

1. Cycle: Vrated to ½ Vrated, 100 A

Standards and certifications

Agency information	UL810A file number: MH46887
Shock and vibration	Telcordia GR-63 Zone 4
Environmental	IP30, RoHS,
Altitude, Operating	10,000 ft / 3,000 meters
Altitude, Non-operating	40,000 ft / 12,000 meters

XLM-62R1137A-R Supercapacitors
62 V Module

Technical Data **10754**
Effective June 2018

Dimensions (mm) and Mass (kg)

Part Number	W	L	H	Typical Mass (kg)
XLM-62R1137A-R	176	635	173	16
Tolerance	± 1.0			

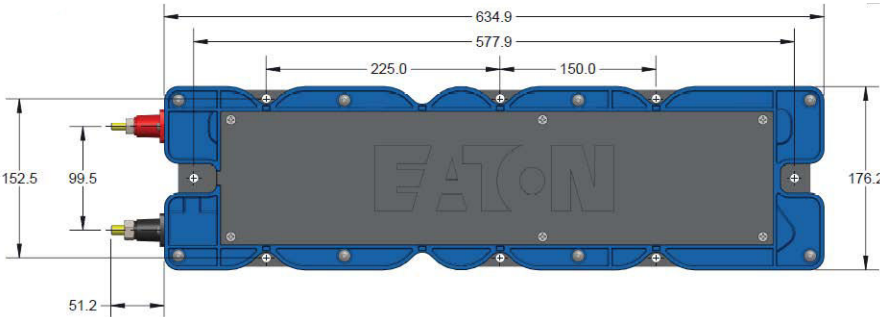

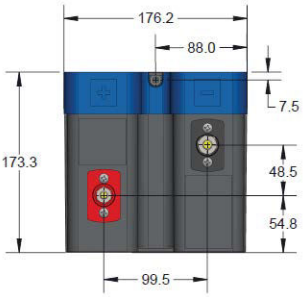

Positive Terminal: 5/16″ – 18 threaded stud

Negative Terminal: 3/8″ – 16 threaded stud

Part numbering system

XLM	— 62R1	13	7	A	-R
Family Code	Voltage (V) R= decimal	Capacitance (µF)			
		Value	Multiplier	Passive balancing	
XLM = Family code	62R1= 62.1 V	Example 130=13 x 10⁷ µF or 130 F			Standard product

Packaging information

- Standard packaging: 1piece per box

Part marking

- Capacitance (F)
- Nominal working voltage (V)
- Family code (lot number & serial #)
- Polarity marking

Eaton
Electronics Division
1000 Eaton Boulevard
Cleveland, OH 44122
United States
www.eaton.com/electronics

Printed in USA
Publication No. 10754 PCN-18008
June 2018

Powering Business Worldwide